8-2011

MULTI-SCALE MODELING OF POLYMERIC MATERIALS: AN ATOMISTIC AND COARSE-GRAINED MOLECULAR DYNAMICS STUDY

Qifei Wang
CHEMICAL ENGINEERING, qwang7@utk.edu

To the Graduate Council:

I am submitting herewith a dissertation written by Qifei Wang entitled "MULTI-SCALE MODELING OF POLYMERIC MATERIALS: AN ATOMISTIC AND COARSE-GRAINED MOLECULAR DYNAMICS STUDY." I have examined the final electronic copy of this dissertation for form and content and recommend that it be accepted in partial fulfillment of the requirements for the degree of Doctor of Philosophy, with a major in Chemical Engineering.

David J Keffer, Major Professor

We have read this dissertation and recommend its acceptance:

David J Keffer, Bamin Khomami, Eric T Boder, Jimmy Mays

Accepted for the Council:
Dixie L. Thompson

Vice Provost and Dean of the Graduate School

(Original signatures are on file with official student records.)

MULTI-SCALE MODELING OF POLYMERIC MATERIALS: AN ATOMISTIC AND COARSE-GRAINED MOLECULAR DYNAMICS STUDY

A Dissertation

Presented for the

Doctor of Philosophy

Degree

The University of Tennessee, Knoxville

Qifei Wang

August 2011

Dedication

To my Father

Acknowledgements

I wish to thank my wonderful advisor, Dr. David Keffer for his great guidance, generous support, and invaluable advice at all stages of this research. He brought me into this amazing molecular modeling world. For many years, his professional mentoring, encouragement and passions for innovations helped me on many occasions in my research and will definitely play an important role in my future academic life.

I would also like to thank professors in my committee: Dr. Bamin Khomami, Dr. Eric Boder and Dr. Jimmy Mays for the instructive discussions and insightful questions that provided an intelligence provoking environment and a wonderful learning experience for me.

I express special gratitude to Dr. Non Nicholson, Dr. Gary Grest, Dr. Brock Thomas, Dr. Simioan Petrovan and Dr. Suxiang Deng for their active participation and insightful feedback at various stages of this research.

I also wish to express my appreciations to the department administrative assistants, Mrs Jane Breder, Ms. Lori Daniels and Ms. Cristina Wilson, for their sincerely kind help in dealing with any non-academic matter during the past four years.

Finally, I greatly appreciate the support and encouragement from my family: My parents, who gave me life, raised me and provided everything I need with the limited resources; My wife, who gave me continuous support; My son, who brought most of the joys to the family.

Abstract

Computational study of the structural, thermodynamic and transport properties of polymeric materials at equilibrium requires multi-scale modeling techniques due to processes occurring across a broad spectrum of time and length scales. Classical molecular-level simulation, such as Molecular Dynamics (MD), has proved very useful in the study of polymeric oligomers or short chains. However, there is a strong, nonlinear dependence of relaxation time with respect to chain length that requires the use of less computationally demanding techniques to describe the behavior of longer chains. As one of the mesoscale modeling techniques, Coarse-grained (CG) procedure has been developed recently to extend the molecular simulation to larger time and length scales. With a CG model, structural and dynamics of long chain polymeric systems can be directly studied though CG level simulation. In the CG simulations, the generation of the CG potential is an area of current research activity.

The work in this dissertation focused on both the development of techniques for generating CG potentials as well as the application of CG potentials in Coarse-grained Molecular Dynamics (CGMD) simulations to describe structural, thermodynamic and transport properties of various polymer systems. First, an improved procedure for generated CG potentials from structural data obtained from atomistic simulation of short chains was developed. The Ornstein-Zernike integral equation with the Percus Yevick approximation was invoked to solve this inverse problem ($OZPY^{-1}$). Then the $OZPY^{-1}$ method was applied to CG modeling of polyethylene terephthalate (PET) and polyethylene glycol (PEG). Finally, CG procedure was applied to a model of sulfonated and cross-linked Poly (1, 3-cyclohexadiene) (sxPCHD) polymer that is designed for future application as a proton exchange membrane material used in fuel cell.

Through above efforts, we developed an understanding of the strengths and limitations of various procedures for generating CG potentials. We were able to simulate entangled polymer chains for PET and study the structure and dynamics as a function of chain length. The work here also provides the first glimpses of the nanoscale morphology of the hydrated sxPCHD membrane. An understanding of this structure is important in the prediction of proton conductivity in the membrane.

Table of Contents

List of Tables

Chapter 5

Chapter 7

List of Figures

Chapter 4

Chapter 6

Chapter 7

CHAPTER 1

Introduction

Polymeric materials like plastics, rubbers and fibers play an important role in our everyday life. Their unique physical and chemical properties like flexibility, transparency, conductivity, roughness and durability can be found in various applications in the modern world. The common feature of this type of polymeric material is the long chain molecular structure. For many years, physicists and chemists have made tremendous efforts to understand and improve the structure and properties of polymeric materials based on understanding at the molecular-level. When the length scale goes down to the nanoscale (molecular level), the experimental study becomes more difficult and unreliable.

With the continued development of computer technology, computer simulation has become a valuable tool in polymer science. When the length scale is less than 10 nm and time scale is less than 100 ns roughly, classical molecular simulation techniques like Molecular Dynamics (MD) or Monte Carlo (MC) simulations are widely used in the study of the structural, thermodynamic and transport properties of polymeric oligomers at equilibrium. MD is based on the time evolution of the molecular system, providing the actual trajectories of each particle in the system. One of the main advantages of MD simulation is the generation of transport properties, such as self-diffusivity, zero-shear-rate viscosity and thermal conductivity. We implemented MD simulations in this work. In molecular simulation (either MC or MD), the force field plays an important role in generating accurate results. An atomistically detailed model is usually used with interaction potential parameters determined from parameterization to either quantum mechanic calculations or experimental data. Many force fields have been developed for polyatomic molecules.[1-5] These force fields generate accurate simulation results that are in good agreements with experiments.

The classical molecular simulation study of structures and properties polymeric materials is limited to short chain oligomers. One of the major reasons is that the longest relaxation time of a polymer is strongly dependent on the chain length. When chain length is small, the molecular simulation is still tractable since the relaxation time is generally less than 100 ns. When chain length increases, the relaxation time increases exponentially. It could easily exceed 1000 ns for long chain polymeric systems. This makes the study of structural and dynamic properties very difficult through classical molecular simulations. Another reason is different simulation techniques have their own advantages and limitations. The major limitation of applying a

molecular model to polymers is the number of degree of freedoms in the atomistically detailed model. The high resolution model generates accurate simulation results but impacts the computational efficiency. Many local interactions like bond stretching, bending and torsion have to be calculated to obtain the total potential energy. Meanwhile, a small step size has to be used for these high frequency modes. For these reasons, the time and length scales used in molecular simulation are far below that of real long chain polymer systems. With finite computational resources, it remains beyond current computational capabilities to use an atomistically detailed simulation technique to obtain long time trajectory of long chains. To study polymer physics at different time and length scales, one has to rely multi-scale modeling, which is actually a combination of different simulation techniques.

The coarse-grained (CG) procedure lifts these computational limitations by eliminating some degrees of freedom in the simulation in exchange for computational efficiency. The reduction in the degrees of freedom is accomplished by grouping atoms in certain fragments of the chain into "beads", which interact with their own CG potential.[6-8] Since the degrees of freedom are greatly reduced in the CG model, many local interactions are neglected.[8] Larger length and time scales can be reached in the CG level simulation. Structural and transport properties can be calculated directly by CG simulation.[9] Furthermore, the CG level properties can be mapped back to molecular level through the use of scaling factors.[8,10,11]

Similar to atomistic simulation, obtaining reliable nonbonded interaction potentials is the important and challenging part of the CG procedure. Three common methods have been adopted in the literatures: (1): adjusting power law type potential parameters (Lennard-Jones 12-6, 7-6, 7-4, 7-5),[6-8,12] (2): iterative Boltzmann inversion (IBI) method[13,14] and (3): method based on integral equation (IE) theory.[15,16] In the first method, the parameters of an analytical potential can be obtained by fitting to either theory or experimental data, which makes the method computationally efficient. Potentials from this method can closely reproduce the atomistic structure. However, depending on the CG model and force fields used in atomistic sampling, complicated nonbonded CG pair correlation functions (PCFs) can be generated. When dealing with complicated nonbonded PCFs, it can be difficult to reproduce the structures of atomistic simulation using this method. As a comparison, the IBI method is designed to reproduce the structure of atomistic sampling. The effective potential is iteratively refined until the structure

from CG level simulation matches the target one from atomistic level simulation. As an iterative method, it negatively impacts computational efficiency obtained from coarse-graining. It may not work for multi-components system like polymer solution or complicated CG models where potentials of different CG beads affect with each other. In the method based on the Ornstein-Zernike (OZ) integral equation theory, the relationship between structure (PCFs) and interaction potentials is expressed in either Percus-Yevick (PY) or hypernetted-chain (HNC) approximations for the direct correlation function in OZ integral. The IE theory is normally used to generate structural properties like PCFs given the interaction potential. It is revisited by researchers recently on CG procedure to obtain nonbonded potential parameters[17] or tabulated potentials coupled with liquid state theory.[10,11,18] This method is based on sound statistical mechanics. Once derived, it is straightforward, fast and generalized to different systems. The difficult part is to solve the integral equation with PY or HNC approximations. Due to these approximations, it may cause problems when applied to high density liquids, where the PY and HNC approximations fail.

In the CG procedure, atomistic simulation normally is first conducted on small systems with polymer oligomers, from which structural distributions for the CG beads are extracted. Then the CG force field is parameterized using one of above methods according to the problems of interests. The CG potential is validated by performing CGMD simulations of the same short chains and directly comparing the results with those from atomistic simulations. Finally, structures and dynamics of large system can be studied though CG level simulation using the CG force field. The CG based multi-scale modeling technique has been used in the study of structure and dynamics of biomacromolecules,[19,20] polymer chain molecules (polysterene (PS),[7,8,12] polymethyl methacrylate (PMMA),[9] polyethylene oxide (PEO),[21] bisphenol-A polycarbonate (BPA-PC)[22] and azobenzene liquid crystal[6]), and recently proton exchange membrane (PEM) polymers.[23,24]

Polyethylene terephthalate (PET) is one of the important engineering plastic used in everyday life. Although the molecular simulation of polyethylene PET has a long history,[25-29] the CG simulation of PET is less prevalent in the literature. Kamio *et al.*[13] performed CG end-bridging MC simulations of PET melts, generating equilibrium structural and entanglement properties. Dynamic properties are not reported in this work. This current work is aimed at

conducting CGMD simulations to investigate the structural and dynamic properties of PET chains with a DP up to 50. Longer chain length is not used, considering the balance on study of both structures and dynamics. This range of DP is also relevant because PET leaving an industrial finishing reactor possesses a DP in the 30 to 50 range.[30]

The study of polymer electrolytes in PEM fuel cells has become of particular interest. Recently, researchers have been trying to find PEM material that can retain moisture at higher operating temperatures in the fuel cell, in order to reduce the amount of expensive noble metal catalyst required in the device. Mays' group at the University of Tennessee, Knoxville, has synthesized a set of novel non-fluoropolymer based, potentially low cost and high temperature fuel cell membranes based on poly(1,3-cyclohexadiene) (PCHD).[31-33] The sulfonated and cross-linked PCHD (sxPCHD) based PEM materials include homopolymer (sxPCHD), polymer blend (sxPCHD/Polyethylene glycol (PEG)) and block copolymer (sxPCHD-PEG). At high humidity, the conductivity of some membranes is about 10 times that of a Nafion based membrane.[34] The researchers believe that the morphology of this type of PEM accounts for the high conductivity. Information on the molecular level structure will help people understand the mechanism of high proton conductivity of this material.

In this work, we aimed to study polymeric materials structure and properties at different time and length scales. Atomistic and CG MD simulations are applied to different polymeric systems with different emphasis. These systems include: bulk PET, bulk PEG, bulk sxPCHD and hydrated sxPCHD membrane. All the CG procedures for these systems start with atomistic MD simulations. The main tasks of this work are summarized in the following paragraphs

In Chapter 2, the OZPY theory is used to generate interaction potentials from PCFs of monatomic and diatomic Lennard-Jones fluids. The aim of the work is to derive a CG potential generation method that can compromise both the computational efficiency and accuracy. The test on simple Lennard-Jones fluids is a self-consistency test before applying to polymer melts.

In Chapter 3, MD simulations of PET oligomers are performed in the isobaric-isothermal (NpT) ensemble at a state point typical of a finishing reactor. The oligomer size ranges from one to ten repeat units. Structural, thermodynamic and transport properties are calculated for systems with different oligomer size. The chain length dependence of these quantities are studied and

compared to experiments and theories. Furthermore, all structural information are obtained and analyzed for the next stage CG procedure.

In Chapter 4, a CG model of PET was developed and implemented in CGMD simulations of PET chains with degree of polymerization up to 50. The CG potential is parameterized to structural distribution functions obtained from atomistic simulations using $OZPY^{-1}$. Average chain end-to-end distance and radius of gyration, relaxation time, self-diffusivity and zero-shear-rate-viscosity's dependence on DP is reported. Scaling exponents have been extracted and compared with Rouse and Reptation models. Entanglement analysis is conducted to further study the Reptation behavior.

In Chapter 5, a CG model of PEG was developed and implemented in CGMD simulations of PEG chains with degree of polymerization (DP) 20 and 40. In the model, two repeat units of PEG are grouped as one CG bead. Atomistic MD simulation of PEG chains with DP = 20 was first conducted to obtain the bonded structural probability distribution functions (PDFs) and nonbonded PCFs of the CG beads. The CG nonbonded potential is parameterized to the PCF using both $OZPY^{-1}$ and a combination of $OZPY^{-1}$ with the IBI method ($OZPY^{-1}$+IBI). Performances of different CG potentials generation methods are compared. The new CG model and CG potentials from $OZPY^{-1}$+IBI method was further tested through CGMD simulation of PEG with DP = 40 system.

In Chapter 6, atomistic and CG models of sxPCHD were developed and implemented in MD simulations of sxPCHD chains with different architectures, which are specifically aimed for application as a PEM used in fuel cells. An atomistic force field for the architectures was tested and applied in the atomistic MD simulation of sxPCHD for the first time. CG potentials are generated by IBI method. Structural distribution functions from CGMD simulations of sxPCHD melt with different architectures is presented.

In Chapter 7, atomistic and coarse-grained (CG) models of sxPCHD are further tested in the hydrated sxPCHD membrane system. The system includes water, hydronium ions and sxPCHD polymer. The atomistic level simulation generates PCFs for all possible pairs. Water and hydronium ion distribution and transport in hydrated sxPCHD membrane are studied. The structure of the polymer under melt and hydrated conditions are compared. To apply the IBI method to obtain the effective potentials for PCHD polymer in the hydrated membrane, water

molecules and hydronium ions are made implicit at the CG level. A comparison on structures from two level simulations is also presented.

Finally, in Chapter 8, the main conclusions from each work described in this dissertation are summarized, and overall impact of the current achievement and views on future work are discussed.

References

[1]W. L. Jorgensen, D. S. Maxwell, and J. TiradoRives, J. Am. Chem. Soc. **118**, 11225 (1996).

[2]W. L. Jorgensen, J. P. Ulmschneider, and J. Tirado-Rives, J. Phys. Chem. B **108**, 16264 (2004).

[3]M. G. Martin and J. I. Siepmann, J. Phys. Chem. B **102**, 2569 (1998).

[4]S. L. Mayo, B. D. Olafson, and W. A. Goddard, Journal of Physical Chemistry **94**, 8897 (1990).

[5]A. K. Rappe, C. J. Casewit, K. S. Colwell, W. A. Goddard, and W. M. Skiff, J. Am. Chem. Soc. **114**, 10024 (1992).

[6]C. Peter, L. Delle Site, and K. Kremer, Soft Matter **4**, 859 (2008).

[7]V. A. Harmandaris, N. P. Adhikari, N. F. A. van der Vegt, and K. Kremer, Macromolecules **39**, 6708 (2006).

[8]V. A. Harmandaris, D. Reith, N. F. A. Van der Vegt, and K. Kremer, Macromol. Chem. Phys. **208**, 2109 (2007).

[9]C. X. Chen, P. Depa, J. K. Maranas, and V. G. Sakai, J. Chem. Phys. **128**, 124906 (2008).

[10]A. J. Clark and M. G. Guenza, J. Chem. Phys. **132**, 044902 (2010).

[11]I. Y. Lyubimov, J. McCarty, A. Clark, and M. G. Guenza, J. Chem. Phys. **132**, 5 (2010).

[12]V. A. Harmandaris and K. Kremer, Macromolecules **42**, 791 (2009).

[13]K. Kamio, K. Moorthi, and D. N. Theodorou, Macromolecules **40**, 710 (2007).

[14]D. Reith, M. Putz, and F. Muller-Plathe, J. Comput. Chem. **24**, 1624 (2003).

[15]J. G. Curro and K. S. Schweizer, Macromolecules **20**, 1928 (1987).

[16]K. S. Schweizer and J. G. Curro, Adv. Chem. Phys. **98**, 1 (1997).

[17]L. Zhao, Y. G. Li, J. G. Mi, and C. L. Zhong, J. Chem. Phys. **123**, 124905 (2005).

[18]M. G. Guenza, J. Phys.: Condens. Matter **20**, 033101 (2008).

[19]A. Villa, C. Peter, and N. F. A. van der Vegt, Phys. Chem. Chem. Phys. **11**, 2077 (2009).

[20]K. Voltz, J. Trylska, V. Tozzini, V. Kurkal-Siebert, J. Langowski, and J. Smith, J. Comput. Chem. **29**, 1429 (2008).

[21]C. X. Chen, P. Depa, V. G. Sakai, J. K. Maranas, J. W. Lynn, I. Peral, and J. R. D. Copley, J. Chem. Phys. **124**, 234901 (2006).

[22]B. Hess, S. Leon, N. van der Vegt, and K. Kremer, Soft Matter **2**, 409 (2006).

[23]K. Malek, M. Eikerling, Q. P. Wang, T. C. Navessin, and Z. S. Liu, J. Phys. Chem. C **111**, 13627 (2007).

[24]K. Malek, M. Eikerling, Q. P. Wang, Z. S. Liu, S. Otsuka, K. Akizuki, and M. Abe, J. Chem. Phys. **129** (2008).

[25]R. K. Bharadwaj and R. H. Boyd, Polymer **40**, 4229 (1999).

[26]S. P. Bravard and R. H. Boyd, Macromolecules **36**, 741 (2003).

[27]M. S. Hedenqvist, R. Bharadwaj, and R. H. Boyd, Macromolecules **31**, 1556 (1998).

[28]H. Eslami and F. Muller-Plathe, Macromolecules **42**, 8241 (2009).

[29]N. C. Karayiannis, V. G. Mavrantzas, and D. N. Theodorou, Macromolecules **37**, 2978 (2004).

[30]Q. F. Wang, D. J. Keffer, S. Petrovan, and J. B. Thomas, J. Phys. Chem. B **114**, 786 (2010).

[31]K. L. Hong, Y. N. Wan, and J. W. Mays, Macromolecules **34**, 2482 (2001).

[32]T. Huang, H. Zhou, K. Hong, J. M. Simonson, and J. W. Mays, Macromol. Chem. Phys. **209**, 308 (2008).

[33]K. Hong, M. Liu, and J. W. Mays, Polym. Prepr. (Am. Chem. Soc., Div. Polym. Chem.) **44**, 657 (2003).

[34]J. W. Mays, S. Deng, K. A. Mauritz, M. K. Hassan, and S. P. Gido, Patent No. US20090306295A1 (2009).

CHAPTER 2

Use of the Ornstein-Zernike Percus-Yevick Equation to Extract Interaction Potentials from Pair Correlation Functions

This chapter is a slightly revised version of a paper by the same title published in the *Journal of Physical Review E* in 2010 by Qifei Wang, David J. Keffer, Donald M. Nicholson, and J. Brock Thomas:

Wang, Q., Keffer, D.J., Nicholson, D.M., Thomas, J.B., "Use of the Ornstein-Zernike Percus-Yevick Equation to Extract Interaction Potentials from Pair Correlation Functions", *Phys. Rev. E* **81**(6) 2010 article # 061204.

The use of "we" in this part refers to the co-authors and the author of this dissertation. My primary contributions to this paper include (1) all of the simulation work (2) analysis of data, and (3) most of the writing

Abstract

In this work, we test the ability of the Ornstein-Zernike equation in the Percus Yevick approximation (OZPY) to generate interaction potentials from pair correlation functions (PCFs) of monatomic and diatomic Lennard-Jones fluids. The PCFs are generated by solving OZPY equation (monatomic fluid) and Molecular Dynamics (MD) simulations (diatomic fluid). Since the interaction potentials are inputs in the OZPY method and the MD simulation, the extraction of the potential from the PCFs using OZPY is a test of self-consistency. This test is necessary if the procedure is to be used to generate coarse-grained (CG) potentials from PCFs. We find that the procedure is completely self-consistent for the monatomic fluid in the whole range of densities studied (reduced density up to 0.55, under reduced temperature 2.0). In the diatomic case, we find that the procedure is generally self-consistent under both low and high densities, although there is a systematic deviation at high densities. The method is able to reproduce the two parameters (ε and σ) of the input Lennard-Jones potential model to within about 1%. This CG potential generating procedure can be straightforwardly extended to more complicated molecules.

2.1 INTRODUCTION

In the development of coarse-grained (CG) potentials for polymers, one can perform the complete atomistic molecular dynamics (MD) simulation (for which the interaction potentials are known) for a system of short chains and, based on the mapping of CG particles to the center of mass of polymer fragments, generate pair correlation functions (PCFs) for stretching, bending, torsion and nonbonded interactions between CG particles. One then must extract the CG interaction potential for each mode from each PCF. For the stretching, bending and torsion modes, there are straightforward approximations that relate the interaction potential directly to the PCF. For example, for the stretching mode, via, the interaction energy between a particle of type α and a particle of type β, $\varphi_{\alpha\beta,S}$, as a function of the separation between particles, r, can (with proper validation) be related to the stretching pair correlation function, $g_{\alpha\beta,S}(r)$, via

$$\varphi_{\alpha\beta,S}(r) = -k_B T \ln\left(g_{\alpha\beta,S}(r)\right) + c_{\alpha\beta,S} \tag{1}$$

where k_B is Boltzmann's constant, T is temperature and $c_{\alpha\beta,S}$ is a constant. Similar expressions apply to the bending and torsion modes [1-3].

For the nonbonded interactions, this level of approximation is inadequate because the pair-wise potential can give rise to large higher order correlations. Thus there is a need to develop a rigorous way to extract a CG nonbonded potential from the PCF.

There are two major methods currently used to extract the nonbonded CG potentials. First, the parameters of an analytic potential such as Lennard-Jones are adjusted to closely reproduce the target PCF in the atomistic liquid/melt. Work from Harmandaris *et al.*[1,2,4] on coarse-grained modeling of polystyrene represents this approach in which target chain molecules are separated into fragments so that the nonbonded interaction between different fragment types, $\{\alpha, \beta \ldots\}$ is based on the fragment corresponding PCF, $g_{\alpha,\beta}$. A problem with this method is that the difference of conformations and orientations between fragment molecules and target molecules may not be reflected correctly on the corresponding coarse-grained potentials.[3,5] For example, the conformations of phenol rings in liquid benzene and that in PS melt where the rings are embedded into a long chain may be different. Consequently, these conformations would be misrepresented in the CG potential.

In the second method, a tabulated potential is numerically determined by iterative Boltzmann inversion[6]. The interaction potential is refined iteratively via

$$\varphi_{\alpha\beta,i+1}(r) = \varphi_{\alpha\beta,i}(r) + k_B T\left(\frac{g_{\alpha\beta,i}(r)}{g_{\alpha\beta}(r)}\right) \tag{2}$$

where $g_{\alpha\beta}(r,r')$ is the target PCF. The convergence of the procedure is guaranteed by the fact that there is a unique functional relationship between the PCF and the pairwise-additive potential. Potentials obtained from this procedure will closely reproduce the CG atomistic liquid PCFs. Using this method, Kamio *et al.*[7] performed CG end bridging Monte Carlo simulations of poly(ethylene terephthalate) melt and obtained CG melt density, characteristic ratio and other conformational properties that agree with experiment. The challenging part of this method is obtaining PCFs from simulations in each iteration. As mentioned by Guenza[8], those simulations have to be performed on length scales and timescales large enough to ensure a reliable numerical predictions of the potential at the length scale characteristic of the coarse-graining procedure. This could strongly limit the computational gain of CG procedure. Thus, extraction of the nonbonded interaction potential for CG models remains an important problem.

We present an alternative procedure based on the Ornstein-Zernike equation with the Percus-Yevick approximation (OZPY) to extract the CG nonbonded potential from the PCFs. This method is approximate only because of the approximate nature of the PY assumption for the direct correlation function. On the other hand, it is simple and fast compared to methods of comparable accuracy. It is a step forward from Eqn. 1 in theoretical rigor; it acknowledges the influence of interactions with surrounding particles that should be present in the determination of pairwise potentials from the PCF.

The OZPY equation is typically used to generate PCFs given the interaction potential. We refer to this as the OZPY procedure. The use of the OZPY equation to extract the interaction potential from the PCFs, we will call inverse OZPY or OZPY^{-1}. Before the OZPY^{-1} procedure can be applied to the development of CG potentials, it must first demonstrate the capability to reproduce known results. To this end, we apply it to two fluids: a monatomic Lennard-Jones fluid and a flexible diatomic Lennard-Jones fluid. We point out that while the OZPY is nonlinear

in the PCF, it is linear in the exponential of the interaction potential, making the inverse OZPY equation relatively straightforward to solve.

The OZPY theory is well established for simple fluids, both pure and in mixtures. The challenging part of OZPY^{-1} is formulating the OZPY theory to account for the presence of a stretching potential between some of the atoms. The OZ integral has been under study for several decades in the fields of monatomic, diatomic and polyatomic fluids theories. Most of the research focuses on the calculation of structural properties of the fluids. A literature survey shows that OZPY gives results that match well the PCFs from molecular simulation of low density monatomic fluids but deviate at high density[9] . For this reason, Verlet and Weis[10] proposed several empirical corrections. Tang and Lu[11] and Yuste *et al.*[12] developed improved expressions that can reproduce the simulation data. These expressions are somewhat more cumbersome that the PY approximation. In the diatomic case, a numerical procedure[13] and sophisticated models[14,15] , have been developed to solve the OZ equation to exactly reproduce the structural properties of diatomic Lennard-Jones[13,15] and hard dumbbell fluids[14] .

The application of integral equation theories to polymers has a long history[16,17] , and continues to be used in the development of modern multiscale models of polymers[18,19] . The Polymer Reference Interaction Site Model (PRISM)[20,21] has become the most fully developed and widely used integral equation approach[22] , with areas of application that include polymer solutions[23] , colloid-polymer suspensions[24] and CG procedures[8,21,22,25] . Most of these applications are related to the calculation of structural properties like PCFs[21,22] or other correlation functions[8,25] .

In the application to CG potentials, Zhao *et al.*[22] adopted an approach similar to iterative Boltzmann inversion method to obtain the two optimized parameters of a CG Lennard-Jones potential model of atactic polystyrene (PS) melt, using PRISM to calculate intermolecular PCFs with intramolecular PCFs with atomistic MD simulation as input. Since it is still a numerical procedure, it suffers the same disadvantage as the iterative Boltzmann inversion method.

The OZPY equation[26] used here is relatively simple and can be easily inverted. The use of OZPY^{-1} method[27] to obtain the interaction potential is currently limited to monatomic

systems[28-31] . In this paper, we demonstrate that this method can also be applied to the diatomic Lennard-Jones fluid.

To this end, using known atomistic interaction potentials, we generated PCFs for two systems, a monatomic Lennard-Jones fluid and a flexible diatomic Lennard-Jones fluid, in which each atom interacts with other nonbonded atoms via the Lennard-Jones interaction potential. For each system we use the OZPY^{-1} procedure to regenerate the nonbonded interaction potential. Given that the nonbonded interaction potential is known a self-consistency test is provided, establishing the reliability of the procedure for generating CG potentials. Note that we are not generating a CG potential in this work; rather we are reproducing atomistic potentials via the same OZPY^{-1} procedure that could be used to generate a CG potential. The procedure is illustrated in Figure 2.1.

2.2 SIMULATION

For the monatomic fluid, PCFs can be generated either from MD simulation or from solution of the OZPY equation. Using the PCFs from OZPY can provide a cleaner test of the OZPY^{-1} procedure than using them from simulation. Therefore, PCFs used here for monatomic fluid were generated by solving the OZPY integral equation, using an established method and code developed by Lee.[32] Different state points were investigated for the monatomic fluid, the corresponding states varies from low-density gas to high density liquid. The dimensionless temperature of the simulation was $T^* = 2.00$ and the dimensionless densities were $\rho^* = 0.005$, 0.15, 0.25, 0.35, 0.45 and 0.55. Classical MD simulations were also run at some of these state points in order to compare the PCFs from simulation and integral equation theory. As a point of reference, the critical point for the Lennard-Jones fluid lies at a reduced temperature of 1.293 and reduced density of 0.313 [33] .

For the diatomic fluid, PCFs were generated from classical MD simulations rather than from the OZPY integral equation, because of the additional complexity introduced by the internal structure of the molecule. For both the monatomic and diatomic fluids, the MD simulations were performed on an in-house code, using a two-time step reversible RESPA algorithm[34] . The diatomic molecules are fully flexible. The stretching potential is a Hookian spring for molecular nitrogen taken from ref. [35] , with equilibrium bond distance r_{eq} = 1.09 Å and

force constant k_S = 3185.788 kcal/mole/Å^2. The nonbonded interactions between atoms on neighboring molecules employ a Lennard-Jones potential with ε/k_B = 36 K and σ = 3.31 Å[35] . The nonbonded interactions were truncated at 15 Å. The time steps for integration were 0.2 fs for the stretching mode and 2 fs for the nonbonded interactions. The simulations were run in the canonical ensemble using the Nosé-Hoover thermostat[34] . The simulations consisted of 1000 molecules and were equilibrated for 1 ns followed by 2 ns of data production. The low density simulations of the diatomic system were run at T^* = 8.3333 and ρ^* = 0.07341. The high density simulations were run at T^* = 5.5556 and ρ^* = 0.5057. ρ^* is the reduced molecular density.

2.3 THEORY

The Ornstein-Zernike Integral Equation for a mixture of simple fluids is[26]

$$g_{\alpha\beta}(r,r') - 1 = c_{\alpha\beta}(r,r') + \sum_{\gamma} \int c_{\alpha\gamma}(r,r'') n_{\gamma}(r'') \left[g_{\gamma\beta}(r'',r') - 1 \right] d^3 r'' \tag{3}$$

where the pair correlation function between particles of type α and β located respectively at r and r', $g_{\alpha\beta}(r,r')$, is related to the direct correlation, $c_{\alpha\beta}(r,r')$, and an integral including the interactions of the α and β particles with a third particle, γ, located at r'' with a singlet density, $n_{\gamma}(r'')$. There is a summation over γ spanning all types of particles. This equation in its present form implicitly allows for a different interaction potential between each pair of types of particles. In essence, the summation over γ is a summation over interaction potentials.

For the diatomic fluid, we need to modify the OZ equation so that it can account for some particles interacting via a stretching potential and some particles interacting via a nonbonded potential. In the case of the single-component diatomic fluid investigated here, the summation over γ becomes explicitly a summation over interaction potentials. In order to emphasize this, we rewrite the OZ equation, replacing the $\alpha\beta$ subscripts, with φ_i subscripts,

$$g_{\varphi_1}(r,r') - 1 = c_{\varphi_1}(r,r') + \sum_{\varphi_2} \sum_{\varphi_3} \int c_{\phi_2}(r,r'') n(r'') \left[g_{\varphi_3}(r'',r') - 1 \right] d^3 r'' \tag{4}$$

There is some ambiguity associated with the PCF of a given potential, when the same particle can interact via different potentials (e.g. stretching or nonbonded). We shall address this shortly.

For the purposes of our work here, we will use this equation to solve for the nonbonded potential, assuming the stretching potential is obtained from equation (1). As such φ_1 is always the nonbonded potential, while the summations of φ_2 and φ_3 include both nonbonded and stretching potentials. Some combinations of φ_2 and φ_3 are not permitted. For the case of a homonuclear diatomic fluid, the three possible combinations are illustrated in Figure 2.2. The third particle can interact (1) with the first via a nonbonded interaction and the second via a nonbonded interation, (2) with the first via a stretching interaction and the second via a nonbonded interation, and (3) with the first via a nonbonded interaction and the second via a stretching interation. The fourth combination, that of the third particle interacting with both the first and second particles via a stretching interaction, does not exist in a diatomic fluid, where each particle has a stretching interaction with one and only one other particle.

The Percus-Yevick approximation expresses the direct correlation function as

$$\mathrm{c}_{\varphi_i}(r,r') = \mathrm{g}_{\varphi_i}(r,r')\left[1-\exp\left(\frac{\varphi_1(r,r')}{k_B T}\right)\right] \tag{5}$$

We follow convention in defining the cavity function[36] and total correlation function

$$\mathrm{y}_{\varphi_i}(r,r') = \mathrm{g}_{\varphi_i}(r,r')\exp\left(\frac{\varphi_1(r,r')}{k_B T}\right) \tag{6}$$

$$\mathrm{h}_{\varphi_i}(r,r') = \mathrm{g}_{\varphi_i}(r,r') - 1 \tag{7}$$

Substitution of equations (5) through (7) into equation (4) yields the Ornstein-Zernike equation with the Percus-Yevick Approximation or the OZPY equation

$$\mathrm{y}_{\varphi_1}(r,r') = 1 + \sum_{\varphi_2}\sum_{\varphi_3}\int \mathrm{c}_{\phi_2}(r,r'')\mathrm{n}(r'')h_{\varphi_3}(r',r'')\mathrm{d}^3 r'' \tag{8}$$

If the fluid is homogeneous in space, the positions can be replaced by displacements

$$r = |r-r'|, s = |r-r''|, t = |r'-r''| \tag{9}$$

and equation (8) rewritten as

$$\mathrm{y}_{\varphi_1}(r) = 1 + \sum_{\varphi_2}\sum_{\varphi_3}\int \mathrm{c}_{\phi_2}(s)\mathrm{n}\, h_{\varphi_3}(t)\mathrm{d}V \tag{10}$$

where the integral is over all volume. Following Lee[32], it is convenient to convert the volume integral to bipolar coordinates, which yields

$$\mathrm{y}_{\varphi_1}(r) = 1 + \sum_{\varphi_2}\sum_{\varphi_3} \frac{2\pi\,\mathrm{n}}{r} \int_0^\infty \mathrm{ds}\, s\, \mathrm{c}_{\phi_2}(s) \int_{|r-s|}^{r+s} \mathrm{dt}\, t\, h_{\varphi_3}(t) \tag{11}$$

Substitution of the PY approximation into the integrand yields

$$\mathrm{y}_{\varphi_1}(r) = 1 + \sum_{\varphi_2}\sum_{\varphi_3} \frac{2\pi\,\mathrm{n}}{r} \int_0^\infty \mathrm{ds}\, s \left[\mathrm{h}_{\phi_2}(s) - \mathrm{y}_{\phi_2}(s) + 1\right] \int_{|r-s|}^{r+s} \mathrm{dt}\, t\, h_{\varphi_3}(t) \tag{12}$$

Conceptually, then we measure all $h_{\varphi_i}(t)$ in the simulation and we solve equation (12) numerically for $\mathrm{y}_{\varphi_1}(r)$ from which the potential can be directly extracted.

We now resolve the ambiguity of the PCF for a given potential, which was introduced above. The PCF for an arbitrary interaction potential is equal to the number of pairs of particles of type α and β interacting via that potential at a distance *r*, averaged over all α particles and normalized by the average density of the β particles,

$$\mathrm{g}_{\alpha\beta,\varphi_i}(r) \equiv \frac{N_{\varphi_1,pairs}(r)}{N_\alpha N_\beta} \cdot \frac{V}{\mathrm{V}(r)} = \frac{N_{\varphi_1,pairs}(r)}{N_\alpha\, \mathrm{V}(r)} \cdot \frac{1}{n_{\beta,\varphi_i}} \tag{13}$$

where V is the system volume and N_α and N_β are the number of particles involved in interaction φ_i in the system and we define a component density as $n_{\beta,\varphi_i} = \frac{N_\beta}{V}$, which itself now is tied to a given potential. In a mixture of simple fluids all of the quantities in equation (13) are completely unambiguous; the number of particles of type α and β are independent of the potential. However, when one looks even at a single-component homonuclear diatomic fluid, the number of α particles is well defined, but the density of β particles interacting only with a single given potential is unclear, since all β particles interact with both stretching and nonbonded potentials. We define an unambiguous pair correlation function, the local density of particles interacting via interaction potential φ_i, $\mathrm{g}'_{\alpha\beta,\varphi_i}(r)$, which is directly calculated in an MD simulation,

$$\mathrm{g}'_{\alpha\beta,\varphi_i}(r) = n_{\beta,\varphi_i}\, \mathrm{g}_{\alpha\beta,\varphi_i}(r) = \frac{N_{\varphi_1,pairs}(r)}{N_\alpha\, \mathrm{V}(r)} \tag{14}$$

where V(r) is the volume of the spherical shell. Now the PCF has units of density and there is no ambiguity in the meaning or evaluation of this quantity because n_{β,φ_i} has been eliminated. This

is the local density of particles of type β around particles of type α, interacting via φ_i. We define analogous variables for the cavity, total and direct correlation functions.

$$\mathrm{y}'_{\alpha\beta,\varphi_i}(r) = n_{\beta,\varphi_i}\mathrm{y}_{\alpha\beta,\varphi_i}(r) = \mathrm{g}'_{\alpha\beta,\varphi_i}(r)\exp\left(\frac{\varphi_1(r)}{k_BT}\right) \tag{15}$$

$$\mathrm{h}'_{\alpha\beta,\varphi_i}(r) = n_{\beta,\varphi_i}\mathrm{h}_{\alpha\beta,\varphi_i}(r) = \mathrm{g}'_{\alpha\beta,\varphi_i}(r) - n_{\beta,\varphi_i} \tag{16}$$

$$\mathrm{c}'_{\alpha\beta,\varphi_i}(r) = n_{\beta,\varphi_i}\mathrm{c}_{\alpha\beta,\varphi_i}(r) = \mathrm{g}'_{\alpha\beta,\varphi_i}(r)\left[1-\exp\left(\frac{\varphi_1(r)}{k_BT}\right)\right] \tag{17}$$

We then recast the OZPY equation in terms of these new variables, where we drop the extraneous $\alpha\beta$ subscripts used in the derivation, since in this work we only have one type of particle.

$$\mathrm{y}'_{\varphi_1}(r) = n_{\beta,\varphi_1} + \sum_{\varphi_2}\sum_{\varphi_3}\frac{2\pi}{r}\int_0^\infty \mathrm{d}s\, s\, c'_{\varphi_2}(s)\int_{|r-s|}^{r+s}\mathrm{d}t\, t\, h'_{\varphi_3}(t) \tag{18}$$

In this rearrangement, we have introduced n_{β,φ_i} into equations (16) and (18). For the monatomic case where only nonbonded interactions are present, this density is the density of atoms in the system. For the stretching potential, we used the following function,

$$n_{\beta,S}(r) = \begin{cases} 0 \; for \; r < r_{S,\min} \\ 1/V_S \qquad for \; r_{S,\min} \le r \le r_{S,\max} \\ 0 \; for \; r > r_{S,\max} \end{cases} \tag{19}$$

where $r_{S,\min}$ is the smallest value for which $\mathrm{g}'_S(r)$ is non-zero, $r_{S,\max}$ is the largest value for which $\mathrm{g}'_S(r)$ is non-zero, and the volume accessible to the stretching molecules is the volume of the spherical shell bound between $r_{S,\min}$ and $r_{S,\max}$. This is an empirical definition of the density of particles interacting via stretching, but it mimics the common definition used for particles interacting via nonbonded interactions, the number of neighbors over the available volume. The value of the stretching potential at $r_{S,\max}$ is 11.5 k_BT, so the occupancy is negligible (exp(-11) ~ 10^{-5}).

We also note that because equation (1) is assumed true for the stretching mode, the cavity and direct correlation functions for the stretching mode become

$$y'_S(r) = n_{\beta,S}(r) \tag{20}$$

$$c'_S(r,r') = g'_S(r) - n_{\beta,S}(r) \tag{21}$$

In the monatomic case, we solved the OZPY equation, which is linear in $y'_{\varphi_1}(r)$. We discretize the radial dimension in increments of 0.05 Å and use the trapezoidal rule to evaluate the integrals. We then solve the system of linear algebraic equations for $y'_{\varphi_1}(r)$ from which the nonbonded potential is easily obtained from equation (15).

2.4 RESULTS

2.4.1 Simple Fluids monatomic molecule

For the monatomic case, we can obtain the PCF either from MD simulation or from solution of the OZPY equation directly. In Figure 2.3, we compare the PCFs from these two methods at reduced densities of 0.55 and 0.9. At the higher density, there is a visible discrepancy between the two methods, attributed to the Percus-Yevick approximation. Up to a density of 0.55 the agreement between simulation and integral equation theory is very good. Similar simulation results are available in ref.[15] . For the monatomic case, we choose to use the PCF from the OZPY equation as the input into the potential generating procedure. This is the preferred approach because it avoids errors due to disagreements between PY-theory and simulation and provides a test of self-consistency for the procedure.

For the monatomic case, we solved the OZPY equation directly to obtain the PCF for reduced densities from 0.005 to 0.55 and a reduced temperature of 2.0. The PCFs are shown in Figure 2.4. They are shifted by increments of 0.25 on the y-axis for visual clarity. We see the low-density PCF reflect a single peak feature that is typical for a low-density monatomic gas. The high density PCF has two peaks with a more pronounced first peak.

These PCFs were input into the $OZPY^{-1}$ procedure to obtain the interaction potentials. The interaction potentials are compared with the original Lennard-Jones 12-6 potential in Figure 2.5. The potentials are shifted by increments of 0.25 on the y-axis for clarity. As expected, excellent agreement is shown in Figure 2.5 for low density cases. As the density increases there is a small but growing discrepancy between the original potential and the potential from the $OZPY^{-1}$ procedure, which we attribute to numerical approximations in the evaluation of the

integrals. Generally, we see that the OZPY^{-1} procedure is able to satisfactorily reproduce the interaction potential.

It is of interest to see where a simple approximation of the nonbonded potential, such as that given in equation (1), is valid. In Figure 2.6, we compared the potential obtained from equation (1), using the PCF from the OZPY method, with the input Lennard-Jones potential. As expected, the two potentials match very well at low density but deviate at high densities. A simple expression like equation (1) fails dramatically at high loading because it introduces one or more longer ranged repulsive components to the potential that are not part of the repulsive core. If one assumes that there is no three-body interactions in the system, then these repulsive regions in the potential are required to generate the observed structure in the PCF.

Figure 2.7 shows the cavity function, $y_N(r)$, obtained from the OZPY^{-1} procedure. $y_N(r)$ is an important property in the OZPY^{-1} algorithm since it is directly related to the interaction potential. The OZPY^{-1} is very sensitive to this function. A small error in $y_N(r)$ may cause a significant deviation in the potential. Notice that when $g_N(r)$ goes to zero, the definition of $y_N(r)$ becomes ambiguous since the corresponding potential goes to infinity. Approximations from both simulation and theory have been applied to get $y_N(r)$ at short range. Our results for the short range $y_N(r)$ are similar to those of Law *et al.*[27], who used a two dimensional predictor-corrector method to obtain the interaction potential of a colloidal monolayer, in which $y_N(r)$ for small *r* was approximated by hard sphere fluid theory. The similarity indicates that the short range $y_N(r)$ is fairly insensitive to the interaction potential, as noted elsewhere[37] . The results for $y_N(r)$ here were calculated directly by the OZPY^{-1}, in which $y_N(r)$ is the unknown variable. This reduces the extra computational work on the approximation of $y_N(r)$ in short range.

2.4.2 Diatomic fluid at low density

In the diatomic case, the stretching and nonbonded Radial Density Functions (RDFs), $g'_N(r)$ and $g'_S(r)$, were generated via MD simulation (of N_2). At low density (T^* = 8.3333 and ρ^* = 0.07341), the nonbonded RDF has a single peak (Figure 2.8.). Note that the plateau for the nonbonded RDF is twice the reduced density, since we are examining a diatomic molecule. The stretching RDF shows a sharp peak around its equilibrium bond distance (r_{eq}). We note that there

are relatively few non-zero points in the stretching RDF, due to the fact that it is resolved on the same discretization as the nonbonded RDF. The smooth curve is a Gaussian, which is the theoretical expectation if the stretching mode is independent of the nonbonded interaction, as assumed in equation (1). The fit between the data and the Gaussian curve is good. We use these RDFs as input for the diatomic OZPY^{-1} algorithm. We note that the stretching RDF obtained from MD simulation satisfies equation (1), when the input stretching potential is inserted. Thus, the validity of equation (1) is established.

In Figure 2.9, we compare the nonbonded interaction potential extracted from the OZPY^{-1} procedure. It matches well with the original Lennard-Jones potential, although there is some noise in the data. If we eliminate the noise by fitting the data to a Lennard-Jones potential and extracting the ε and σ parameters, we see that the fit is excellent. The percent error between the estimated and original values for ε and σ are respectively 1.1% and 1.0%. Thus, we see that the OZPY^{-1} procedure can extract a highly accurate nonbonded potential from the simulation data of a diatomic fluid, at least at low density.

2.4.3 Diatomic fluid at high density

The PCFs generated from MD simulations at high density for (T^* = 5.5556 and ρ^* = 0.5057) are shown in Figure 2.10. The nonbonded RDF shows four peaks within a distance of 5σ. Similar structural features under both low and high densities can be found in the work of Lue and Blankschtein[38] in Monte Carlo simulation of a flexible diatomic Lennard-Jones fluid, indicating that our MD simulation correctly captured the structure of the fluid. The peak of $g_S'(r)$ is much higher than at low density. We compare the potential from the OZPY^{-1} procedure with the input potential in Figure 2.11. The potentials agree well at distances below 1.2 and above 1.7. From 1.2 to 1.3, the extracted potential is slightly low and from 1.4 to 1.7, it is significantly high. Again, for the stretching interaction, the smooth curve is a Gaussian, which is expected if the stretching mode is independent of the nonbonded interaction.

We now discuss the possible sources of error and their impact. A potential source of error is that we have assumed that equation (1) is true for the stretching potential. Equation (1) implies the stretching distribution is independent of the nonbonded distribution. This error can be

determined to be small in this case, since the stretching potential extracted from equation (1) matches the stretching potential used in the MD simulation.

The error could be due to the fact that the MD simulation and the OZPY description of the diatomic fluid are not the same. In other words, the error is a manifestation of the approximation in the integral equation theory. Such errors have been noted before. For example, using the Hyper-Netted Chain (HNC) closure, Bresme *et al.*[13] has proven that the bond length and stretching interaction potential could affect the comparison of structural properties of diatomic Lennard-Jones fluids calculated by OZ integral theory with simulation data. This is because solving the OZ integral with HNC closure using a central force model cannot satisfy the condition that the number of bonds per atom is unity, compared with the real diatomic Lennard-Jones fluid. In our inverse procedure, we use the PCFs from MD simulation of the Lennard-Jones fluid and we carefully checked the above mentioned condition by integrating the PCFs over space. The average number of bonds per atom is about 1.05 for both low and high density cases. (The error is due to the small number of points in which the stretching distribution is non-zero and the approximate numerical integration.) So, while we do have the correct number of stretching modes per atom, we may still be subject to other impacts of the PY approximation[27] .

In Figure 2.11, we fit a Lennard-Jones potential to the interaction potential extracted from the $OZPY^{-1}$ procedure in the range from $r = 0$ to 1.3, which yields errors between the estimated and original values for ε and σ of respectively 1.1% and 1.0%. We do not know the generalizability of the value of r = 1.3, however, we report it here in order to indicate, at least in this case, where the reliable portion of the potential was located. This excellent agreement shows that the $OZPY^{-1}$ procedure can be used to generate a potential, containing at least a portion of the original potential that is quantitatively the same. In the context of developing coarse-grained potentials molecules this degree of quantitative agreement should represent an improvement. Specifically, this procedure delivers a highly accurate value of ε, compared to other polymer course-graining procedures that assign a value of k_BT to ε^1 . The procedure can be easily extended to obtain the CG nonbonded interaction potential parameters for a polymer system, by including allowable bending and torsion interactions in the potential summation in equation (18).

In this work, we have demonstrated that the inverse application of the OZPY equation is capable of reproducing known interaction potentials, establishing the validity of the method, at

least for the simple systems studied here. The future application of this procedure to the development of coarse grain potentials for nanoparticles or polymers or other materials can be pursued with some confidence based on these results, although there are certainly differences in the relative complexity of these systems. The choice of Percus-Yevick closure is not mandatory for this inverse method and may not be the best closure for all applications. The PY closure yields accurate results for systems that have a short-range, hard-core potentials, while the HNC closure is more accurate for systems that have soft-core, long-range interactions[8] . In the application to the coarse-graining of polymers, as the extent of coarse-graining increases, the number of configurations averaged into the CG bead increases and consequently the interaction potentials become softer, perhaps indicating that HNC is more appropriate. As the systems become more complex, the limitations of the method may also become more pronounced.

2.5 CONCLUSIONS

We have demonstrated that the OZPY equation can be used to extract interaction potentials given distribution functions for monatomic and diatomic fluids. In the monatomic fluid case, the procedure is able to reliably reproduce the original Lennard-Jones 12-6 potential up to moderate densities. In the diatomic case, we first obtained the density distributions for stretching and nonbonded interaction sites from classical equilibrium MD simulation of nitrogen under low and high density cases. By incorporating the stretching potential into the OZPY equation, we extracted a nonbonded interaction potential which matched the original Lennard-Jones 12-6 potential at low densities. At higher densities, there was a systematic difference between the original potential and that extracted from the $OZPY^{-1}$ procedure, which we attribute to the PY approximation. However, the short-range portion of the potential is reproduced sufficiently well that the ε and σ parameters can be reproduced to within 1.1% and 1.0% respectively. This level of accuracy would represent an improvement in the development of coarse-grained potentials. Application to polymeric systems is underway.

2.6 ACKNOWLEDGMENT

This research was supported by the Eastman Chemical Company and by the U.S. Department of Energy, Office of Basic Energy Sciences, Division of Materials Sciences and Engineering.

This research project used resources of the National Institute for Computational Sciences (NICS) supported by NSF under agreement number: OCI 07-11134.5.

References

[1]V. A. Harmandaris, N. P. Adhikari, N. F. A. van der Vegt, and K. Kremer, Macromolecules **39**, 6708 (2006).

[2]V. A. Harmandaris, D. Reith, N. F. A. Van der Vegt, and K. Kremer, Macromol. Chem. Phys. **208**, 2109 (2007).

[3]A. Villa, C. Peter, and N. F. A. van der Vegt, Phys. Chem. Chem. Phys. **11**, 2077 (2009).

[4]V. A. Harmandaris and K. Kremer, Macromolecules **42**, 791 (2009).

[5]C. Peter, L. Delle Site, and K. Kremer, Soft Matter **4**, 859 (2008).

[6]D. Reith, M. Putz, and F. Muller-Plathe, J. Comput. Chem. **24**, 1624 (2003).

[7]K. Kamio, K. Moorthi, and D. N. Theodorou, Macromolecules **40**, 710 (2007).

[8]M. G. Guenza, J. Phys.: Condens. Matter **20**, 033101 (2008).

[9]C. Barrio and J. R. Solana, Phys. A **351**, 387 (2005).

[10]L. Verlet and J. J. Weis, Phys. Rev. A **5**, 939 (1972).

[11]Y. P. Tang and B. C. Y. Lu, J. Chem. Phys. **103**, 7463 (1995).

[12]S. B. Yuste, M. L. deHaro, and A. Santos, Phys. Rev. E **53**, 4820 (1996).

[13]F. Bresme, J. L. F. Abascal, and E. Lomba, J. Chem. Phys. **105**, 10008 (1996).

[14]G. Munao, D. Costa, and C. Caccamo, J. Chem. Phys. **130**, 144504 (2009).

[15]M. Marucho and B. M. Pettitt, J. Chem. Phys. **126**, 124107 (2007).

[16]J. G. Curro and K. S. Schweizer, Macromolecules **20**, 1928 (1987).

[17]K. S. Schweizer and J. G. Curro, Adv. Chem. Phys. **98**, 1 (1997).

[18]J. McCarty, I. Y. Lyubimov, and M. G. Guenza, J. Phys. Chem. B **113**, 11876 (2009).

[19]A. J. Clark and M. G. Guenza, J. Chem. Phys. **132** (2010).

[20]C. J. Grayce, A. Yethiraj, and K. S. Schweizer, J. Chem. Phys. **100**, 6857 (1994).

[21]K. S. Schweizer, E. F. David, C. Singh, J. G. Curro, and J. J. Rajasekaran, Macromolecules **28**, 1528 (1995).

[22]L. Zhao, Y. G. Li, J. G. Mi, and C. L. Zhong, J. Chem. Phys. **123**, 124905 (2005).

[23]S. Mendez and J. G. Curro, Macromolecules **37**, 1980 (2004).

[24]M. Fuchs and K. S. Schweizer, J. Phys.: Condens. Matter **14**, R239 (2002).

[25]E. J. Sambriski, G. Yatsenko, M. A. Nemirovskaya, and M. G. Guenza, J. Chem. Phys. **125** (2006).

[26]H. T. Davis, *Statistical mechanics of phases, interfaces, and thin films* (VCH, New York, 1996).

[27]A. D. Law and D. M. A. Buzza, J. Chem. Phys. **131**, 094704 (2009).

[28]J. R. Silbermann, S. H. L. Klapp, M. Schoen, N. Chennamsetty, H. Bock, and K. E. Gubbins, J. Chem. Phys. **124**, 074105 (2006).

[29]S. H. Behrens and D. G. Grier, Phys. Rev. E **6405**, 050401 (2001).

[30]M. Brunner, C. Bechinger, W. Strepp, V. Lobaskin, and H. H. von Grunberg, Europhys. Lett. **58**, 926 (2002).

[31]R. Rajagopalan and K. S. Rao, Phys. Rev. E **55**, 4423 (1997).

[32]L. L. Lee, *Molecular thermodynamics of nonideal fluids* (Butterworths, Boston, 1988).

[33]J. T. Fern, D. J. Keffer, and W. V. Steele, J. Phys. Chem. B **111**, 13278 (2007).

[34]D. J. Keffer, C. Baig, P. Adhangale, and B. J. Edwards, Mol. Simul. **32**, 345 (2006).

[35]J. J. Potoff and J. I. Siepmann, AIChE J. **47**, 1676 (2001).

[36]D. Henderson and S. Sokolowski, J. Chem. Phys. **104**, 2971 (1996).

[37]D. A. McQuarrie, *Statistical mechanics* (Harper & Row, New York, 1976).

[38]L. Lue and D. Blankschtein, J. Chem. Phys. **102**, 4203 (1995).

Appendix A

Tables and Figures

Table 2.1. Necessary combinations for single component diatomic case.

α	β	γ	$\alpha\beta$	$\alpha\gamma$	$\gamma\beta$	$\alpha\gamma\beta$	Allowed
A	A	A	N	N	N	NN	YES
A	A	A	N	S	N	SN	YES
A	A	A	N	N	S	NS	YES
A	A	A	N	S	S	SS	No, not in a diatomic system

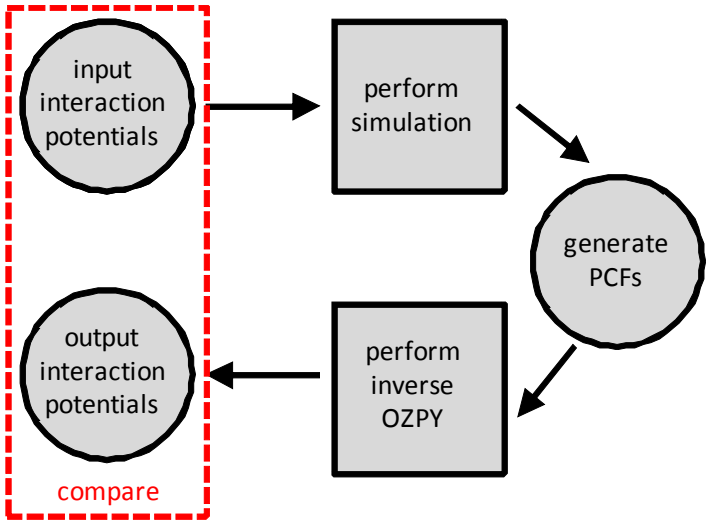

Figure 2.1. Schematic of the validation procedure.

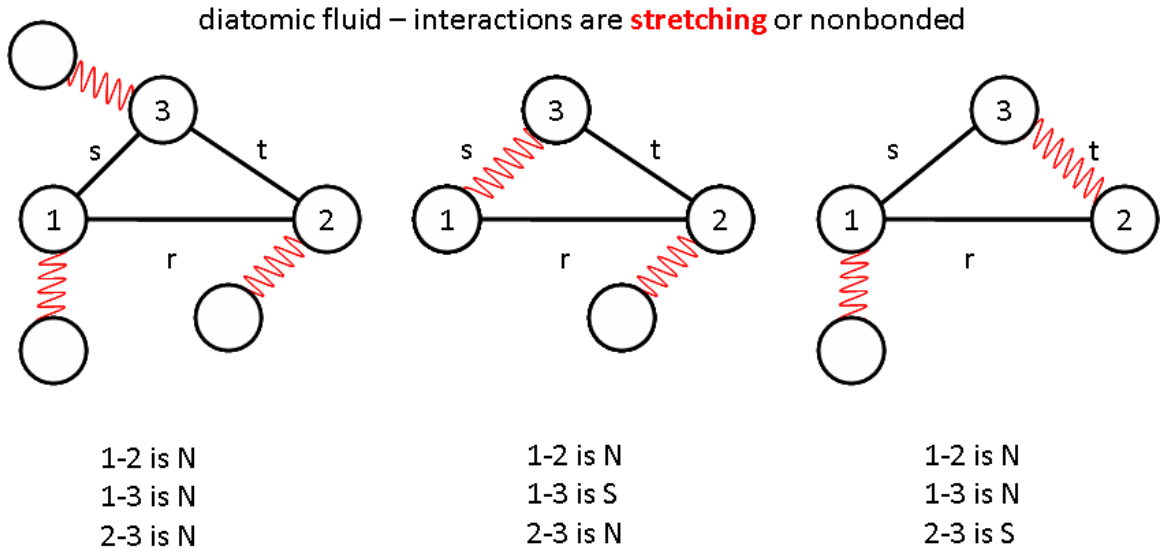

Figure 2.2. Schematic of allowed interaction combinations of diatomic case. The three choices for particle three are shown for a diatomic molecule. The "red" springs represent an interaction via stretching. The "black" bars represent an interaction via the nonbonded potential. Additional atoms are shown for completeness, although they do not appear in the OZPY equation.

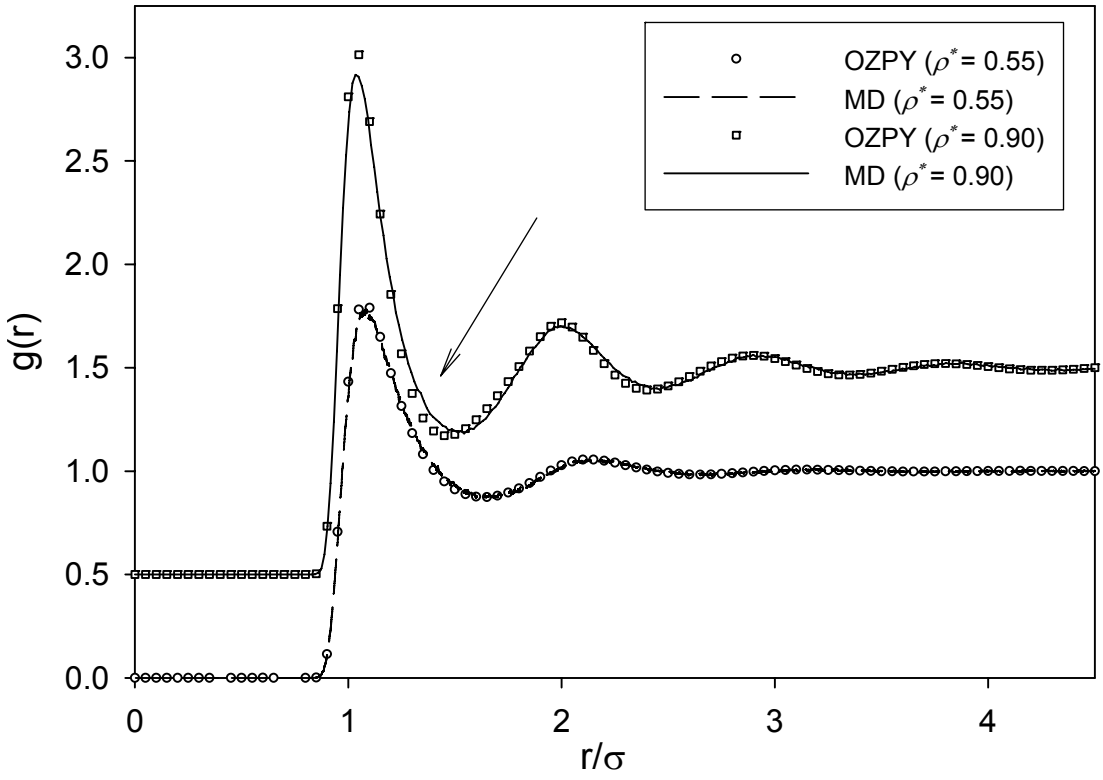

Figure 2.3. Comparison of Pair Correlation Functions (PCFs) obtained by solving OZPY equation directly and MD simulation of a Lennard-Jones fluid at $T^* = 2.0$, $\rho^* = 0.55$ and 0.90, here $T^* = T/\varepsilon$; $\rho^* = \rho\,\sigma^3$. The data has been shifted in the vertical direction for clarity.

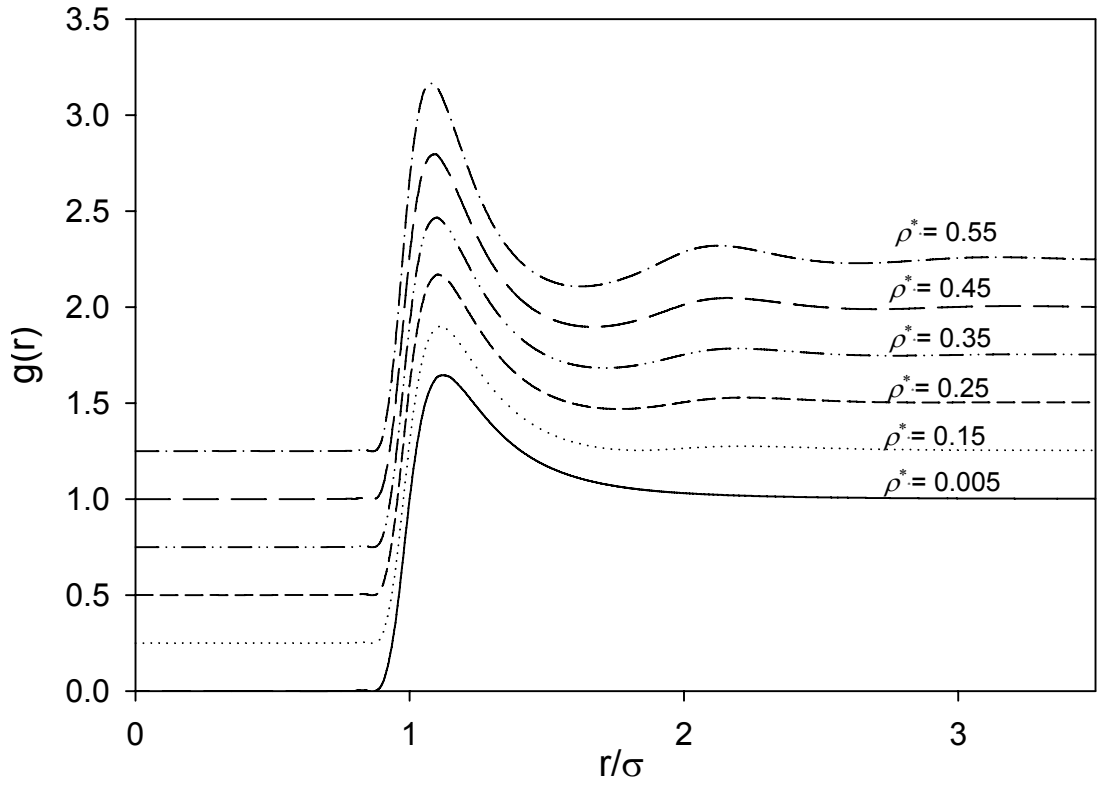

Figure 2.4. PCFs obtained by solving OZPY equation directly, under $T^* = 2.0$, ρ^* from 0.005 to 0.55. The data has been shifted in the vertical direction for clarity.

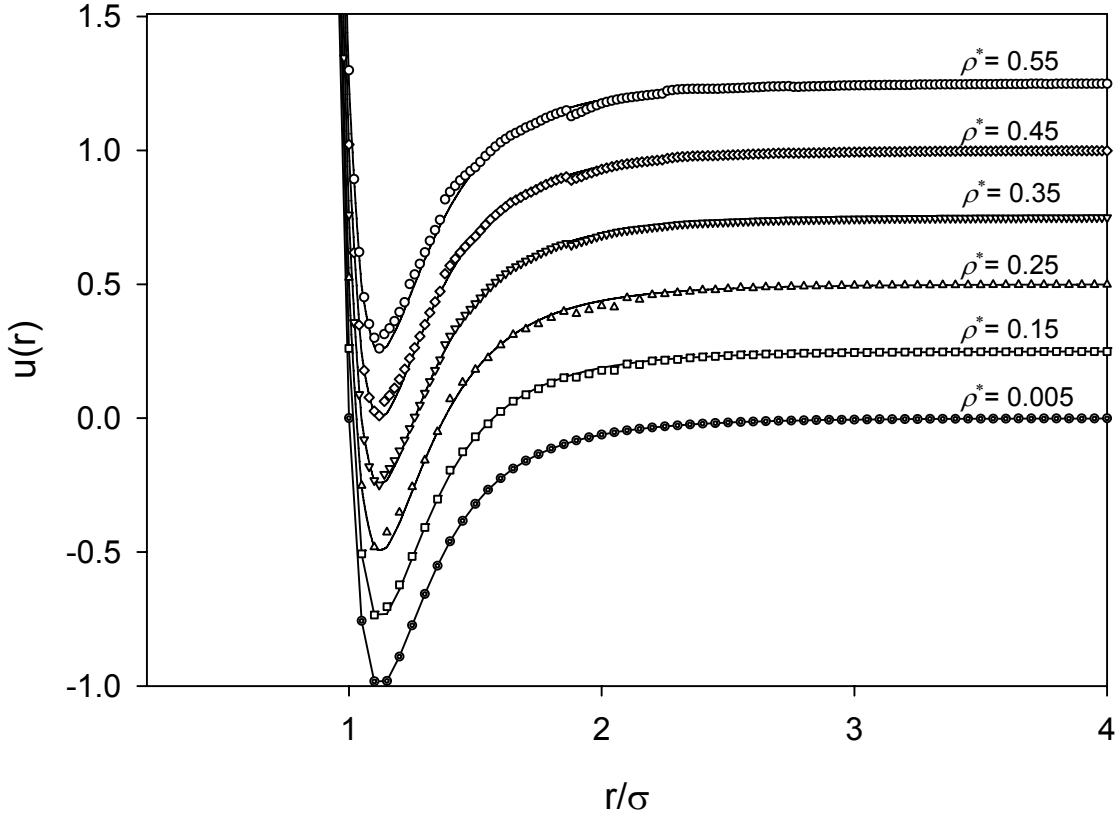

Figure 2.5. Comparison of nonbonded interaction potentials obtained by solving the OZPY equation inversely (symbol) and the input Lennard-Jones potential (line), under the same conditions as Figure 3. The data has been shifted in the vertical direction for clarity.

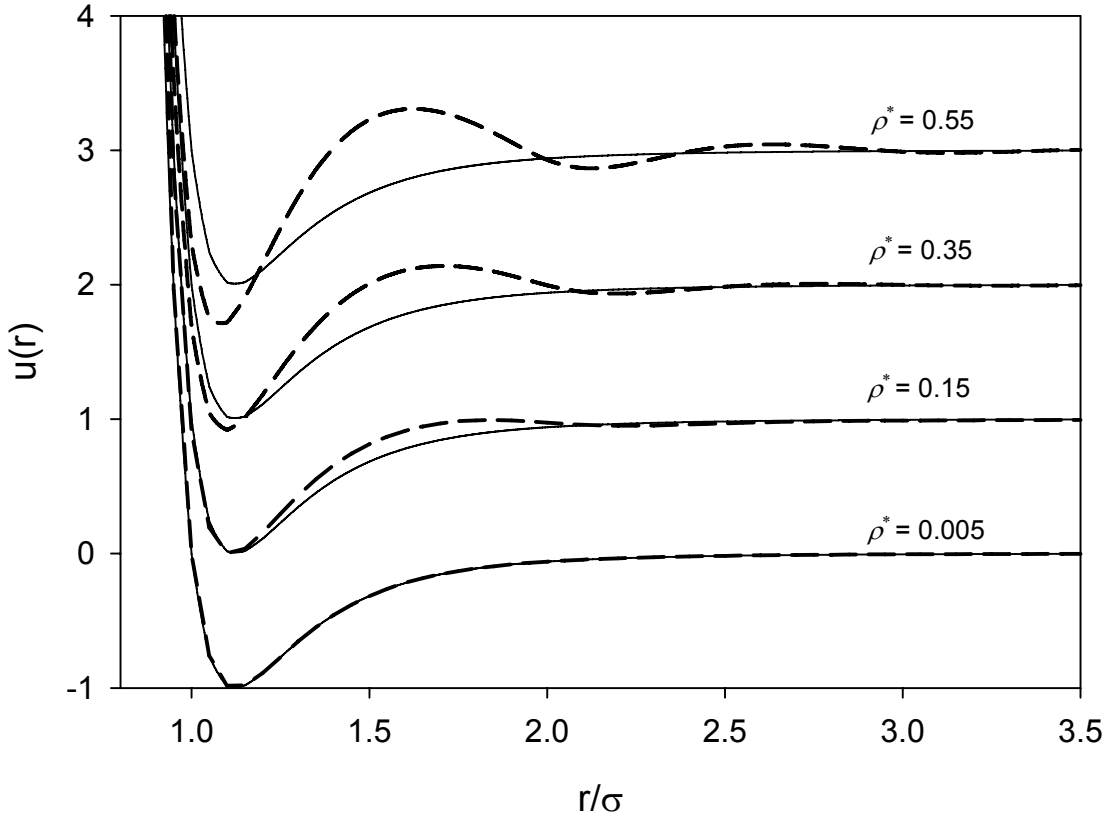

Figure 2.6. Comparison of nonbonded interaction potentials obtained by eqn (1) (dashed line) and the input Lennard-Jones potential (solid line), under $T^* = 2.0$, $\rho^* = 0.005$, 0.15, 0.35 and 0.55. The data has been shifted in the vertical direction for clarity.

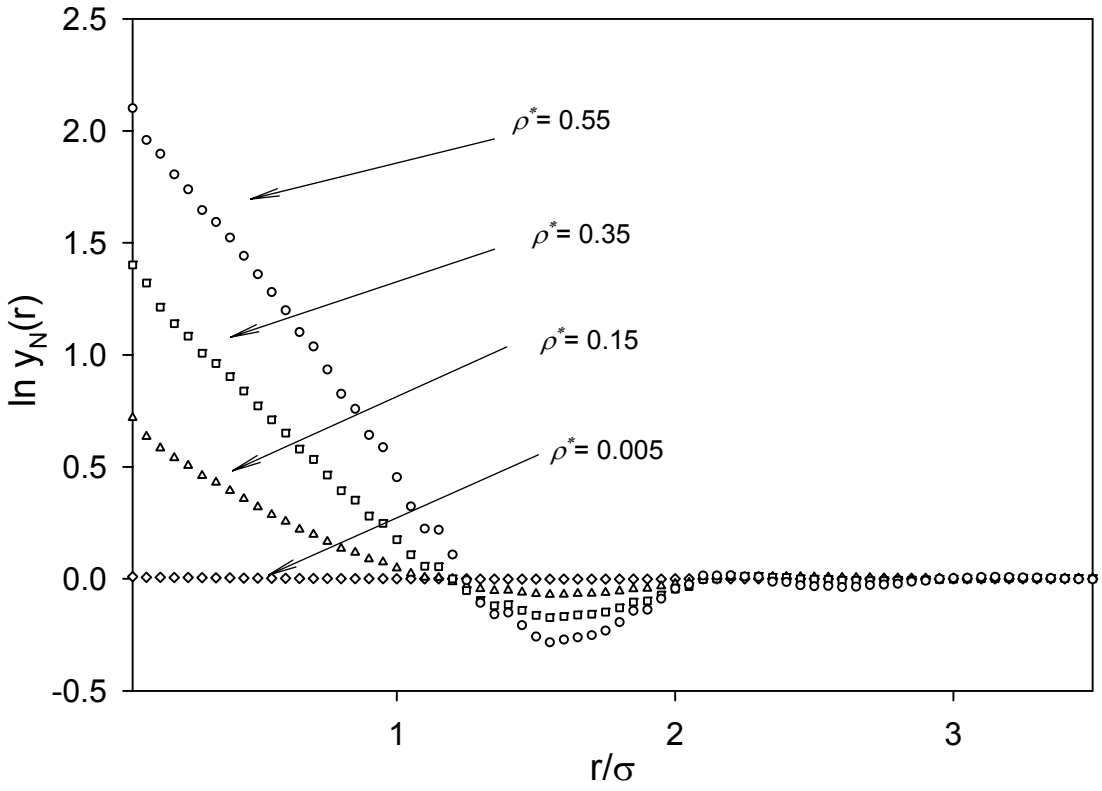

Figure 2.7. Cavity function $y_N(r)$ calculated by solving the OZPY equation inversely (monatomic), under T^* = 2.0, ρ^* = 0.005, 0.15, 0.35 and 0.55.

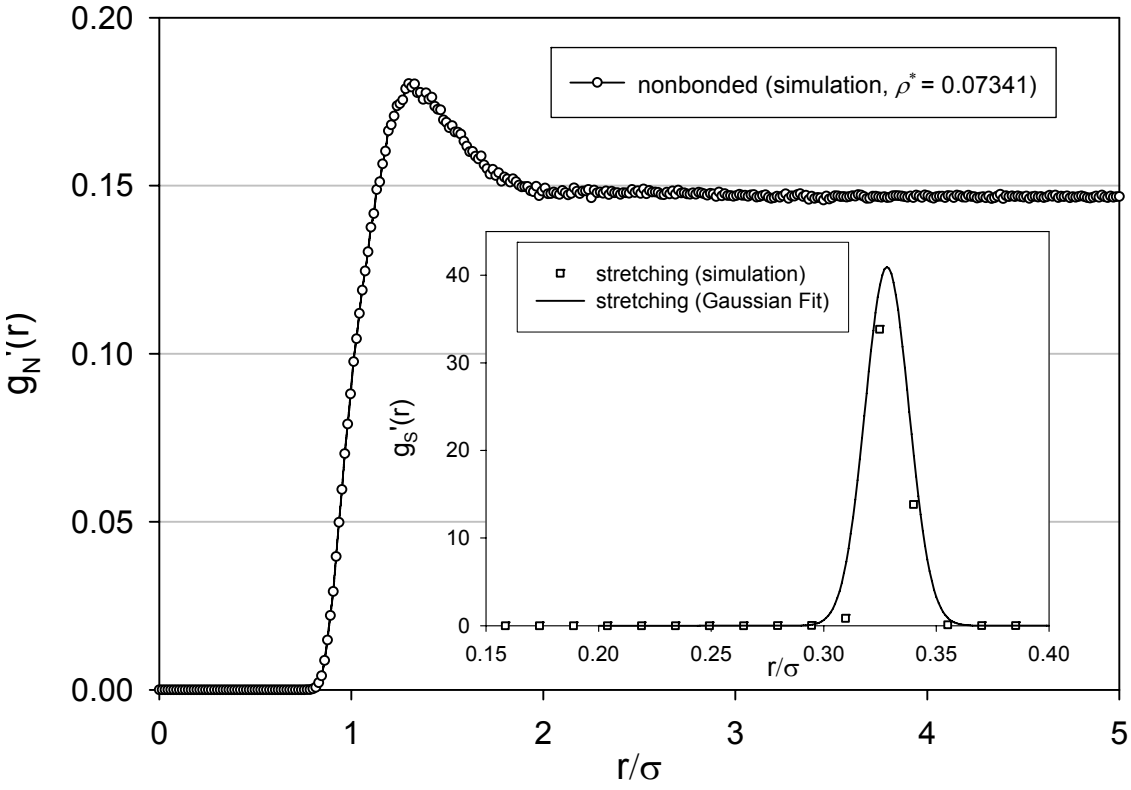

Figure 2.8. Bonded and nonbonded Radial Density Functions (RDFs) obtained from MD simulation of the diatomic fluid at T^* = 8.3333, ρ^* = 0.07341.

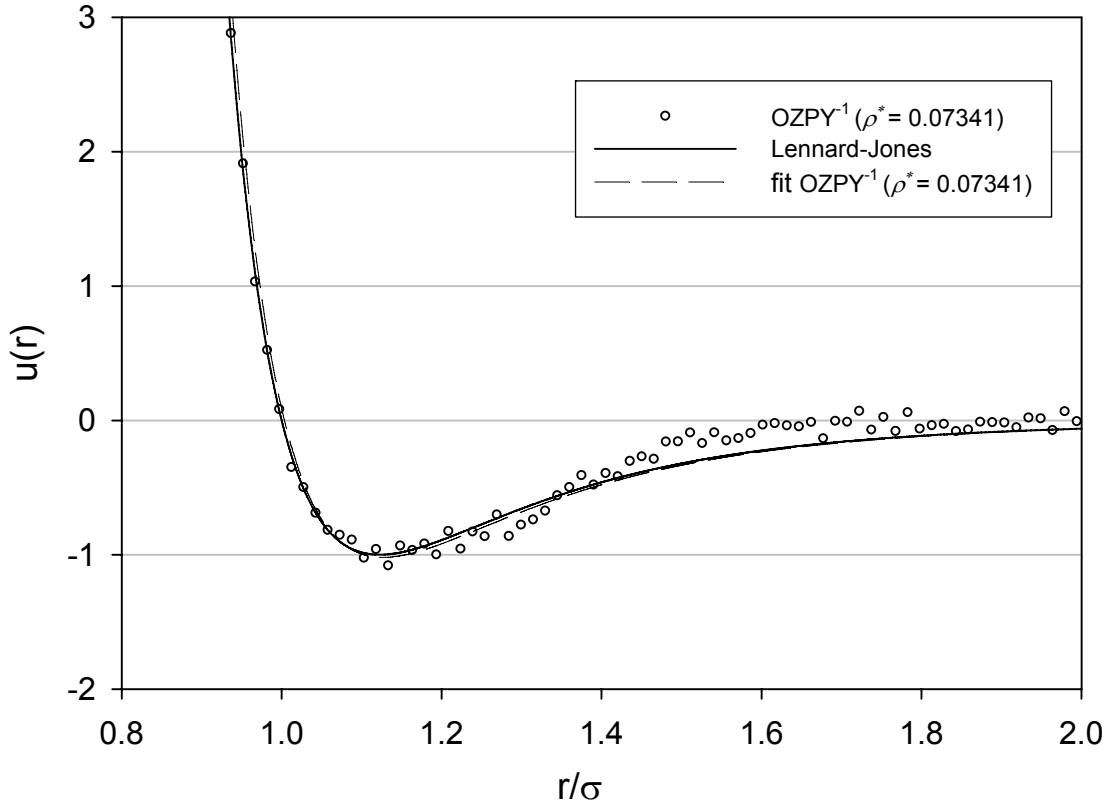

Figure 2.9. Comparison of nonbonded potentials for the diatomic fluid at $T^* =$ 8.3333 and $\rho^* =$ 0.07341. We show the input Lennard-Jones potential, the data from the OZPY^{-1} procedure, and a L-J fit to the data.

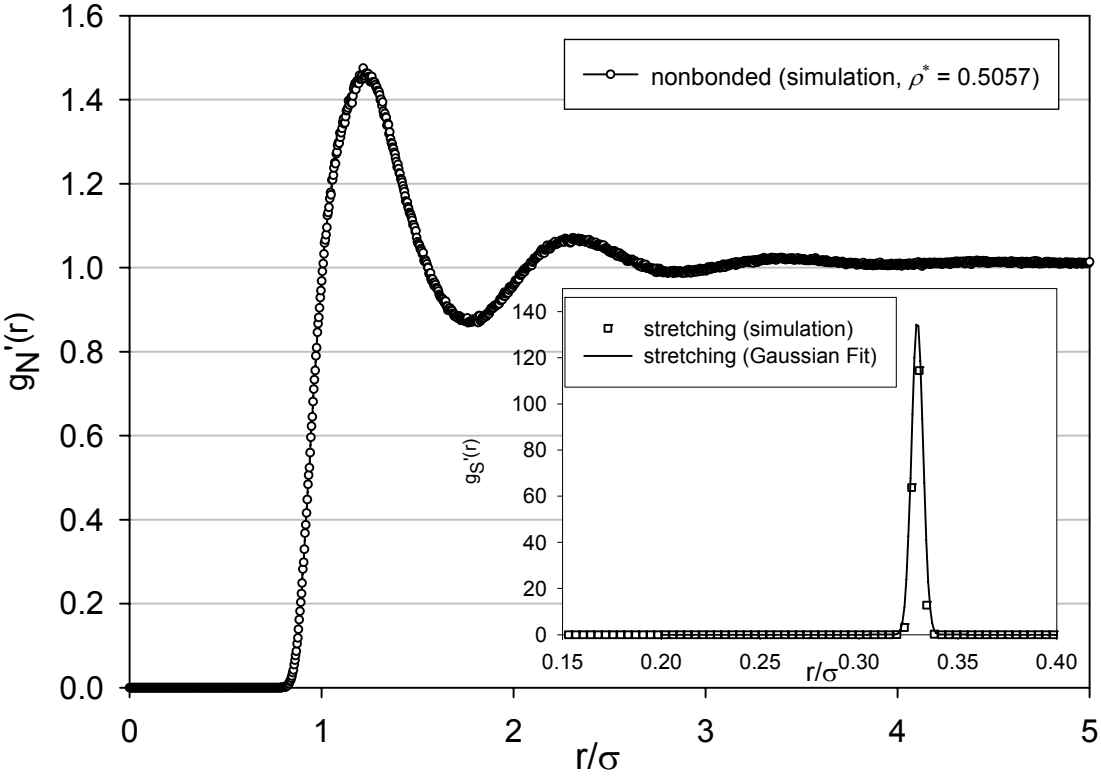

Figure 2.10. Bonded and nonbonded RDFs obtained from MD simulation of the diatomic fluid at T^* = 5.5556 and ρ^* = 0.5057.

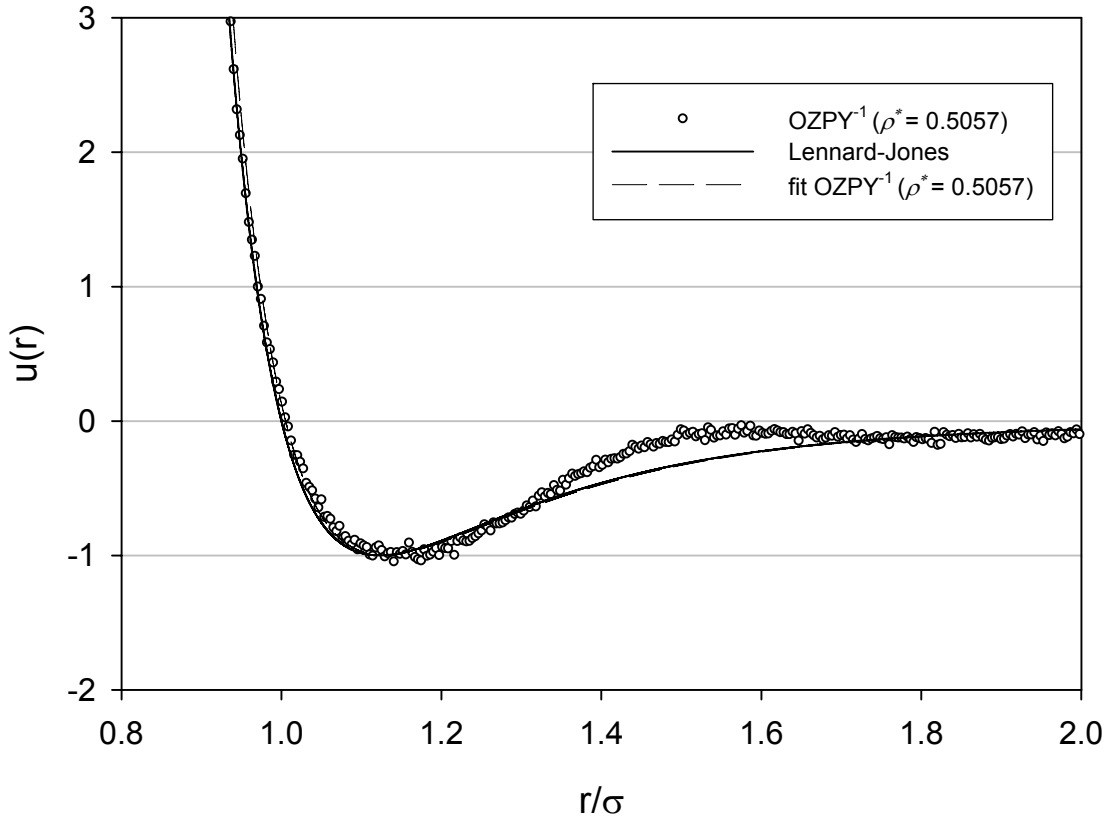

Figure 2.11. Comparison of nonbonded potentials for the diatomic fluid under $T^* = 5.5556$ and $\rho^* = 0.5057$. We show the input Lennard-Jones potential, the data from the OZPY^{-1} procedure, and a L-J fit to the data.

CHAPTER 3

Molecular Dynamics Simulation of Polyethylene Terephthalate Oligomers

This chapter is a slightly revised version of a paper by the same title published in the *Journal of Physical Chemistry B* in 2010 by Qifei Wang, David J. Keffer, Simioan Petrovan, and J. Brock Thomas:

Wang, Q., Keffer, D.J., Petrovan, S., Thomas, J.B., "A Molecular Dynamics Simulation of Polyethylene Terephthalate Oligomers", *J. Phys. Chem. B* **114**, 2 (2010).

The use of "we" in this part refers to the co-authors and the author of this dissertation. My primary contributions to this paper include (1) all of the simulation work (2) analysis of data, and (3) most of the writing

Abstract

Molecular Dynamics simulations of polyethylene terephthalate (PET) oligomers are performed in the isobaric-isothermal (NpT) ensemble at a state point typical of a finishing reactor. The oligomer size ranges from one to ten repeat units. We report thermodynamic properties (density, potential energy, enthalpy, heat capacity, isothermal compressibility, and thermal expansivity), transport properties (self-diffusivity, zero-shear-rate viscosity, thermal conductivity), and structural properties (pair correlation functions, hydrogen bonding network, chain radius of gyration, chain end-to-end distance) as a function of oligomer size. We compare the results with existing molecular-level theories and experimental data. Scaling exponents as a function of degree of polymerization are extracted. The distribution of the end-to-end distance is bimodal for the dimer and gradually shifts to a single peak as the degree of polymerization (DP) increases. The scaling exponents for the average chain radius of gyration and end to end distance are 0.594 and 0.571, respectively. The values of the heat capacity, isothermal compressibility, and thermal expansivity agree well with the available experimental data, which are of much longer PET chains. The scaling exponents for the self-diffusivity and zero-shear-rate viscosity are respectively -2.01 and 0.96, the later one is close to the theoretical predictions 1.0 for short chain polymers.

3.1 INTRODUCTION

Polyethylene Terephthalate (PET) is one of the most important engineering plastics and is widely used in bottles, fibers, and packaging films. Industrially, one way to produce PET is through the polycondensation of ethylene glycol (EG) and pure terephthalic acid (PTA), the production process includes two steps: First, PTA is esterified with EG to form a prepolymer consisting of the monomer bis-hydroxy ethylene terephthalate (BHET) and short-chain oligomers (dimer, trimer etc.). Second, the prepolymer is condensed into PET in the melt phase by polycondensation. Clearly, the prepolymer is the bridge between the two steps. Therefore, understanding the thermodynamic and transport properties of the monomer and oligomers will help in the modeling of finishing reactors. For example, to understand the temperature profile in the reactor it is necessary to know the heat capacities and thermal conductivities of the components. However, these physical properties are not available currently and could be obtained either by experiments or by computer simulation techniques.

The macroscopic structure/property relationships of PET and their composites have been well understood by researchers through experiments, while the experimental work on that of PET monomers and oligomers is rare[1,2] . One reason for scarcity of oligomer data is that, experimentally, it is difficult to trace the initial polymerization process and separate the oligomers under reaction state point and often unsafe for sampling during reaction[3,4] . An alternative way to generate these physical properties is through molecular simulation.

The bulk properties of polymers have molecular origins, which can be revealed through molecular simulation. In addition to simply providing a property data point as a function of polymer architecture, molecular simulations can also provide insight into the structural changes ultimately responsible for the behavior. For example, molecular simulations have shown how polyethylene molecular weight impacts shear and extensional viscosities[5-7] . As another example, molecular simulations have shown how changes in the backbone architecture of perfluoropolyethers impact rheological properties[8,9] . In addition , molecular simulation is able to provide insights on the formation of intermolecular and intramolecular hydrogen bonding though corresponding pair correlation functions[10 ,11] , which is helpful in understanding the microstructure and macroscopic properties of materials. Consequently, molecular simulation can provide a useful path for the determination of the physical properties (thermodynamic, transport

and structural) of PET oligomers as a function of degree of polymerization. A detailed and systematic atomistic understanding of PET oligomers can contribute to the optimization of the operation of finishing reactors.

PET has previously been studied via molecular simulation. Hedenqvist *et al.*[12] developed an atomistic model for PET (hereafter referred to as the HBB model) and studied the PVT and structure behavior of PET chains. The specific volume, solubility parameters and dipolar correlation factors obtained from Molecular Dynamics (MD) simulation are in good agreement with the experimental results. Implementing the HBB model for PET in MD simulations, Bharadwaj[13] further studied the diffusion of methane in amorphous PET and other two aromatic polyesters and investigated the diffusion coefficients of PET in the temperature ranges of 450–625 K. Boyd *et al.* modified the torsion component of the HBB potential to satisfy chain dynamics and relaxation[14] . Using the modified HBB model, Kamio *et al.*[15] performed atomistic simulations of PET dimers and decamers to derive a coarse grained model for long PET chain molecule. Other models used in the molecular simulation of PET include the Polymer-Consistent Force Field (PCFF) model to study the structural, conformational, dynamic, and barrier properties of the amorphous (glassy and melt) phases PET and PEI [poly(ethylene isophthalate)] by Karayiannis *et al.* [16] . The Open.Force-Field (OFF) model to study diffusion of O_2 and CO_2 in PET and related alkylene and isomeric polyesters reported by Shanks and Pavel[17] . The Rotational Isomeric State (RIS) conformational model was used to study PET chain conformation and relaxation by Cail *et al.*[18] , conformational and elastic behavior of PET network by Saunders *et al.*[19] and conformational characteristics of PET and PEI by Tonelli[20] .

Compared to long chains of PET, the simulation work on PET oligomers is limited. Cho[21] studied the formation of cyclic oligomers by ester interchange reaction in PET through Monte Carlo method on the basis of rotational isomeric state (RIS) model. Using the same model, Aoki[22] reported that neighboring phenyl-phenyl ring interactions enhance the probability of small end-to-end distances based on the conformational analysis of a linear trimer of PET. Recently, West *et al.*[2] did a similar conformational analysis on the PET dimer and justified the presence of a low energy conformation involving hydrogen bonding between the terminal hydroxyl and the carbonyl, which is given as the reason for low reactivity of the dimer compared with other oligomers.

In this work, we performed a systematic set of molecular dynamic simulations of PET oligomers in the isobaric-isothermal (NpT) ensemble. We studied thermodynamic properties (density, potential energy, enthalpy, heat capacity, isothermal compressibility, and thermal expansivity), transport properties (self-diffusivity, zero-shear-rate viscosity, thermal conductivity), and structural properties (pair correlation functions, hydrogen bonding network, end-to-end chain distance) as a function of degree of polymerization from one to ten repeat units. This paper is organized as follows. The details on the potential and simulation techniques are given in section 2. The results and discussion are presented in section 3. The conclusions are listed in section 4.

3.2 SIMULATION METHOD

We use the anisotropic united atom HBB potential model developed by Hedenqvist, Bharadwaj and Boyd[12,14] for PET to describe the intramolecular and intermolecular potential of BHET and oligomers molecules. All atoms of the PET oligomer molecule are explicitly represented expect for the hydrogen bound to carbon. The intramolecular interaction includes bond stretching, bond bending, bond torsion, bond out-of-plane bending and electrostatic and Lennard–Jones interactions, intramolecular electrostatic and Lennard–Jones interactions are counted for sites separated by at least four bonds. Intermolecular interactions are described by electrostatic and Lennard–Jones potentials. All the parameters are from Hedenqvist *et al.* except for the partial charges for the end -OH group, which are thus taken from the alcohol work of Chen *et al*.[23] The hydrogen in the –OH group is the only explicit hydrogen in the model. It is important to have an explicit O and H in the alcohol group in order to observe hydrogen bonding. See Figure 1 for a schematic of the molecule.

For the evaluation of the electrostatic energy, we use the spherically truncated charge-neutralized method developed by Wolf *et al.*[24] The electrostatic and Lennard-Jones interactions are truncated at a cut-off distance of 15 Å.

We simulated in the isobaric-isothermal (NpT) ensemble since the industrially relevant state points of interest are defined by pressure (p) and temperature (T). We implemented the Hamiltonian-based thermostat and barostat of Keffer *et al.*[25,26] . Both the thermostat and barostat frequencies were set to 10^{-4} fs. We used the XI-RESPA NPT algorithm developed by Tuckerman

et al.[27] to solve the equation of motion. The large time step is 2 fs and the small timestep is 0.2 fs.

The parallel code we used was built in-house and is written in FORTRAN-90, using MPI for interprocessor communication. It has been tested rigorously across a variety of applications. For the simulations in this work, we verified conservation of the Hamiltonian in order to validate our choices of time step, cut-off distance and to minimize the possibility of bugs in the potential. The simulations are executed on 16 nodes. The wall-clock time required for the execution of 1 ns of simulation is about a day for DP=1 (216 molecules) and a week for DP=10 (125 molecules) systems. Thus, to finish a run of 30 ns for DP equals 10, it took roughly 6 months.

For degrees of polymerization (DP) of 1, 2 and 3, we simulated 216 molecules. For DP from 4 to 10, we simulated 125 molecules. The state point was set at 0.13 kPa and 563 K, as this corresponds to conditions within a finishing reactor[28] . As for the initial conditions, we estimated the initial density and placed the particles in the simulation volume, avoiding significant overlap. We equilibrated the particle positions first, keeping the density and temperature constant. Then we performed a second equilibration in which the thermostat and barostat were activated and the system equilibrated to the correct density. Typically, this equilibration lasted for 1 ns. Data production followed and lasted from 1 ns for the monomer to over 30 ns for the octamer and decamer. These lengths of data production were chosen to be greater than the longest rotational relaxation time as determined in the simulation.

3.3 RESULTS AND DISCUSSIONS

In this section, we present the results of the MD simulations for the full set of degrees of polymerization, DP = 1, 2, 3, 4, 6, 8, and 10, in three sections: structural properties, equilibrium thermodynamic properties, and transport properties. A summary of the properties generated from the simulations is presented in Table 3.1.

3.3.1. Structural Properties

In Figure 3.2, we show snapshots from the MD simulations. All of the simulated systems correspond to dense liquids. For the purposes of visualization of the individual chain conformations, we render all but a few of the chains invisible in the snapshots (b) through (f). Compare for example, the monomer snapshots in Figure 3.2(a), in which all molecules are

shown, and Figure 3.2(b) in which only a few are shown. We will refer back to this figure in the discussion of the structural properties below.

In Figure 3.3, we show the distribution of chain end-to-end distance for the full set of DPs studied in this work, DP = 1, 2, 3, 4, 6, 8, and 10. The end-to-end distance is defined as the distance between the carbons attached to the terminal alcohol groups. The end-to-end distance for the monomer shows a single peak centered at 9.8 Å, as expected since the monomer is relatively inflexible. In Figure 3.2(b), we show a snapshot of selected monomer molecules, all of which have very similar end-to-end distances. The end-to-end curve of the dimer displays two peaks, one on either side of the monomer peak. The peak centered at 4.5 Å corresponds to a folded configuration, as shown in Figure 3.2(c). The broader peak extending from 7 to 22 Å, with a maximum at 16.2 Å corresponds to the unfolded conformation. These two peaks in the end-to-end distance distribution of the PET dimer molecule have also been reported by West[2] . As the DP of polymerization increases, the qualitative two-peak behavior of the dimer is still observed, but the magnitude of the first peak diminishes. Also, the distance at which the maximum in the second peak occurs increases with DP and the breadth of the curve increases with DP. The average end-to-end distance increases with DP, as can be seen in Table 3.1.

In Figure 3.4, we plot the average end-to-end distance and the average radius of gyration as a function of DP on a log-log plot. In order to determine scaling exponents, we fit these data to an equation of the form,

$$X = a(DP)^b \tag{1}$$

where X is a property related to DP via the scaling exponent, b. Both structural measures can be well fitted by equation (1). The scaling exponents for the radius of gyration and the chain end-to-end distance are 0.594 and 0.571 respectively. These exponents are close to 0.589, which is the scaling exponent for characteristic polymer size in the case of a dilute solution of chains in a good solvent, where the chains behave as self-avoiding walks (SAWs)[29] . In a melt of sufficiently long PET chains, chains should behave as random walks and the exponent should be close to 0.5 as shown by Kamio *et al.*[15] . That our chains display scaling behavior closer to the dilute solution limit is an indication of the fact that our chains are too short to display the behavior of an entangled polymer melt. Furthermore, Laso and Karayiannis[30,31] studied scaling laws of freely joint chain systems under various packing densities. Very similar values (0.58-0.60) for

scaling exponents are obtained for short chains in the whole range of volume fractions from dilute up to very dense samples and the departure from the Gaussian coil concept is attributed to the short chain length studied, suggesting a universal character in the scaling behavior of oligomers.

In addition to the distribution of the chain end-to-end distance, we can extract useful information from the dynamics of the end-to-end vector auto correlation function. In Figure 3.5, we plot the end-to-end vector auto correlation function as a function of elapsed time for all DPs studied. Each curve is normalized such that it is unity at the origin. By fitting this data to the Rouse model (a simple exponential) or the KWW model[32] (a stretched exponential), one can extract chain relaxation times, τ_R and τ_{kww} respectively. These times correspond to the longest rotational relaxation time. The relaxation times are reported in Table 3.1. The stretching exponent, β_{KWW}, is also reported in Table 3.1. The fits are reasonably good. When viewed on a log axis (see the Supplementary Information), there is evidence of deviation from the fits at very short times, which may hint at a different mechanism for the initial relaxation, corresponding to decorrelation events specific to PET chemistry. The relaxation times from the Rouse and the KWW model agree relatively well. The relaxation times increase strongly with DP. The scaling exponent *b* for τ_{kww} is 2.78. We note that our oligomers are too short to be entangled and our simulation time is not long enough to see a Rouse scaling[32], for which b=2.

The relaxation times determined above were used to set the duration of the MD simulations. Ideally, we would like the MD simulation to be run for some time significantly longer than the longest relaxation time, in order to average out fluctuations that occur at that longest period. For the simulation of the monomer, when we simulated 1 ns, we were simulating about 8 times longer than the longest relaxation time. As the DP increased, we had to also increase the duration of the simulation. For the octamer and decamer we simulated 30 ns, which is slightly longer than the relaxation time for DP=8 and slightly shorter than the relaxation time for DP =10. This limitation imposed by finite computational resources renders the estimation of τ_{kww} less accurate for the longer chains.

Another structural property investigated in this work is the extent of hydrogen bonding. We characterized the hydrogen bonding of the system in terms of the oxygen-hydrogen pair correlation function (PCF) for DP=1, 2, 3, 4, 6, 8, and 10, as shown in Figure 3.6. In Figure 3.6,

there are two characteristic peaks of hydrogen bonding; the first is located at approximately 1.8 Å and the second at about 3.3 Å. The first peak corresponds to the distance between the O of one alcohol group and the H in another alcohol group participating in the hydrogen bond. The second peak corresponds to the H and O in each of the alcohol groups that are not participating directly in the hydrogen bond. While it is clear that the number of alcohol groups per repeat unit decreases with DP, the intensity of the peaks increases with DP. This is because the PCF is normalized by the average density of alcohol groups. In other words, the number of alcohol groups decreases with DP, but on a per alcohol basis, the tendency to form hydrogen bonds increases. In Table 3.1, we report some statistics describing the hydrogen bonding network as a function of DP. The hydrogen bond fraction is the percentage of OH groups involved in hydrogen bonding, being calculated through the integration of the oxygen-hydrogen pair correlation functions (Figure 3.6), we see that the percentage of OH involved in hydrogen bonding decreases with DP, which is mainly because the number density of OH groups decreases with increasing chain length. .

3.3.2 Thermodynamic Properties

The melt density, potential energy, enthalpy, heat capacity, isothermal compressibility, and thermal expansivity at 0.13 kPa and 563 K have been calculated from the MD simulations. All of these thermodynamic properties are listed in Table.3.1. In this section, we discuss the properties individually and compare to experiment, where possible.

Figure 3.7 shows the density changing as a function of DP. The densities of PET oligomers obtained from the simulations are near 1.3 g/cm^3. There is a literature value for the monomer density, but it is at the state point of 293 K and 1 atm, rather than the state point chosen to model the interior of the finishing reactor. Therefore, we also ran a simulation of the monomer at 293 K and 1 atm to provide a validation of the density predictions of our model. The density of the monomer at 293 K and 1 atm from simulation is 1.313±0.02 g/cm^3, which can be compared with the reported value of 1.315±0.06 g/cm^3 from the CAS database (#959-26-2). The difference is within 0.2%.

We observe that the simulation value of the oligomers is higher than that of PET and it is not sensitively changing with DP, because of the hydrogen bonding in the oligomer system.For reference, we show the melt density of PET is around 1.2 g/cm^3 (under p = 1 atm, T = 563 K)[33] .

In Figure 3.8, the non-bonded contributions to the potential energy are plotted as a function of DP on a per DP basis. (The number of non-bonded contributions fluctuates during the simulation and makes reporting on a per mode basis less useful.) All non-bonded interactions are negative (attractive) as the reference state (zero energy) for these interactions is infinite separation, and the pressure is not sufficiently high to force repulsive energies. Intuitively, as the chain length increases, one expects intramolecular interactions to increase in magnitude and intermolecular interactions to decrease in magnitude since a given atom will be on average interacting with a greater fraction of molecules of its chain. The total intermolecular interaction does indeed follow the intuitive understanding that, as DP increases, the magnitude decreases. However, the total intramolecular interaction also decreases, which is somewhat counterintuitive until one considers hydrogen bonding. The end groups of the chain form hydrogen bonds. As the chain length increases, the relative number of end groups per DP decrease. Therefore, we see a decrease in the electrostatic contribution to the potential energy on a per DP basis. Some portion of the electrostatic energy is due to intramolecular interactions. Apparently, the loss of intramolecular electrostatic interactions is sufficient to overwhelm the other gains in intramolecular interactions, resulting in a total intramolecular interaction that decreases in magnitude with DP, but not quite as quickly as the electrostatic term.

The enthalpy is composed of a kinetic energy term, a potential energy term (which together constitute the internal energy) and a pV term. In Figure 3.9, we plot the enthalpy per molecule as a function of DP on both a per molecule basis and on a per DP basis (inset). The enthalpy approaches a linear behavior with respect to DP at large DPs, as expected since the kinetic energy and potential energy should scale roughly linearly with DP when the change in density, accounted for by the pV term, is relatively small. The pronounced deviation from linearity at low DP is due to the fact that the end groups are slightly different than the repeat units in the interior of the chain. The slight deviation from linearity at high DP is better seen on a per DP basis and is largely accounted for by the non-bonded contributions to the potential energy shown in Figure 3.9.

Thermodynamic properties that correspond to partial derivatives, such as the constant-pressure heat capacity, C_p, the isothermal compressibility, β, and the thermal expansivity, α, can

be calculated from statistical thermodynamics based on fluctuations in the NpT ensemble[34] . The constant pressure heat capacity is proportional to the variance of the enthalpy

$$C_p = \frac{1}{Vk_BT^2} < \sigma_H{}^2 > \tag{2.a}$$

The isothermal compressibility is obtained through the variance of volume,

$$\beta = \frac{1}{Vk_BT} < \sigma_V{}^2 > \tag{2.b}$$

The thermal expansion coefficient is based on the covariance of volume and enthalpy of the

$$\alpha = \frac{1}{Vk_BT^2} < \sigma_{(V)(H)} > \tag{2.c}$$

where V is the volume, T is the temperature of the system and k_B is Boltzmann's constant. The angled brackets indicate an ensemble average. These fluctuations provide an elegant method to obtain these thermodynamic properties, since we can obtain all these three properties from one single MD simulation at the desired state point.

For reasons that will be made clear shortly, we also calculated C_p, β, and α using a second procedure, namely centered finite difference. In this approach, one runs three simulations for each thermodynamic property. For example, for the heat capacity, one runs a simulation at the statepoint defined by (p,T), then two other simulations at ($p,T+\varepsilon$) and ($p,T-\varepsilon$). The choice of ε is made so that one can observe statistically valid differences in the enthalpy between the state points. Thus the heat capacity can be determined as

$$C_p = \frac{H(p,T+\varepsilon) - H(p,T-\varepsilon)}{2\varepsilon} \tag{3.a}$$

Similarly, the isothermal compressibility and thermal expansivity can be expressed as

$$\beta = -\frac{1}{V(p,T)} \frac{V(p+\varepsilon,T) - V(p-\varepsilon,T)}{2\varepsilon} \tag{3.b}$$

$$\alpha = \frac{1}{V(p,T)} \frac{V(p,T+\varepsilon) - V(p,T-\varepsilon)}{2\varepsilon} \tag{3.c}$$

In Table 3.2, we report C_p, β, and α for the monomer at a state point of 10 MPa and 563 K[35] . We choose this state point rather than the one corresponding to the interior of the finishing reactor, which has been used in all other simulations, in order to compare with experimental data.

We see that using the finite difference approach yields better mean values in agreement with experimental data for PET[35,36] and yields much smaller uncertainties, showing the simulation results are reasonable (exact agreement with experimental data was not expected due to the difference in DP) and the method is statistical reliable. The uncertainties from the quantities obtained from the fluctuations in some cases approach 100%. These uncertainties were calculated by dividing the simulation into 10 blocks of time, computing the average heat property in each block, and the corresponding standard error in the block average. In Table 3.1, we report the values of C_p, β, and α using the centered finite difference formulae as a function of DP at the finishing reactor state point. The uncertainties for β are larger than the uncertainties for C_p and α because, β is based upon simulations run at different pressures, whereas C_p and α are based upon simulations run at different temperatures, and the greater fluctuations in the pressure increase the uncertainty of the resulting finite difference.

In Figure 3.10, we show the dependence of C_p and α on DP on a log-log plot. The heat capacity on a per mass basis decreases with DP. The thermal expansivity also decreases with DP. Both of these trends have been observed experimentally[37]. We extracted scaling exponents for C_p and α of -0.081 and -0.218 respectively. We do not report a scaling exponent for β due to increased uncertainty in this property for reasons mentioned above.

In the simulations, the hydrogens attached to the carbon are not modeled explicitly. Thus the contributions to the thermodynamic properties, including the heat capacity, due to the high-frequency C-H vibrations are not included. Thus we under-estimate the heat capacity. For methane at room temperature, the vibrational modes contribute less than 10% to the heat capacity and this serves as an extreme limit on the under estimation[38].

3.3.3 Transport Properties

One can obtain transport properties from equilibrium simulations using Green-Kubo relations[39-41]. In this work, we report the self-diffusivity (*D*), zero-shear rate viscosity (η) and thermal conductivity (λ) as a function of DP. The self-diffusivity is obtained from the mean-square displacements (MSD) through Einstein's equation given as

$$\mathbf{D} = \frac{1}{6}\lim_{t\to\infty}\frac{1}{t}\left\langle\left[\mathbf{r}_{cm}(t) - \mathbf{r}_{cm}(0)\right]^2\right\rangle \quad (4)$$

where $\mathbf{r_{cm}}$ is the center of mass position of the molecule.

For the case of the self-diffusivity, this integral can also be expressed in terms of the mean square displacement via the Einstein Relation. In Figure 3.11, we plot the mean square displacement versus observation time on a log-log plot. In order to satisfy the infinite time limit, the slopes of the curves must be unity. These slopes are reported in the legend of Figure 3.11 and are all very close to unity. This is evidence that the simulations have been run sufficiently long to achieve valid self-diffusivities. The numerical values of the self-diffusivities are reported in Table 3.1 and plotted in Figure 3.12 as a function of DP. The self-diffusivity decreases with DP as expected. The scaling exponent for the self-diffusivity is -2.01.

The zero-shear-rate viscosity is based on time integration of the momentum auto-correlation function

$$\eta_{xy} = \frac{1}{Vk_BT}\int_0^\infty < \sigma_{xy}(t)\sigma_{xy}(0) > dt \tag{5}$$

where σ_{xy} is the xy component of the stress tensor defined to have a potential and kinetic contribution,

$$\sigma_{xy} = \frac{1}{2}\sum_{i=1}^{N}\sum_{j\neq i}^{N} F_{ijx} r_{ijy} + m_i \sum_{i=1}^{N} u_{ix} u_{iy} \tag{6}$$

where r_{ijx} and F_{ijx} are respectively the separation and force between particles i and j in the x dimension, m_i is the mass of particle i.

The momentum auto-correlation functions are shown in Figure 3.13. The auto-correlation functions decay to zero in an oscillatory manner. There is one interesting feature in Figure 3.13, as is clear in the inset, the magnitude of the oscillations decreases as DP increases. While the correlations may appear to have died out in less than 4 ps, we will see that this is not the case.

In Figure 3.14, we plot the zero-shear-rate viscosity as a function of the upper limit of integration in equation (5). Following a previously tested procedure[42] , we then average the values of the viscosity that occur on the plateau. The arrows in Figure 3.14 indicate where we decided the plateau began. In general, the start of the plateau increases with DP. For some DP, the plateau begins long after the 4 ps period in which the auto-correlation functions appear to have died out based on visual inspection of Figure 3.13. Therefore, fluctuations in the auto-correlation functions beyond about 4 ps are not statistical noise. Nevertheless, for bigger DP, we

do see the beginning of the plateau well before an observation time of τ_{KWW}. (We cannot evaluate the auto-correlation function for observation times up to τ_{KWW} for long chains due to the decreasing statistical reliability with increase in observation time.) The implication is that long time-scale relaxation modes impact the zero-shear-rate viscosity only nominally. The numerical values of the zero-shear-rate viscosities are given in Table 3.1. The scaling exponent for the zero-shear-rate viscosity is 0.96, which is in agreement with the theoretical value of 1 for short chains[29].

With both the self-diffusivity and zero-shear-rate viscosity in hand, we can test the Stokes-Einstein (SE) relation[43,44], which according to hydrodynamic theory applies well to the diffusion of large spherical molecules in solvent of low molecular weight,

$$\frac{D\eta}{k_B T} = \frac{1}{4\pi R_{SE}} \tag{7}$$

where R_{SE} is the particle size. We can use the SE relation to calculate particle size based upon the self-diffusivity and zero-shear-rate viscosity reported above. In Figure 3.15, we plot on a log-log scale the radius from the SE relation and the radius of gyration from MD. We find that for small molecules (monomer and dimer) there is excellent agreement between the particle size predicted by the SE relation and the radius of gyration. For larger molecules, there is a significant variation, presumably because (i) the longer chains violate the assumption of a spherical particle and (ii) the longer chains violate the assumption of a low molecular weight solvent. More details and generalized equations on the relationship between the effective particle's shape and the translational diffusion coefficient can be found in the work of Kröger *et al.*[45]. The scaling exponent for the SE radius is found to be 1.00, which is dictated by the fact that is it determined from the self-diffusivity and zero-shear-rate viscosity with scaling exponents respectively of -2.01 and 0.96. The fluctuations around this best fit are presumably due to statistical noise.

The last transport property obtained in this work is the thermal conductivity, λ, which via a Green-Kubo integral can be expressed as a function of an auto-correlation of the heat flux, **J**,

$$\lambda = \frac{1}{3Vk_B T^2}\int_0^\infty < \mathbf{J(t)} \bullet \mathbf{J(0)} > dt \tag{8}$$

where the heat flux **J** is defined as

$$\mathbf{J} = \sum_{i=1}^{N} \mathbf{u_i} E_i + \frac{1}{2} \sum_{i=1}^{N} \sum_{j \neq i}^{N} \mathbf{r_{ij}} \mathbf{F_{ij}} \bullet \mathbf{u_i} \tag{9}$$

to have contributions from energy carried by a mass flux (the first term) and intermolecular interactions (the second term). The energy carried by a particle is composed of kinetic and potential contributions.

$$E_i = \frac{1}{2} m_i u_i^2 + \frac{1}{2} \sum_{j \neq i}^{N} U_{ij} \tag{10}$$

The above atomic heat flux expression has been successfully applied to the systems governed by pair potentials as reported in many articles[41,46-48] , in which the Green-Kubo integral is used to obtain thermal conductivity of small molecules (methane[47] and SiH_4[41]). These molecules can be treated as particles by ignoring the intramolecular bond stretching, bond bending and bond torsion interactions so there will be only intermolecular Lennard-Jones interaction potential contributing to the heat flux. The simulation results based on this procedure are in good agreements with the experimental data. For larger molecules (butane[49] , alkanes[50]), the heat flux expression is often taken as molecular based in order to calculate the molecular heat flux, a heat flux whose description is based on the view that the individual atomic contributions to the local energy density are localized at the molecular centers of mass[51] . This expression applies well to polyatomic molecules with moderate chain length. When the chain length increases, this center of mass based heat flux will be problematic[52] . If the chain is very long, the energy transport along each chain is not ignorable. Therefore, the atomic heat flux expression is needed for prediction of thermal conductivity of polymer chain molecules. Marechal and Ryckaert[53] derived the atomic heat flux expression for polyatomic molecules (n-butane), in which only bond torsion was included, but the thermal conductivity obtained is too large based on experimental comparison with alkanes. An alternative way for faithful prediction of thermal conductivity is to modify the force field or molecular dynamic model. Lussetti *et al.*[52] transformed the molecule model for Polyamide-6,6 by grouping some atoms in the chain together to have less quantum degree of freedoms in the system as they assume that the high value of thermal conductivity obtained from the MD simulation is due to the incorrect treatment of these fast quantum degrees of freedom in molecular dynamics. They compared the NEMD simulation results of thermal conductivity from different force fields and found that the united atom model

with complete rigid bond generated the best result for comparison with the experimental data. Based on the collective conclusions of the work above, we only included non-bonded interactions in the heat flux of our PET oligomer molecules. These non-bonded interactions include both intramolecular and intermolecular Lennard-Jones and electrostatic interactions. Thus, we neglect stretching, bending and torsion contributions. The heat flux autocorrelation function as a function of DP is shown in Figure 3.16.

In Figure 3.17, we plot the thermal conductivity as a function of the upper limit of integration in equation (8). Again, we look for a plateau and report an average beyond the plateau. The data is relatively noisy. We report the numerical values of the thermal conductivities as a function of DP in Table 3.1. The thermal conductivities of the oligomers fluctuate from 0.12 to 0.30 (W/m/K), which is the reported experimental value range of thermal conductivity for commercial PETs with different crystallinity and molecular weight under 1 atm and 300 K[33] . We plot the thermal conductivity as a function of DP in Figure 3.18. There is not sufficient statistical reliability in these values to report a scaling exponent (the R^2 measure of fit is 0.04), which in any event would be close to zero.

An alternative approach to obtaining the thermal conductivity is to use Bridgman's theory of energy transport in pure liquids[54,55] .

$$\lambda = 3(N/V)^{2/3} k_B v_s \tag{11}$$

where v_s is the speed of sound in the liquid, given by

$$v_s = \sqrt{\frac{C_p}{C_v}\left(\frac{\partial p}{\partial \rho}\right)_T} \tag{12}$$

where C_v is the constant volume heat capacity and ρ is the mass density. The partial derivative $\left(\frac{\partial p}{\partial \rho}\right)_T$ is contained with the isothermal compressibility, which we have already reported. Typically, the ratio of constant-pressure and constant-volume heat capacities is close to unity for liquids. In order to test this assumption, we ran some additional MD simulations on the monomer at constant volume (NVT ensemble) to obtain C_v. We found the ratio to be 1.15 and this is what we used in equation (12) for all DP. The calculated data for velocity of sound is listed in Table 3.1. It is noted that empirically, a coefficient of 2.8 gives a better fit to experimental data than 3

in equation (10)[54] , so we used 2.8. The experiments of Bridgman were based on small molecules. Therefore, in equation (11), we used the number density not of chains but of repeat units, which taken independently constitute relatively small molecules. This prediction of the thermal conductivity is also shown in Figure 3.18. On average the Bridgman thermal conductivity is 26% low. The Bridgman thermal conductivity shows almost a constant with DP (scaling exponent of -0.11), which is similar in the thermal conductivity obtained from the Green-Kubo integral.

3.4 CONCLUSIONS

We obtained structural, thermodynamic and transport properties for PET oligomers with degrees of polymerization from 1 to 10 at the industrially relevant state point (T = 563 K, p = 0.13 kPa) by molecular dynamics simulation using a modified HBB model.

The end-to-end distance distribution for oligomers larger than the monomer shows a bimodal distribution in which the chains are either folded or extended. The presence of the folded peak diminishes with DP. The extended peak broadens with DP. The degree of hydrogen bonding, as judged by the fraction of alcohol groups engaged in hydrogen bonding, decreases with DP. The longest rotational relaxation time, radius of gyration and average end-to-end distance scale with exponents of 2.78, 0.594 and 0.571 respectively.

We generated a suite of thermodynamic properties. We found that both the intramolecular (unexpectedly) and intermolecular (expectedly) non-bonded contributions to the potential energy decrease in magnitude with increasing DP, due to the diminished role of hydrogen bonding in the system. All other contributions on a per mode basis are relatively unaffected by DP.

We compared two methods for obtaining properties based on thermodynamic partial derivatives, such as the heat capacity, isothermal compressibility and thermal expansivity. The fluctuation method yielded greater statistical uncertainty and poorer agreement with experiment than a method based on using centered finite difference across three simulations. We extracted scaling exponents for C_p and α of -0.081 and -0.218 respectively.

We obtained the self-diffusivity, zero-shear-rate viscosity and thermal conductivity as a function of DP. The scaling exponents for the self-diffusivity and zero-shear rate viscosity are

respectively -2.01 and 0.96. The evaluation of the thermal conductivity from both the Green-Kubo integral and Bridgman theory are both approximate, but yield results that fall in the range of experimental data.

Work is in progress to fit the structural and dynamic information obtained from these atomistic simulations to a coarse-grained model of PET, capable of simulating much larger PET oligomers and polymers.

3.5 ACKNOWLEDGMENT

This research was supported by the Eastman Chemical Company. This research project used resources of the National Institute for Computational Sciences (NICS) supported by NSF under agreement number: OCI 07-11134.5.

References

[1]V. Vermylen, P. Lodefier, J. DeVaux, R. Legras, W. A. Mac Donald, R. Rozenberg, and E. De Hoffmann, J. Polym. Sci., Part A: Polym. Chem. **38**, 416 (2000).

[2]S. M. West, A. J. Smallridge, A. Uhlherr, and S. Volker, Macromol. Chem. Phys. **201**, 2532 (2000).

[3]T. Amari and Y. Ozaki, Macromolecules **34**, 7459 (2001).

[4]T. Amari and Y. Ozaki, Macromolecules **35**, 8020 (2002).

[5]C. Baig, B. J. Edwards, and D. J. Keffer, Rheol. Acta **46**, 1171 (2007).

[6]C. Baig, B. J. Edwards, D. J. Keffer, H. D. Cochran, and V. A. Harmandaris, J. Chem. Phys. **124**, 084902 (2006).

[7]J. M. Kim, B. J. Edwards, and D. J. Keffer, J. Mol. Graphics Modell. **26**, 1046 (2008).

[8]B. Jiang, N. J. Crawford, D. J. Keffer, B. J. Edwards, and J. L. Adcock, Mol. Simul. **33**, 871 (2007).

[9]B. Jiang, J. M. Kim, D. J. Keffer, and B. J. Edwards, Mol. Simul. **34**, 231 (2008).

[10]H. Ohgi, T. Sato, S. H. Hu, and F. Horii, Polymer **47**, 1324 (2006).

[11]A. G. Martinez, E. T. Vilar, A. G. Fraile, and P. Martinez-Ruiz, J. Chem. Phys. **124** (2006).

[12]M. S. Hedenqvist, R. Bharadwaj, and R. H. Boyd, Macromolecules **31**, 1556 (1998).

[13]R. Bharadwaj and R. H. Boyd, J. Chem. Phys. **110**, 10203 (1999).

[14]S. U. Boyd and R. H. Boyd, Macromolecules **34**, 7219 (2001).

[15]K. Kamio, K. Moorthi, and D. N. Theodorou, Macromolecules **40**, 710 (2007).

[16]N. C. Karayiannis, V. G. Mavrantzas, and D. N. Theodorou, Macromolecules **37**, 2978 (2004).

[17]R. Shanks and D. Pavel, Mol. Simul. **28**, 939 (2002).

[18]J. I. Cail, R. F. T. Stepto, D. J. R. Taylor, R. A. Jones, and I. M. Ward, Phys. Chem. Chem. Phys. **2**, 4361 (2000).

[19]L. S. Saunders, I. M. Ward, J. I. Cail, and R. F. T. Stepto, Polymer **45**, 2357 (2004).

[20]A. E. Tonelli, J. Polym. Sci., Part B: Polym. Phys. **40**, 1254 (2002).

[21]J. S. Cho, J. H. Youk, D. I. Yoo, S. W. Ko, and W. S. Ha, Polym-Korea **22**, 99 (1998).

[22]A. Aoki, Kobunshi Ronbunshu **51**, 283 (1994).

[23]G. Kamath, J. Robinson, and J. J. Potoff, Fluid Phase Equilib. **240**, 46 (2006).

[24]D. Wolf, P. Keblinski, S. R. Phillpot, and J. Eggebrecht, J. Chem. Phys. **110**, 8254 (1999).

[25]D. J. Keffer, C. Baig, P. Adhangale, and B. J. Edwards, J. Non-Newtonian Fluid Mech **152**, 129 (2008).

[26]D. J. Keffer, C. Baig, P. Adhangale, and B. J. Edwards, 129 (2008).

[27]M. Tuckerman, B. J. Berne, and G. J. Martyna, J. Chem. Phys. **99**, 2278 (1993).

[28]D. Feldman and A. Barbalata, *Synthetic polymers : technology, properties, applications* (Chapman & Hall, London, 1996).

[29]M. Doi and S. F. Edwards, *The theory of polymer dynamics* (Oxford University Press, New York, 1986).

[30]M. Laso and N. C. Karayiannis, J. Chem. Phys. **128** (2008).

[31]N. C. Karayiannis and M. Laso, Macromolecules **41**, 1537 (2008).

[32]G. Tsolou, V. G. Mavrantzas, and D. N. Theodorou, Macromolecules **38**, 1478 (2005).

[33]J. P. Valcarcel, J. Palacios, and J. J. Alvarado-Gil, J. Mater. Sci. **34**, 2113 (1999).

[34]M. P. Allen and D. J. Tildesley, *Computer simulation of liquids* (Oxford University Press, New York, 1987).

[35]J. Brandrup, E. A. Grulke, and E. H. Immergut, *Polymer handbook*, 4th ed. (Wiley-Interscience, New York, 1999).

[36]U. Buchenau and A. Wischnewski, Phys Rev B **70**, 092201 (2004).

[37]D. H. Huang, S. L. Simon, and G. B. McKenna, J. Chem. Phys. **122**, 084907 (2005).

[38]D. A. McQuarrie, *Statistical mechanics* (Harper & Row, New York, 1976).

[39]N. J. English, Mol. Phys. **106**, 1887 (2008).

[40]A. E. Nasrabad, N. M. Oghaz, and B. Haghighi, J. Chem. Phys. **129** (2008).

[41]Y. Sakiyama, S. Takagi, and Y. Matsumoto, J. Chem. Phys. **122** (2005).

[42]D. J. Keffer, B. J. Edwards, and P. Adhangale, J. Non-Newtonian Fluid Mech. **120**, 41 (2004).

[43]K. Saalwachter and W. Burchard, Macromolecules **34**, 5587 (2001).

[44]S. K. Das, J. Horbach, K. Binder, M. E. Fisher, and J. V. Sengers, J. Chem. Phys. **125**, 024506 (2006).

[45]M. Kroger and P. Ilg, J. Chem. Phys. **127** (2007).

[46]J. W. Che, T. Cagin, W. Q. Deng, and W. A. Goddard, J. Chem. Phys. **113**, 6888 (2000).

[47]E. J. Rosenbaum, N. J. English, J. K. Johnson, D. W. Shaw, and R. P. Warzinski, J. Phys. Chem. B **111**, 13194 (2007).

[48]P. Ungerer, C. Nieto-Draghi, B. Rousseau, G. Ahunbay, and V. Lachet, J. Mol. Liq. **134**, 71 (2007).

[49]P. J. Daivis and D. J. Evans, J. Chem. Phys. **103**, 4261 (1995).

[50]D. K. Dysthe, A. H. Fuchs, and B. Rousseau, J. Chem. Phys. **112**, 7581 (2000).

[51]D. Torii, T. Nakano, and T. Ohara, J. Chem. Phys. **128** (2008).

[52]E. Lussetti, T. Terao, and F. Muller-Plathe, J. Phys. Chem. B **111**, 11516 (2007).

[53]G. Marechal and J. P. Ryckaert, Chem. Phys. Lett. **101**, 548 (1983).

[54]R. B. Bird, W. E. Stewart, and E. N. Lightfoot, *Transport phenomena*, 2nd ed. (J. Wiley, New York, 2002).

[55]P. W. Bridgman, P Am Acad Arts Sci **59**, 141 (1923).

Appendix B

Tables and Figures

Table 3.1. Simulation data for DP = 1, 2, 3, 4, 6, 8 and 10 at p = 0.13 kPa, T = 563 K.

DP	1	2	3	4	6	8	10
N	216	216	216	125	125	125	125
V (10^5 Å^3)	0.70 ± 0.04	1.21 ± 0.06	1.71 ± 0.03	1.28 ± 0.01	1.87 ± 0.01	2.46 ± 0.01	3.06 ± 0.01
ρ (g/cm^3)	1.30 ± 0.01	1.26 ± 0.01	1.28 ± 0.02	1.29 ± 0.01	1.29 ± 0.01	1.29 ± 0.01	1.29 ± 0.01
U (10^2 aJ)	-0.15 ±0.01	0.20 ± 0.05	1.26± 0.03	1.39± 0.05	3.38 ± 0.17	5.44± 2.03	7.43± 4.06
H (10^2 aJ)	-0.15 ±0.01	0.20 ± 0.05	1.26± 0.03	1.38± 0.05	3.38± 0.17	5.44± 2.03	7.43± 4.06
C_p (10^3 J/K/kg)	2.73 ± 0.09	2.56 ± 0.06	2.47 ± 0.06	2.45 ± 0.07	2.35 ± 0.05	2.29 ± 0.04	2.25 ± 0.05
β (10^{-1} GPa^{-1})	2.17 ± 0.77	3.02 ± 1.12	4.70 ± 3.27	4.51 ± 1.65	3.44 ± 0.44	6.40 ± 3.06	5.21 ± 4.43
α (10^{-4} K^{-1})	6.73 ± 1.02	5.26± 0.38	4.81± 0.55	4.80± 0.17	4.53± 0.27	4.28± 0.16	3.75± 0.79
D (10^{-10} m^2/sec)	5.68 ± 1.14	2.05 ± 0.23	0.71 ± 0.14	0.40 ± 0.09	0.17 ± 0.02	0.10 ± 0.03	0.07 ± 0.01
η (10^{-2} Pa.s)	0.27 ± 0.01	0.55 ± 0.08	0.58 ± 0.09	0.65 ± 0.07	1.95± 0.65	2.23± 0.60	3.03± 0.80
v_S (10^3 m/sec)	2.01	1.75	1.39	1.41	1.62	1.18	1.31
λ_{GK} (W/m/K)	0.16	0.16	0.13	0.14	0.16	0.12	0.13
λ_B (W/m/K)	0.21 ± 0.02	0.20 ± 0.05	0.31 ± 0.02	0.13 ± 0.11	0.12 ± 0.07	0.22 ± 0.03	0.18 ± 0.01
H-bond (2.0 Å)(%)	54.22	42.72	42.57	38.84	28.55	22.25	20.55
H-bond (2.5 Å)(%)	69.50	57.16	55.11	51.02	38.01	30.18	27.44
$\langle R_{ete} \rangle$ (Å)	9.8 ± 1.0	13.6 ± 4.9	18.3 ± 6.6	21.1 ± 7.5	26.8 ± 10.2	28.6 ± 11.2	34.2 ± 9.4
$\langle R_g \rangle$ (Å)	4.0 ± 0.7	5.6 ± 2.8	7.6 ± 2.7	8.9 ± 5.2	11.2 ± 4.4	12.5 ± 5.3	13.2 ± 3.8
R_{SE} (Å)	4.06	5.54	14.96	23.70	19.23	28.02	31.9
τ_R (ns)	0.128	0.552	2.42	5.59	15.26	27.8	37.5
τ_{KWW} (ns)	0.129	0.502	2.81	5.59	15.78	25.3	38.6
β_{KWW}	0.98	0.92	0.76	0.76	0.77	0.77	0.74

Table 3.2. Comparison of thermodynamic properties from finite difference and fluctuation methods for the monomer at T = 563 K and p = 100 atm. As a reference point, experimental values for PET are also provided.

Thermodynamic properties	MD (fluctuation)	MD (finite difference)	Experimental data (PET)
Heat capacity (10^3 J K^{-1} kg^{-1})	1.41 ± 1.38	2.68 ± 0.08	2.66[35]
Isothermal compressibility (10^{-1} GPa^{-1})	17.61 ± 10.20	3.14 ± 0.06	3.24[36]
Thermal expansion coefficient (10^{-4} K^{-1})	21.40 ± 19.71	6.42 ± 0.96	6.55[35]

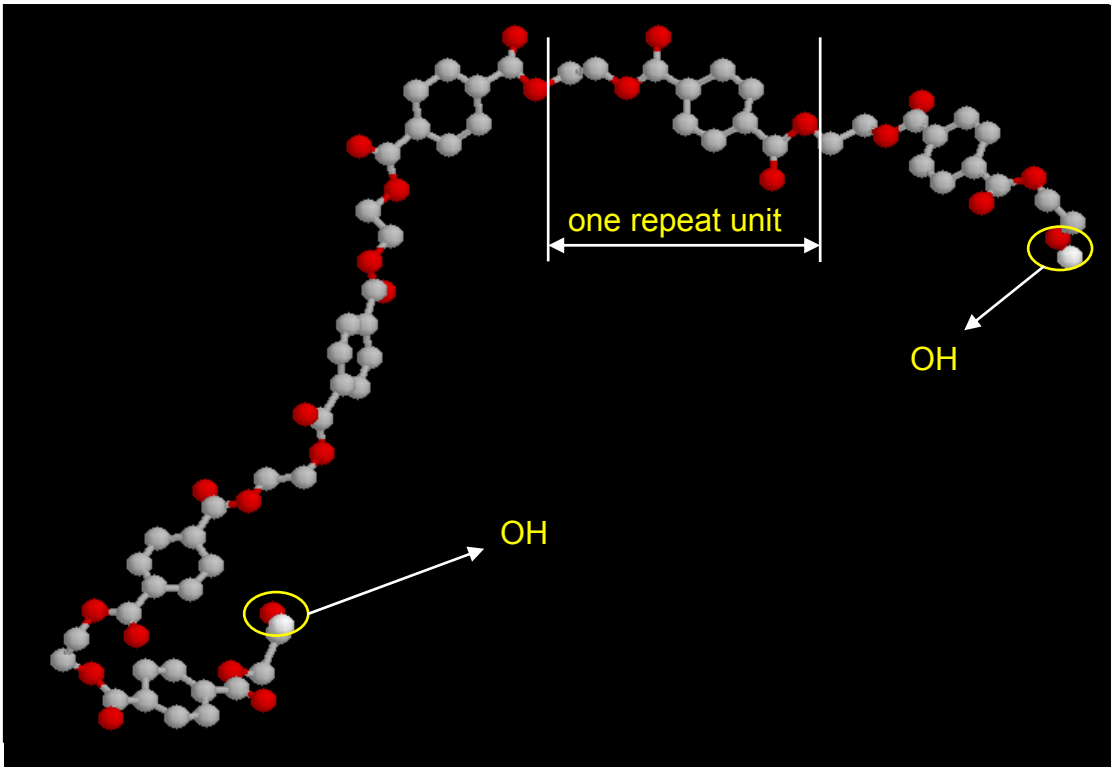

Figure 3.1. Model of the PET hexamer molecule, showing a repeat unit. The only explicit hydrogens are those in the terminal alcohol group.

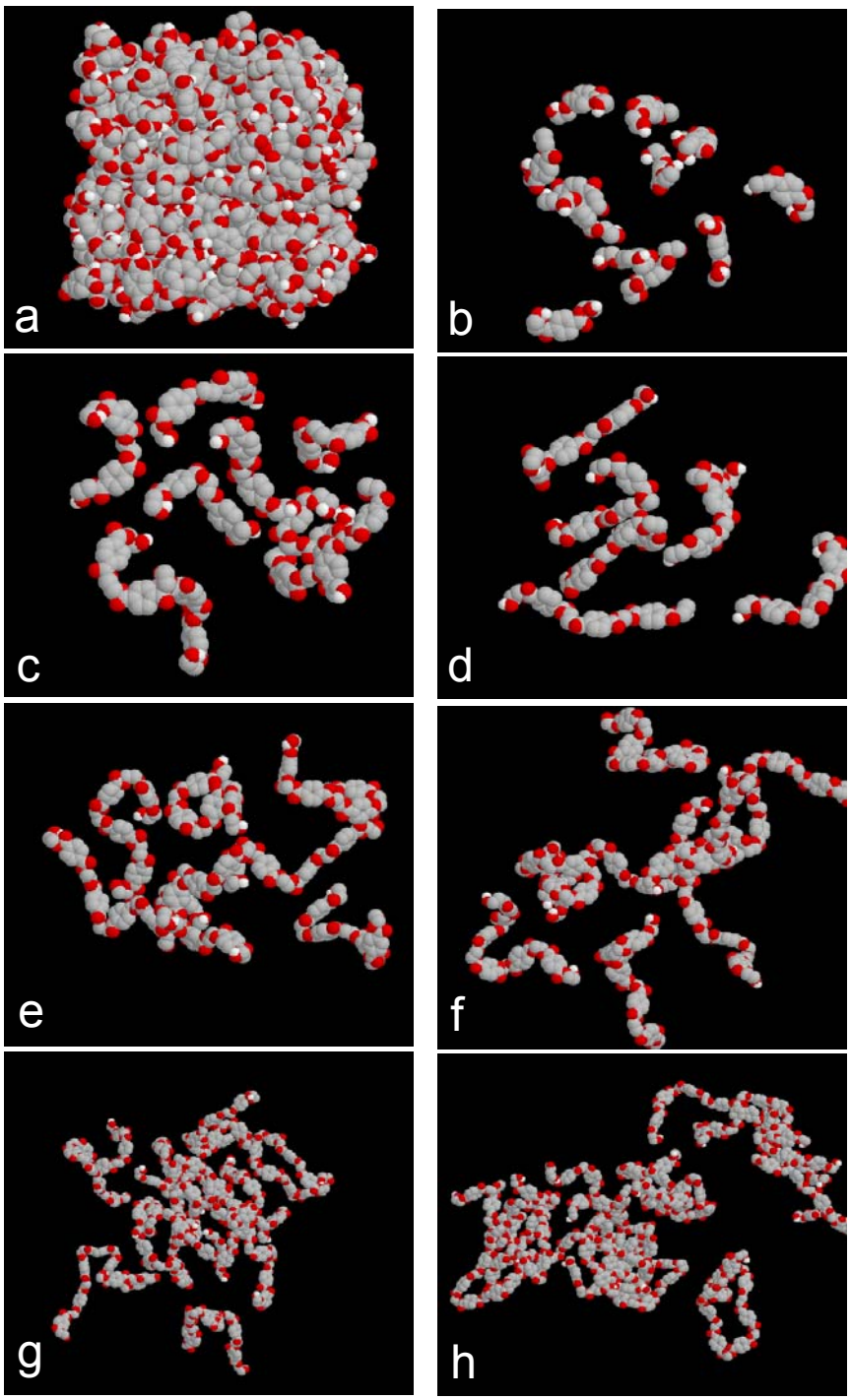

Figure 3.2. Snapshots of equilibrium configurations from simulations at T = 563 K, p= 0.13 kPa. (a) monomer, all molecules shown; (b)-(h) oligomers, selected molecules; (b) monomer; (c) dimer; (d) trimer; (e) tetramer; (f) hexamer; (g) octamer; (h) decamer.

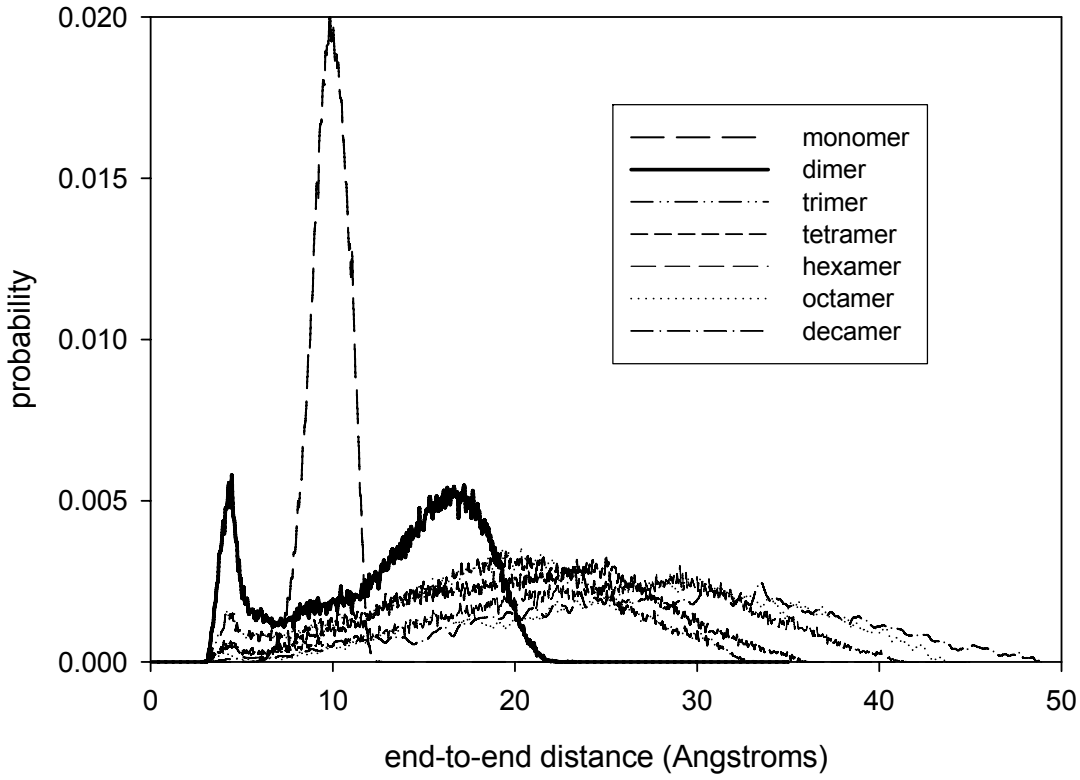

Figure 3.3. Chain end-to-end distance distributions as a function of degree of polymerization (DP).

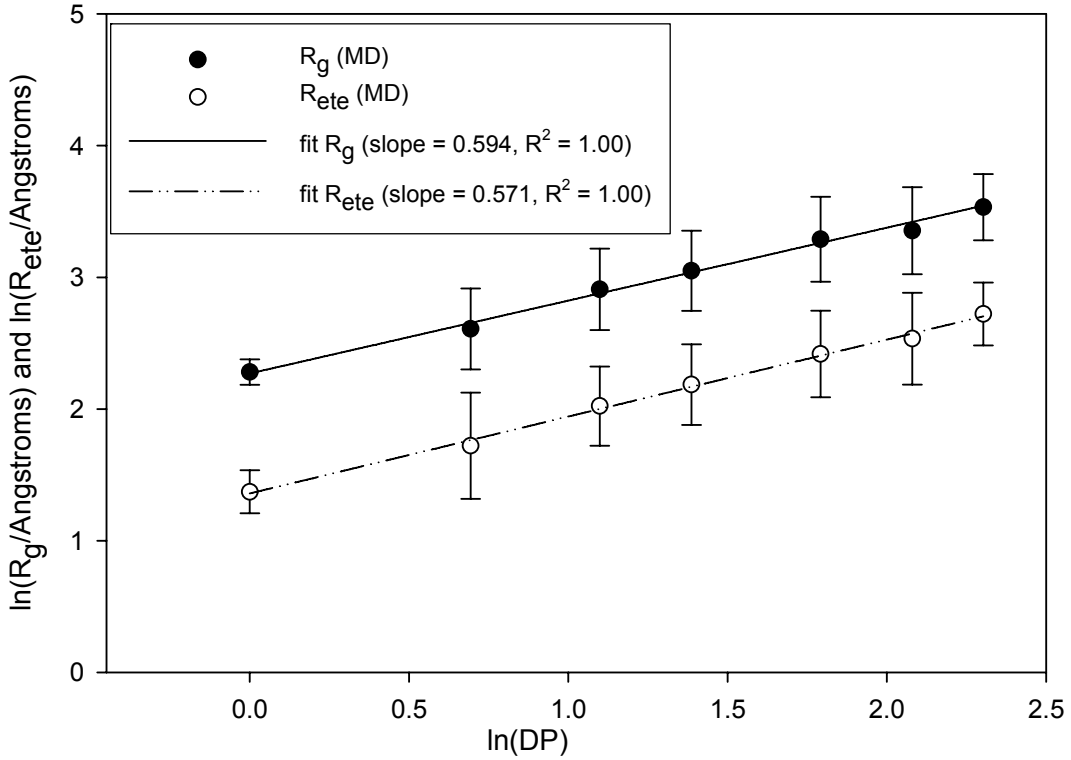

Figure 3.4. Average chain end-to-end distance (R_{ete}) and chain radius of gyration (R_g) as a function of DP.

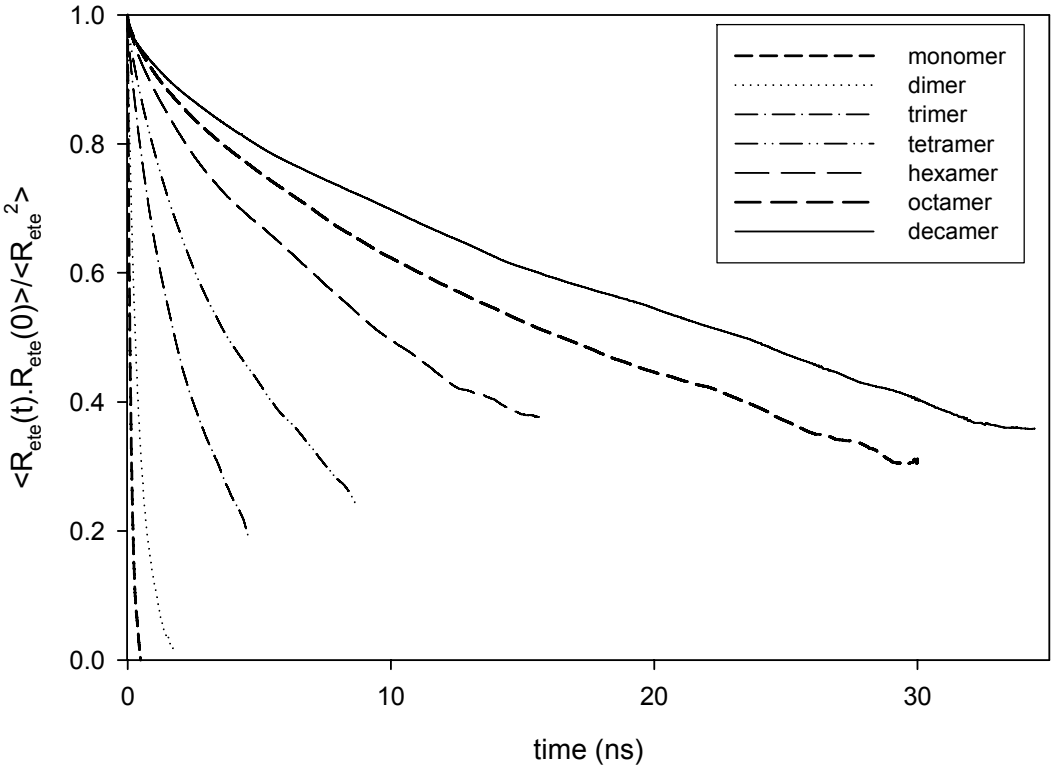

Figure 3.5. Chain end-to-end distance (R_{ete}) auto correlation functions as a function of observation time for all DPs studied.

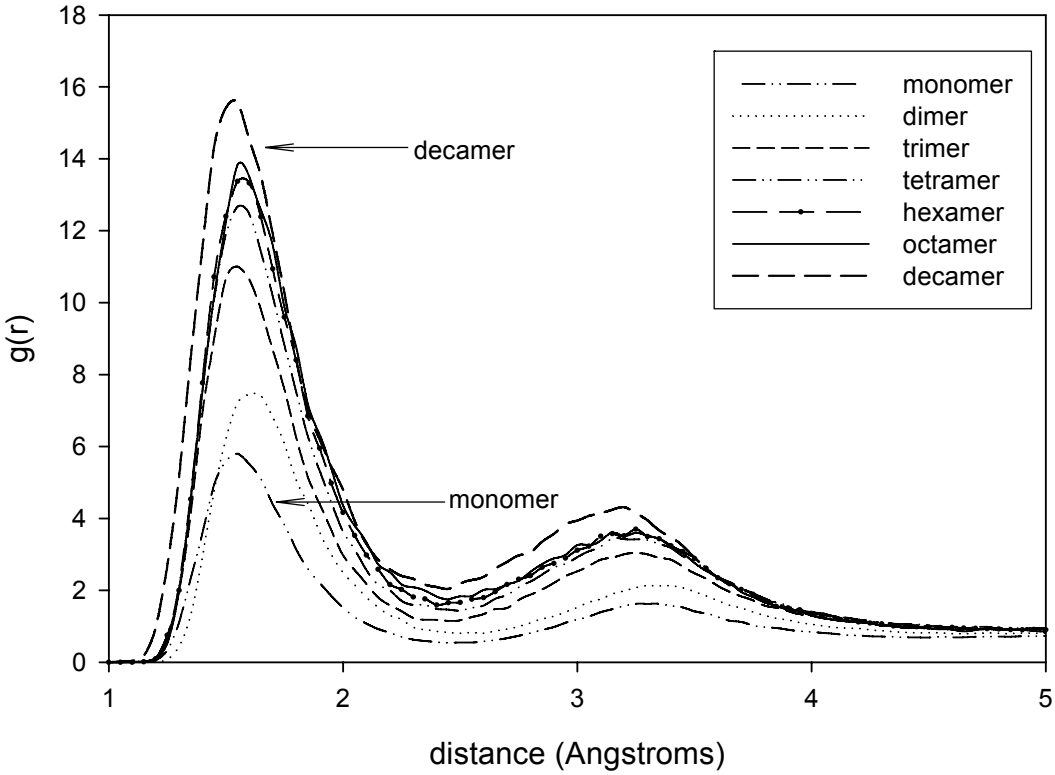

Figure 3.6. Intermolecular oxygen-hydrogen pair correlation function as a function of DP.

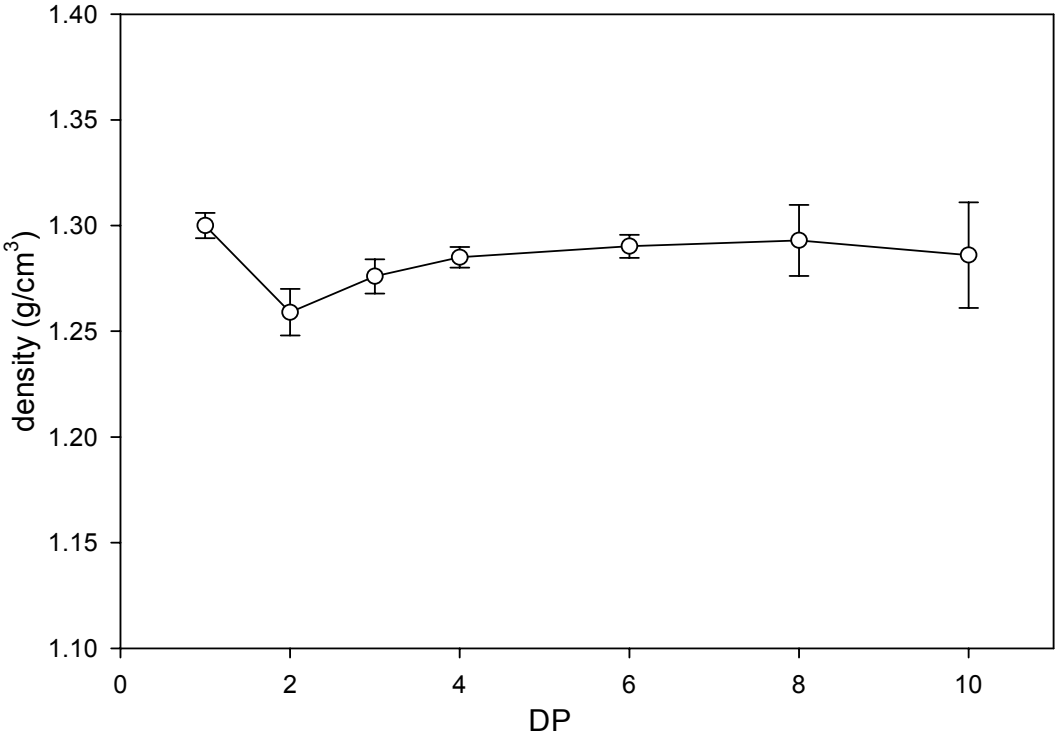

Figure 3.7. Mass density (ρ) as a function of DP.

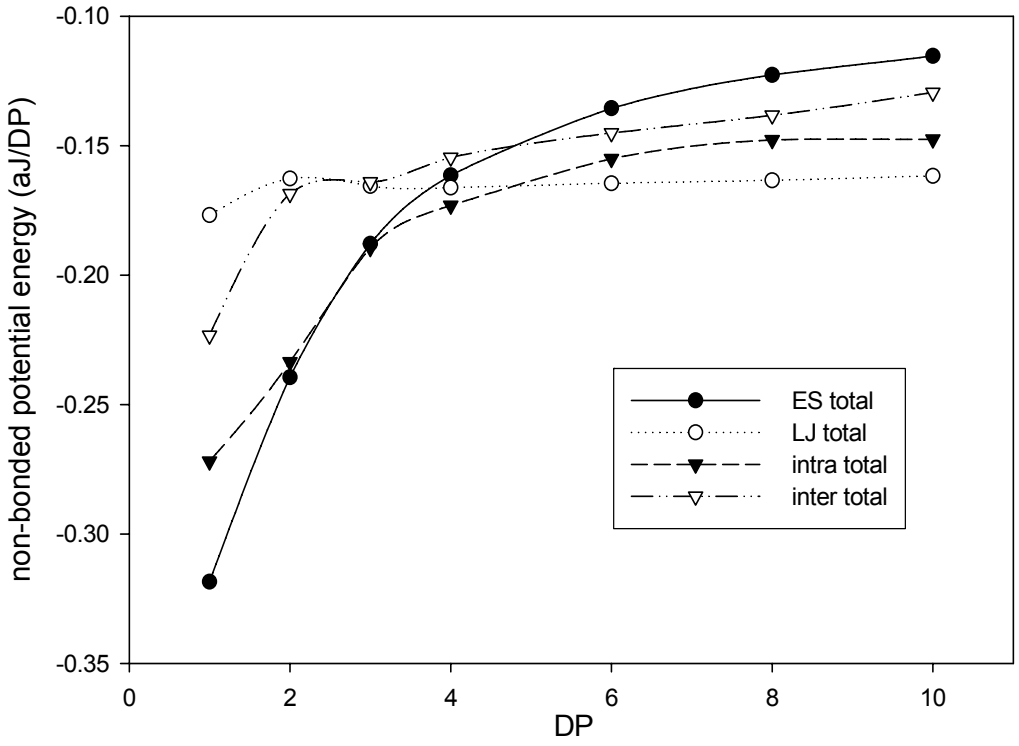

Figure 3.8. Individual non-bonded contributions to the potential energy as a function of DP. ES=electrostatic; LJ = Lennard-Jones; intra = intramolecular; inter = intermolecular. These contributions are normalized by the degree of polymerization.

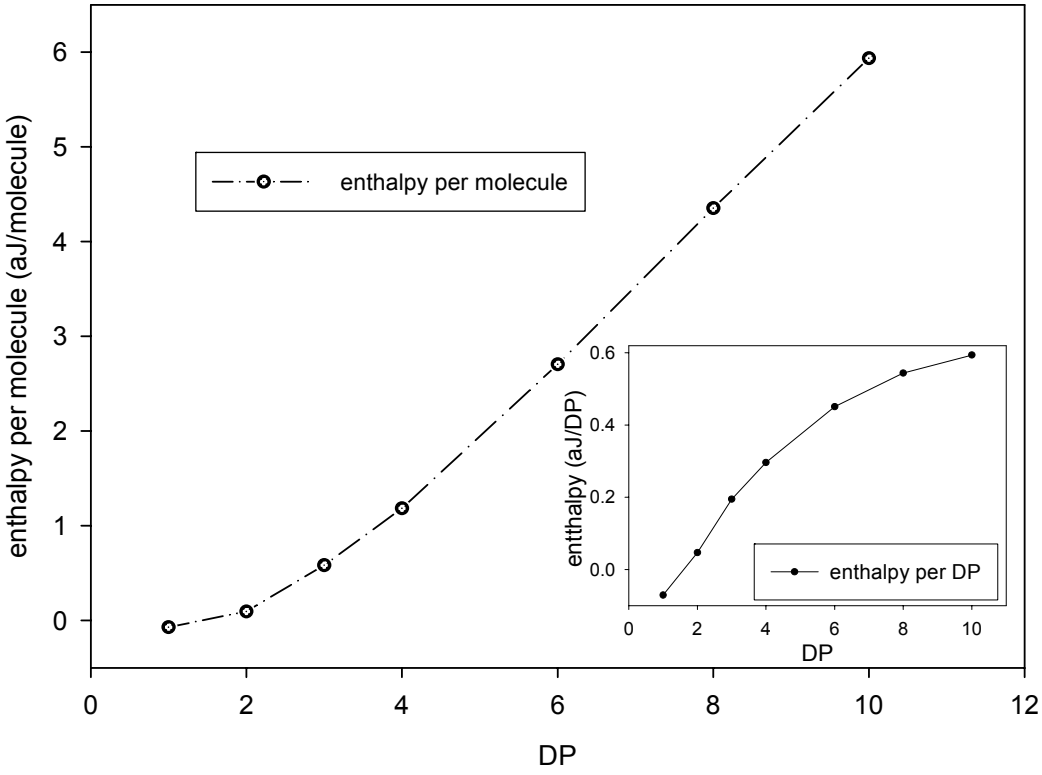

Figure 3.9. Enthalpy as a function of DP. The main figure is plotted on a molecular basis. The inset is normalized by DP.

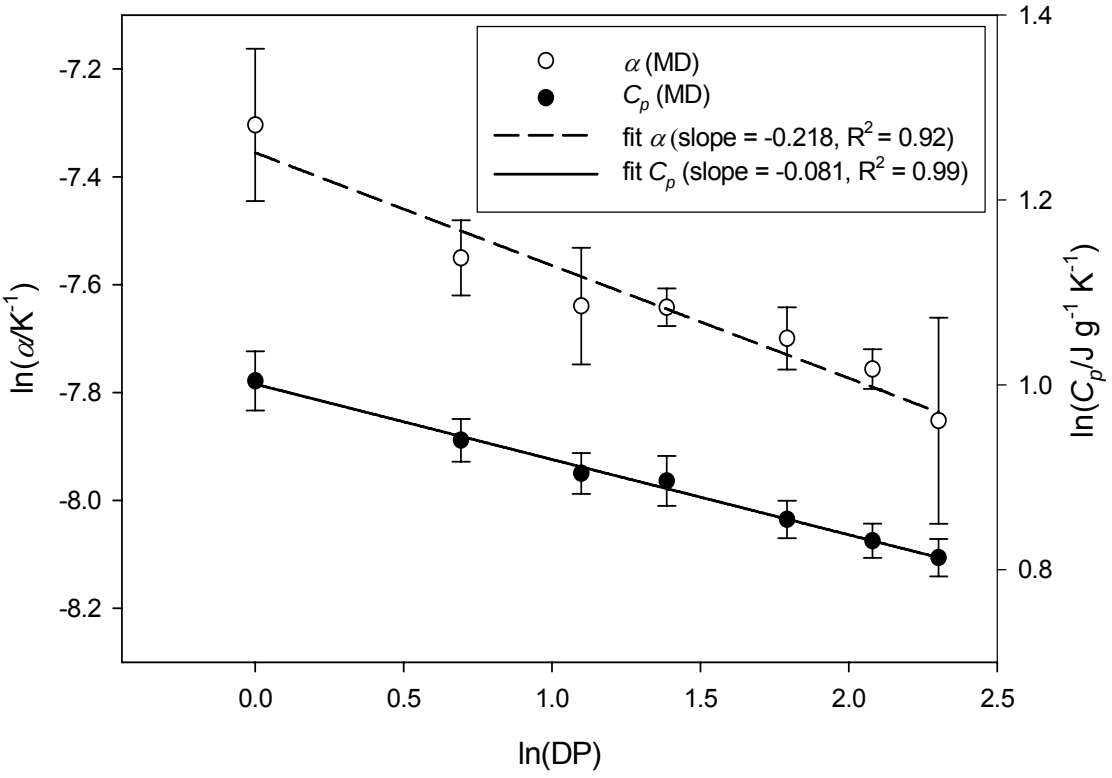

Figure 3.10. Heat capacity (C_p) and thermal expansivity (α) as a function of DP. The fits are to equation (1). The R^2 measure of fit is also reported in the legend.

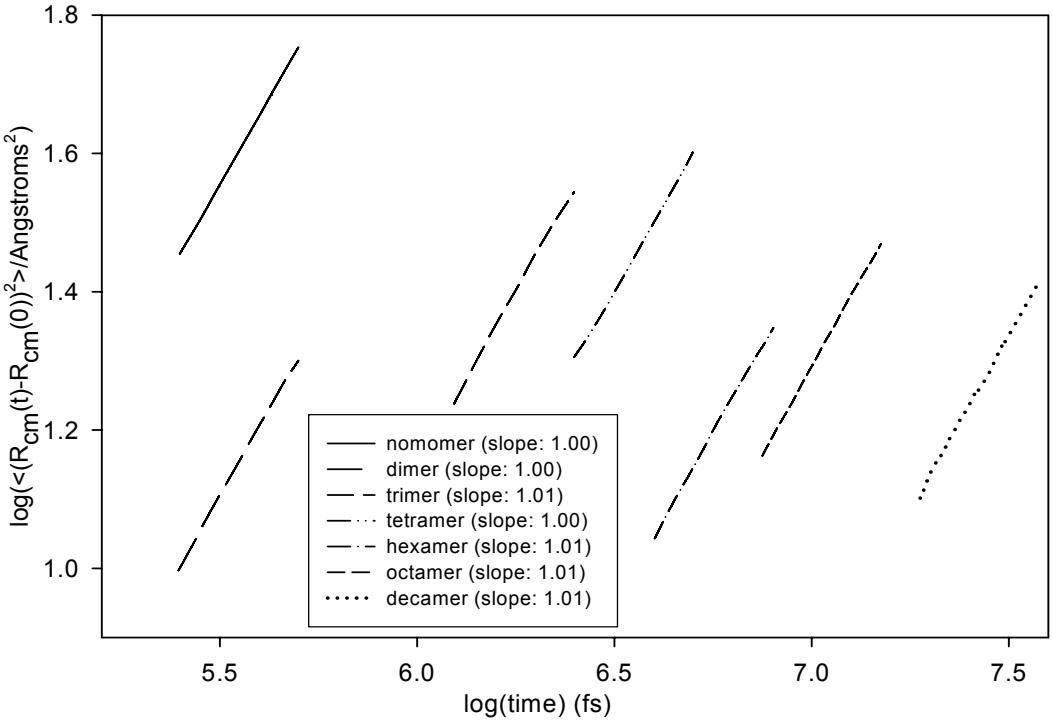

Figure 3.11. The mean square displacement of chain center of mass as a function of observation time for all DPs. The slope reported in the legend should be unity to satisfy the long-time limit of the Einstein relation.

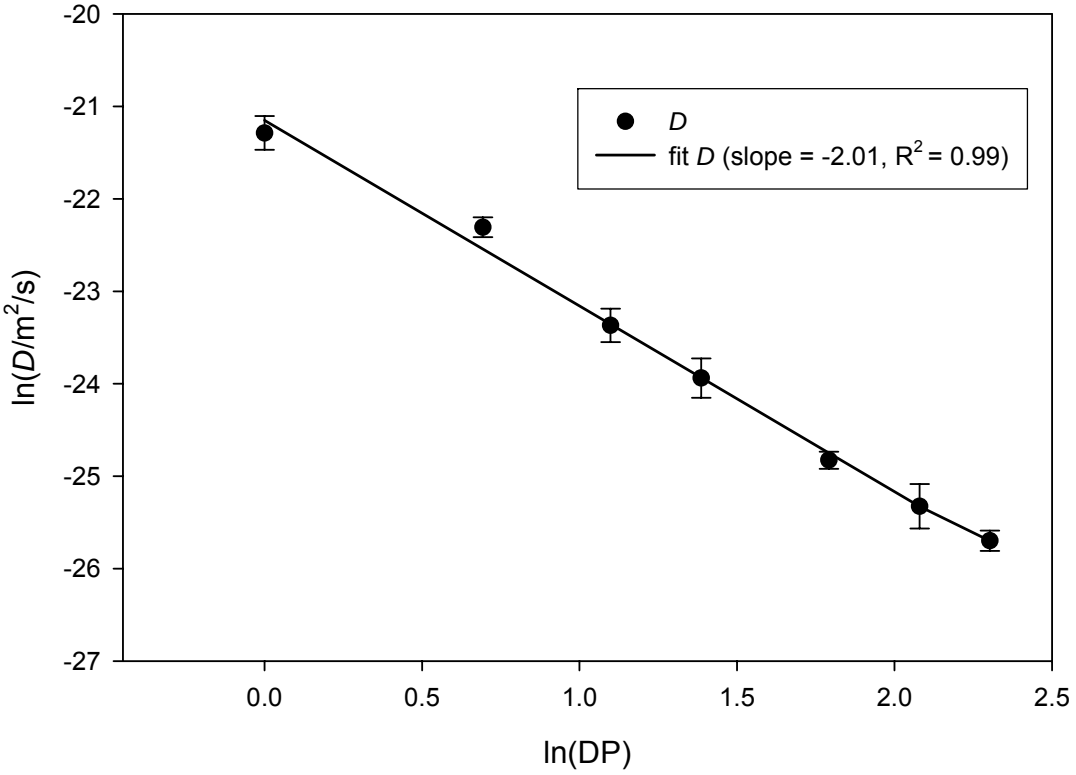

Figure 3.12. Self-diffusivity (*D*) as a function of DP.

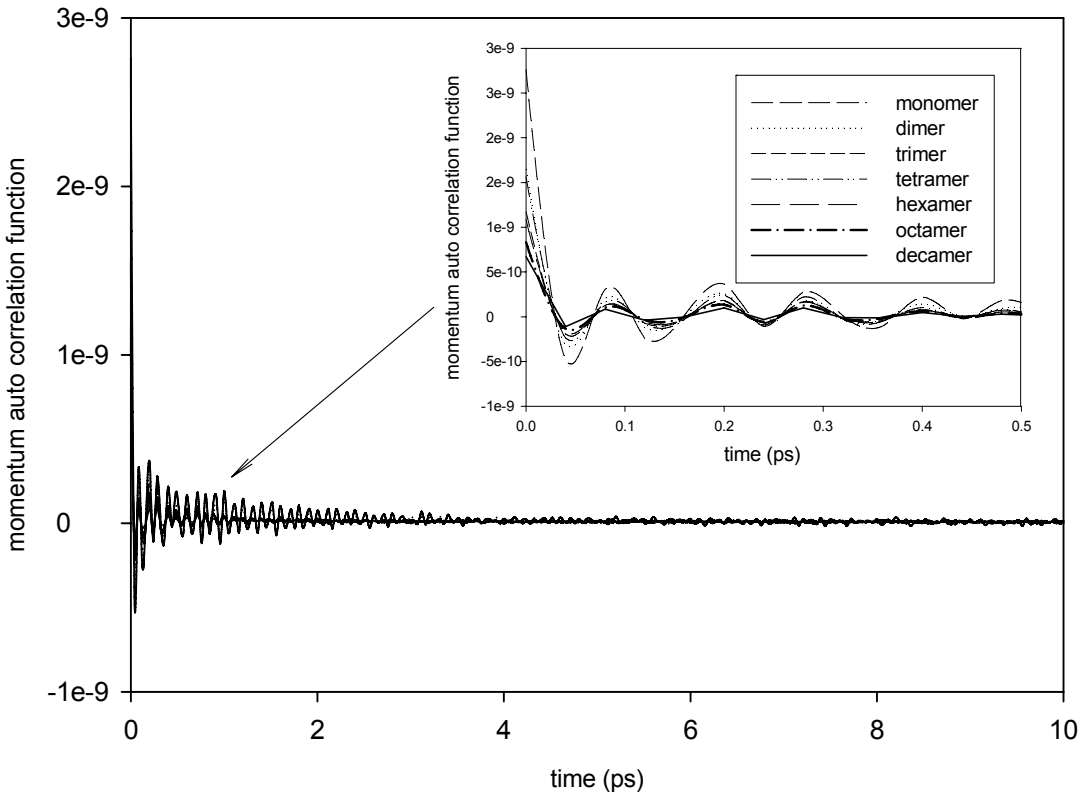

Figure 3.13. Momentum auto correlation functions as a function of observation time for all DP. The inset is a close-up of short time behavior.

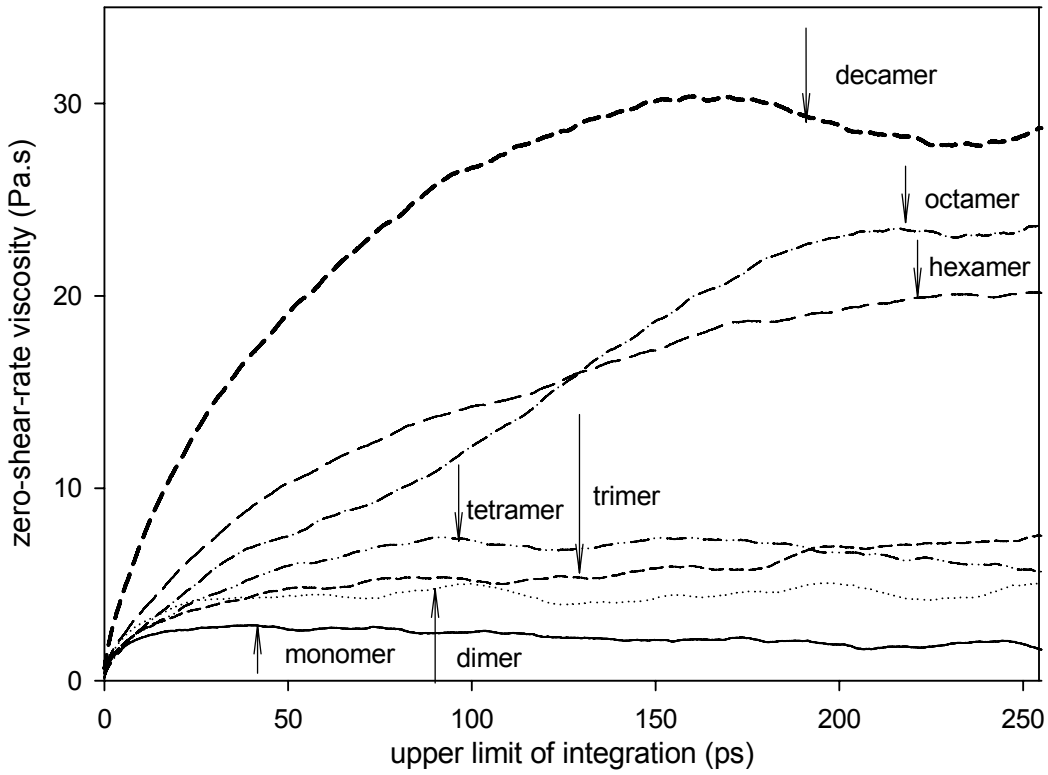

Figure 3.14. Zero-shear-rate viscosity (η) as a function of the upper limit of integration in equation (5). The arrows indicate the observation time at which a plateau begins.

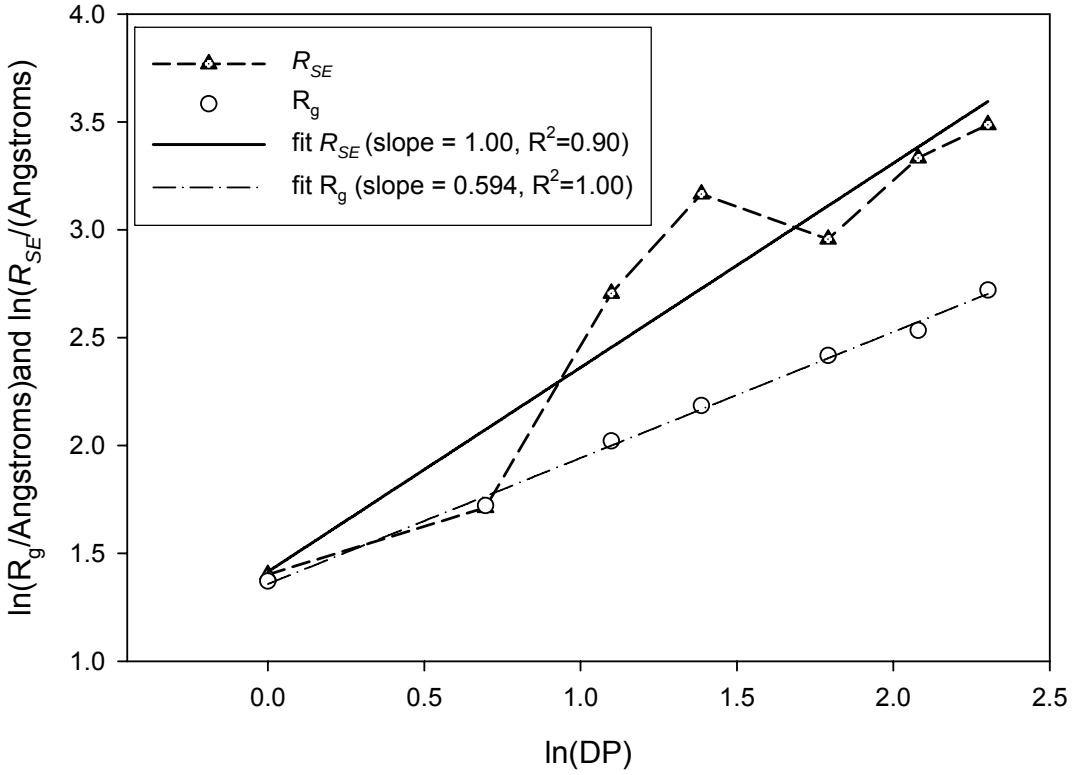

Figure 3.15. Radius of gyration (R_g) and particle radius from the Stokes Einstein relation (R_{SE}) as a function of DP.

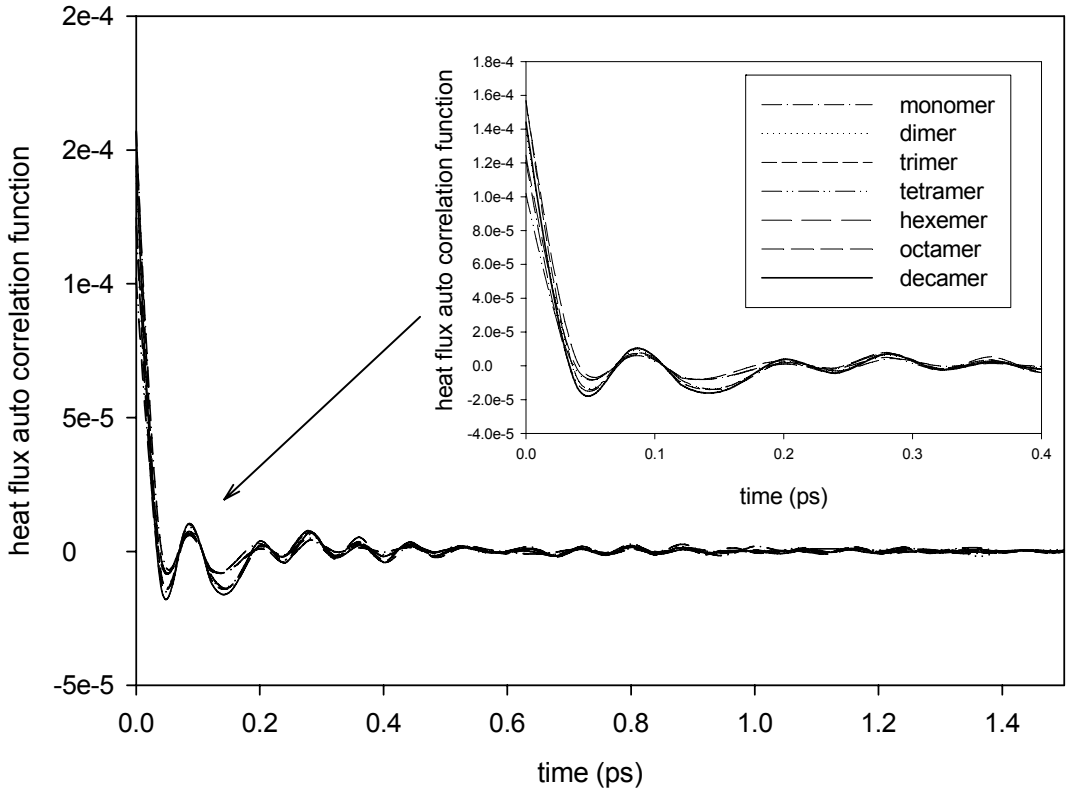

Figure 3.16. Heat flux auto correlation functions as a function of observation time for all DP. The inset is a close-up of short time behavior.

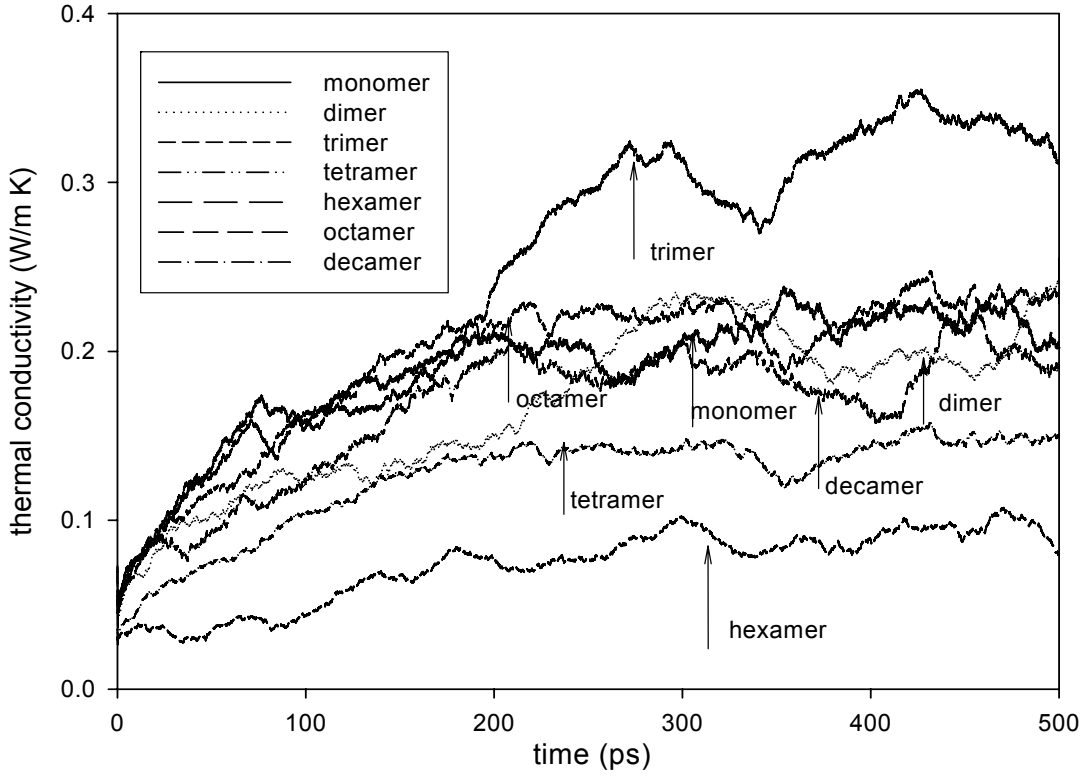

Figure 3.17. Thermal conductivity (λ) as a function of the upper limit of integration in equation (8). The arrows indicate the observation time at which a plateau begins.

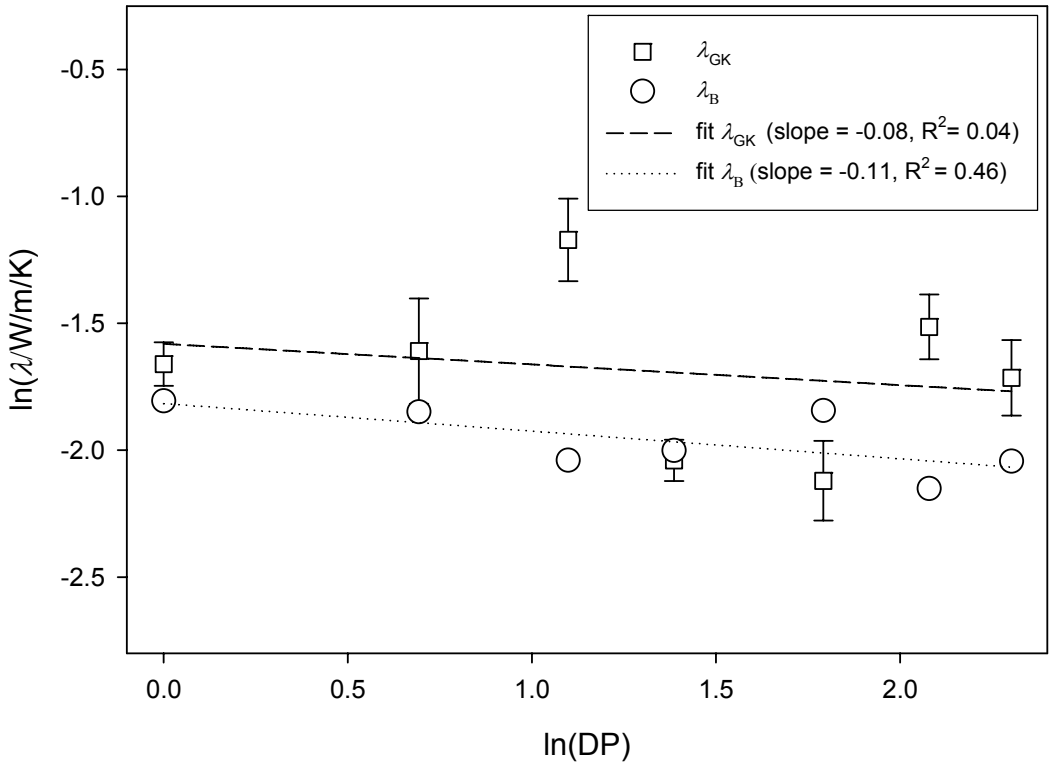

Figure 3.18. Thermal conductivity obtained from the Green-Kubo integral (λ_{GK}) and the Bridgman equation (λ_B) as a function of DP.

CHAPTER 4

Coarse-grained Molecular Dynamics Simulation of Polyethylene Terephthalate (PET)

This chapter is a slightly revised version of a paper by the same title published in the *Journal of Macromolecules* in 2010 by Qifei Wang, David J. Keffer, Donald M. Nicholson, and J. Brock Thomas:

Wang, Q., Keffer, D.J., Nicholson, D.M., Thomas, J.B., "Coarse-grained Molecular Dynamics Simulation of Polyethylene Terephthalate (PET)", *Macromolecules*, 43 (24), 2010, pp 10722–10734.

The use of "we" in this part refers to the co-authors and the author of this dissertation. My primary contributions to this paper include (1) all of the simulation work (2) analysis of data, and (3) most of the writing

Abstract

A coarse-grained (CG) model of Polyethylene Terephthalate (PET) was developed and implemented in CG Molecular Dynamics (MD) simulations of PET chains with degree of polymerization up to 50. The CG potential is parameterized to structural distribution functions obtained from atomistic simulations [Wang *et al.* J. Phys. Chem. B **2010,** *114,* 786] using an inversion procedure based on the Ornstein-Zernike equation with the Percus Yevick approximation (OZPY) [Wang *et al. Phys. Rev. E* **2010,** *81,* 061204]. The CGMD simulation of PET chains satisfactorily reproduces the structural and dynamic properties from atomistic MD simulation of the same systems. We report the average chain end-to-end distance and radius of gyration, relaxation time, self-diffusivity and zero-shear-rate-viscosity's dependence on degree of polymerization. For the longest chains, we find the scaling exponents of 0.51, 0.50 and -2.00 for average chain end-to-end distance, radius of gyration and self-diffusivity respectively. The exponents are very close to the theoretical values of entangled polymer melt systems (0.50, 0.50 and -2.0). The study of entanglement in the longer chains shows that the tube diameter, number of monomers between entanglement points and interentanglement strand length are in close agreement with the reported values for an entangled PET melt.

4.1 INTRODUCTION

Polyethylene Terephthalate (PET) is one of the most important engineering plastics and is widely used in packaging industry as bottles, fibers, and packaging films. The macroscopic structural and dynamic properties of PET have been widely studied through experiments. The computational studies of structural and dynamic properties of PET are limited due to the fact that the polymer's physical properties depend on several time and length scales,[1] which require multi-scale modeling techniques.

Molecular-level simulation has proved to be a useful computational technique to study structural, physical and transport properties of polymers of short length. The structural and transport properties have been studied via molecular simulation with different force fields. Hedenqvist *et al.*[2] developed an atomistic model for PET (hereafter referred to as the HBB model). The specific volume, solubility parameters and dipolar correlation factors obtained from (MD) simulation using this model are in good agreement with the experimental results. Implementing the HBB model for PET in MD simulations of a single chain with 60 monomers, Bharadwaj[3] further studied the diffusion of methane in amorphous PET. Boyd *et al.* modified the torsion component of the HBB potential to satisfy chain dynamics and relaxation.[4] Using a modified HBB model, Wang *et al.*[5] studied the structural, thermodynamic and transport properties of PET oligomers of 125 chains with degree of polymerization (DP) varying from 1 to 10 each. Kamio *et al.*[6] generated structural properties needed to obtain the CG potentials. Other models used in the molecular simulation of PET include the Polymer-Consistent Force Field (PCFF) model,[7] the Open Force-Field (OFF) model,[8] the Rotational Isomeric State (RIS) conformational model,[9-11] and a more recently developed model.[12] All of these studies involve either a single chain or chains with a degree of polymerization (DP) less than or equal to 20. However, the time and length scales used in molecular simulation are far below that of real long chain polymer systems. With finite computational resources, it is beyond current computational capabilities to use an atomistically detailed simulation technique to obtain long time trajectories of long chains. For example, to determine the self-diffusivity of long polymer chains, the simulation must reach the long-time limit required by the Einstein relation. The simulation time can easily be on the order of microseconds or milliseconds and the corresponding real time for the computation is on the order of years or decades.

The motivation behind a coarse-grained (CG) procedure is to lift these computational limitations by eliminating some degrees of freedom in the simulation in exchange for computational efficiency. The reduction in the degrees of freedom is accomplished by grouping atoms in certain fragments of the chain into "superatoms", which interact with their own CG potential.[6,13] Since the degrees of freedom are greatly reduced in the CG model and softer CG potentials are often obtained[13] , larger length and time scales can be reached in the CG level simulation. Structural and transport properties can be calculated directly by CG simulation[14] . Furthermore, the CG level properties can be mapped back to the molecular level through the use of scaling factors.[13-15] This multi-scale modeling technique has been used in the study of structure and dynamics of biomacromolecules[16,17] and polymer chain molecules (polysterene (PS),[13,18,19] polymethyl methacrylate (PMMA),[14] polyethylene (PE),[20] polyethylene oxide (PEO),[14,21,22] polyisoprene/polystyrene blend,[23,24] bisphenol-A polycarbonate (BPA-PC)[25] and azobenzene liquid crystal[26]). Although the molecular simulation of PET has a long history, the CG simulation of PET is less prevalent in the literature. Kamio *et al.*[6] performed CG end-bridging Monte Carlo simulations of PET melts, generating equilibrium structural and entanglement properties. This current work is aimed at conducting CGMD simulations to investigate the structural and dynamic properties of PET chains with a DP up to 50. This range of DP is relevant because PET leaving an industrial finishing reactor possesses a DP in the 30 to 50 range.

There is an up front price that must be paid for the computational efficiency of the CG procedure; the price is the development of an accurate interaction potential for the CG superatoms. Obtaining reliable nonbonded interaction potentials is particularly challenging. Two common methods have been adopted to obtain nonbonded CG potentials, namely adjusting power law type potential parameters (Lennard-Jones 12-6, 7-6, 7-4, 7-5),[13,18,19,26] and iterative Boltzmann inversion method.[6,27] CG level simulations have been conducted using CG potentials from both of the above methods. Using CGMD simulation with power law type of nonbonded potential, Harmandaris *et al.*[13,18,19] studied structural and dynamic properties of long chain Polystyrene (PS) systems. A scaling factor is reported for the speed up of chain dynamics based on the difference on mean square displacements. Using potentials from the iterative Boltzmann inversion[27] method, Kamio *et al.*[6] performed CG end-bridging Monte Carlo simulations of PET

melt. Both methods used to obtain CG potentials need improvements with respect to computational accuracy and efficiency.[16,26,28,29]

Alternative methods have been developed recently to improve computational accuracy and efficiency of the CG procedure. Fritz *et al.* [30] recently present a new approach that obtains both the bonded and nonbonded interactions of the CG model of PS from the sampling of isolated atomistic chains and pairs of oligomers in vacuum. The method is computationally inexpensive. The CG model of PS using the calculated CG potentials reproduces the melt packing, the density and local chain conformations of atactic as well as stereoregular PS.

The Ornstein-Zernike integral equation (IE) theory[31,32] is also widely used to study the structural properties of polymer systems.[28,33-36] In most cases, the IE theory is used to generate structural properties like pair correlation functions (PCFs) given the interaction potential. Although, it has been used to obtain the nonbonded potential parameters,[37] the iterative nature of the procedure limits the computational gain from coarse-graining. Non-iterative procedures also exist in which structural properties and interaction potentials can also be obtained from the theory and a description of the atomistic system.[34-36]

An alternative procedure based on the Ornstein-Zernike equation with the Percus-Yevick approximation (OZPY equation)[38,39] is to extract the CG nonbonded potential from the PCFs, which is referred as inverse OZPY or $OZPY^{-1}$. The use of $OZPY^{-1}$ method[40] to obtain the interaction potential has been reported in the study of monatomic systems.[41-44] The $OZPY^{-1}$ method is approximate only because of the approximate nature of the PY assumption for the direct correlation function. On the other hand, it is simple and fast compared to the current methods of comparable accuracy. Wang *et al.*[29] demonstrated that this method can be applied to systems that have intramolecular degrees of freedom, such as the diatomic Lennard-Jones fluid. Here, we apply the $OZPY^{-1}$ method to extract nonbonded CG potential for PET chains with PCFs from atomistic MD simulations.

In previous work,[5] atomistic simulations of PET oligomers of degree of polymerization 1, 2, 3, 4, 6, 8 and 10, using the HBB model were performed. For the tetramer, hexamer, octamer and decamer, PCFs (based on center of mass position of the CG beads), relaxation times and diffusion coefficients from these simulations were obtained. In this work, we use the structural

results from the atomistic simulations of PET as input into the OZPY^{-1} method to generate a CG potential of PET. We perform CGMD simulations of longer chain PET with DP equal to 4, 6, 8, 10, 20, 30, 40 and 50. Structural and transport properties are studied at the CG level and mapped back to molecular level. Finally, the entanglement of long chain systems are studied by the Z algorithm.[45] This paper is organized as follows. The details of the potential and simulation techniques are given in section 2. The results and discussion are presented in section 3. The conclusions are listed in section 4.

4.2 SIMULATION METHOD

4.2.1 Atomistic simulation of PET tetramer, hexamer, octamer and decamer.

Although no additional atomistic simulations were performed for this work beyond those previously reported,[5] this work does present new properties from the atomistic simulations. Therefore, we briefly review the simulation procedure that was used in the previous work,[5] where a more detailed description is provided. We use the modified anisotropic united atom HBB potential model developed by Hedenqvist, Bharadwaj and Boyd[2,4] for PET to describe the intra-molecular and inter-molecular potential of oligomers molecules. We simulated in the isobaric-isothermal (NpT) ensemble and implemented the Hamiltonian-based thermostat and barostat of Keffer *et al.*[46] with controller frequencies set to 10^{-4} fs. The XI-RESPA NPT algorithm developed by Tuckerman *et al.*[47] was used to integrate the equations of motion. The large time step was 2 fs and the small time step was 0.2 fs. The parallel code we used was built in-house and is written in FORTRAN-90, using MPI for inter-processor communication. It has been tested rigorously across a variety of applications. For the simulations in this work, we verified conservation of the Hamiltonian in order to validate our choices of time step, cut-off distance and to minimize the possibility of bugs in the potential. For DP from 4 to 10, we simulated 125 molecules. The state point was set at 0.13 kPa and 563 K, as this corresponds to conditions within a finishing reactor.[48] As for the initial conditions, we estimated the initial density and placed the particles in the simulation volume, avoiding significant overlap. To accelerate equilibration, we started with a higher temperature. Then we gradually decreased the temperature of the system and equilibrated to the correct density. Typically, each equilibration stage lasted for 1 ns. The details of the equilibration procedure can be found in elsewhere.[2,5,6]

Data production followed and lasted over 30 ns for the octamer and decamer. These lengths of data production were chosen to be greater than the longest rotational relaxation time as determined in the simulation.

4.2.2 CGMD simulations of longer PET chains with DP = 4, 6, 8, 10, 20, 30, 40 and 50.

We propose that PET can be modeled at a coarse-grained level with two spherical beads of type A and B. The A bead corresponds to the benzene fragment, C_6H_4, and the B bead corresponds to all of the atoms between benzene fragments, $C_4H_4O_4$. In the construction of the PCFs involving A and B from the atomistic simulations, the A and B beads are placed at the center-of-mass of the atoms in the corresponding fragment, as shown in Figure 4.1. This definition introduces a small error due to end effects in the B beads terminating each chain, which in the atomistic simulation are actually $C_3H_5O_3$. This mapping scheme contains a reduction in the number of degrees of freedom that enhances computational efficiency making the study of the dynamics of longer-chains tractable, while at the same time keeping sufficient structural details to reproduce the atomistic chain conformations. The validation of this choice of mapping scheme is given in the Results and Discussion section.

The CG potential includes bond stretching (BA), bond bending (BAB and ABA), bond torsion (BABA), intra-molecular nonbonded interactions (for beads over four bonds) and inter-molecular nonbonded interactions (BB, BA and AA). Probability distribution functions (PDFs) for stretching, bending, torsion and nonbonded interactions between CG particles were generated from the atomistic simulations. In the development of coarse-grained (CG) potentials, for the stretching, bending and torsion modes, there are straightforward approximations that relate the interaction potential directly to the PDFs.[13] The effective interaction potential between a particle of type α and a particle of type β, $\varphi_{\alpha\beta}$, as a function of the separation between particles, r, can be related to the probability distribution function, $g_{\alpha\beta}(r)$, via

$$\varphi_{\alpha\beta}(r) = -k_B T \ln\left(g_{\alpha\beta}(r)\right) + c_{\alpha\beta} \quad (1)$$

where k_B is Boltzmann's constant, T is temperature and $c_{\alpha\beta}$ is a constant. Note here coordinates need to be changed for the bending (from r to θ (bending angle)) and torsion (from r to ϕ (torsion angle)) modes.[13,18,26]

To extract the nonbonded CG potentials, there are two major methods currently used. First, the parameters of an analytic potential such as Lennard-Jones are adjusted to closely reproduce the target PCF in the atomistic liquid/melt. A problem with this method is that the difference of conformations and orientations between fragment molecules and target molecules may not be reflected correctly on the corresponding coarse-grained potentials.[16,26] For example, the conformations of phenol rings in liquid benzene and that in PS melt where the rings are embedded into a long chain may be different. Consequently, these conformations would be misrepresented in the CG potential. The calculated potentials cannot be used under ambient pressure condition or be applied to study the formation of ordered structures driven by enthalpic interactions.[30] Fritz *et al.*[30] recently developed a new method that addresses these drawbacks. The method derives nonbonded potentials from constraint dynamics with the all–atom model of two trimers (or tetramers) of PS in vacuum. In this way, the atomistic melt properties are not used in the parameterization while the potential can still be used in the condensed melt phase. To some extent, the multibody contributions to the effective potential are taken into account.

In the second method, a tabulated potential is numerically determined by simulation iteration. The interaction potential is refined iteratively via

$$\varphi_{\alpha\beta,i+1}(r) = \varphi_{\alpha\beta,i}(r) + k_B T \ln\left(\frac{g_{\alpha\beta,i}(r)}{g_{\alpha\beta}(r)}\right) \tag{2}$$

where $g_{\alpha\beta}(r)$ is the target PCF. Potentials obtained from this procedure will closely reproduce the CG atomistic liquid PCFs. The challenging part of this method is obtaining PCFs from simulations in each iteration. As mentioned by Guenza[28] , those simulations have to be performed on length scales and timescales large enough to ensure a reliable numerical predictions of the potential at the length scale characteristic of the coarse-graining procedure. This could strongly limit the computational gain of CG procedure.

In this work, we use the form of the bonded potentials from eqn. 1 and nonbonded potentials from the OZPY^{-1} method to describe both the intra-molecular and inter-molecular potential of CG PET chains. The Ornstein-Zernike Integral Equation for a mixture of simple fluids[38] is

$$g_{\alpha\beta}(r,r')-1=c_{\alpha\beta}(r,r')+\sum_{\gamma}\int c_{\alpha\gamma}(r,r'')n_{\gamma}(r'')\left[g_{\gamma\beta}(r'',r')-1\right]d^3\,r'' \tag{3}$$

where the pair correlation function between particles of type α and β located respectively at r and r', $g_{\alpha\beta}(r,r')$, is related to the direct correlation, $c_{\alpha\beta}(r,r')$, and an integral including the interactions of the α and β particles with a third particle, γ, located at r'' with a singlet density, $n_{\gamma}(r'')$. There is a summation over γ spanning all types of particles. This equation in its present form implicitly allows for a different interaction potential between each pair of types of particles. In essence, the summation over γ is a summation over interaction potentials. To emphasize this, the Percus-Yevick approximation of the direct correlation function can be written as

$$c_{\varphi_i}(r,r')=g_{\varphi_i}(r,r')\left[1-\exp\left(\frac{\varphi_1(r,r')}{k_BT}\right)\right] \tag{4}$$

Substitute this to OZ equation yields the OZPY equation[29]

$$y_{\varphi_1}(r)=1+\sum_{\varphi_2}\sum_{\varphi_3}\frac{2\pi n}{r}\int_0^{\infty}ds\,s\left[h_{\phi_2}(s)-y_{\phi_2}(s)+1\right]\int_{|r-s|}^{r+s}dt\,t\,h_{\varphi_3}(t) \tag{5}$$

With the definition of cavity function[49] and total correlation function respectively as

$$y_{\varphi_i}(r,r')=g_{\varphi_i}(r,r')\exp\left(\frac{\varphi_1(r,r')}{k_BT}\right) \tag{6}$$

$$h_{\varphi_i}(r,r')=g_{\varphi_i}(r,r')-1 \tag{7}$$

where φ_1 is always the unknown nonbonded potential, while the summations of φ_2 and φ_3 include both nonbonded and bonded potentials. Conceptually, then we measure all $h_{\varphi_i}(t)$ in the simulation and we solve eqn. (5) numerically for $y_{\varphi_1}(r)$ from which the potential can be directly extracted. The details of the application of the OZPY^{-1} method to polyatomic fluid is given as supplementary information of this paper. The method requires a meticulous accounting of the allowable combinations of interaction potentials in the summations of φ_2 and φ_3, which are dependent on the connectivity of the polymer chain. For example, for the diatomic molecule, there were three combinations of φ_2 and φ_3 (stretching-nonbonded, nonbonded-stretching, and nonbonded-nonbonded). One can't have stretching-stretching in a diatomic system. For PET,

there are 34 such combinations. All the calculated potentials are presented in the discussion section.

In addition to CG model and potentials, we also require reliable initial configurations to start the CGMD simulation. For DP = 4, 6, 8 and 10, the initial configurations of CG chains are based on center of mass positions of the fragments from the atomistic simulations. For DP = 20, 30, 40 and 50, we estimated the initial density and placed the particles in the simulation volume carefully with proper bond length and angles, then gradually introduced the nonbonded interactions to avoid overlap.

We again simulated in the isobaric-isothermal (NpT) ensemble under the same pressure and temperature as the atomistic simulation. The time steps of CGMD simulation are 10 times larger than those used in the atomistic MD simulation. The simulation method is similar to that used in the atomistic MD. After an equilibrium stage, the systems reach the equilibrium densities. The equilibrium densities of different systems are in the range of 1.18 to 1.29 g/cm^3, which is close to the finding of Kamio *et al.*[6] by a different method. End effects exist but become smaller with increasing chain length.

Apparent speed up is observed in CG level simulation. Based on wall-clock time, the CGMD simulations are about 50 times faster than the atomistic simulations. Note here that in our atomistic simulations, a united-atom model was used for hydrogen bound to carbon, already eliminating some degrees of freedom. The speed up factor would be larger if the hydrogens were explicitly accounted for in the atomistic simulation. The procedure is still computationally intensive, to finish a run of 4300 ns for a system of chains with DP of 50, it took roughly 3 months on 16 processors. However, such a run would have been infeasible with atomistic simulation. The duration of data production was chosen to be 4 or 5 times the longest rotational relaxation time as determined in the simulation for DP from 4 to 30. These simulations ran as long as 1600 ns. For DP equals 40 and 50, the simulation times were 2800 ns and 4300 ns respectively, which are roughly equal to the longest relaxation times of these systems, which represents a compromise based on finite computational resources.

4.3 RESULTS AND DISCUSSION

In this section, we present the results of the CGMD simulations for PET with DP = 4, 6, 8, 10, 20, 30, 40 and 50. For the four shortest chains, we compare the results with those of the corresponding atomistic simulations. The results are broken into three parts: structural properties, transport properties and entanglement analysis. A summary of raw properties generated from the CGMD simulations is presented in Table 1. Note that these properties have not been adjusted by any time or length scaling factors. When mapping the CGMD simulation results back to the molecular level, scaling factors based on the time scale difference of the two level simulations are used.[13,25] A comparison of structural and dynamic properties from atomistic MD simulation and corresponding scaled values from CGMD simulation for DP equals 4, 6, 8 and 10 are listed in Table 2. All the time related properties in the figures (end-to-end autocorrelation functions, self-diffusivity, mean square displacement and zero-shear-rate viscosity) are scaled with the appropriate time-scaling factor. A detailed explanation of each scaling factor is contained in the discussion of its related property. In the sections below, our discussion is largely confined to comparison between the atomistic MD and CGMD simulations, as well as comparison of the observed results with the Rouse and reptation theories. Comparison of the results of the atomistic simulations with experimental measurements, which was in general quantitative, is available elsewhere.[5]

4.3.1 Structural Properties

In Figure 4.2, we show the distributions of bonded and nonbonded CG beads obtained from atomistic simulations. These distribution functions are based on the analysis of configurations from atomistic MD of the tetramer, hexamer, octamer and decamer. As shown in Figure 4.1, these distribution functions are calculated according to the center of mass position of CG beads. In our CG model, there is only one type of stretching mode (BA), two types of bending modes (BAB and ABA) and three types of nonbonded modes (BB, BA and AA). The stretching mode shows a Gaussian type distribution with the equilibrium bond distance around 5.0 Å. The bending BAB shows single peak centered at 150˚, while the bending ABA displays bimodal distribution with one peak centered at 110˚, the other centered at 170˚. The torsional mode distribution is similar to that of Kamio *et al.*[6] 's work, although they used a different CG model. Similar features for stretching and bending distributions are also reported in the work of

Hamandaris *et al.*[18] on polystyrene. We believe this similarity is due to a common treatment of phenol rings in the three CG models. The nonbonded BB, BA and AA distributions show multiple peaks with the first peak centered at 5.0 Å. Figure 4.2 also shows that both bonded and nonbonded distributions are not significantly changing with DP, which indicates that our proposed CG model is able to capture the structural features of PET chains with different chain lengths. Any discrepancy based on chain length is probably due to end effects, which will diminish as we explore longer chains. We obtained the bonded stretching, bending and torsion CG potentials through eqn. 1, based on the bonded distribution functions of the decamer. The distribution functions of the decamer from atomistic simulation also serve as the target distributions, which we will compare later with the distribution functions from CGMD simulations of the decamer.

In Figure 4.3, we plot the bonded and nonbonded CG potentials of different interaction modes extracted from the PCFs of the atomistic simulation of the decamer. The bonded potentials are generated via eqn. 1 and the nonbonded potentials are generated using the $OZPY^{-1}$ procedure. The bonded potentials are shifted to have zero energy at the minima. The three nonbonded interaction potentials obtained from $OZPY^{-1}$ method are shown in Figure 4.3. These nonbonded potentials are close to Lennard-Jones 7-6 potential. Therefore, the calculated potentials were fit to a LJ 7-6 form to avoid (i) numerical noise and (ii) deficiencies due to the approximate nature of the Percus-Yevick equation. These deficiencies include a softer repulsive potential resulting in greater overlap than observed in the atomistic simulations and an overestimation of the rate at which the potential rises at separations immediately beyond the first minimum. The specific procedure to obtain these nonbonded interaction potentials are presented in the supplementary information. Note here that the nonbonded potentials are used in both intra-molecular and inter-molecular parts. Clearly, the nonbonded potential indicates the strongest interaction between two B beads, and the weakest interaction between two A beads. We can attribute this to the polar nature of the fragments in the B beads and the nonpolar nature of the benzene ring in the A bead.

Because we have simulated the chains with DP = 4, 6, 8 and 10 using both atomistic and CG simulations, there are a variety of properties that can be evaluated to determine the validity of the coarse-graining procedure. First, the equipartition of energy was checked. In both the

atomistic and CG simulations, the average system temperature of a MD simulation is calculated based on the equipartition theorem, but it can also be computed by measuring the velocity distribution and fitting it to a Maxwell-Boltzmann distribution. For the CG simulation of the decamer, we computed the temperature of the A and B beads in the simulation in the x, y, and z dimensions using both procedures. The results are shown in Table 3 and Figure 4.4. The CG simulation results show that the average temperature equals to the set temperature with 0.2% standard deviation. The Figure 4.3 shows the velocity distribution of CG beads B and A in the x direction, compared to the expected Maxwell-Boltzmann distribution based on the target temperature and fragments masses. Thus, in our CG simulations, we confirm both the equipartition of energy and the Maxwell-Boltzmann distribution of velocities. Consequently, the temperature of these CG simulations is well established. In fact, the equipartition theorem could be violated in CGMD simulations when the mass ratio of CG beads is very large. The mass ratio of the two CG beads (B/A) in our PET model is 1.45, closer to 1 than that in the polystyrene models (6.5 and 2.8) of Harmandaris *et al*. ,[13,18] in which the mass was assumed to be evenly distributed between two CG beads to use a larger step size. Their later work shows that this assumption affects the scaling factor of dynamic properties.[13] Based on the above analysis, we avoided this assumption.

The second check between the atomistic and CG simulations that can be done is based on a comparison of the bonded PDFs. Equation 1, which is used to generate the bonded potentials, is subject to the assumption that all the interactions are independent of each other. The above potentials can only correctly reproduce the conformational sampling of atomistic description if all degrees of freedom are uncorrelated.[16] Villa *et al.*[16] and Harmandaris *et al.*[13,18] discuss the validation of this assumption. In Figure 4.5, we present the comparisons of all the bonded PDFs from atomistic MD and CGMD simulations of the decamer. The stretching, bending and torsion PDFs agree reasonably well between the two techniques. All of the peaks are present. The largest discrepancy occurs in the ABA bending distribution, in which the CGMD results under-predict the population of the smaller peak at about 170°. We have validated the assumption of independence of the bonded modes through direct comparison of the distribution from the atomistic and CG simulations. Further understanding of the statistical interdependencies of

different interaction modes could be achieved through additional analysis described in the literature.[13,16,30]

The third check between the atomistic and CG simulations that can be done is based on a comparison of the nonbonded PCFs and is a validation of the $OZPY^{-1}$ coarse-graining procedure. The nonbonded distributions BB, BA and AA from CGMD also match the targets well. This indicates that the calculated CG potentials are able to reproduce the structural features of PET chain at CG level. To further test this, we also compared the distributions of hexamer and octamer from CGMD with the atomistic PCFs, and found equivalent agreement (not shown). As presented elsewhere in most CG level simulation work[6,13,18,27] , one of the most important points of validation of the CG process is the reproduction of conformations from atomistic sampling. Having done this, we can further investigate the other physical properties from the CG simulations.

In Figure 4.6, we show snapshots from the CGMD simulations. All of these snapshots are taken from the equilibrium ensemble. In Figure 4.6(a) all molecules are shown to make it clear that we are simulating a dense melt. In Figures 4.6(b) through 6(f), all but five chains are rendered invisible to better indicate the shape of the chains. These structures are available to view and download at an archived site. [50]

In Figure 4.7, we show the distribution of chain end-to-end distance for DP = 10, 20, 30, 40 and 50. The end-to-end distance is defined as the distance between the two end BB groups. The end-to-end curve of the decamer displays two peaks. The peak centered at 4.5 Å corresponds to a folded configuration, as shown in Figure 4.6(b). The folded structure in PET oligomers has been reported by the other simulation work of PET[5,51] . The broader peak extending from 7 to 50 Å, with a maximum at 28.3 Å corresponds to the unfolded conformation. The end-to-end distribution of the decamer from atomistic MD simulation is also presented in Figure 4.7 (solid black line). The comparison is excellent. As DP increases, the qualitative two-peak behavior of the decamer disappears and the distribution becomes more Gaussian-like[6] , as shown for DP =50. As expected, the position of the maximum in the peak increases with DP and the breadth of the curve increases with DP. The average end-to-end distance increases with DP, as can be seen in Table 4.1.

Figure 4.8 shows that the average chain end-to-end distance and radius of gyration as a function of DP in a log-log plot. Note here the results for tetramer, hexamer, octamer and decamer from atomistic MD simulations are also shown (open circle with back error bar). The lengths associated with the GCMD simulations are consistently slightly smaller than those of the atomistic MD simulations, because the beads are located at fragment center-of-masses. The polymer's structure and dynamic properties have the following chain length or molecular weight dependence.

$$X = a(DP)^b \tag{8}$$

where X is a property related to DP via the scaling exponent, b. The values of b for various properties as a function of chain length and degree of model resolution are listed in table 4.4. Both structural measures can be well fit by equation (8). The scaling exponents for the radius of gyration and the chain end-to-end distance are 0.594 and 0.571 respectively for DP up to 10 and 0.510 and 0.501 for DP from 20 to 40. Laso and Karayiannis [52,53] studied the scaling behaviors of oligomer systems, and found very similar values (0.58-0.60) for the scaling exponents are obtained in the whole range of volume fractions from dilute up to very dense samples suggesting universal character in the scaling behavior of oligomers. Indeed the value of 0.59 corresponds to specific folded (ring-like) and extended chain configurations that, because of their small size, markedly deviate from Gaussian coils. In a melt of sufficiently long PET chains, chains should behave as random walks and the exponent should be close to 0.5 as shown by Kamio *et al.*[6] Our scaling exponents of R_{ete} and R_g for longer chain systems (for DP greater than 20) are close to 0.5, which indicates that for DP greater than 20, the systems become entangled. Indeed, the critical entangled molecular weight (M_e) of PET (3500 g/mole)[54] is between the molecular weight of decamer (1901 g/mole) and DP = 20 (3802 g/mole). The molecular weight of the highest DP (DP = 50) system is (9505 g/mole) 2.7 times of M_e. Therefore, a transition from Rouse like behavior to reptation behavior is possible. We will refer this issue back during the discussion of entanglement analysis.

Figure 4.9 (a) and (b) shows the normalized chain end-to-end vector autocorrelation functions changing with observation time for the tetramer, hexamer, octamer and decamer systems. In Figure 4.9(a), the black lines represent data from atomistic MD simulation using the molecular model, while the red lines represent values scaled from CGMD simulations using our

CG model. The autocorrelation functions all decay to zero, which means the chains are fully relaxed. The atomistic simulations do not extend out as far as the CGMD simulations simply due to restrictions in computational resources. Thus the benefits of applying the CG procedure are evident. Note here the observation time was scaled.

We can extract useful information from the end-to-end vector autocorrelation function. By fitting this data to the exponential model or the KWW model[55] (a stretched exponential), one can extract chain relaxation times, τ_R^* and τ_{kww}^* respectively. These times correspond to the longest rotational relaxation time. The relaxation times and the stretching exponent, β_{KWW}^*, are reported in Table 4.1. As shown in Figure 4.9(b), the fits to KWW model are reasonably good for DP equals 20, 30, 40 and 50. The relaxation times from the Rouse and the KWW model deviate at short chain length but agree relatively well for long chain length. The relaxation times increase strongly with DP. Based on chains with DP of 20, 30, 40 and 50, the scaling exponent *b* for τ_{kww}^* is 3.7. The scaling exponent obtained for the DP = 1 to 10 from the atomistic simulations was 2.78. Since there is a statistically significant change in the exponent from short to long chains, it is possible that this is a consequence of moving from an unentangled to an entangled regime. As a point of reference, the Rouse model predicts a scaling exponent of 2 and reptation theory predicts a scaling exponent of 3.[56]

Another important issue investigated on the analysis of end-to-end vector autocorrelation functions is the scaling factor of relaxation times from atomistic MD and CGMD simulation of the tetramer, hexamer, octamer and decamer. We obtained two sets of relaxation times, τ_{kww} (from atomistic MD), which are listed in Table 4.2, and τ_{kww}^* (from CGMD), which are listed in Table 4.1. The average of the ratio of $\tau_{kww} / \tau_{kww}^*$ of tetramer, hexamer, octamer and decamer is 7.5. In other words, the polymers relax on average 7.5 times faster in the CGMD simulation than they do in the atomistic simulation. This is because fewer degrees of freedom are used in the CG model, which accordingly causes faster dynamics in the CGMD simulation than the full atomistic MD simulation.[13] This scaling factor is reported in the top row of Table 4.2. As a point of clarification, note that we now have scaling *exponents* relating the behavior of a property to degree of polymerization and scaling *factors*, providing proportionalities between properties of the CGMD simulations to those of the atomistic MD simulations.

We also report the kinetic, bonded potential (stretching, bending and torsion) and nonbonded potential (intramolecular and intermolecular) energies in Table 4.1 (raw data) and Table 4.2 (scaled data). These energies are reported in units of aJ/bead. The scaling factors reported in Table 4.2 were generated by calculating the average ratio of the property from CGMD and atomistic simulations. The use of a single constant for scaling the kinetic energy across all DP is excellent, as can be judged by comparison of the scaled energies from atomistic and CGMD simulation in Table 4.2. The scaling for the potential energies is reasonably good with an average error of 6.2% and 2.2% for the bonded and nonbonded terms respectively. These scaling factors for the energies allow one to compute thermodynamic properties, such as the internal energy, of the atomistic chain from the CGMD simulation.

4.3.2 Transport Properties

In this section, we report the self-diffusivity (*D)* and zero-shear rate viscosity (η) as a function of DP. The self-diffusivity is obtained from the mean-square displacements (MSD) through Einstein's equation given as

$$D = \frac{1}{6}\lim_{t\to\infty}\frac{1}{t}\left\langle \left[r_{cm}(t) - r_{cm}(0)\right]^2 \right\rangle \tag{9}$$

where r_{cm} is the center of mass position of the chain.

In Figure 4.10, we plot the mean square displacement versus observation time on a log-log plot. In order to satisfy the infinite time limit, the slopes of the curves must be unity. These slopes are reported in the legend of Figure 4.10 and are all very close to unity. This is evidence that the simulations have been run sufficiently long to achieve valid self-diffusivities. The numerical values of the self-diffusivities from CGMD simulation are reported in Table 4.1. We acknowledge that it is likely that the statistical accuracy of the estimate diminishes as the chain length increases due to the fact that we have not been able to simulate for as many relaxation times with the long chains as we did with the short chains. This is reflected in the uncertainties reported in Table 4.1 where the standard deviation is 19% for DP=10 and 40% for DP=50. Scaled values are plotted in Figure 4.11 as a function of DP. The self-diffusivity decreases with DP as expected. The scaling exponent for the self-diffusivity for DP = 20 to 50 is -2.00. The scaling exponent obtained for DP = 4 to 10 is -1.91, which can be compared to the DP = 1 to 10

from the atomistic simulations, which was -2.01.[5] Since this exponent changes very little from short to long chains, it is not a useful measure of degree of entanglement. As a point of reference, the theoretical prediction of the scaling exponent from reptation theory for entangled polymer melts is -2. We do not observe any behavior predicted by the Rouse model (for which b = -1.0) for any chain lengths. Indeed, it has been reported in the literature that the dynamic properties deviate from the Rouse model for short-chain unentangled polymer systems.[57] This is attributed to the presence of chain stiffness, nonbonded interactions, and chain uncrossability, which are not accounted for by the Rouse model.[57]

If we compare the numerical values of the diffusivities from atomistic simulations (Table 4.2) and CGMD simulations (Table 4.1) for chains with DP of 4, 6, 8 and 10, we find that the average ratio of diffusivities (CG over atomistic) is 0.186. (The diffusivities in Figure 4.11 are scaled by this number.) The inverse of this is 5.38. In other words, diffusion is occuring 5.38 times faster in the CGMD simulation than in the atomistic MD simulation. Recall that the polymer relaxed 7.5 times faster in the CGMD simulation based on an analogous comparison of τ_{kww}. One might have expected these numbers to be the same. At this point, we do not have a complete explanation for the discrepancy. The use of a time scaling constant has only an empirical basis. The different dynamic properties (relaxation time, diffusivity, viscosity) represent mechanisms of entropy generation. Because the entropy of the atomistic and coarse-grained models are different, it may well turn out that the use of a single time-scaling constant gives only a first order approximation of the diverse effects of a more complicated issue. However, in Table 4.2, when we provide the scaled properties from the CGMD simulations to compare with the atomistic MD simulations, we provide all of the scaling factors in the top row of the table.

The zero-shear-rate viscosity is based on time integration of the momentum auto-correlation function

$$\eta_{xy} = \frac{1}{Vk_BT}\int_0^\infty < \sigma_{xy}(t)\sigma_{xy}(0) > dt \tag{10}$$

where σ_{xy} is the xy component of the stress tensor defined to have a potential and kinetic contribution,

$$\sigma_{xy} = \frac{1}{2}\sum_{i=1}^{N}\sum_{j\neq i}^{N} F_{ijx} r_{ijy} + m_i \sum_{i=1}^{N} u_{ix} u_{iy} \tag{11}$$

where r_{ijx} and F_{ijx} are respectively the separation and force between particles i and j in the x dimension, m_i is the mass of particle i.

Following a previously tested procedure,[5,58] we obtained numerical values of the zero-shear-rate viscosities from the CGMD simulations, which are given in Table 4.1. Scaled values are plotted in Figure 4.12 as a function of DP. The scaling exponent for the zero shear rate viscosity for DP = 20 to 50 is 2.0. The scaling exponent obtained for DP = 4 to 10 is 1.6, which can be compared to the DP = 1 to 10 from the atomistic simulations, which was 0.96.[5] The values deviate from the theoretical prediction (b = 1 for the Rouse model and b = 3.0 for the reptation model). The deviation from Rouse model is expected[57,59] due to the reasons mentioned above. The exponent for short chains b = 1.6 is close to the finding of other simulation work (b = 1.8[60] and b = 1.5[57]). For entangled long chain systems, the exponents b = 3.6[60] and b = 3.2[57] have been observed.

To map zero-shear-rate viscosity from CGMD simulation back to the molecular level, we again calculate an average scaling factor between the viscosities of the CGMD and atomistic MD simulations for DP = 4, 6, 8 and 10. The average ratio is 6.62. If we invoke the Stokes-Einstein (SE) relation,[61,62] which according to hydrodynamic theory applies well to the diffusion of large spherical molecules in solvent of low molecular weight (admittedly not the system here), then

$$\frac{D\eta}{k_B T} = \frac{1}{4\pi R_{SE}} \tag{12}$$

where R_{SE} is the particle size. R_{SE} can also be represented by the chain radius of gyration (R_g). Thus, according to the Stokes-Einstein relation, the scaling factor for viscosity is simply the inverse of the scaling factor the diffusivity (since we have assumed a scaling of 1 for the radius of gyration), which is 5.38. The values of the viscosity in Table 4.2 and Figure 4.12 have been scaled by 5.38. There is relatively good agreement between the viscosities from the CGMD and atomistic MD simulations. There is scatter in the data, (as is typical for zero shear rate viscosities obtained in this way), but no systematic discrepancy.

We would like to better understand the degree of entanglement in these systems. As we mentioned above, the actual molecular weight of DP = 20 systems has exceeded the

entanglement molecular weight of PET. The scaling exponents for the end-to-end distance, radius of gyration and the slowest relaxation time showed a statistically significant decrease when moving from short chains (DP ≤ 10) to longer chains (DP ≥ 20). However, the scaling exponent for the self-diffusivity did not show any statistically significant change between short and long chains.

4.3.3 Entanglement Analysis

A clearer understanding of entanglement can emerge from a more geometric approach in which one extracts entanglement information directly from configurations of the chains. To this end, we analyzed snapshots of DP = 10, 20, 30, 40 and 50 systems using the Z-code[45] . The Z-code and CReTA package[63] are two common algorithms to study the entanglements in polymeric systems. Kamio *et al.*[6] studied the entanglements of long chain PET using the above two algorithms. The calculated quantities like primitive path length and entanglement spacing are in good agreement. In this work, we implement only the Z-code to study the entanglements in longer chain systems. The details of the Z-code and its application can be found elsewhere.[45,64,65] The calculated mean contour length of primitive path ($<L_{pp}>$), tube diameter (d), number of monomers between entanglement points (N_e) and number of entanglements (Z) for PET with DP from 10 to 50 are listed in Table 4.5. These values were generated by averaging over 1000 snapshots distributed through-out the simulation, each containing 125 chains. The value of tube diameter is in good agreements with rheological data reported in the literature[66-68] for DP from 20 to 50. The average value is 35.42 (Å), which can be compared with the reported value of 35 (Å).[68] The difference is within 1.2%. The tube diameter for the DP = 10 system deviates from that of the other simulations and from reports in the literature, which may results from it being unentangled. The values of $<L_{pp}>$ for entangled systems are lower than that reported by Kamio *et al.*[6] . This is probably because a longer chain length used in their work. It has been shown that the value of $<L_{pp}>$ increases with chain length.[64] To further compare our results with the literature, we also reported the values of interentanglement strand length (N_{ES}) in Table 4.4. N_{ES} is defined as[6]

$$N_{ES} = \frac{N(N-1)}{Z(N-1)+N} \tag{13}$$

where N is the number of beads in a chain. The average value for DP from 20 to 50 is 13.59 ± 1.63 , which is in agreements with that reported in the literature,[6] in which the value from CReTA is 13.87 and from Z is 14.9. The slight dependence of N_{ES} on DP may be due to differences in the densities. The agreement of the tube diameter and N_{ES} comparisons also indicates that good equilibration of the melt topological structure has been achieved, which is further verified by the fact that no significant difference is observed on these the statistical properties from the analysis of multiple configurations taken at different times.

4.4 CONCLUSIONS

A coarse-grained (CG) model of Polyethylene Terephthalate (PET) was developed and implemented in CG Molecular Dynamics (MD) simulations of PET chains with degree of polymerization up to 50. The CG potential is parameterized to structural distribution functions obtained from atomistic simulations[5] using an inversion procedure based on the Ornstein-Zernike equation with the Percus Yevick approximation (OZPY).[29] The CGMD simulation of PET chains satisfactorily reproduces the structural and dynamic properties from atomistic MD simulation of the same systems. From the CGMD simulations, we obtained structural and transport properties for PET with degrees of polymerization from 4 to 50 at the industrially relevant state point (T = 563 K, p = 0.13 kPa).

Scaling exponents are reported for five properties as a function of DP: the end-to-end distance, the radius of gyration, longest rotational relaxation time, the self-diffusivity and the zero shear rate viscosity. We calculated scaling exponents for both short chains (DP ≤ 10) and longer chains (DP ≥ 20). We observed that the scaling exponents for the end-to-end distance, the radius of gyration, longest rotational relaxation time and the zero shear rate viscosity show a statistically significant different between short and long chains. However, the scaling exponent for the self-diffusivity did not show any statistically significant change between short and long chains. The exponents for long chains for the end-to-end distance, the radius of gyration and the self-diffusivity are in good agreement with predictions from reptation theory. The exponents for the viscosity fall between the Rouse model and reptation theory for both short and long chains. The exponents for the longest rotational relaxation time exceed the Rouse model and reptation theory for both short and long chains respectively.

In an effort to understand how dynamic properties from CGMD simulations can be scaled, we compared CGMD and atomistic MD simulations of PET for DP up to 10. Comparison of structural properties, such as end-to-end distance or radius of gyration, show that no length scaling is necessary. Using the longest rotational relaxation time as a standard, we find that the time scaling factor in the CGMD simulations is 7.5. However, using the self-diffusivity as the standard, the time scaling factor is 5.38. The viscosity yields a scaling factor of 6.22.

The entanglement analysis, using the Z-code,[45] shows that for DP = 20 to 50, tube diameter (d), number of monomers between entanglement points (N_e) and interentanglement strand length (N_{ES}) are very close to the reported values for entangled PET melts. For DP=50, there are on average 6 entanglements per chain. Thus we have at least a partially entangled system for the longer chains, explaining some of the intermediate scaling exponents observed in the simulations.

4.5 ACKNOWLEDGMENTS

This research was supported by the Eastman Chemical Company and by a grant from the National Science Foundation (DGE-0801470) and by the U.S. Department of Energy, Office of Basic Energy Sciences, Division of Materials Sciences and Engineering. This research project used resources of the National Institute for Computational Sciences (NICS) supported by NSF under agreement number: OCI 07-11134.5.

References

[1]K. Kremer, Macromol. Chem. Phys. **204**, 257 (2003).

[2]M. S. Hedenqvist, R. Bharadwaj, and R. H. Boyd, Macromolecules **31**, 1556 (1998).

[3]R. K. Bharadwaj and R. H. Boyd, Polymer **40**, 4229 (1999).

[4]S. U. Boyd and R. H. Boyd, Macromolecules **34**, 7219 (2001).

[5]Q. F. Wang, D. J. Keffer, S. Petrovan, and J. B. Thomas, J. Phys. Chem. B **114**, 786 (2010).

[6]K. Kamio, K. Moorthi, and D. N. Theodorou, Macromolecules **40**, 710 (2007).

[7]N. C. Karayiannis, V. G. Mavrantzas, and D. N. Theodorou, Macromolecules **37**, 2978 (2004).

[8]D. Pavel and R. Shanks, Polymer **44**, 6713 (2003).

[9]J. I. Cail, R. F. T. Stepto, D. J. R. Taylor, R. A. Jones, and I. M. Ward, Phys. Chem. Chem. Phys. **2**, 4361 (2000).

[10]L. S. Saunders, I. M. Ward, J. I. Cail, and R. F. T. Stepto, Polymer **45**, 2357 (2004).

[11]A. E. Tonelli, J. Polym. Sci., Part B: Polym. Phys. **40**, 1254 (2002).

[12]H. Eslami and F. Muller-Plathe, Macromolecules **42**, 8241 (2009).

[13]V. A. Harmandaris, D. Reith, N. F. A. Van der Vegt, and K. Kremer, Macromol. Chem. Phys. **208**, 2109 (2007).

[14]C. X. Chen, P. Depa, J. K. Maranas, and V. G. Sakai, J. Chem. Phys. **128**, 124906 (2008).

[15]I. Y. Lyubimov, J. McCarty, A. Clark, and M. G. Guenza, J. Chem. Phys. **132**, 5 (2010).

[16]A. Villa, C. Peter, and N. F. A. van der Vegt, Phys. Chem. Chem. Phys. **11**, 2077 (2009).

[17]K. Voltz, J. Trylska, V. Tozzini, V. Kurkal-Siebert, J. Langowski, and J. Smith, J. Comput. Chem. **29**, 1429 (2008).

[18]V. A. Harmandaris, N. P. Adhikari, N. F. A. van der Vegt, and K. Kremer, Macromolecules **39**, 6708 (2006).

[19]V. A. Harmandaris and K. Kremer, Macromolecules **42**, 791 (2009).

[20]L. J. Chen, H. J. Qian, Z. Y. Lu, Z. S. Li, and C. C. Sun, J. Phys. Chem. B **110**, 24093 (2006).

[21]C. X. Chen, P. Depa, V. G. Sakai, J. K. Maranas, J. W. Lynn, I. Peral, and J. R. D. Copley, J. Chem. Phys. **124**, 234901 (2006).

[22]H. Lee, A. H. de Vries, S. J. Marrink, and R. W. Pastor, J. Phys. Chem. B **113**, 13186 (2009).

[23]Q. Sun and R. Faller, J. Chem. Theory Comput. **2**, 607 (2006).

[24]Q. Sun and R. Faller, J. Chem. Phys. **126**, 144908 (2007).

[25]B. Hess, S. Leon, N. van der Vegt, and K. Kremer, Soft Matter **2**, 409 (2006).

[26]C. Peter, L. Delle Site, and K. Kremer, Soft Matter **4**, 859 (2008).

[27]D. Reith, M. Putz, and F. Muller-Plathe, J. Comput. Chem. **24**, 1624 (2003).

[28]M. G. Guenza, J. Phys.: Condens. Matter **20**, 033101 (2008).

[29]Q. Wang, D. J. Keffer, D. M. Nicholson, and J. B. Thomas, Phys. Rev. E **81**, 061204 (2010).

[30]D. Fritz, V. A. Harmandaris, K. Kremer, and N. F. A. van der Vegt, Macromolecules **42**, 7579 (2009).

[31]J. G. Curro and K. S. Schweizer, Macromolecules **20**, 1928 (1987).

[32]K. S. Schweizer and J. G. Curro, Adv. Chem. Phys. **98**, 1 (1997).

[33]K. S. Schweizer, E. F. David, C. Singh, J. G. Curro, and J. J. Rajasekaran, Macromolecules **28**, 1528 (1995).

[34]J. McCarty, I. Y. Lyubimov, and M. G. Guenza, J. Phys. Chem. B **113**, 11876 (2009).

[35]A. J. Clark and M. G. Guenza, J. Chem. Phys. **132**, 044902 (2010).

[36]G. Yatsenko, E. J. Sambriski, M. A. Nemirovskaya, and M. Guenza, Phys. Rev. Lett. **93**, 257803 (2004).

[37]L. Zhao, Y. G. Li, J. G. Mi, and C. L. Zhong, J. Chem. Phys. **123**, 124905 (2005).

[38]H. T. Davis, *Statistical mechanics of phases, interfaces, and thin films* (VCH, New York, 1996).

[39]L. L. Lee, *Molecular thermodynamics of nonideal fluids* (Butterworths, Boston, 1988).

[40]A. D. Law and D. M. A. Buzza, J. Chem. Phys. **131**, 094704 (2009).

[41]J. R. Silbermann, S. H. L. Klapp, M. Schoen, N. Chennamsetty, H. Bock, and K. E. Gubbins, J. Chem. Phys. **124**, 074105 (2006).

[42]S. H. Behrens and D. G. Grier, Phys. Rev. E **6405**, 050401 (2001).

[43]M. Brunner, C. Bechinger, W. Strepp, V. Lobaskin, and H. H. von Grunberg, Europhys. Lett. **58**, 926 (2002).

[44]R. Rajagopalan and K. S. Rao, Phys. Rev. E **55**, 4423 (1997).

[45]M. Kroger, Comput. Phys. Commun. **168**, 209 (2005).

[46]D. J. Keffer, C. Baig, P. Adhangale, and B. J. Edwards, Mol. Simul. **32**, 345 (2006).

[47]M. Tuckerman, B. J. Berne, and G. J. Martyna, J. Chem. Phys. **99**, 2278 (1993).

[48]D. Feldman and A. Barbalata, *Synthetic polymers : technology, properties, applications* (Chapman & Hall, London, 1996).

[49]D. Henderson and S. Sokolowski, J. Chem. Phys. **104**, 2971 (1996).

[50]D. J. Keffer, *Molecular Simulation Structures from the Computational Materials Research Group at the University of Tennessee Knoxville, TN* (2010).

[51]S. M. West, A. J. Smallridge, A. Uhlherr, and S. Volker, Macromol. Chem. Phys. **201**, 2532 (2000).

[52]M. Laso and N. C. Karayiannis, J. Chem. Phys. **128** (2008).

[53]N. C. Karayiannis and M. Laso, Macromolecules **41**, 1537 (2008).

[54]S. M. Aharoni, Makromolekulare Chemie-Macromolecular Chemistry and Physics **179**, 1867 (1978).

[55]G. Tsolou, V. G. Mavrantzas, and D. N. Theodorou, Macromolecules **38**, 1478 (2005).

[56]C. Tzoumanekas, F. Lahmar, B. Rousseau, and D. N. Theodorou, Macromolecules **42**, 7474 (2009).

[57]F. Lahmar, C. Tzoumanekas, D. N. Theodorou, and B. Rousseau, Macromolecules **42**, 7485 (2009).

[58]D. J. Keffer, B. J. Edwards, and P. Adhangale, J. Non-Newtonian Fluid Mech. **120**, 41 (2004).

[59]J. T. Padding and W. J. Briels, J. Chem. Phys. **117**, 925 (2002).

[60]D. S. Pearson, G. V. Strate, E. Vonmeerwall, and F. C. Schilling, Macromolecules **20**, 1133 (1987).

[61]K. Saalwachter and W. Burchard, Macromolecules **34**, 5587 (2001).

[62]S. K. Das, J. Horbach, K. Binder, M. E. Fisher, and J. V. Sengers, J. Chem. Phys. **125**, 12 (2006).

[63]C. Tzoumanekas and D. N. Theodorou, Macromolecules **39**, 4592 (2006).

[64]J. M. Kim, D. J. Keffer, M. Kroger, and B. J. Edwards, J. Non-Newtonian Fluid Mech. **152**, 168 (2008).

[65]S. Shanbhag and M. Kroger, Macromolecules **40**, 2897 (2007).

[66]L. J. Fetters, D. J. Lohse, D. Richter, T. A. Witten, and A. Zirkel, Macromolecules **27**, 4639 (1994).

[67]G. Lorentz and J. F. Tassin, Polymer **35**, 3200 (1994).

[68]L. J. Fetters, D. J. Lohse, and R. H. Colby, In *Physical Properties of Polymers Handbook* (James E. Mark, Ed.; Springer, New York, 2007).

Appendix C

Tables and Figures

Table 4.1. Unscaled structural, thermodynamic and transport properties of PET with different DP from CGMD simulations (for DP = 4, 6, 8, 10, 20, 30, 40 and 50) at p = 0.13 kPa, T = 563 K.

DP	4	6	8	10	20	30	40	50
N	125	125	125	125	125	125	125	125
ρ^* (g/cm^3)	1.22 ± 0.03	1.29 ± 0.01	1.29 ± 0.01	1.29 ± 0.01	1.18 ± 0.02	1.20 ± 0.01	1.25 ± 0.02	1.24 ± 0.01
D^* (10^{-10} m^2/sec)	2.71 ± 0.2	0.76 ± 0.15	0.47 ± 0.13	0.32 ± 0.06	0.16 ± 0.03	0.08 ± 0.02	0.045 ± 0.022	0.025 ± 0.01
η^* (10^{-2} Pa.s)	0.1 ± 0.01	0.26 ± 0.09	0.41 ± 0.09	0.43 ± 0.04	0.44± 0.03	0.65 ± 0.13	1.50 ± 0.17	2.31 ± 0.40
$\langle R_{ete} \rangle^*$ (Å)	17.5 ± 6.2	22.1± 7.8	24.7± 9.1	28.3 ± 10.2	44.2 ± 15.9	56.6 ± 21.0	63.0 ± 23.0	69.8 ± 22.7
$\langle R_g \rangle^*$ (Å)	8.1 ± 1.7	9.5 ± 5.4	10.5 ± 6.3	12.2 ± 6.4	19.6 ± 7.0	24.7 ± 9.1	28.0 ± 7.7	30.9 ±10.6
τ_R^* (ns)	0.96	3.04	4.69	10.33	51.28	128.20	476.25	909.10
τ_{KWW}^* (ns)	0.56	2.34	3.99	7.88	34.39	95.05	491.21	1006.81
β_{KWW}^*	0.92	0.84	0.86	0.81	0.75	0.70	0.61	0.58
kinetic energy* ($aJ/bead)*10^{-2}$	1.16 ± 0.04	1.16 ± 0.02	1.17 ± 0.02	1.17 ± 0.02	1.17 ± 0.02	1.17 ± 0.02	1.17 ± 0.03	1.16 ± 0.06
bonded energy* ($aJ/bead)*10^{-2}$	0.92 ± 0.03	1.06 ± 0.02	1.11 ± 0.02	1.14 ± 0.02	1.19 ± 0.01	1.21 ± 0.02	1.22 ± 0.01	1.22 ± 0.04
nonbonded energy* ($aJ/bead)*10^{-3}$	-1.24 ± 0.03	-1.23 ± 0.06	-1.18 ± 0.09	-1.18 ± 0.04	-1.25 ± 0.04	-1.21 ± 0.03	-1.20 ± 0.03	-1.21 ± 0.03

Table 4.2. Comparison of structural, thermodynamic and transport properties of PET from atomistic MD simulation DP = 4, 6, 8 and 10 and CGMD simulations for all DP at p = 0.13 kPa, T = 563 K. Properties from CGMD simulation have been scaled with scaling factors listed for each property in the second row.

DP	Simulation method	ρ (g/cm^3)	D (10^{-10} m^2/sec)	η (10^{-2} Pa.s)	$\langle R_{ete} \rangle$ (Å)	$\langle R_g \rangle$ (Å)	τ_{KWW} (ns)	*kinetic energy (aJ/bead) *10^{-2}*	*bonded energy (aJ/bead) *10^{-2}*	*nonbonded energy (aJ/bead) *10^{-2}*
		1.0	***0.186***	***5.38***	***1.0***	***1.0***	***7.5***	***1.0***	***1.09***	***16.35***
4	Atomistic MD	1.29 ± 0.01	0.40 ± 0.09	0.65 ± 0.07	21.1 ± 7.5	8.9 ± 5.2	5.6	1.17 ± 0.01	1.14 ± 0.01	-2.12 ± 0.01
	CGMD-scaled	1.22 ± 0.03	0.50 ± 0.02	0.54 ± 0.06	17.5 ± 6.2	8.1 ± 1.7	5.5	1.17 ± 0.04	1.00 ± 0.04	-2.05 ± 0.04
6	Atomistic MD	1.29 ± 0.01	0.17 ± 0.02	1.95± 0.65	26.8 ± 10.2	11.2 ± 4.4	15.8	1.16 ± 0.01	1.15 ± 0.01	-2.00 ± 0.01
	CGMD-scaled	1.29 ± 0.01	0.14 ± 0.01	1.40 ± 0.48	22.1±7.8	9.48 ± 5.4	17.4	1.16 ± 0.03	1.15 ± 0.03	-2.05 ± 0.11
8	Atomistic MD	1.29 ± 0.01	0.10 ± 0.03	2.23± 0.60	28.6 ± 11.2	12.5 ± 5.3	25.3	1.17 ± 0.07	1.15 ± 0.07	-1.94 ± 0.02
	CGMD-scaled	1.29 ± 0.01	0.09 ± 0.01	2.21 ± 0.48	24.7± 9.1	10.49 ± 6.3	26.8	1.17 ± 0.02	1.21 ± 0.02	-1.91 ± 0.12
10	Atomistic MD	1.29 ± 0.01	0.07 ± 0.01	3.03± 0.80	34.2 ± 9.4	13.2 ± 3.8	38.6	1.17 ± 0.06	1.15 ± 0.06	-1.90 ± 0.01
	CGMD-scaled	1.29 ± 0.01	0.06 ± 0.01	2.31± 0.16	28.3 ± 10.2	12.18 ± 6.4	59.1	1.16 ± 0.02	1.24 ± 0.02	-1.93 ± 0.08
20	CGMD-scaled	1.18 ± 0.02	0.030 ± 0.006	2.37± 0.16	44.2 ± 15.9	19.6 ± 7.0	257.9	1.17 ± 0.02	1.30 ± 0.01	-2.04 ± 0.07
30	CGMD-scaled	1.20 ± 0.01	0.015 ± 0.004	3.50 ± 0.70	56.6 ± 21.0	24.7 ± 9.1	712.9	1.17 ± 0.02	1.32± 0.02	-1.98 ± 0.05
40	CGMD-scaled	1.25± 0.02	0.008 ± 0.004	8.07 ± 0.91	63.0 ± 23.0	28.0 ± 7.7	3684.0	1.17 ± 0.03	1.33 ± 0.01	-1.96 ± 0.05
50	CGMD-scaled	1.24 ± 0.01	0.005 ± 0.002	13.37 ± 2.2	69.8 ± 22.7	30.9 ±10.6	7551.0	1.16 ± 0.06	1.33 ± 0.04	-1.98 ± 0.05

Table 4.3. Comparison of structural, thermodynamic and transport properties of PET from atomistic MD simulation DP = 4, 6, 8 and 10 and CGMD simulations for all DP at p = 0.13 kPa, T = 563 K. Properties from CGMD simulation have been scaled with scaling factors listed for each property in the second row.

species	$(T_x)^{ET}$	$(T_x)^{MB}$	$(T_x)^{Diff}$	$(T_y)^{ET}$	$(T_y)^{MB}$	$(T_y)^{Diff}$	$(T_z)^{ET}$	$(T_z)^{MB}$	$(T_z)^{Diff}$	$(T_{avg})^{ET}$	$(T_{avg})^{MB}$	$(T_{avg})^{Diff}$	$(T_{avg})^{total}$
A	563	563	0.00%	566	564	0.35%	566	571	0.88%	565	566	0.18%	563.603
B	562	564	0.36%	562	563	0.18%	563	563	0.00%	562	563	0.18%	

Table 4.4. Scaling exponents for various properties as a function of chain length and degree of model resolution.

DP	Simulation method	D	η	τ_{KWW}	$\langle R_{ete} \rangle$	$\langle R_g \rangle$
1~10	Atomistic MD	-2.01	0.96	2.78	0.594	0.571
4~10	Atomistic MD	-1.91	1.6	2.81	0.59	0.57
20~50	CGMD	-2.0	2.0	3.7	0.51	0.50
Rouse model	N/A	-1	1	2	0.59	0.59
Reptation model	N/A	-2	3	3	0.50	0.50

Table 4.5. Calculated properties from Z algorithm for DP = 10, 20, 30, 40 and 50 systems at p = 0.13 kPa, T = 563 K.

DP	$\langle L_{pp} \rangle$ (Å)	d (Å)	N_e	Z	N_{ES}
10	31.99	19.07	8.82	1.87	7.19
20	62.08	33.08	14.60	2.44	11.16
30	92.17	35.38	18.67	3.51	13.48
40	110.22	38.49	22.16	4.34	15.13
50	133.23	34.74	22.60	6.02	14.37
rheology models	N/A	35[68], 38-43[66]	30.2[68], 24.2[66], 25.0[67]	N/A	N/A

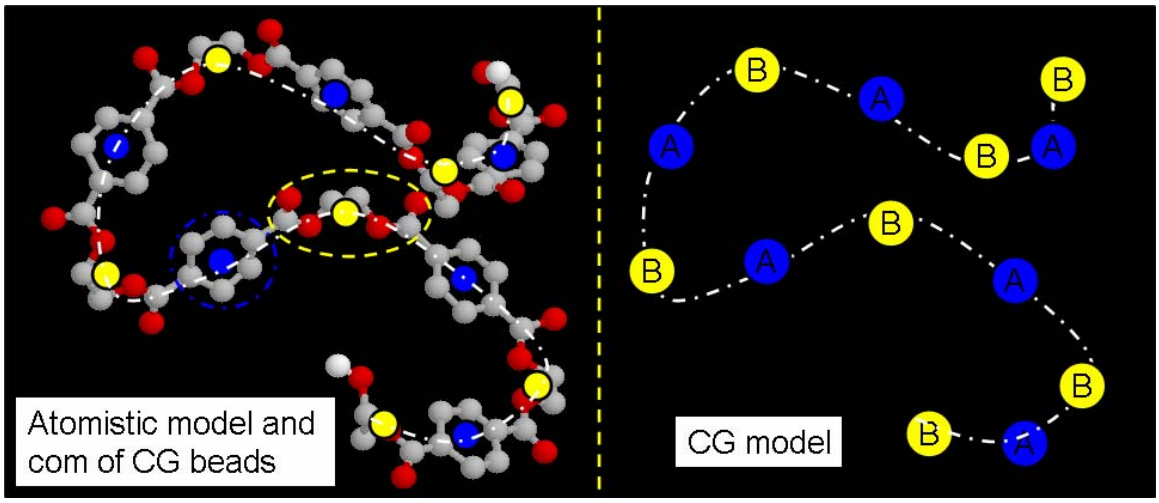

Figure 4.1. Molecular and CG Models of the PET hexamer molecule. Molecular model and center of mass (com) position of CG beads are shown the left. CG model is shown on the right.

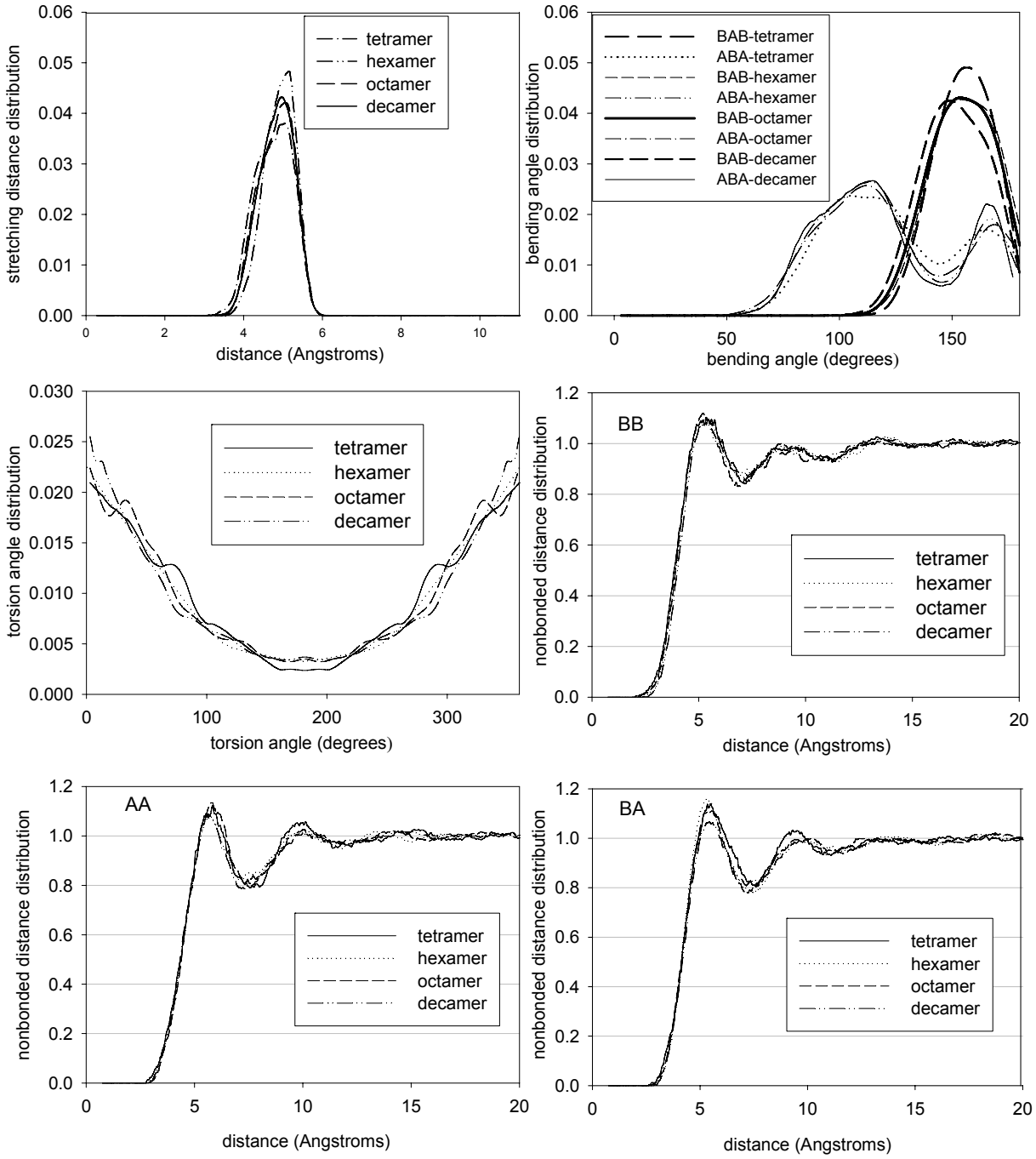

Figure 4.2. Bonded (stretching, bending and torsion) CG probability distribution functions (PDFs) and nonbonded CG pair correlation functions (PCFs) of tetramer, hexamer, octamer and decamer. PCFs are based on the center of mass position of the CG beads, obtained by analyzing the atomistic MD simulations of these oligomers.

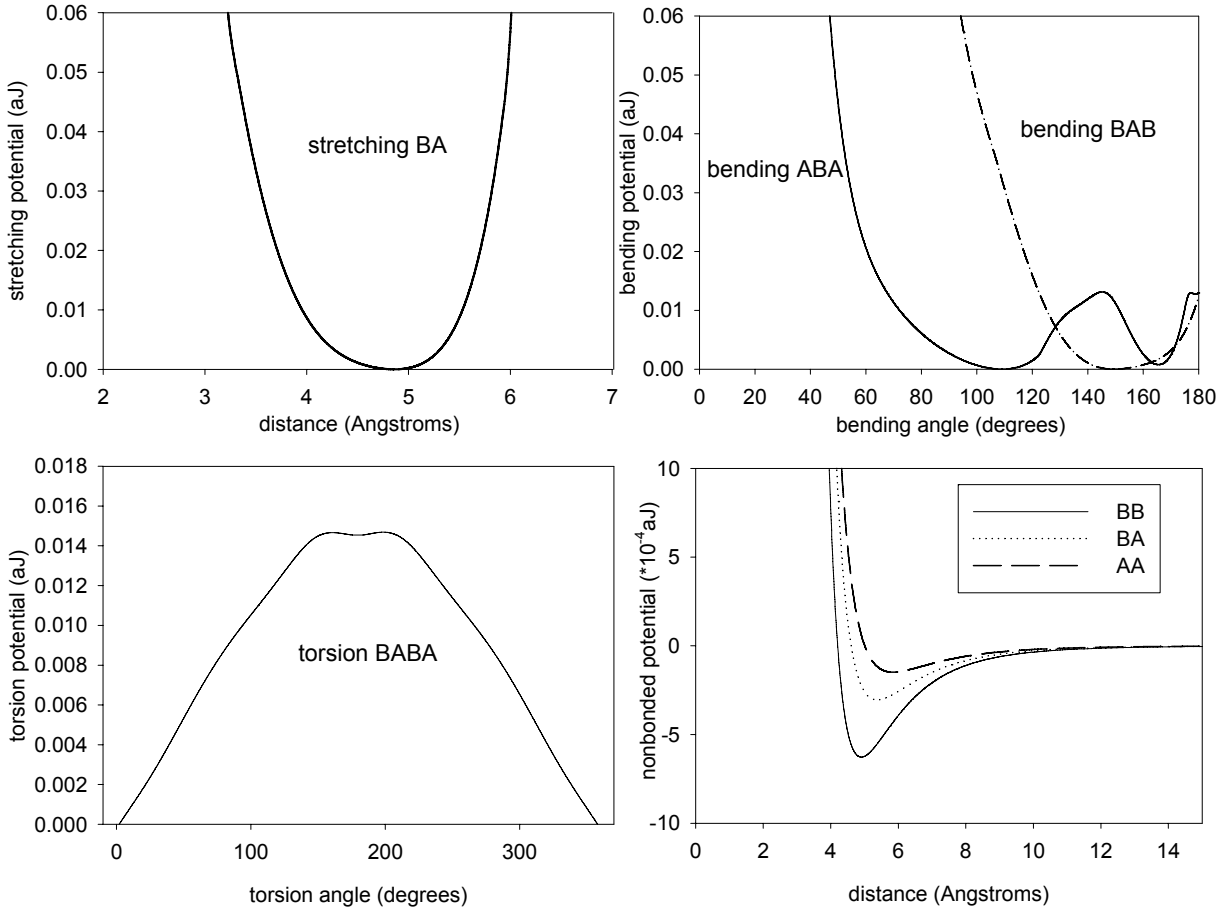

Figure 4.3. Bonded (stretching, bending and torsion) and nonbonded CG potentials.

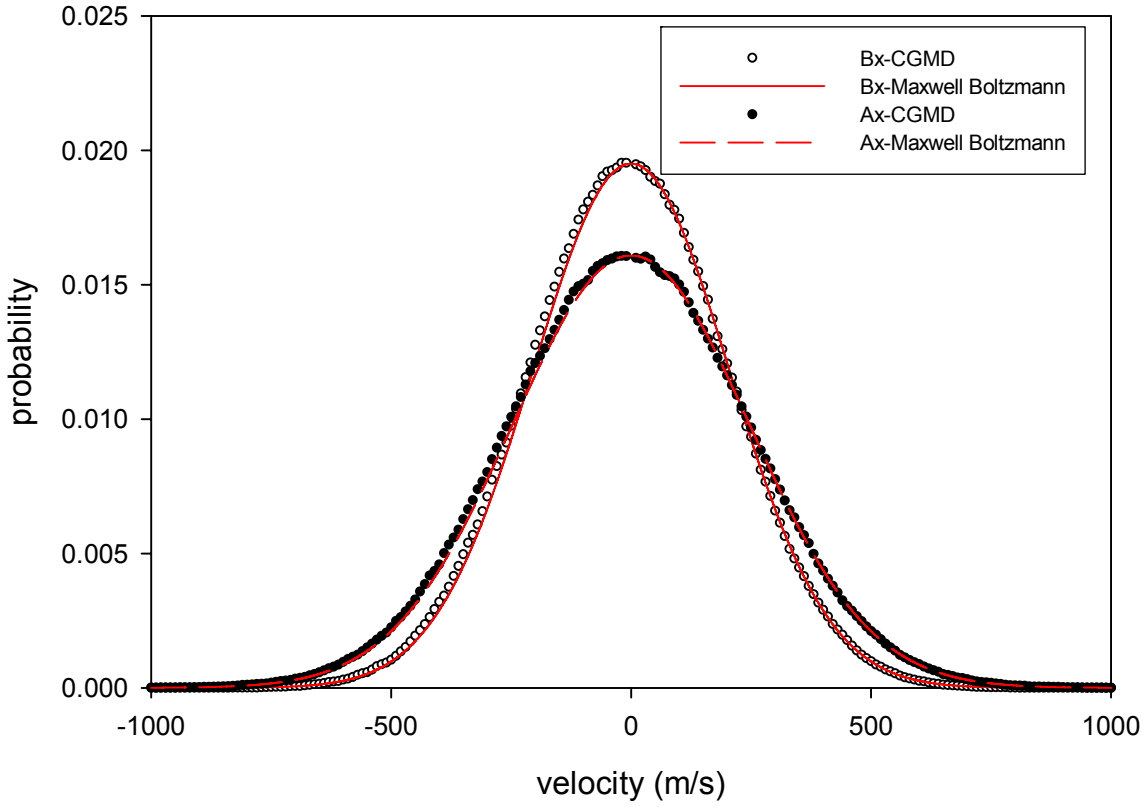

Figure 4.4. Comparison of x-direction velocity distribution of CG beads from CGMD simulation (data points) and the fitting of velocity distribution data to the Maxwell-Boltzmann distribution (line). The temperature can be extracted and compared with that of CGMD. Temperatures for all directions are shown in Table 4.1.

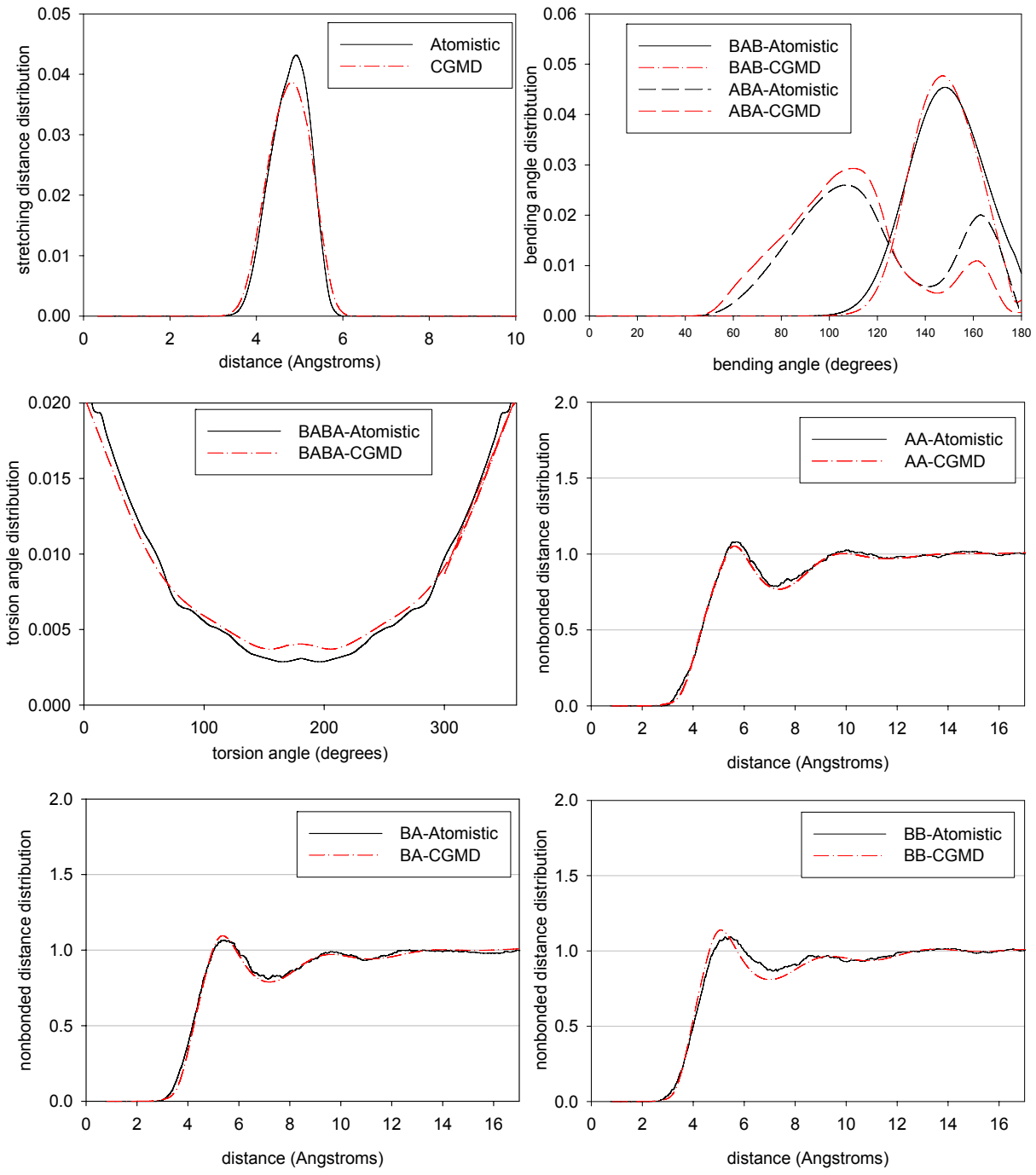

Figure 4.5. Comparisons of bonded (stretching, bending and torsion) CG probability distribution functions (PDFs) and nonbonded CG pair correlation functions (PCFs) of decamer from atomistic MD simulation (target) and CGMD simulation.

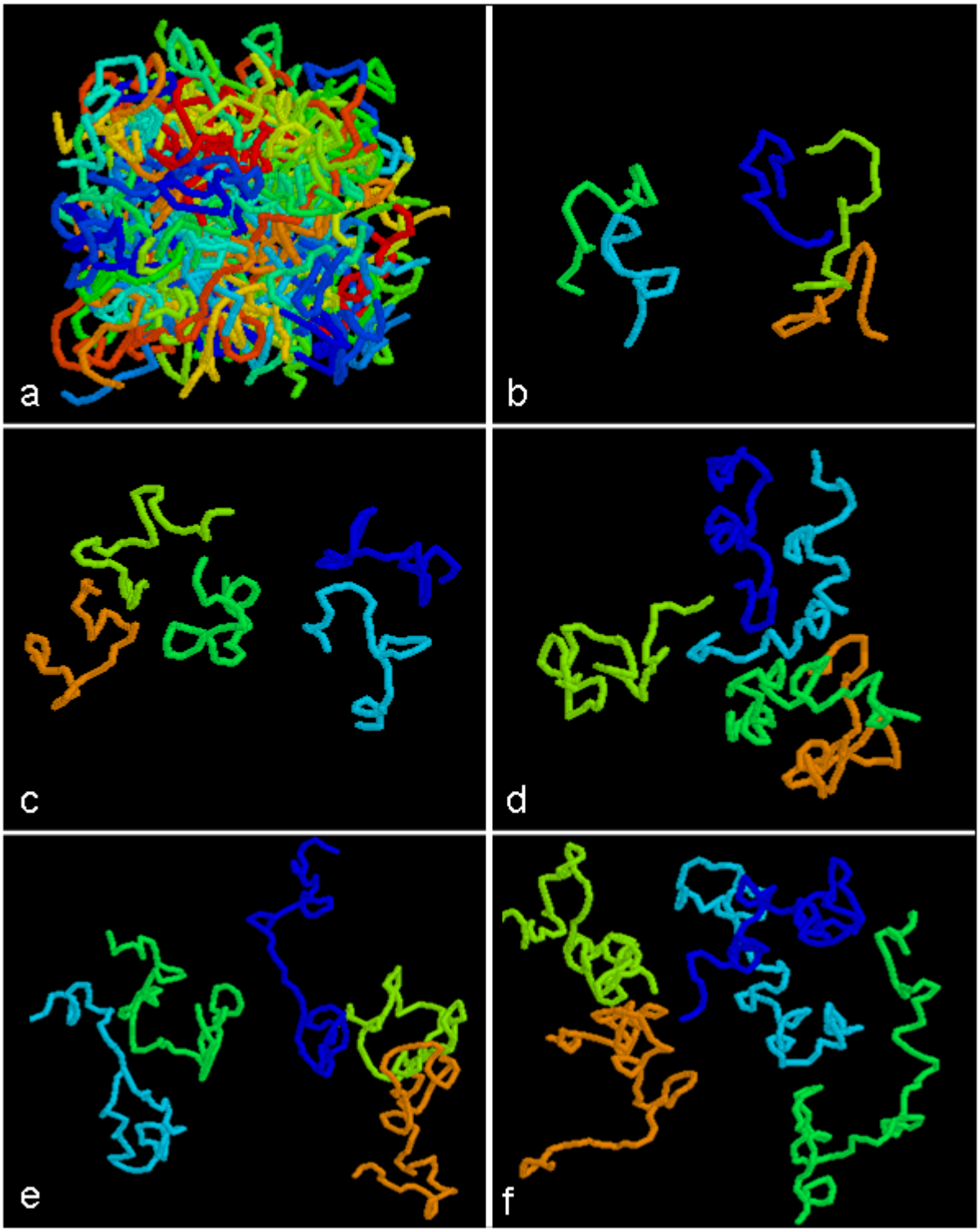

Figure 4.6. Snapshots of equilibrium configurations from CGMD simulations at T = 563 K, p = 0.13 kPa. (a) DP = 10, all molecules shown; (b)-(f) PET with different chain length (DP), selected molecules; (b) DP = 10; (c) DP = 20; (d) DP = 30; (e) DP = 40; (f) DP = 50.

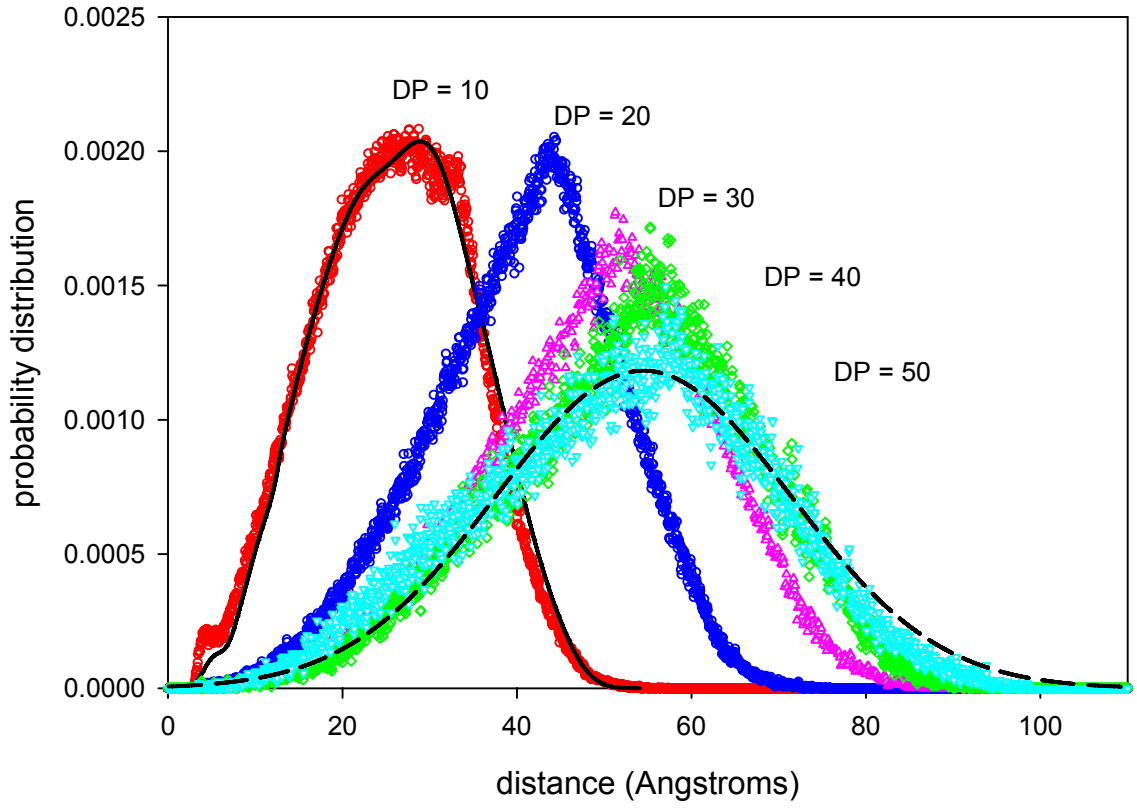

Figure 4.7. Comparisons of the chain end-to-end distance probability distributions for DP = 10, 20, 30, 40 and 50 from CGMD. For DP = 10, the solid line represents the distribution from atomistic MD simulation; For DP = 50, the dash line represents the distribution predicted by Gaussian function.

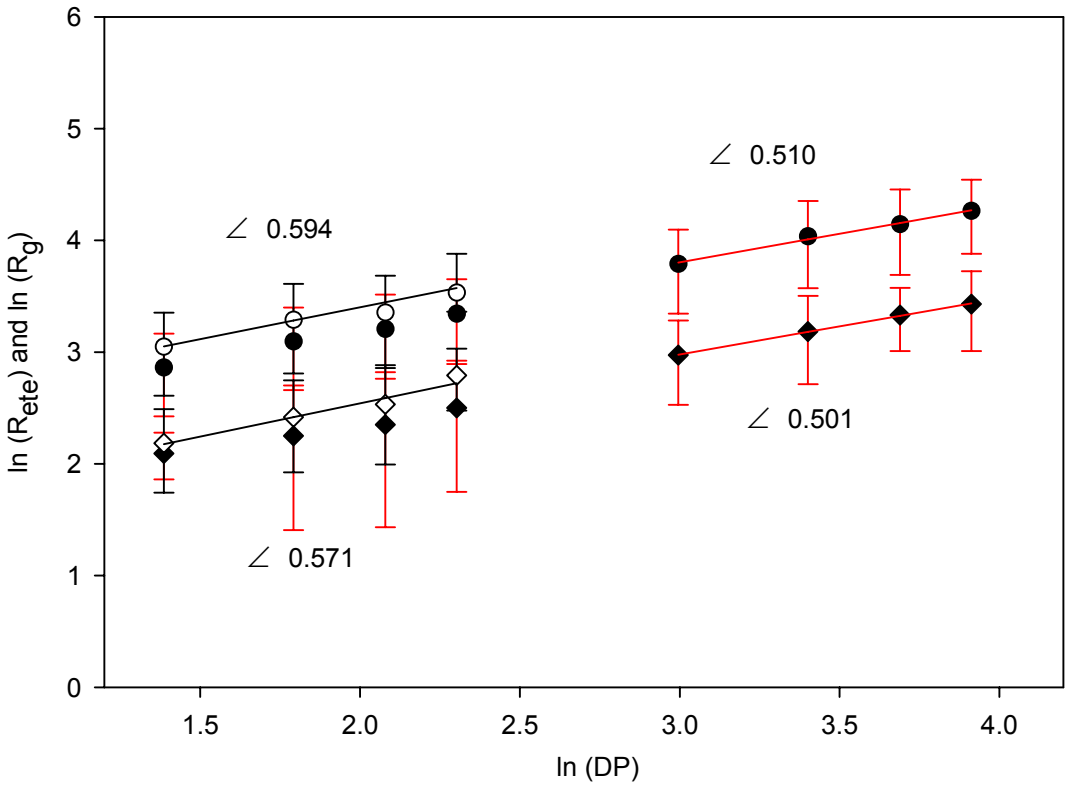

Figure 4.8. The average chain end-to-end distance (R_{ete}, circles) and radius of gyration (R_g, diamonds) as a function of DP from atomistic MD (open symbols) and CGMD (solid symbols). The error bars are one standard deviation. Linear regressions of the MD data (short chains) and CGMD data (long chains) are shown with the slope reported.

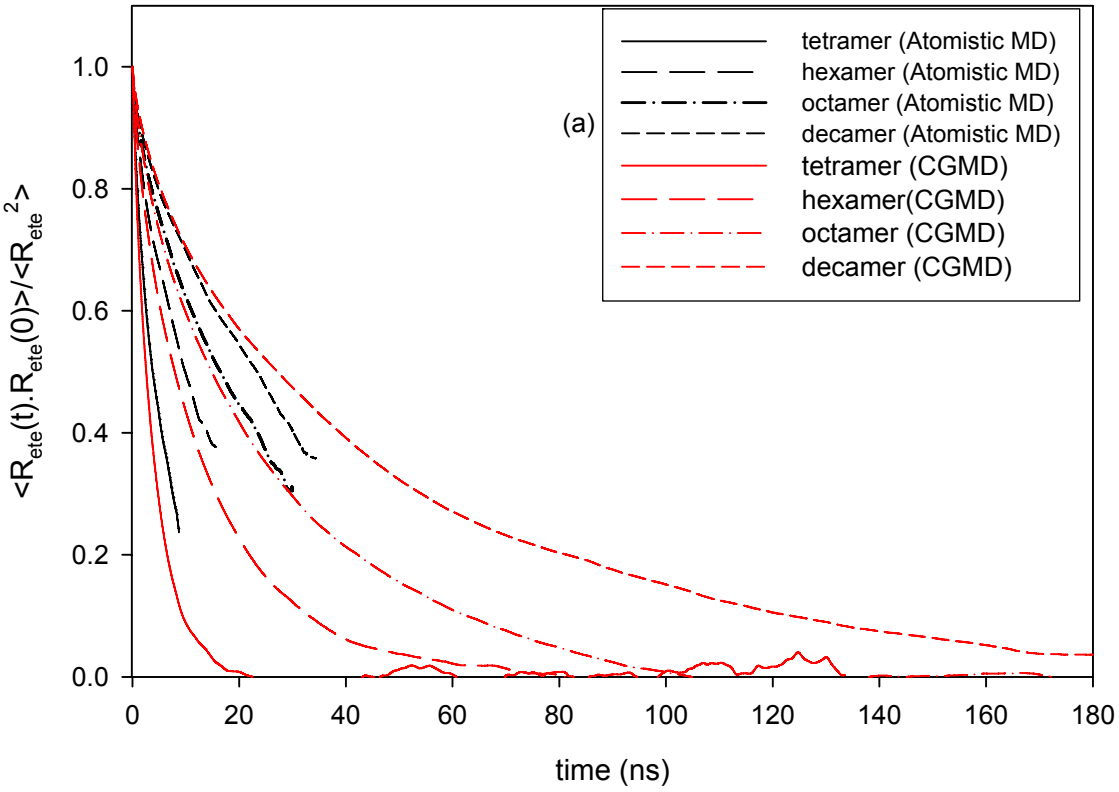

Figure 4.9. (a) Comparison of the end-to-end distance auto-correlation functions for the tetramer, hexamer, octamer and decamer from atomistic MD and CGMD simulations (with time scaled).

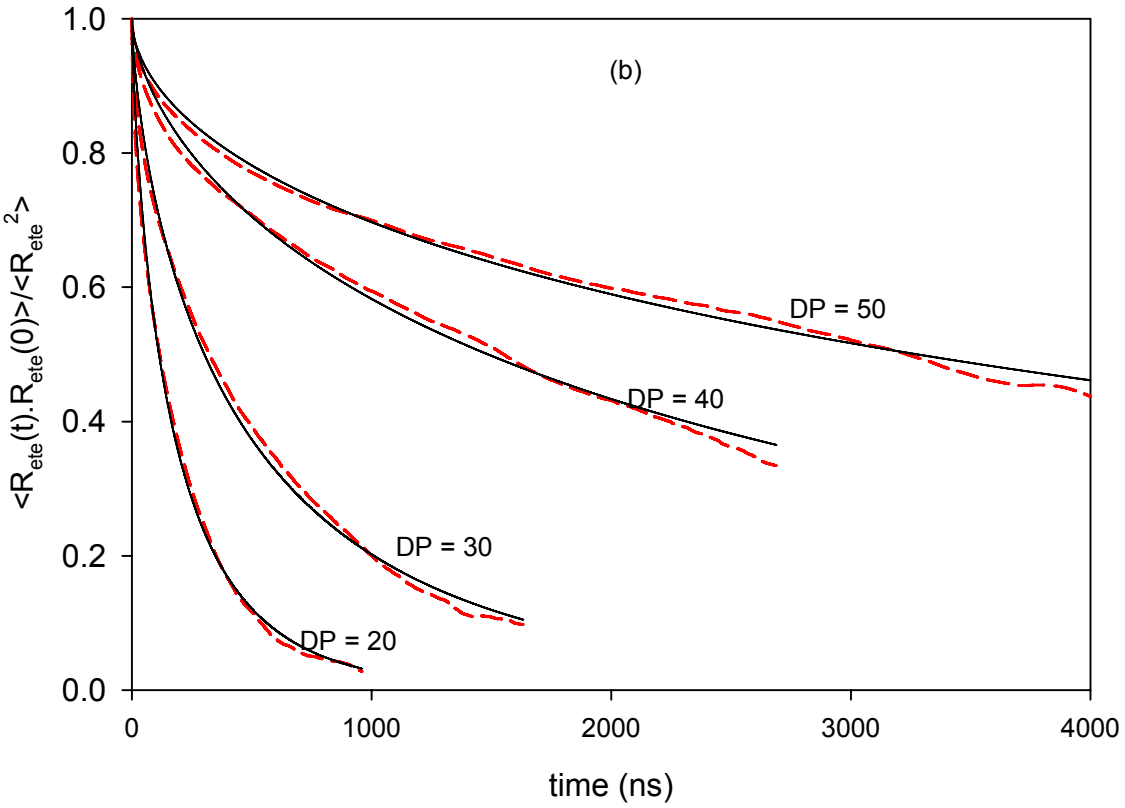

Figure 4.9. (b) The end-to-end distance auto-correlation function and its fitting to the KWW model for DP = 20, 30, 40 and 50 from the CGMD simulations.

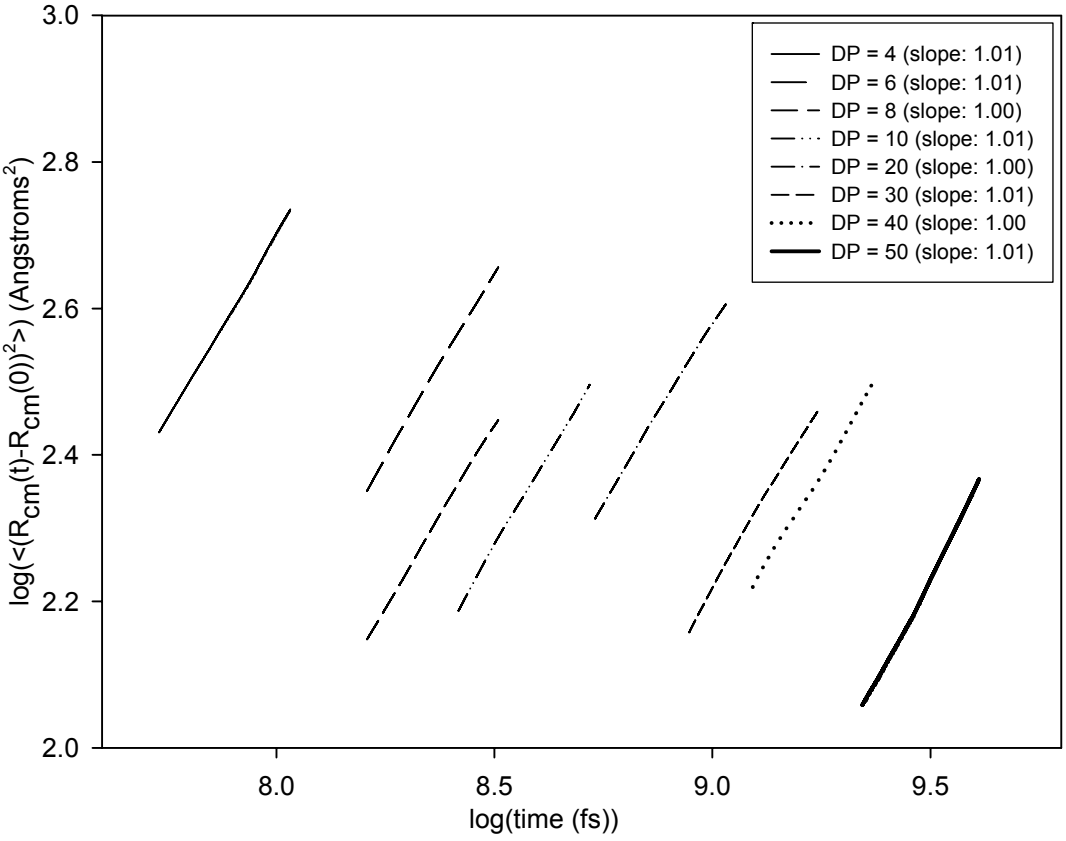

Figure 4.10. The mean square displacement of chain center of mass as a function of observation time for all DPs. The slope reported in the legend should be unity to satisfy the long-time limit of the Einstein relation.

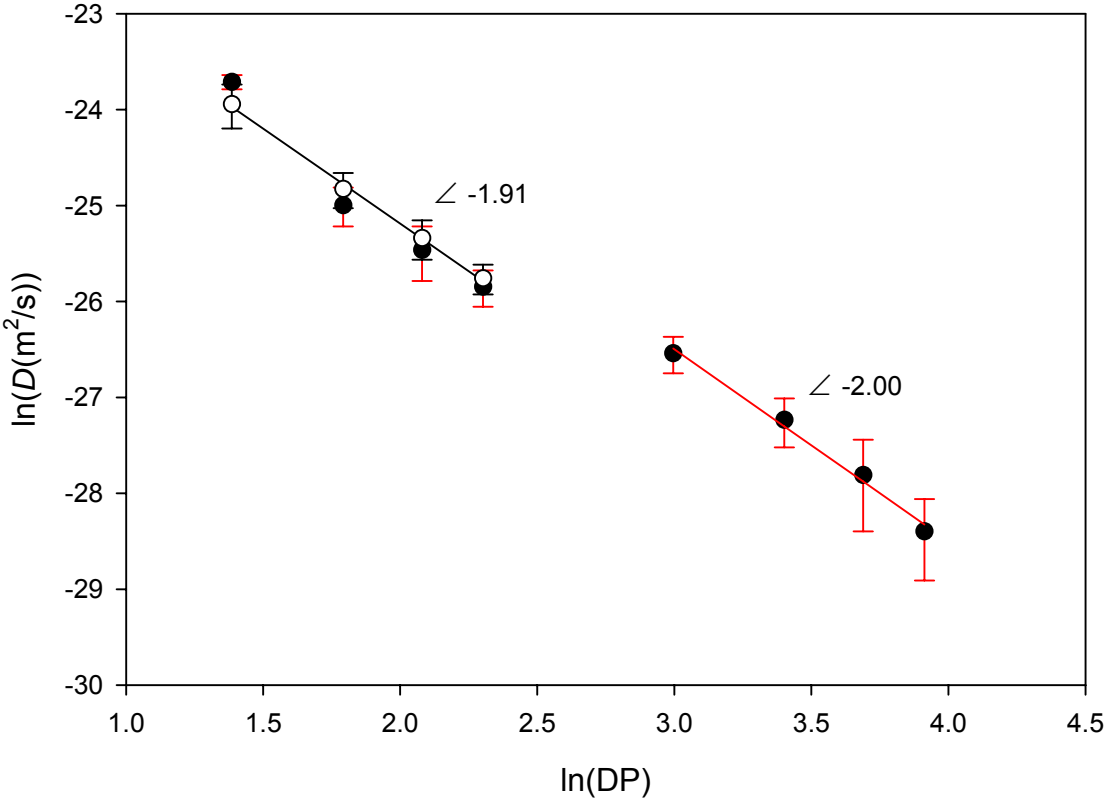

Figure 4.11. The average self-diffusivity (*D*) as a function of DP from atomistic MD (open symbols) and CGMD (solid symbols). The error bars are one standard deviation. Linear regressions of the MD data (short chains) and CGMD data (long chains) are shown with the slope reported.

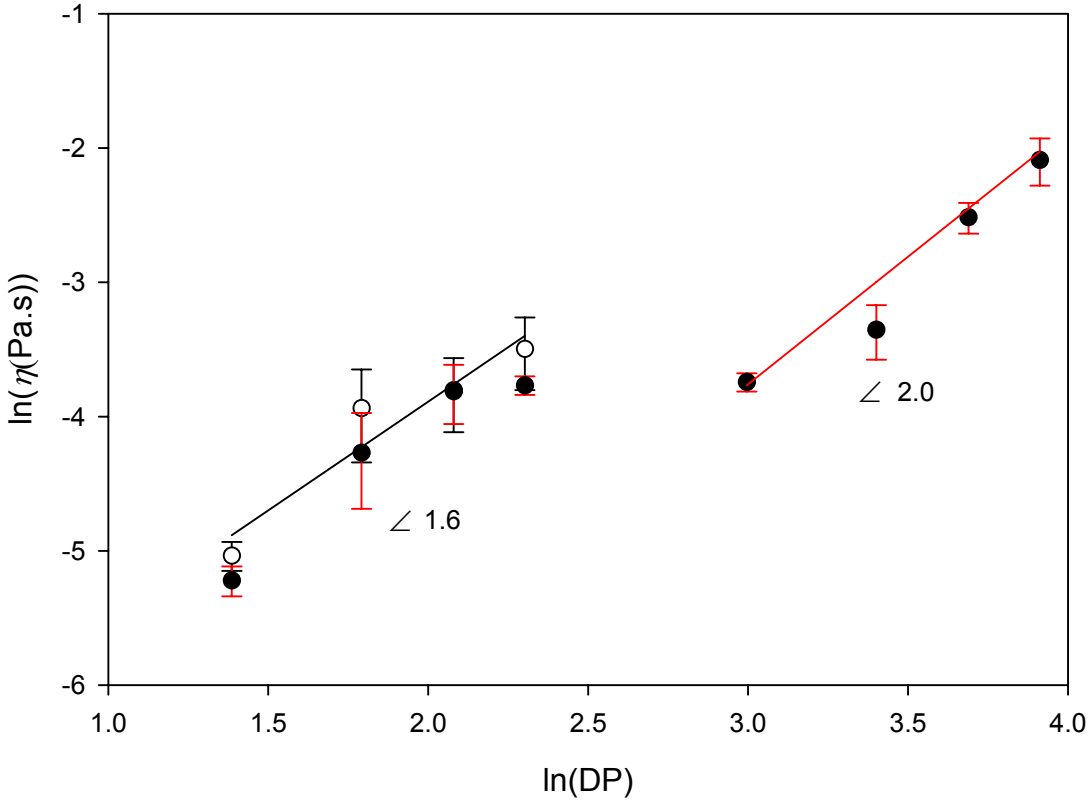

Figure 4.12. The average zero-shear-rate-viscosity (η) as a function of DP from atomistic MD (open symbols) and CGMD (solid symbols). The error bars are one standard deviation. Linear regressions of the MD data (short chains) and CGMD data (long chains) are shown with the slope reported.

CHAPTER 5

A Coarse-grained Model for Polyethylene Glycol (PEG) Polymer

This chapter is a revised version of a paper (minor revisions to reflect its inclusion as a chapter in the dissertation) by the same title in preparation for a journal by Qifei Wang, David J. Keffer, and Donald M. Nicholson:

The use of "we" in this part refers to the co-authors and the author of this dissertation. My primary contributions to this paper include (1) all of the simulation work (2) analysis of data, and (3) most of the writing.

Abstract

A coarse-grained (CG) model of Polyethylene Glycol (PEG) was developed and implemented in CG Molecular Dynamics (MD) simulations of PEG chains with degree of polymerization (DP) 20 and 40. In the model, two repeat units of PEG are grouped as one CG bead. Atomistic MD simulation of PEG chains with DP = 20 was first conducted to obtain the bonded structural probability distribution functions (PDFs) and nonbonded pair correlation function (PCF) of the CG beads. The bonded CG potentials are obtained by simple inversion of the corresponding PDFs. The CG nonbonded potential is parameterized to the PCF using both an inversion procedure based on the Ornstein-Zernike equation with the Percus Yevick approximation ($OZPY^{-1}$) and a combination of $OZPY^{-1}$ with the iterative Boltzmann inversion (IBI) method ($OZPY^{-1}$+IBI). As a simple one step method, the $OZPY^{-1}$ method possesses an advantage in computational efficiency. Using the potential from $OZPY^{-1}$ as an initial guess, the IBI method shows fast convergence. The CGMD simulations of PEG chains with DP = 20 using potentials from both methods satisfactorily reproduce the structural properties from atomistic MD simulation of the same systems. The $OZPY^{-1}$+IBI method yields better agreement than the $OZPY^{-1}$ method alone. The new CG model and CG potentials from $OZPY^{-1}$+IBI method was further tested through CGMD simulation of PEG with DP = 40 system. No significant changes are observed in the comparison of PCFs from CGMD simulations of PEG with DP = 20 and 40 systems, indicating that the potential is independent of chain length.

5.1 INTRODUCTION

Polyethylene Glycol (PEG, formula: $HO\text{-}(CH_2\text{-}CH_2\text{-}O)_n\text{-}H$) is one of the most important polymers widely used in biotechnology and the life science industry in applications of peptide drugs,[1,2] biodegradable hydrogels,[3] dendrimers,[4,5] protein crystallization[6] and drug delivery.[7] Due to the fact that the polymer's physical properties depend on chain length, there is interest in understanding the structural and dynamic properties of PEG at all length scales in order to better target new applications. The macroscopic structural and dynamic properties of PEG and its family member Polyethylene Oxide (PEO, formula: $H_3C\text{-}O\text{-}(CH_2\text{-}CH_2\text{-}O)_n\text{-}CH_3$) have been well studied through both experiment and theoretical computation. The structural, physical and transport properties of short-chain PEG and PEO have been previously studied through molecular-level simulation using different force fields,[8-19] in which the degree of polymerization is less than 40. In order to simulate longer chains, one must overcome the computational limitations imposed by exclusively using an atomically detail model through the introduction of multi-scale modeling techniques, which incorporate coarse-grained (CG) interaction potentials.

The CG technique removes computational limitations by eliminating some degrees of freedom in the atomistic model. To perform the CG procedure, a fully atomistic (or united atom (UA)) simulation of short chains is conducted first in order to obtain the CG structural distribution functions for different interactions modes assigned in the CG model. The CG potentials are then generated to correspond to these distribution functions. Since the degrees of freedom are greatly reduced in the CG model, structural and transport properties of long chain polymers can be calculated directly by CG simulation. This multi-scale modeling technique has been used in the study of structure and dynamics of biomacromolecules and polymer chain molecules.[20-27]

Using this approach, CG models and force fields of PEG and PEO have been developed. The MARTINI CG force field [28,29] has been successfully applied to study conformation and hydrodynamics of PEG and PEO,[30] in which united-atom C-O-C and O-C-C are treated as CG beads of PEO and PEG respectively. There are also CG studies of the interfacial properties of PEG surfactant/water [31,32] and PEG lipid [33] systems, in which united-atom C-O-C of the PEG chain was treated as one CG bead. The same mapping scheme was used by Fischer *et al.* [34] in their mesoscale simulation of PEO solution and by Bendov *et al.* [35] in their multi-scale modeling

approach for simulation of poly(ethylene oxide)-poly(propylene oxide)-poly(ethylene oxide) (PEO-PPO-PEO) triblock copolymer micelles in aqueous solution. In these models, the coarse-graining levels are limited within one repeat unit of PEG or PEO chain. Although using rather small degrees of coarsening leads to better potential transferability to temperature or chain length, [34] it limits the computational gain from CG procedure. A greater degree of coarse-graining was applied in a model of PEO developed by Chen *et al.* [36] In this model, united-atom O-C-C-O-C-C of the PEO chain are treated as one CG bead. Analytical potentials are used for bond stretching, bending and nonbonded interactions while the torsion potential is not included since the CG torsional mode distribution is featureless. [36] The dynamic observables in the CG model are in excellent agreement with their UA counterparts. [36] However, there was no indication of its transferability to longer chains.

In the CG procedure, obtaining reliable nonbonded interaction potential is particularly challenging since the effective potential is of no particular form. Two common methods have been adopted to obtain nonbonded CG potentials, namely adjusting power law type potential parameters (Lennard-Jones 12-6, 7-6, 7-4, 7-5, 8-6), [21,22,30,33,36,37] and iterative Boltzmann inversion (IBI) method. [25,34,35] The parameters of an analytical potential can be obtained by fitting to either theory or experimental data, which makes the first method computationally efficient. Potentials from this method can closely reproduce the atomistic structure. Depending on the CG model and force fields used in atomistic sampling, complicated nonbonded CG pair correlation functions (PCFs) can be generated. When dealing with complicated nonbonded PCFs, it can be difficult to reproduce the structures of atomistic simulation. The IBI method is designed to reproduce the structure of atomistic sampling, however the iterative nature of the method negatively impacts computational efficiency since the PCFs may not be very sensitive to changes in the CG potentials and the CG simulation has to run sufficiently long to obtain a reliable PCF.

Alternative methods have been developed recently to improve computational accuracy and efficiency of the CG procedure. Fritz *et al.* [38] recently presented an approach that obtains both the bonded and nonbonded interactions of the CG model of Polystyrene (PS) from the sampling of isolated atomistic chains and pairs of oligomers in vacuum. The CG model of PS using the calculated CG potentials reproduces local chain conformations of atactic as well as stereoregular PS. The Ornstein-Zernike integral equation (IE) theory is also widely used to

obtain nonbonded CG potentials.[27,39-41] Guenza [39] presented a procedure in which CG potentials can be obtained from a combination of liquid state and IE theories. The procedure has been successfully applied in higher level of CG models of polymers. [39,40,42] Wang *et al.* [43] recently developed an inverse procedure based on the Ornstein-Zernike equation with the Percus-Yevick approximation ($OZPY^{-1}$). In this method, the CG nonbonded potentials are extracted directly from the PCFs obtained from atomistic simulation of the short chain in a single calculation. The method has been applied to monatomic and diatomic fluids [43] as well as to PET polymer melts.[27] The $OZPY^{-1}$ method is approximate only because of the approximate nature of the PY assumption for the direct correlation function. As a one step method, it is simple and fast compared to the current methods of comparable accuracy.

In the application to monatomic and diatomic fluids [43] , the $OZPY^{-1}$ was applied to beads without any coarse-graining and was shown to self-consistently reproduce the interaction potentials input into the atomistic MD simulation for low and intermediate densities. As density increases, the PY approximation becomes less accurate. Thus we observe in these cases that the $OZPY^{-1}$ is generating potentials that are independent of the thermodynamic state (temperature and density) at which the simulations are performed.

Here, the aim of this work is to develop a highly coarse-grained model of PEG, in which each bead is composed of two monomer units. First, atomistic MD simulations of PEG chains with a degree of polymerization (DP) of 20 were conducted, from which bonded probability distribution functions (PDFs) and nonbonded pair correlation function (PCF) were obtained. Second, these structural results from the atomistic simulations were used to generate CG potentials, using both the $OZPY^{-1}$ method alone and the $OZPY^{-1}$ + IBI methods together. Third, the CG potentials are implemented in CGMD simulations of the same system (PEG with DP = 20), from which the bonded PDFs and nonbonded PCFs can be obtained and directly compared with those from the atomistic simulation. Finally, we performed CGMD simulations of longer chain PEG with DP of 40 to test the transferability of the proposed model in terms of chain length.

5.2 SIMULATION METHOD

5.2.1 Atomistic simulation of PEG with DP = 20.

We use the modified UA potential model based on the force field developed by Tritopoulou and Economou[12] for PEG to describe the intra-molecular and inter-molecular potential of PEG molecules. In the modified potential model, all the parameters for bond bending, bond torsion and nonbonded potentials are taken from work of Tritopoulou and Economou, while the potential forms are transformed to that of OPLS-AA.[44] The bond stretching of OPLS-AA force field is included here with parameters from the work of Fern *et al.* [45] for the O-H bond and Fischer *et al.* [11] for C-O and C-C bonds. The spherically truncated charge-neutralized method developed by Wolf *et al.* [46] is used to evaluate the electrostatic energy. We simulated in the isobaric-isothermal (NpT) ensemble and implemented the Hamiltonian-based thermostat and barostat with controller frequencies set to 10^{-4} fs^{-1}. [47] The XI-RESPA NPT algorithm developed by Tuckerman *et al.* [48] was used to integrate the equations of motion. The large time step was 2 fs and the small time step was 0.2 fs. The parallel code was built in-house and was written in FORTRAN-90, using MPI for inter-processor communication. It has been tested rigorously across a variety of applications. For the simulations in this work, we verified conservation of the Hamiltonian in order to validate our choices of time step, cut-off distance and to minimize the possibility of bugs in the potential. For all the simulations in this work, we used 125 chains. The state point was set at 1 atm and 353 K. Following the procedure described elsewhere,[49] we estimated the initial density and placed the particles in the simulation volume, avoiding significant overlap. We started with a higher temperature then gradually decreased the temperature and equilibrated to the correct density.[24,27,49] Data production followed and lasted over 40 ns.

5.2.2 CGMD simulations of longer PEG chains with DP = 20 and 40.

We propose that PEG can be modeled at a coarse-grained level with one spherical bead, which corresponds to two monomer units of PEG, $C_4H_8O_2$. In the construction of the PCFs from the atomistic simulations, the bead is placed at the center-of-mass of the atoms in the corresponding fragment, a convention that is adopted in most CG mapping schemes. Chain end sites are treated as being identical to sites in the middle. This mapping scheme introduces a small error due to end effects terminating each chain, which in the atomistic simulation are actually two OHs. This error is reduced as chain length increases. This model contains a greater reduction in the number of degrees of freedom compared with existing CG models while at the

same time it does not lose too many of the structural details of the atomistic chain conformations compared with much higher level coarse-graining models. This enhances computational efficiency, making the study of the dynamics of longer, entangled chains tractable.[27]

In this model, the CG interaction modes include bond stretching, bond bending, bond torsion, and nonbonded interactions for both intra-molecular (for beads separated by at least four bonds) and inter-molecular pairs. The same CG nonbonded potential is used for both intra-molecular and inter-molecular interactions. Probability distribution functions for stretching, bending, torsion and nonbonded interactions between CG beads were generated from the atomistic simulations. In the development of coarse-grained (CG) potentials, for the stretching, bending and torsion modes, there are straightforward approximations that relate the interaction potential directly to the PDFs. [22] The effective bonded interaction potential between a particle of type α and a particle of type β, $\varphi_{\alpha\beta}$, as a function of the separation between particles, *r*, can be related to the PDF, $g_{\alpha\beta}(r)$, via

$$\varphi_{\alpha\beta}(r) = -k_B T \ln\left(g_{\alpha\beta}(r)\right) + c_{\alpha\beta} \tag{1}$$

where k_B is Boltzmann's constant, T is temperature and $c_{\alpha\beta}$ is a constant to set the potential minimum to zero. Note here that the coordinates need to be changed for the bending (from *r* to θ (bending angle)) and torsion (from *r* to ϕ (torsion angle)) modes. In this work, we use the form of the bonded potentials from eqn. 1. Note here eqn. 1 is subject to the assumption that all the interactions are independent of each other. [22] One straightforward way to show this independence is simply to show that the CG simulations using the CG potentials generate PDFs that agree with those obtained from the atomistic simulations.

The nonbonded potential for intra-molecular (for beads over four bonds) and inter-molecular interactions is first calculated through the OZPY[-1] method. The Ornstein-Zernike Integral Equation for a mixture of simple fluids[50] is

$$g_{\alpha\beta}(r,r') - 1 = c_{\alpha\beta}(r,r') + \sum_{\gamma} \int c_{\alpha\gamma}(r,r'') n_{\gamma}(r'') \left[g_{\gamma\beta}(r'',r') - 1\right] d^3 r'' \tag{2}$$

where the PCF between particles of type α and β located respectively at r and r', $g_{\alpha\beta}(r,r')$, is related to the direct correlation, $c_{\alpha\beta}(r,r')$, and an integral including the interactions of the α and

β particles with a third particle, γ, located at r'' with a singlet density, $\mathrm{n}_\gamma(r'')$. There is a summation over γ spanning all types of particles. The OZ equation describes the relationship between PCF and effective potential through its different closures. As one of the closures, the Percus-Yevick approximation of the direct correlation function is written as

$$\mathrm{c}_{\alpha\beta}(r,r') = \mathrm{g}_{\alpha\beta}(r,r')\left[1 - \exp\left(\frac{\varphi_{\alpha\beta}(r,r')}{k_B T}\right)\right] \tag{3}$$

Substitution of the PY approximation into the OZ equation yields the OZPY equation

$$\mathrm{y}_{\alpha\beta}(r) = 1 + \sum_\gamma \frac{2\pi\,\mathrm{n}}{r}\int_0^\infty \mathrm{dss}\left[\mathrm{h}_{\alpha\gamma}(s) - \mathrm{y}_{\alpha\gamma}(s) + 1\right]\int_{|r-s|}^{r+s} \mathrm{dtt}\, h_{\gamma\beta}(t) \tag{4}$$

with the definition of cavity function and total correlation function respectively as

$$\mathrm{y}_{\alpha\beta}(r,r') = \mathrm{g}_{\alpha\beta}(r,r')\exp\left(\frac{\varphi_{\alpha\beta}(r,r')}{k_B T}\right) \tag{5}$$

$$\mathrm{h}_{\alpha\beta}(r,r') = \mathrm{g}_{\alpha\beta}(r,r') - 1 \tag{6}$$

The OZPY equation as written here assumes a homogeneous system and has been expressed in bipolar coordinates following Lee. [50] We have previously shown how the summation over components can be converted to a summation over potentials, so that stretching, bending and torsion modes can be includes in the OZPY equation.[43] Further details of the OZPY^{-1} method[43] and its application to polymers[27] can be found elsewhere. The method requires a meticulous accounting of the allowable combinations of interaction potentials involving $\alpha\gamma$ and $\gamma\beta$ pairs, which are dependent on the connectivity of the polymer chain. For PEG, there are 13 such combinations. The allowable combinations are summarized in Table 5.1.

The nonbonded potential can also be generated by the IBI method for comparison. In the IBI method, a tabulated potential is numerically determined by simulation iteration. The interaction potential is refined iteratively [25] via

$$\varphi_{\alpha\beta,i+1}(r) = \varphi_{\alpha\beta,i}(r) + \mathrm{k_B T}\ln\left(\frac{\mathrm{g}_{\alpha\beta,i}(r)}{\mathrm{g}_{\alpha\beta}(r)}\right) \tag{7}$$

with initial guess

$$\varphi_{\alpha\beta,0}(r) = -\mathrm{k_B T}\ln\left(\mathrm{g}_{\alpha\beta}(r)\right) \tag{8}$$

where $g_{\alpha\beta}(r)$ is the target PCF, which is from atomistic simulation. The challenging part of this method is obtaining PCFs from CG simulations iteratively, which could strongly limit the computational gain of CG procedure. [39] In this work, we combined this iterative method with the non-iterative method ($OZPY^{-1}$) by using the output from the $OZPY^{-1}$ method as the source of the initial guess for the IBI method, rather than eqn 8. The combined method, the $OZPY^{-1}$+IBI method, is investigated to determine whether this new approach can improve the performance of the two methods alone.

After obtaining all the CG potentials, we performed CGMD simulations for PEG with DP = 20 and 40. In the CGMD simulations, we estimated the initial density and placed the particles in the simulation volume carefully with proper bond length and angles, then gradually introduced the nonbonded interactions to avoid overlap, as has been done before. [27] We again simulated in the isobaric-isothermal (NpT) ensemble under the same pressure and temperature as the atomistic simulation. The time steps of CGMD simulation are the same as those used in the atomistic MD simulation. Using bigger time steps impacts the conservation of Hamiltonian. In this case, the computational speed up is due strictly to the reduction in degrees of freedom. Based on wall-clock time, the CGMD simulations are approximately 200 times faster than the atomistic simulations. (Note here that in the atomistic simulations, a united-atom model was used for hydrogen bound to carbon, already eliminating some degrees of freedom even in the "atomistic" model.) The CGMD simulation code is the same as that used in the atomistic MD simulations.

5.3 RESULTS AND DISCUSSION

In this section, we present (1) the results of the atomistic MD simulation of PEG with DP = 20, (2) CG potentials from the $OZPY^{-1}$ and $OZPY^{-1}$+IBI methods and (3) CGMD simulation results for PEG with DP = 20 and 40. Finally, we compare the structural distribution functions from CGMD simulations with that of atomistic simulation.

Because the atomistic and CG simulations were run in the NpT ensemble, the density is an output. The output equilibrium densities of the CG simulations of PEG with DP = 20 and 40 are respectively 1.093 to 1.099 g/cm^3, which are close to the experimental finding of 1.094 g/cm^3 (1atm, 333K) by Li *et al.* [51] . The equilibrium density of the DP = 20 system is the same as that in the atomistic simulation.

In Figure 5.1, we show equilibrated snapshots from both the atomistic and the CGMD simulations. In Figure 5.1(b), (d) and (f), all molecules are shown to make it clear that we are simulating a dense melt. In Figures 5.1(a), (c) and (e), all but five chains are rendered invisible to better indicate the shape of the chains. Note here two repeat units in the atomistic model are grouped as one CG bead in the CG model.

5.3.1 Atomistic MD simulation of DP = 20 chains

In Figure 5.2, we show the bonded distributions of the CG beads obtained from atomistic simulation. These distribution functions are based on the analysis of configurations from atomistic MD simulation. As shown in Figure 5.1, these distribution functions are calculated according to the center of mass position of CG beads. The stretching mode displays a bimodal distribution with the major peak centered at 7.15 Å and a much smaller centered at 7.8 Å. The bending angle distribution shows a single asymmetric peak centered at 163˚. The torsion angle distribution shows a single symmetric peak centered at 0˚. This feature is similar to other simulation work for PEO.[34,35] The features of the stretching and bending distributions are different from those reported by Chen *et al.* for PEO, [36] in which a similar CG model but a different mapping scheme was adopted. In their mapping scheme, every other oxygen atom is considered a CG center and six united atoms are replaced by a CG bead. This mapping scheme caused a featureless torsion angle distribution. In this work, we use the center of mass of six united atoms as a CG center. The difference of mapping schemes and chemical structure on the end groups of PEG and PEO may be responsible for the variation in the bonded CG PDFs.

The nonbonded PCF of the CG beads obtained from the atomistic simulations is shown in Figure 5.3. The PCF shows multiple peaks with the first three peaks centered at 4.7 Å, 9.0 Å and 13.10 Å respectively. Similar features can be found in the intermolecular nonbonded PCF by Chen *et al.* [36] work on PEO, in which peak positions are almost the same as that reported here while the intensity of the peaks are weaker. Note here the nonbonded PCF in this work includes both intramolecular (for CG beads separated by at least four bonds) and intermolecular parts.

5.3.2 Generation of CG potentials and CGMD simulation of chains with DP = 20

Based on the bonded distribution functions, we obtained the bonded stretching, bending and torsion CG potentials (not shown) through eqn. 1. As noted above, eqn. 1 is subject to the assumption that all the interactions are independent of each other. We have validated the

assumption of independence of the bonded modes through direct comparison of the PDFs from the atomistic and CG simulations. Further understanding of the statistical interdependencies of different bonded interaction modes can be found in the literature.[20-22]

In Figure 5.2, we also report the bonded PDFs from the CGMD simulations of PEG with DP = 20. The stretching distribution from the atomistic and CG descriptions is virtually identical, capturing the position and magnitude of both peaks as well as the long interior shoulder of the larger peak. The comparison of the bending distribution is also very good, although there is a small error as one approaches 180˚. A similar discrepancy was observed for the comparison of atomistic and CG simulations of PET. [27] There is a steep slope leading to a minimum at 180˚. It is possible that the discrepancy is due to the curve fitting and interpolation scheme used to generate smooth, continuous energies and forces across this point of symmetry. The comparison of the torsion distribution between the atomistic and CG simulations is also very good. In short, the bonded PDFs from the two levels of simulation match relatively well, providing evidence that the assumption of independence between the modes invoked for eqn. 1 is well-founded.

The agreement between the PDFs of the bonded modes is not impacted by the procedures used here to generate the nonbonded potential ($OZPY^{-1}$ or $OZPY^{-1}$+IBI). The distributions for all iterations (not shown) are virtually the same as those presented in Figure 5.2. In Figure 5.2, we show the results using the last CG potential from the last iteration of $OZPY^{-1}$+IBI method.

We explored three ways of generating the nonbonded CG potential. First, the $OZPY^{-1}$ procedure alone was used based on the structural properties (bonded PDFs and nonbonded PCF) from the atomistic simulation as input. With the four distributions in hand, it takes only a couple of seconds on a laptop to calculate the CG nonbonded potential using the $OZPY^{-1}$ procedure. The CG nonbonded interaction potential for PEG obtained from the $OZPY^{-1}$ method is shown in Figure 5.4. There are multiple minima in the potential. The positions of these minima are slightly different from that of the peaks on the corresponding PCF. Note that none of the local maxima in the potential are actually repulsive; the energy is always less than zero beyond the repulsion of the core.

In Figure 5.5, we compare the PCF from the CGMD simulations of PEG (DP = 20) using the nonbonded potential from $OZPY^{-1}$ with that of atomistic MD simulation. Generally, the CGMD simulation can reproduce all the peaks of the target PCF. However, the first peak is

over-estimated and the first trough is under-estimated. The error diminishes as the separation increases. It is important to remember that the PCF is not a particularly sensitive variable. Small changes in the quantitative structure of the PCF can correspond to large changes in thermodynamic properties. Thus, while the agreement between the PCF is fairly good and at least semi-quantitative, it is nevertheless of interest to explore the source of the error and potential means by which it might be eliminated.

In integral equation theory, the PY closure yields accurate results for systems that have short-range, hard-core potentials.[39] In the coarse-graining process, soft potentials have been reported as effective potentials for different CG models.[22,36,40] In these models, the coarse-graining is kept to the monomer scale. When the coarse-graining level increases, the effective potential may become even softer. Previous work shows that when the coarse-graining level is low (within monomer scale), the OZPY^{-1} works well on reproducing the structures of atomistic sampling although a soft type nonbonded CG potential is observed.[27] In this work, we increased the degree of coarse-graining by grouping two monomers as one CG bead. Thus, the degree of coarse-graining could be one source of error.

However, if we wish to maintain this CG model, we remain interested in improving the accuracy of the CG non-bonded potential using other potential generating methods. The OZPY^{-1} method is not iterative. It takes as inputs structural information from the atomistic simulation and generates a CG potential. We can however, use the OZPY^{-1} method to provide the first estimate of the CG potential to an iterative method, like the Iterative Boltzmann Inversion method. The IBI is developed based on the fact that there is a unique functional relationship between PCF and effective potential.[39] Using the IBI method compromises the computational efficiency of the approach since each iteration requires a new CGMD simulation. However, if the iteration is done on relatively short chains, the exercise is still tractable. For example in this work, to obtain the PCF from CGMD simulation of the PEG (DP = 20) system, each IBI iteration required 32 processor-hours on a cluster (2 hours using 16 processors).

In Figure 5.6, we show the CG potential from the first four iterations of the IBI method for PEG (DP=20), using the CG potential from the OZPY^{-1} procedure as an initial guess. There are significant changes in the shape of the CG potential. The first well becomes shallower and the first peak becomes smaller. Interestingly, the second peak continues to grow until it becomes

repulsive (greater than zero). We shall postpone discussion on this feature until after we have presented the corresponding PCFs.

In Figure 5.7, the PCFs from CGMD simulation of PEG (DP=20) are shown as a function of iteration step in the IBI procedure. There are modest changes in the PCF due to the iterative procedure, indicating that the initial guess provided by the $OZPY^{-1}$ procedure was relatively good. In Figure 5.7(a), we observe that the changes in the PCF induced by the IBI procedure are qualitatively correct. The height of the first peak diminishes monotonically as the iteration step increases. The depth of the first trough rises monotonically as the iteration step increases. These trends should be expected based on the comparison of the CG PCF from $OZPY^{-1}$ procedure and the atomistic (target) PCF shown in Figure 5.3.

In Figure 5.7(b), the CG nonbonded PCFs from the last two iterations of the IBI procedure are compared to the atomistic PCF. The difference between the third and fourth iterations is negligible. However, there is still a much larger error between the fourth iteration and the atomistic PCF. This indicates that either (1) the IBI method is converging to the wrong solution or (2) further convergence is extremely slow. Previous investigations have revealed that there are elements of both causes.[24,25,39,52] Convergence is slow but small statistical noise in the procedure results in practical difficulties in converging to the solution within in an arbitrary tolerance. One consequence of these practical issues is that, while theoretically there is a unique relationship between interaction potential and PCF, practically (because of statistical noise and truncations of the interactions), there are multiple potentials that effectively yield the same PCF.[25,34,35,53]

To illustrate this point, we applied the original IBI method with eqn. 8 as the initial guess. The potentials from IBI method are presented in Figure 5.8 while the nonbonded PCFs from CGMD using these potentials are shown in Figure 5.9. The potentials in Figure 5.8 change dramatically for the first three iterations but change relatively little after the fifth iteration. In Figure 5.9, the changes on nonbonded PCFs are invisible to the eye from the fifth to the sixth iteration. The same phenomena are observed at the seventh iteration (not shown here), which means further convergence is extremely slow.

The comparison of potentials from the three methods and corresponding nonbonded PCFs from CGMD simulations using these potentials are shown in Figure 5.10 and 5.11 respectively.

Figure 5.11 shows that the nonbonded PCFs from CGMD simulation using potentials OZPY^{-1}+IBI and IBI methods are almost identical while the potentials deviate substantially. This illustrates the practical issues involved in coarse-graining that effectively undermine the unique relationship between interaction potential and PCF.

The OZPY^{-1}+IBI method generates PCFs that more accurately reproduce the atomistic PCFs than does the OZPY^{-1} method alone. It requires a significant change in the interaction potential, including non-core repulsive regions in the potential. In nonbonded potentials used in atomistic simulations one typically does not observe repulsion beyond that which is known at short-distances due to electron-electron repulsion and which originates in the Pauli exclusion principle. In this regard, the CG potential obtained from the OZPY^{-1}+IBI is unphysical. It may seem contradictory to speak of an unphysical potential when discussing coarse-grained beads, which themselves do not exist, but the Ornstein-Zernike equation is not an approximation and is based on sound statistical physics. The Percus-Yevick approximation is based on a reasoning of the effects of molecular correlations. Therefore, it is worth pondering the question whether the introduction of unphysical traits to a CG potential in exchange for quantitative improvement in the potential is either necessary or productive.

We have previously shown that in the absence of any coarse-graining, the OZPY^{-1} procedure can reproduce the physically meaningful interaction potentials used in the atomistic simulation that generated the PCFs.[43] These potentials have the advantage that they are independent of the thermodynamic state at which the PCF was generated. If we abandon, and tie the interaction potentials too closely to the PCFs, which themselves are functions of the thermodynamics state, then perhaps this feature of an interaction potential independent of thermodynamic state will be lost.

Alternatively, if a CG potential is a practical tool only, intended to reproduce strictly the target PCF, then the shape of the CG potential and its possession of unphysical traits is irrelevant. However, in such a case, we have a potential that is clearly tied to the thermodynamic state at which the PCF was generated. It has lost its transferability.

The PCFs shown in this work, such as those in Figure 5.3 have multiple peaks with diminishing magnitude as the separation increases. Such PCFs can be qualitatively generated from physically meaningful potentials, such as a LJ 12-6 potential, where the repulsion term

represents electron-electron repulsion and the attractive term represents induced-dipole-induced-dipole interactions. The pairwise potential gives rise directly to the first peak in the PCF. Subsequent peaks arise due to pairwise interactions involving two particles that are not the central particle. The CG potential obtained from the $OZPY^{-1}$ approach generates such a PCF.

As noted above the PCFs are not extremely sensitive measures of changes in the system. This lack of sensitivity impacts convergence. The simulations have to be run sufficiently long to obtain PCFs that are reliable to more significant figures than are required for other applications. If there is slight statistical noise in the PCFs, the resulting change in the potential is large and spurious.

Another interesting aspect on the speed of converging is the number of iterations taken to reach convergence. The number of iterations taken on obtaining the converged nonbonded CG potential using accelerated IBI methods has been reported in the literature. Eight iterations has been reported by Bedrov *et al.* [35] in the CG modeling work of PEO-PPO-PEO triblock copolymer using a modified IBI method, in which a Lennard-Jones type potential is used as initial guess. Ten iterations is reported by Fischer *et al.*[34] on the development of CG model of PEO by keeping the starting potential as short-ranged as possible to accelerate the IBI method. In this work, it took three iterations using the $OZPY^{-1}$ + IBI method to reach the convergence as indicated in Figure 5.6, compared with five iterations using the original IBI method as shown in Figure 5.9. Thus the use of the $OZPY^{-1}$ method to initialize the IBI method presents some computational advantage.

5.3.3 Structural Properties from CGMD simulations of PEG with DP = 20 and 40

At this point, both bonded CG potentials (from eqn. 1) and the nonbonded CG potential (from $OZPY^{-1}$+IBI method) are ready to be used. With all of the above CG potentials, we simulated PEG chains with DP = 20 and 40. The snapshots are shown in Figure 5.1(c) to (f). The bonded PDFs and nonbonded PCFs along with those of atomistic MD simulation are shown in Figure 5.2(a) to (c) and Figure 5.3 . For the three bonded modes (stretching, bending and torsion), the distribution function of CGMD simulation of DP = 20 and DP = 40 systems are almost identical and match very well with that of atomistic simulation. In Figure 5.3, the nonbonded PCF from CGMD simulation matches well with that of atomistic simulation and also shows no apparent chain length dependence. A small discrepancy exists on the comparison of

PCFs from the two levels of simulation. To this end, we have shown that newly proposed CG model of PEG can be used to study the structures of PEG with much longer chain length. As presented elsewhere in most CG level simulation work, one of the most important points of validation of the CG process is the reproduction of conformations from atomistic sampling.[27] Having done this, we can further investigate the other physical properties from CG simulation of long chain PEG by using this model. In Figure 5.12, we show the distribution of chain end-to-end distance for DP = 20 and 40 from CGMD simulation (data points). The end-to-end distance is defined as the distance between the two end EE groups. The end-to-end curves of the DP = 20 and DP = 40 in Figure 5.12 roughly show Gaussian like distribution. For DP = 20, there is a small deviation from the Gaussian distribution in the short range, which is believed due to the formation of folded structures when short chain length (small DP) is used, as observed in the literatrues.[27,30] As DP increases, the distribution becomes more Gaussian-like, as shown for DP = 40. The position of the maximum in the peak and the breadth of the curve also increase with DP, as expected. The end-to-end distribution of the DP = 20 from atomistic MD simulation is also presented in Figure 5.12 (solid red line). The comparison is very good. This is a further evidence that the CG model is able to capture the chain conformation of the atomistic description.

5.4 CONCLUSIONS

A coarse-grained (CG) model of Polyethylene Glycol (PEG) was developed and implemented in CG Molecular Dynamics (MD) simulations of PEG chains with degree of polymerization (DP) 20 and 40. To obtain the CG potentials for different interaction modes, atomistic MD simulation of PEG chains with DP = 20 was first conducted to obtain the structural distribution functions of CG beads. Analysis on the structural distribution functions shows that this level of coarse-graining generates complicated nonbonded PCF. The CG nonbonded potential is parameterized to PCF obtained using both an inversion procedure based on the Ornstein-Zernike equation with the Percus Yevick approximation ($OZPY^{-1}$), a combination of $OZPY^{-1}$ and IBI method ($OZPY^{-1}$+IBI) and the original IBI method. All the three methods yield different non-bonded interaction potentials, but generate similar PCFs. The CGMD simulation of PEG chains with DP = 20 using potentials from both the three methods satisfactorily reproduces the structures from atomistic MD simulation of the same systems. The new CG model and CG

potentials from OZPY^{-1}+IBI method was further tested through CGMD simulation of PEG with DP = 40 system. No significant changes are observed on the comparison of PCFs from CGMD simulations of PEG with DP = 40 and 20 systems, which means the potentials are transferable to chain length. The new CG model can be further applied to study the structure and dynamics of PEG longer chain system through CG simulations.

5.5 ACKNOWLEDGMENTS

This research was supported by the Eastman Chemical Company and by a grant from the National Science Foundation (DGE-0801470) and by the U.S. Department of Energy, Office of Basic Energy Sciences, Division of Materials Sciences and Engineering. This research project used resources of the National Institute for Computational Sciences (NICS) supported by NSF under agreement number: OCI 07-11134.5.

References

[1]Y. Imura, M. Nishida, Y. Ogawa, Y. Takakura, and K. Matsuzaki, Biochimica Et Biophysica Acta-Biomembranes **1768**, 1160 (2007).

[2]Y. Imura, M. Nishida, and K. Matsuzaki, Biochimica Et Biophysica Acta-Biomembranes **1768**, 2578 (2007).

[3]J. A. Burdick and K. S. Anseth, Biomaterials **23**, 4315 (2002).

[4]D. Chun, F. Wudl, and A. Nelson, Macromolecules **40**, 1782 (2007).

[5]D. Luo, K. Haverstick, N. Belcheva, E. Han, and W. M. Saltzman, Macromolecules **35**, 3456 (2002).

[6]B. Cudney, S. Patel, K. Weisgraber, and Y. Newhouse, Acta Crystallographica Section D-Biological Crystallography **50**, 414 (1994).

[7]M. L. Adams, A. Lavasanifar, and G. S. Kwon, J. Pharm. Sci. **92**, 1343 (2003).

[8]D. Bedrov and G. D. Smith, J. Phys. Chem. B **103**, 3791 (1999).

[9]H. T. Dong, J. K. Hyun, C. Durham, and R. A. Wheeler, Polymer **42**, 7809 (2001).

[10]J. Fischer, D. Paschek, A. Geiger, and G. Sadowski, J. Phys. Chem. B **112**, 8849 (2008).

[11]J. Fischer, D. Paschek, A. Geiger, and G. Sadowski, J. Phys. Chem. B **112**, 2388 (2008).

[12]E. A. Tritopoulou and I. G. Economou, Fluid Phase Equilibria **248**, 134 (2006).

[13]D. Bedrov, M. Pekny, and G. D. Smith, J. Phys. Chem. B **102**, 996 (1998).

[14]G. D. Smith and D. Bedrov, Macromolecules **35**, 5712 (2002).

[15]M. Winger, A. H. de Vries, and W. F. van Gunsteren, Molecular Physics **107**, 1313 (2009).

[16]G. D. Smith, D. Y. Yoon, R. L. Jaffe, R. H. Colby, R. Krishnamoorti, and L. J. Fetters, Macromolecules **29**, 3462 (1996).

[17]B. Lin, P. T. Boinske, and J. W. Halley, J. Chem. Phys. **105**, 1668 (1996).

[18]S. Neyertz, D. Brown, and J. O. Thomas, J. Chem. Phys. **101**, 10064 (1994).

[19]C. D. Wick and D. N. Theodorou, Macromolecules **37**, 7026 (2004).

[20]A. Villa, C. Peter, and N. F. A. van der Vegt, Phys. Chem. Chem. Phys. **11**, 2077 (2009).

[21]V. A. Harmandaris, N. P. Adhikari, N. F. A. van der Vegt, and K. Kremer, Macromolecules **39**, 6708 (2006).

[22]V. A. Harmandaris, D. Reith, N. F. A. Van der Vegt, and K. Kremer, Macromol. Chem. Phys. **208**, 2109 (2007).

[23]B. Hess, S. Leon, N. van der Vegt, and K. Kremer, Soft Matter **2**, 409 (2006).

[24]K. Kamio, K. Moorthi, and D. N. Theodorou, Macromolecules **40**, 710 (2007).

[25]D. Reith, M. Putz, and F. Muller-Plathe, J. Comput. Chem. **24**, 1624 (2003).

[26]K. Voltz, J. Trylska, V. Tozzini, V. Kurkal-Siebert, J. Langowski, and J. Smith, J. Comput. Chem. **29**, 1429 (2008).

[27]Q. F. Wang, D. J. Keffer, D. M. Nicholson, and J. B. Thomas, Macromolecules **43**, 10722 (2010).

[28]S. J. Marrink, A. H. de Vries, and A. E. Mark, J. Phys. Chem. B **108**, 750 (2004).

[29]S. J. Marrink, H. J. Risselada, S. Yefimov, D. P. Tieleman, and A. H. de Vries, J. Phys. Chem. B **111**, 7812 (2007).

[30]H. Lee, A. H. de Vries, S. J. Marrink, and R. W. Pastor, J. Phys. Chem. B **113**, 13186 (2009).

[31]W. Shinoda, R. Devane, and M. L. Klein, Mol. Simul. **33**, 27 (2007).

[32]W. Shinoda, R. DeVane, and M. L. Klein, Soft Matter **4**, 2454 (2008).

[33]W. Shinoda, R. DeVane, and M. L. Klein, J. Phys. Chem. B **114**, 6836 (2010).

[34]J. Fischer, D. Paschek, A. Geiger, and G. Sadowski, J. Phys. Chem. B **112**, 13561 (2008).

[35]D. Bedrov, C. Ayyagari, and G. D. Smith, J. Chem. Theory Comput. **2**, 598 (2006).

[36]C. X. Chen, P. Depa, V. G. Sakai, J. K. Maranas, J. W. Lynn, I. Peral, and J. R. D. Copley, J. Chem. Phys. **124**, 11 (2006).

[37]R. DeVane, M. L. Klein, C. C. Chiu, S. O. Nielsen, W. Shinoda, and P. B. Moore, J. Phys. Chem. B **114**, 6386 (2010).

[38]D. Fritz, V. A. Harmandaris, K. Kremer, and N. F. A. van der Vegt, Macromolecules **42**, 7579 (2009).

[39]M. G. Guenza, J. Phys.: Condens. Matter **20**, 033101 (2008).

[40]A. J. Clark and M. G. Guenza, J. Chem. Phys. **132**, 044902 (2010).

[41]L. Zhao, Y. G. Li, J. G. Mi, and C. L. Zhong, J. Chem. Phys. **123**, 124905 (2005).

[42]J. McCarty and M. G. Guenza, J. Chem. Phys. **133** (2010).

[43]Q. F. Wang, D. J. Keffer, D. M. Nicholson, and J. B. Thomas, Phys. Rev. E **81**, 061204 (2010).

[44]W. L. Jorgensen, D. S. Maxwell, and J. TiradoRives, J. Am. Chem. Soc. **118**, 11225 (1996).

[45]J. T. Fern, D. J. Keffer, and W. V. Steele, J. Phys. Chem. B **111**, 13278 (2007).

[46]D. Wolf, P. Keblinski, S. R. Phillpot, and J. Eggebrecht, J. Chem. Phys. **110**, 8254 (1999).

[47]D. J. Keffer, C. Baig, P. Adhangale, and B. J. Edwards, Mol. Simul. **32**, 345 (2006).

[48]M. Tuckerman, B. J. Berne, and G. J. Martyna, J. Chem. Phys. **99**, 2278 (1993).

[49]M. S. Hedenqvist, R. Bharadwaj, and R. H. Boyd, Macromolecules **31**, 1556 (1998).

[50]L. L. Lee, *Molecular thermodynamics of nonideal fluids* (Butterworths, Boston, 1988).

[51]C. Y. Li, M. J. Birnkrant, L. V. Natarajan, V. P. Tondiglia, P. F. Lloyd, R. L. Sutherland, and T. J. Bunning, Soft Matter **1**, 238 (2005).

[52]A. K. Soper, J. Chem. Phys. **202**, 295 (1996).

[53]H. S. Ashbaugh, H. A. Patel, S. K. Kumar, and S. Garde, J. Chem. Phys. **122** (2005).

Appendix D

Tables and Figures

Table 5.1. Necessary Combinations for CG PEG chain, with symbols E: CG bead; N: nonbonded interaction; S: stretching interaction; B: bending interaction; T: torsion interaction.

No.	**particle type**			**potential type**			**potentials in summation**
No.	**α**	**β**	**γ**	**αβ**	**αγ**	**γβ**	**αγβ**
1	E	E	E	N_{EE}	S_{EE}	T_{EE}	$S_{EE}T_{EE}$
2	E	E	E	N_{EE}	S_{EE}	N_{EE}	$S_{EE}N_{EE}$
3	E	E	E	N_{EE}	B_{EE}	B_{EE}	$B_{EE}B_{EE}$
4	E	E	E	N_{EE}	B_{EE}	T_{EE}	$B_{EE}T_{EE}$
5	E	E	E	N_{EE}	B_{EE}	N_{EE}	$B_{EE}N_{EE}$
6	E	E	E	N_{EE}	T_{EE}	S_{EE}	$T_{EE}S_{EE}$
7	E	E	E	N_{EE}	T_{EE}	B_{EE}	$T_{EE}B_{EE}$
8	E	E	E	N_{EE}	T_{EE}	T_{EE}	$T_{EE}T_{EE}$
9	E	E	E	N_{EE}	T_{EE}	N_{EE}	$T_{EE}N_{EE}$
10	E	E	E	N_{EE}	N_{EE}	S_{EE}	$N_{EE}S_{EE}$
11	E	E	E	N_{EE}	N_{EE}	B_{EE}	$N_{EE}B_{EE}$
12	E	E	E	N_{EE}	N_{EE}	T_{EE}	$N_{EE}T_{EE}$
13	E	E	E	N_{EE}	N_{EE}	N_{EE}	$N_{EE}N_{EE}$

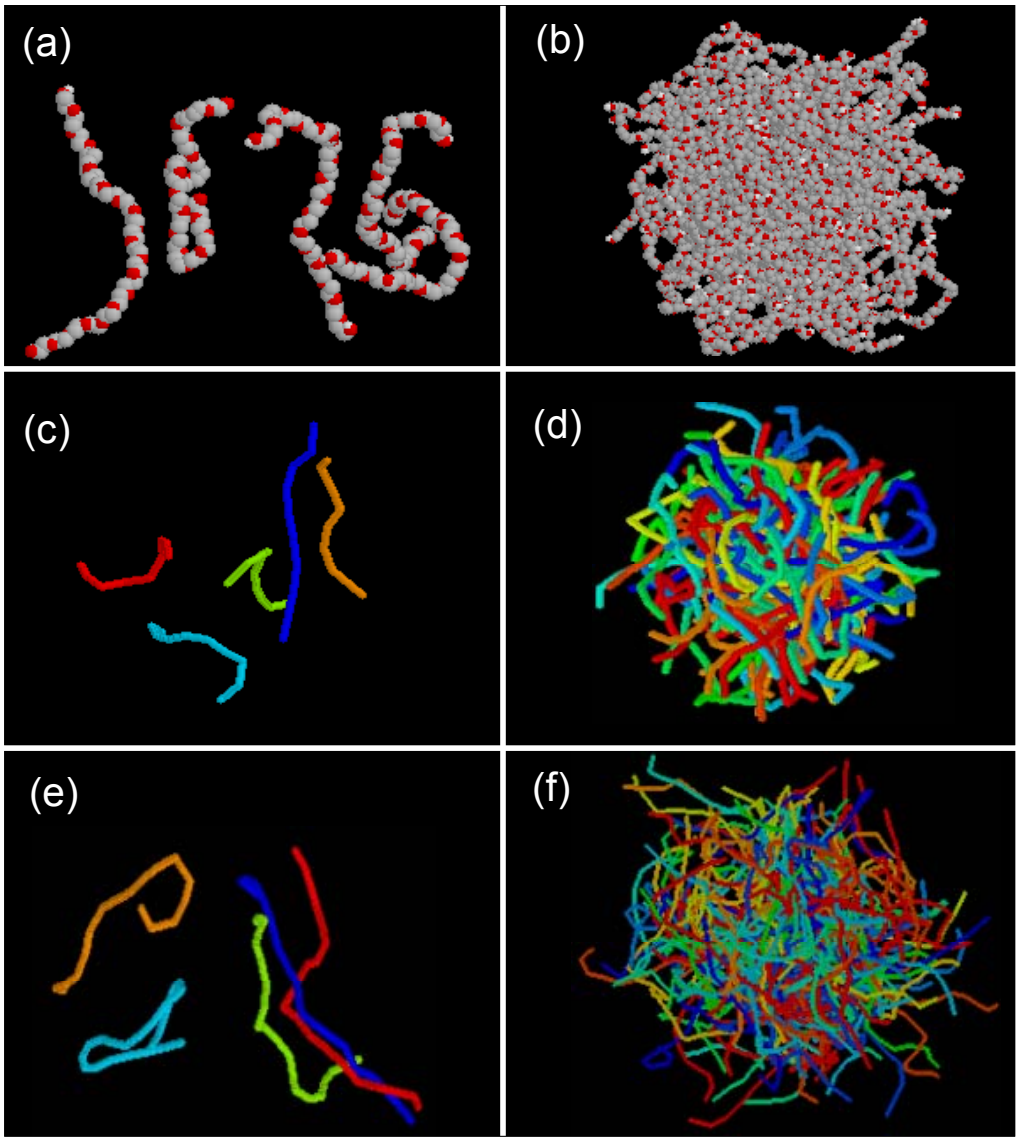

Figure 5.1. Snapshots of equilibrium configurations from atomistic ((a) and (b)) and CGMD ((c)-(f)) simulations at T = 353 K, p = 1 atm. (a) and (b): DP = 20; (c) and (d) DP = 20; (e) and (f): DP = 40. The atomistic and CG representations of PEG chains are shown in (a), (c) and (f), in which 5 molecules are taken from (b), (d) and (f) respectively.

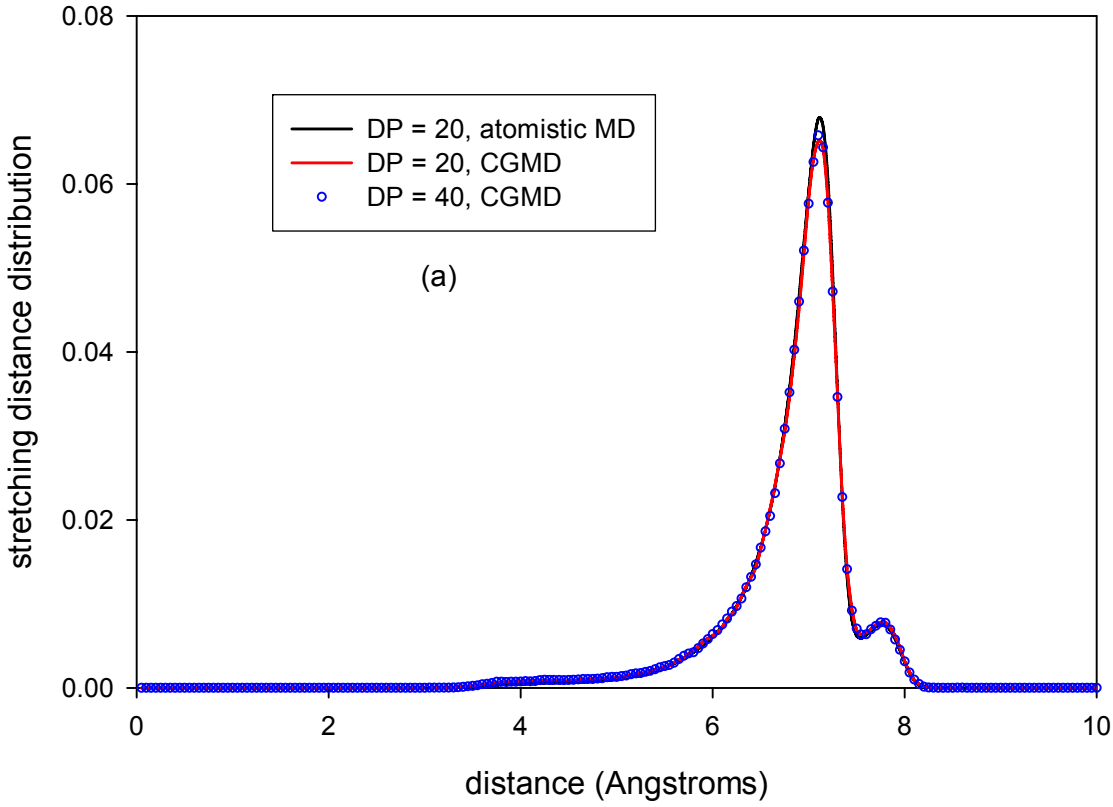

Figure 5.2. Bonded probability distribution functions for CG beads of PEG from atomistic MD simulations (DP=20) and CGMD simulations (DP=20 and 40). (a) Stretching. The GCMD simulations used the potentials from the OZPY^{-1}+IBI method.

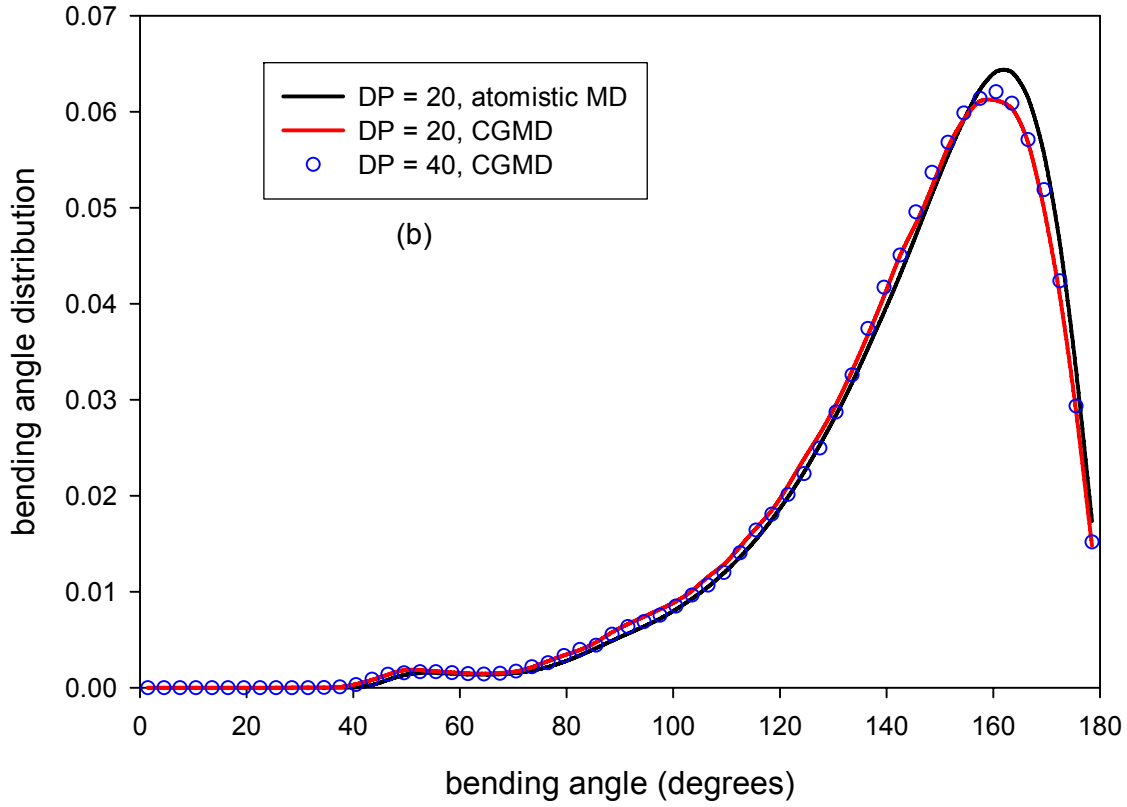

Figure 5.2. Bonded probability distribution functions for CG beads of PEG from atomistic MD simulations (DP=20) and CGMD simulations (DP=20 and 40). (b) Bending. The GCMD simulations used the potentials from the OZPY^{-1}+IBI method.

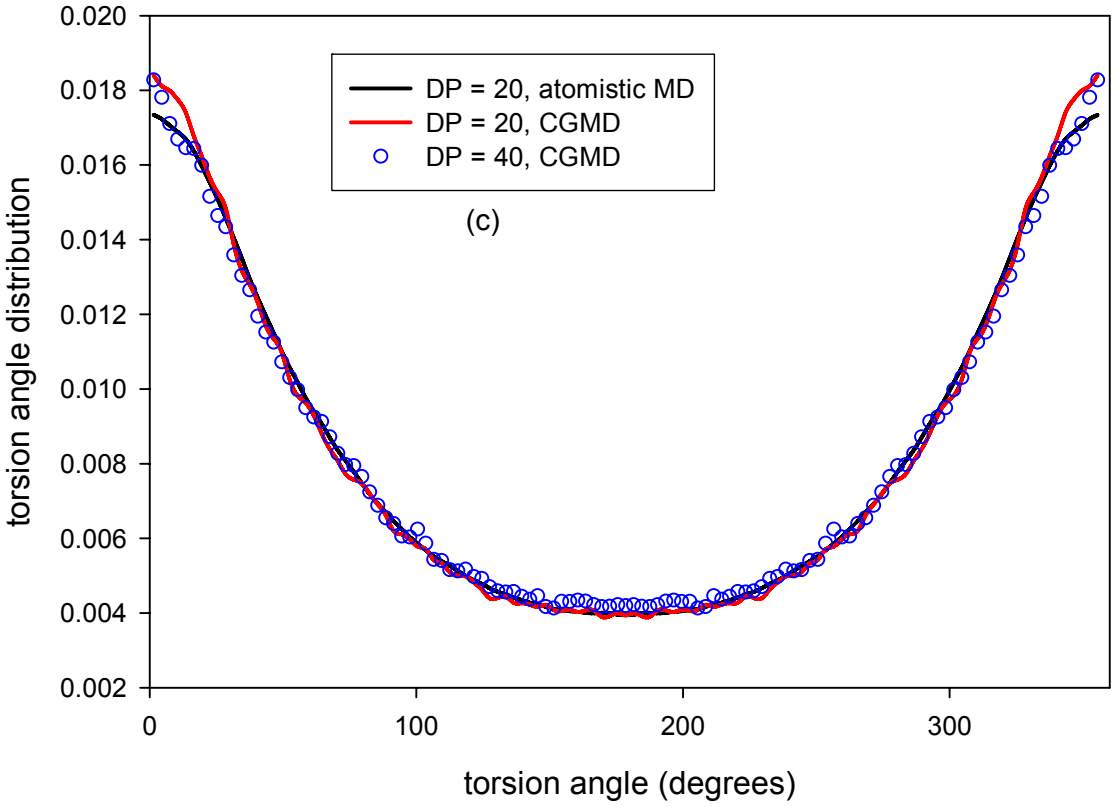

Figure 5.2. Bonded probability distribution functions for CG beads of PEG from atomistic MD simulations (DP=20) and CGMD simulations (DP=20 and 40). (c) Torsion. The GCMD simulations used the potentials from the OZPY^{-1}+IBI method.

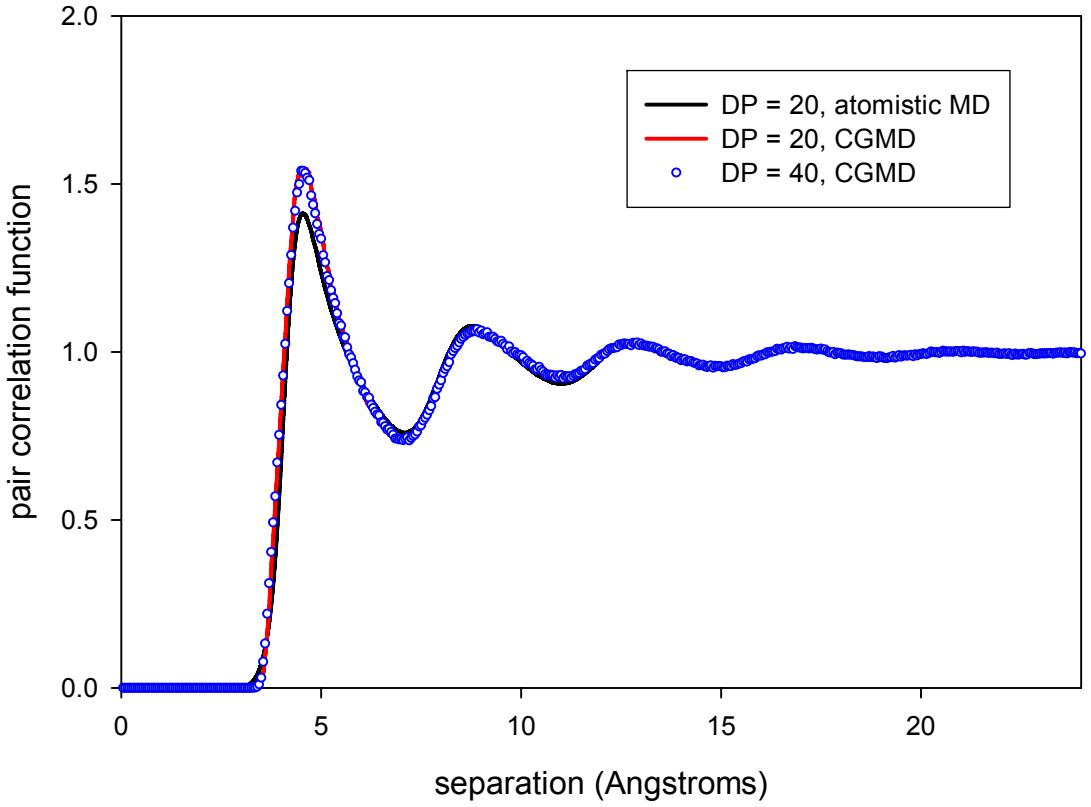

Figure 5.3. Nonbonded pair correlation functions for CG beads of PEG from atomistic MD simulations (DP=20) and CGMD simulations (DP=20 and 40). The GCMD simulations used the potentials from the OZPY^{-1}+IBI method.

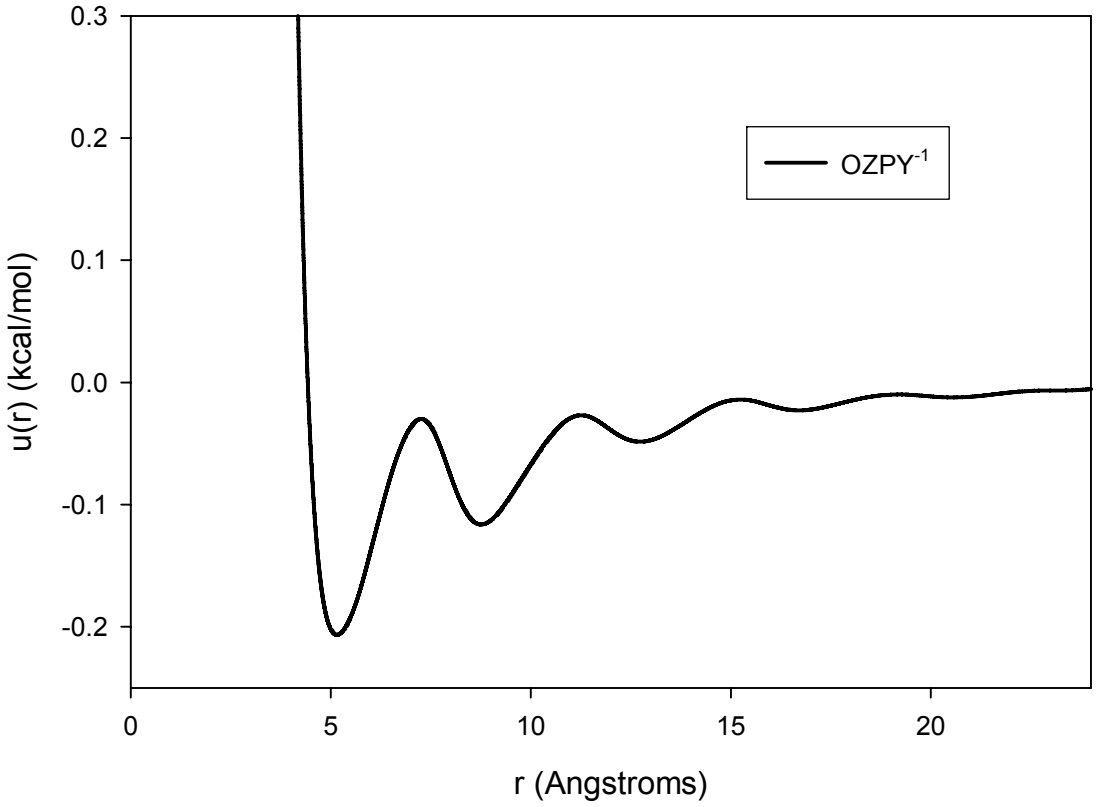

Figure 5.4. Coarse-grained nonbonded potential from the $OZPY^{-1}$ method.

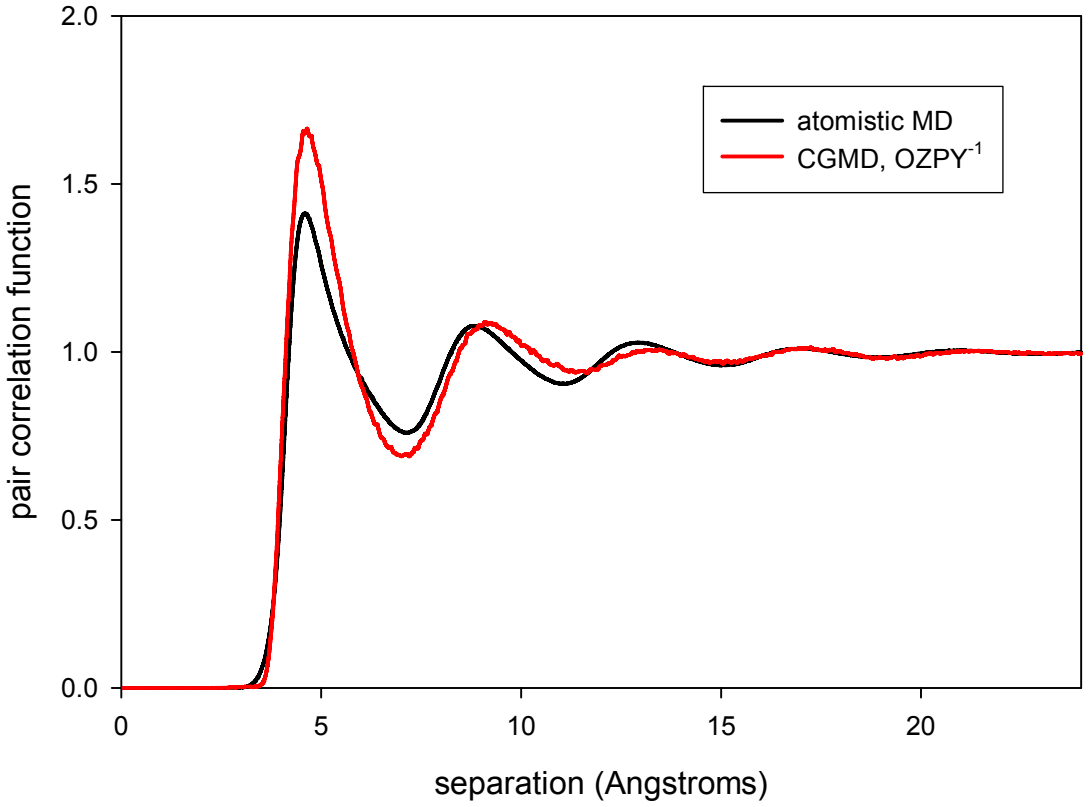

Figure 5.5. Comparison of CG nonbonded pair correlation functions for PEG (DP = 20) from atomistic and CGMD simulations, using the potential from the OZPY^{-1} method.

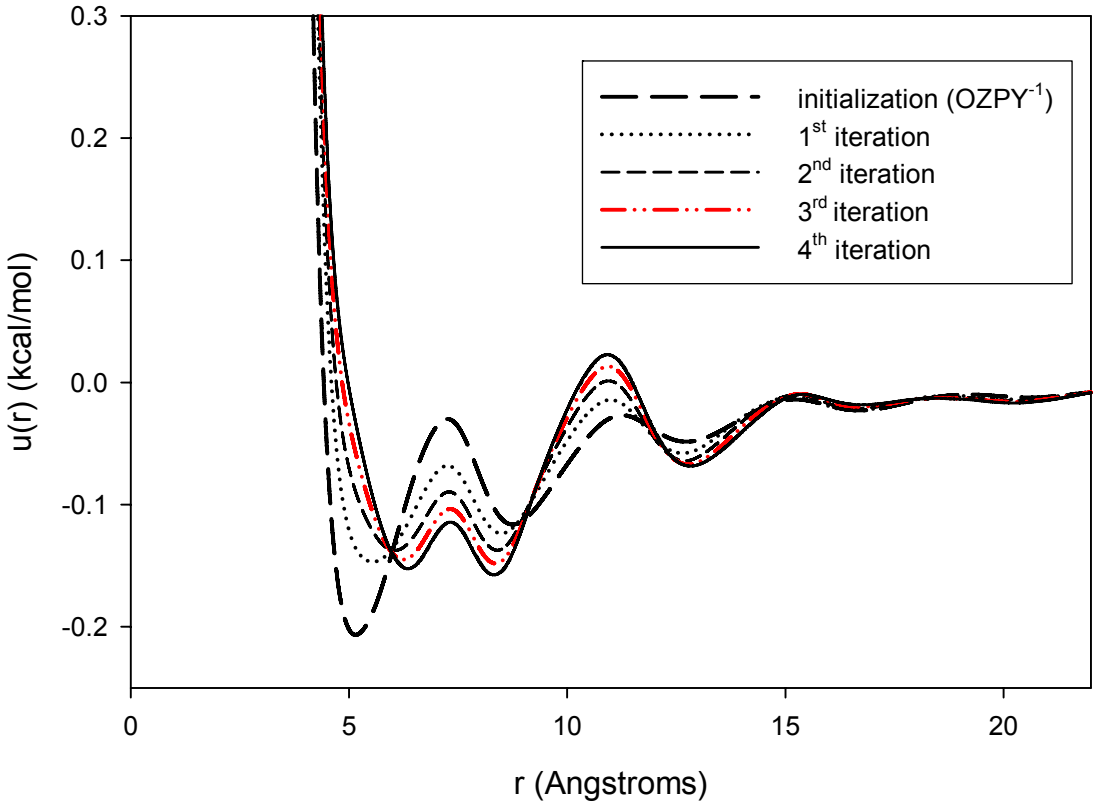

Figure 5.6. Coarse-grained nonbonded potentials for PEG (DP=20) from the OZPY^{-1}+IBI method. The potential from OZPY^{-1} (Figure 4) serves as initial guess for the IBI method.

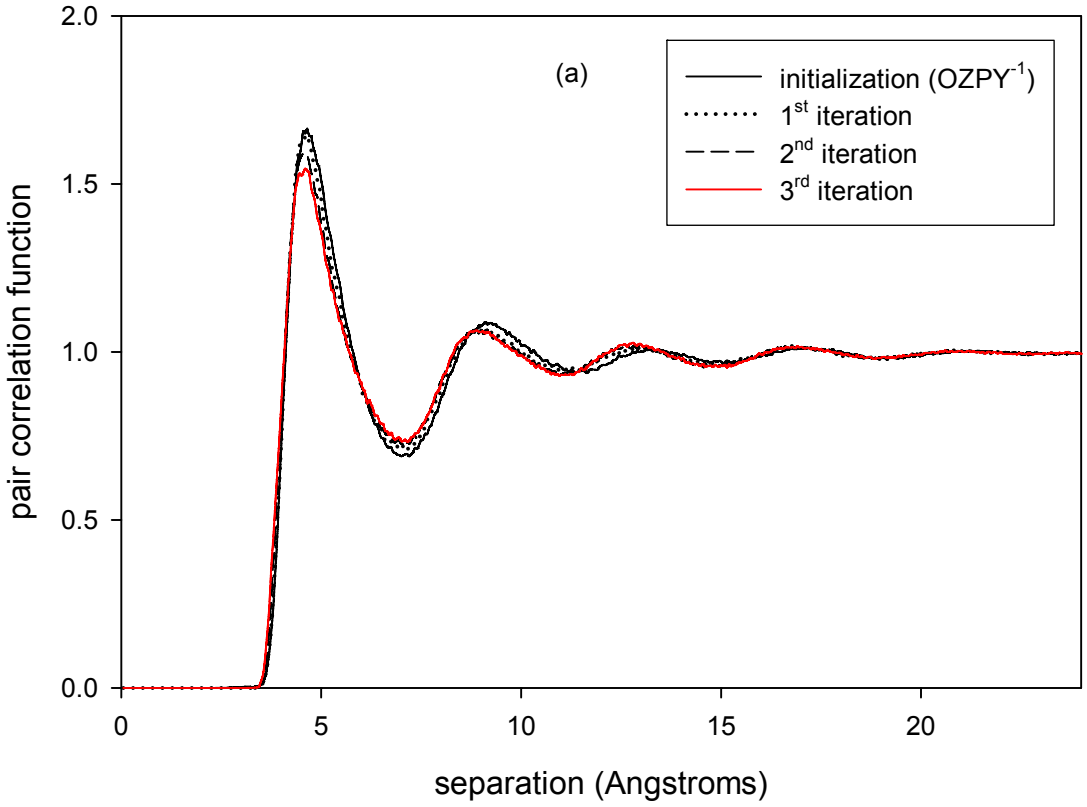

Figure 5.7. Comparison of CG nonbonded pair correlation functions for PEG (DP = 20) from atomistic and CGMD simulations. (a) There are substantial changes in the PCF for the first three iterations of the OZPY^{-1}+IBI method.

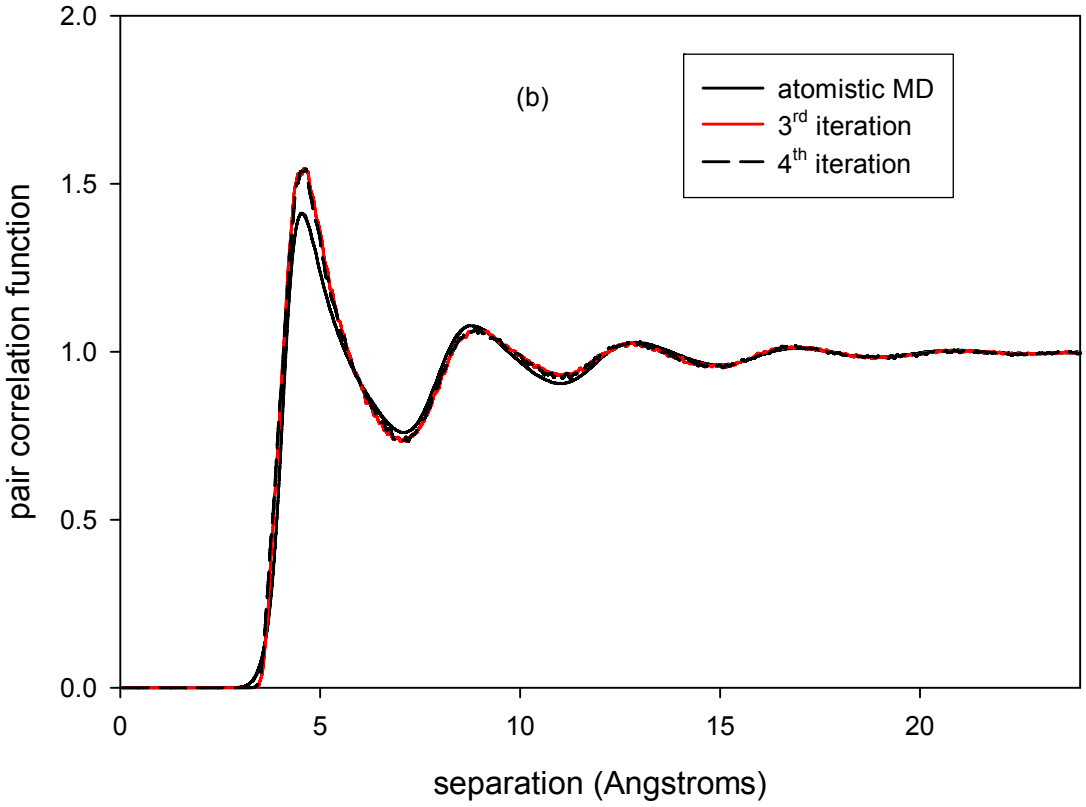

Figure 5.7. Comparison of CG nonbonded pair correlation functions for PEG (DP = 20) from atomistic and CGMD simulations. (b) The third and fourth iteration change little, although there is still discrepancy with the target PCF from atomistic simulation.

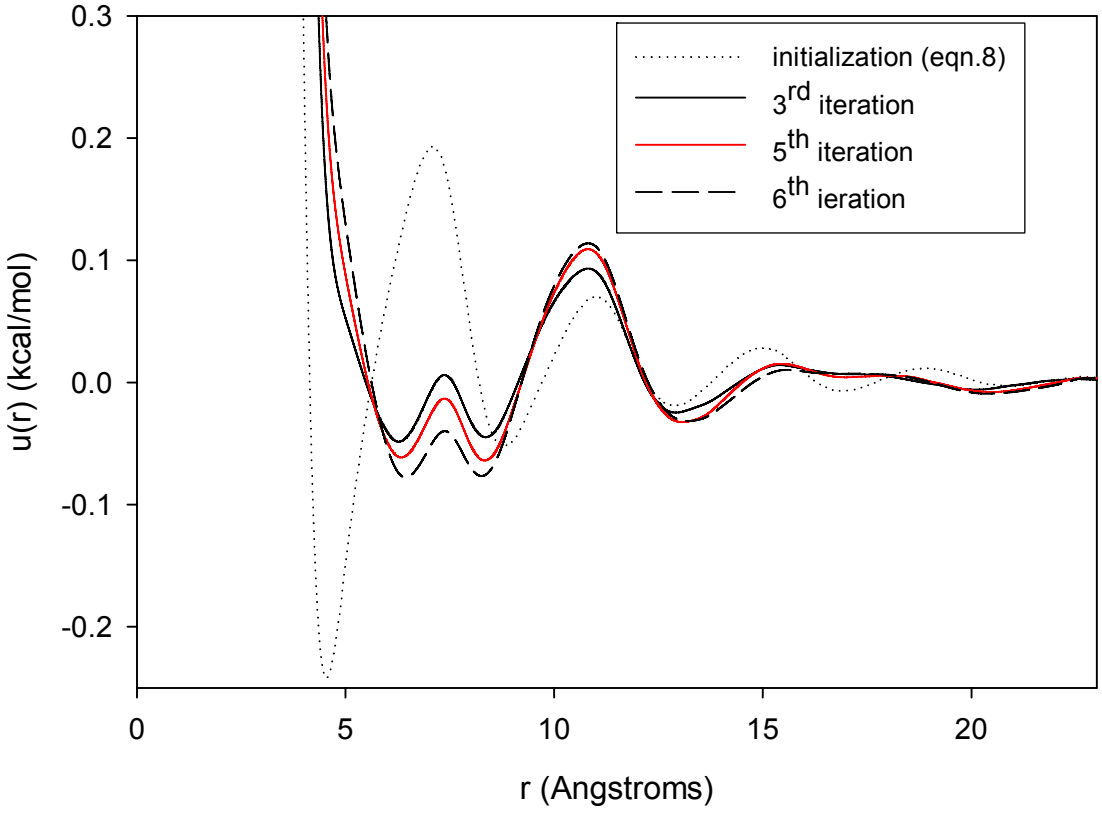

Figure 5.8. Coarse-grained nonbonded potentials for PEG (DP=20) from the IBI method. The potential from eqn.8 serves as initial guess for the IBI method.

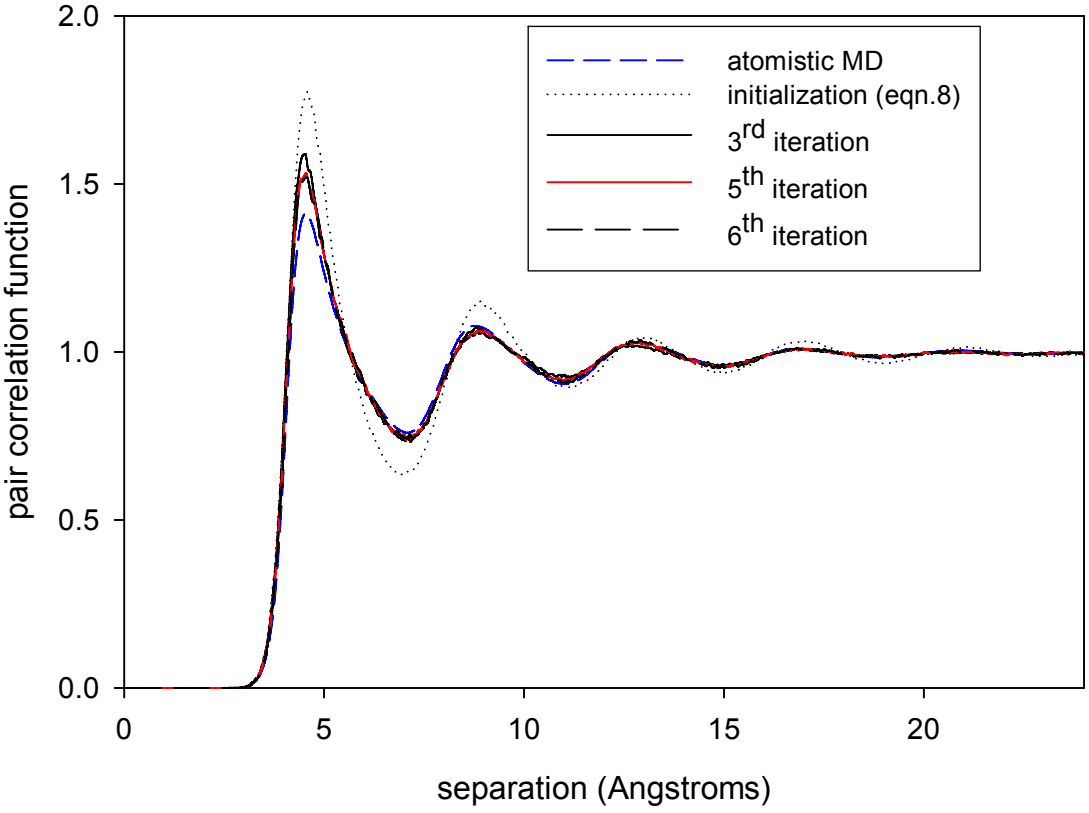

Figure 5.9. Comparison of CG nonbonded pair correlation functions for PEG (DP = 20) from atomistic and CGMD simulations. (a) There are substantial changes in the PCF for the first five iterations of the IBI method. (b) The fifth and sixth iteration change little, although there is still discrepancy with the target PCF from atomistic simulation.

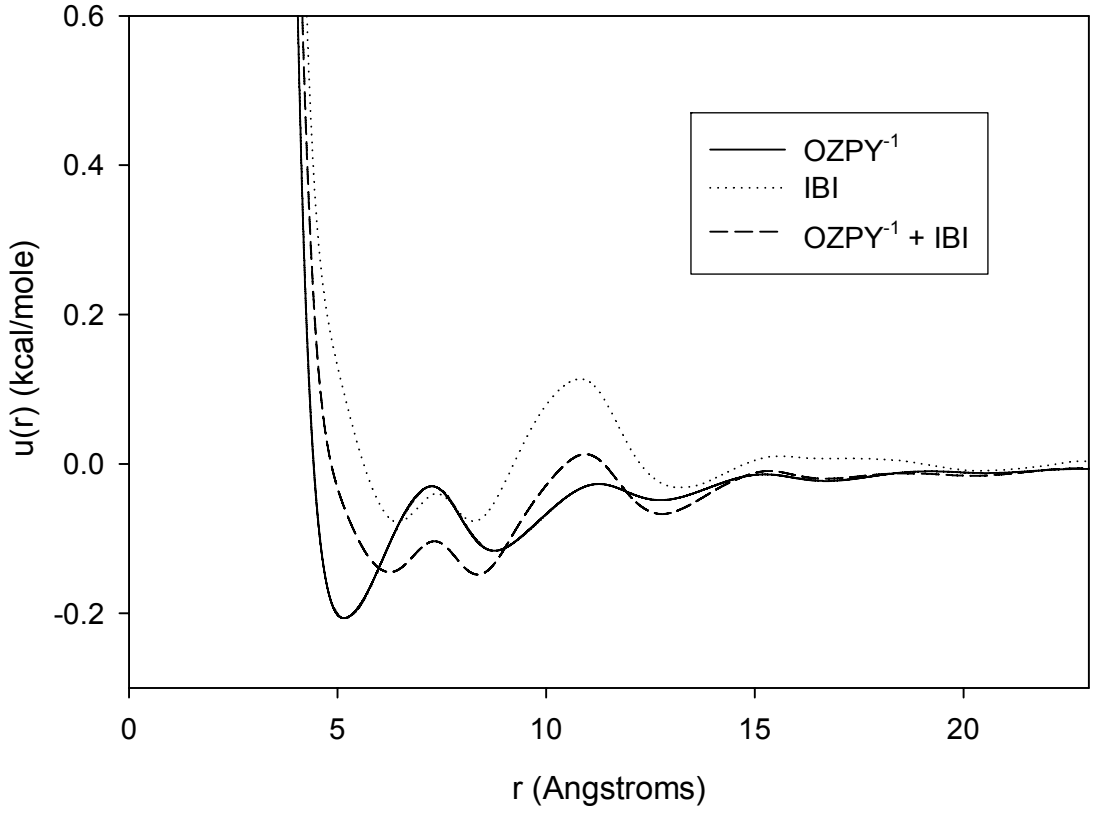

Figure 5.10. Comparison of potentials from $OZPY^{-1}$, IBI (the fifth iteration) and $OZPY^{-1}$ + IBI (the third iteration) methods.

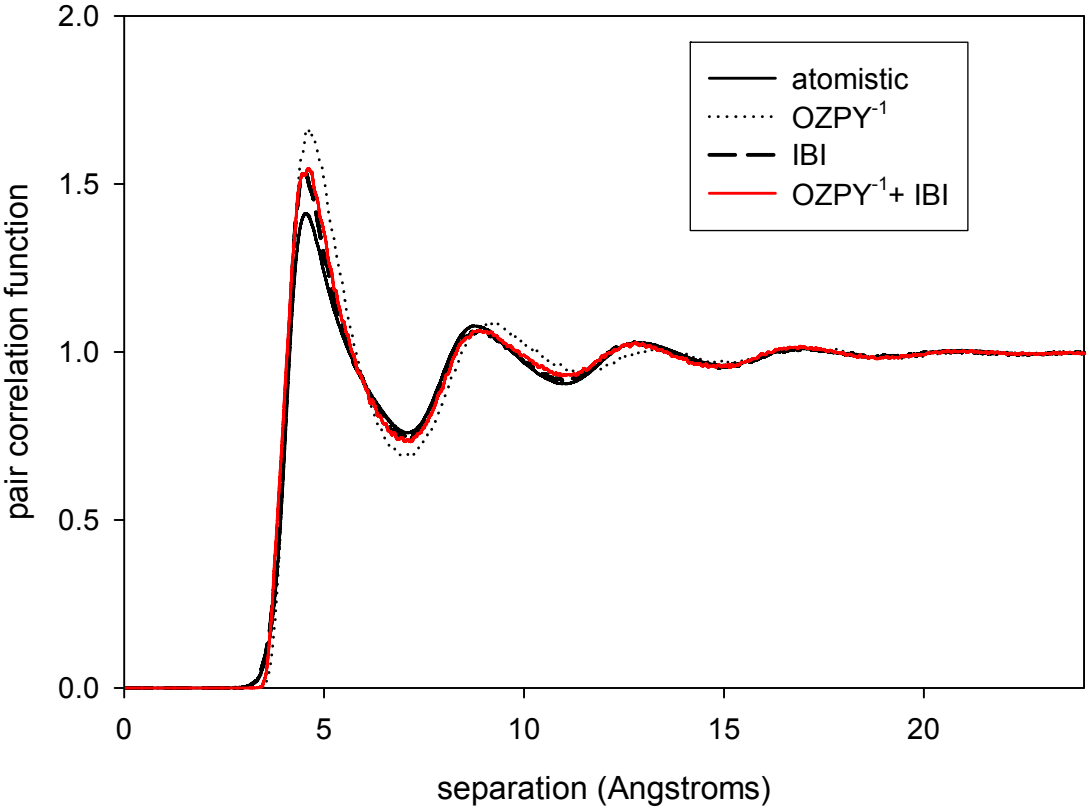

Figure 5.11. Comparison of Comparison of nonbonded pair correlation functions for PEG (DP = 20) system from atomistic and CGMD simulation using potentials from $OZPY^{-1}$, IBI (the fifth iteration) and $OZPY^{-1}$ + IBI (the third iteration) methods.

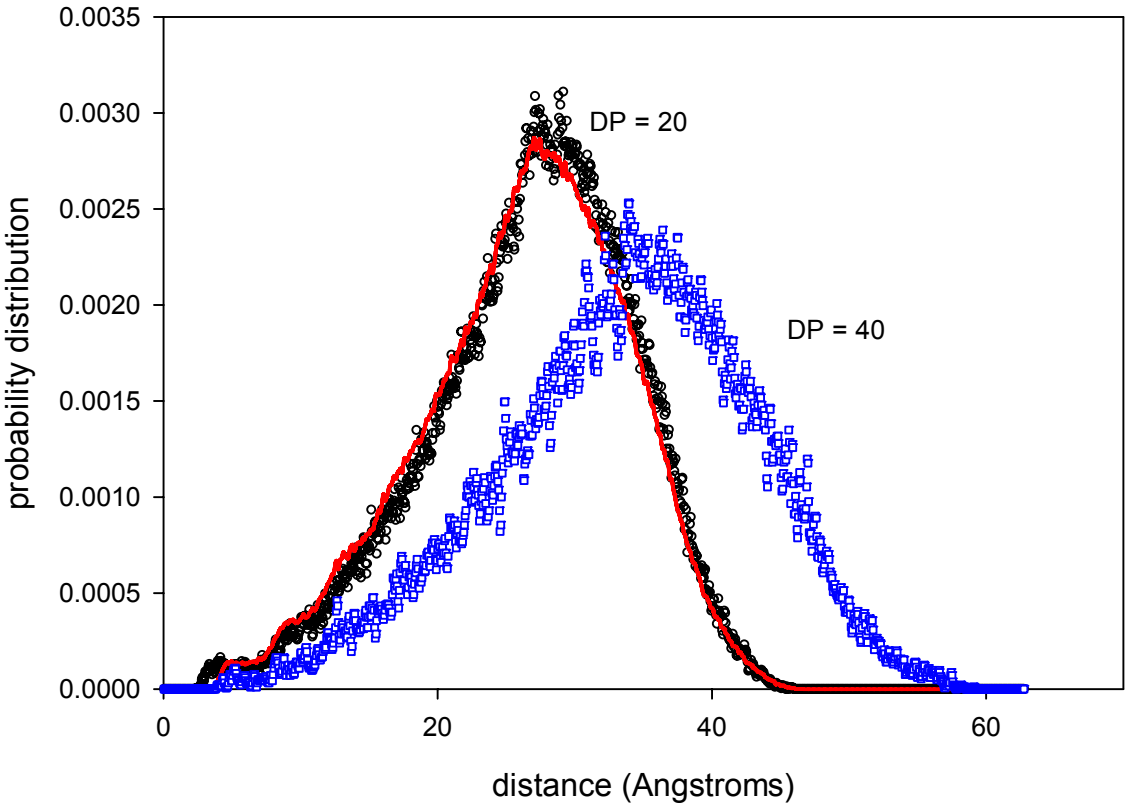

Figure 5.12. Comparisons of the chain end-to-end distance probability distributions for PEG with DP = 20 and 40 from CGMD. For DP = 20, the solid line represents the distribution from atomistic MD simulation.

CHAPTER 6

Multi-scale Models for Sulfonated Cross-linked Poly (1, 3-cyclohexadiene) (PCHD) Polymer

This chapter is a revised version of a paper (minor revisions to reflect its inclusion as a chapter in the dissertation) by the same title in preparation for a journal by Qifei Wang, David J. Keffer, Suxiang Deng and Jimmy Mays:

The use of "we" in this part refers to the co-authors and the author of this dissertation. My primary contributions to this paper include (1) all of the simulation work (2) analysis of data, and (3) most of the writing.

Abstract

Atomistic and coarse-grained (CG) models of Sulfonated Cross-linked Poly (1, 3-cyclohexadiene) (sxPCHD) were developed and implemented in Molecular Dynamics (MD) simulations of sxPCHD chains with different architectures. In the atomistic model, sxPCHD chains are cross linked by a sulfur-sulfur bond. Sulfonic acid groups are evenly distributed along the chain. The architecture is specifically aimed for application as a proton exchange membrane used in fuel cells. An atomistic force field for this architecture was tested and applied in the atomistic MD simulation of sxPCHD for the first time. The atomistic simulations generate the density and chain end-to-end distance distribution. To further study the structural properties of longer chain systems, a CG model was proposed. The bonded structural probability distribution functions (PDFs) and nonbonded pair correlation function (PCF) of the CG beads were obtained from the atomistic simulation results. The bonded CG potentials are obtained by simple inversion of the corresponding PDFs. The CG nonbonded potential is parameterized to the PCF using the Iterative Boltzmann Inversion (IBI) method. The CGMD simulations of sxPCHD chains using potentials from above method satisfactorily reproduce the structural properties from atomistic MD simulation of the same system. The transferability of the CG potentials has been further tested through CGMD simulation of sxPCHD melt with different architectures.

6.1 INTRODUCTION

Poly (1,3-Cyclohexdiene) (PCHD) polymers and their derivatives are of interest due to their unique chemical structure: the six-member rings and the isolated double bond in the main chain. The PCHD homopolymer has better thermal and chemical stability, mechanical strength and photochemical properties as compared to other common vinyl polymers.[1-5] PCHD block copolymers have shown unusual phase separation behavior.[6] This unique property has been further investigated through the recent development of PCHD-based proton exchange membranes.[7-9] The unique phase separation behavior of the PCHD homopolymer, PCHD/PEG (polyethylene glycol) blend and PCHD-PEG block copolymer membranes generate higher proton conductivity than that of the common Nafion membrane at high temperatures.[9] Such phase behavior and many other properties strongly depend on the conformation of the polymer in solution or bulk.[2,10] The experimental study of the conformation of PCHD is rare probably due to the lack of well-defined and well-characterized samples.[2] The computational study of polymer chain's conformation in solution or bulk is easy to be implemented with respect to the simplicity of defining a sample (in this case a molecule). However, due to problems at different length scales (10 to 100 nm approximately) in the membrane systems, a multi-scaling modeling technique is needed.

Molecular simulation has proved to be useful in the study of chain conformation when the length scale is less that 10 nm roughly.[11,12] In molecular simulation (either Molecular Dynamics or Monte Carlo simulation), the most important thing is a reliable force field. For common vinyl polymers, different force fields have been successfully applied in the molecular simulation.[13] For PCHD, no atomistic force filed has been developed and tested probably due to the complexity of the chain architecture.

An atomistic-level force field provides accurate simulation results but impairs the computation efficiency due to the number of degree of freedoms in the model. For example, many local interactions like bond stretching, bending and torsion have to be calculated to obtain the total potential energy. Meanwhile, a small step size has to be used for these high frequency modes. On the other hand, a polymer's relaxation time has strong chain length dependence. When chain length is small, the atomistic simulation is still tractable since the relaxation time is generally less than 100 ns. When chain length increases, the relaxation time increases

exponentially. The relaxation time of a long chain polymeric system could be in order of 1000 ns or longer. As a consequence, the atomistic simulation of long chain polymeric systems is no longer computationally feasible. Therefore, the application of classic molecular simulation technique is limited and integration with a coarser model is needed to break these limitations.

The coarse-grained (CG) technique removes computational limitations by eliminating some degrees of freedom in the atomistic model. This is done by grouping some atoms in the atomistic model together to "super atoms". These super atoms interact with their own potentials. Since the degrees of freedom are greatly reduced in the CG model, structural and transport properties of long chain polymers can be calculated directly by CG simulation at length scale from 10 to 100 nm. In the CG procedure, normally a fully atomistic (or united atom (UA)) simulation of short chains are conducted first. From the atomistic simulation, the CG structural distribution functions for different interactions modes assigned in the CG model are obtained. The CG potentials are then parameterized to these distribution functions. This part is challenging since the CG potentials are of no particular form. For bonded CG potentials, a simple Boltzmann inversion has been proved sufficient to generate potentials that reproduce the atomistic description of local structures if different CG bonded interaction modes are not correlated with each other. [14,15] For nonbonded CG interactions, different methods have been proposed to obtain the CG potentials. For example, adjusting power law type potential parameters (Lennard-Jones 12-6, 7-6, 7-4, 7-5, 8-6),[14-16] Ornstein-Zernike integral equation (IE) theory[12,17-20] and iterative Boltzmann inversion (IBI) method[21-25] are reported in the literatures of CG modeling of polymeric systems. Different methods have their advantages in the systems to which they are applied. Overall, the IBI method has the advantage to reproduce the structure of atomistic sampling compared to the other two methods especially when complicated nonbonded structures are obtained from the atomistic simulation.

Here, the aim of this work is to develop an atomistic and coarse-grained model of the PCHD homopolymer. In the CG model, CG beads are assigned with respect to its application as a proton exchange membrane material. The multi-scale modeling procedure is summarized as follows: first, atomistic MD simulations of a short-chain sulfonated cross-linked PCHD (sxPCHD) system is performed, from which bonded probability distribution functions (PDFs) and nonbonded pair correlation function (PCF) were obtained. Second, these structural results

from the atomistic simulations were used to generate CG potentials, using Boltzmann inversion for bonded modes and the IBI method for nonbonded modes. Third, the CG potentials are implemented in CGMD simulations of the same system, from which the bonded PDFs and nonbonded PCFs can be obtained and directly compared with those from the atomistic simulation. Finally, we performed CGMD simulations of longer-chain cross-linked PCHD systems to test transferability of the proposed model.

6.2 SIMULATION METHOD

6.2.1 Atomistic simulation of sxPCHD with two chains cross-linked.

We combined the OPLS-AA[26,27] and the OPLS-UA[28] (for hydrocarbon groups CH_2 and CH) force field to describe the intra-molecular and inter-molecular potential of sxPCHD molecules. In the combined potential model, OPLS-AA potential forms are used with most of the force field parameters are taken from either the OPLS-UA or OPLS-AA force fields for hydrocarbons. When necessary, some of the parameters for bond bending, bond torsion and nonbonded potentials are taken from the simulation work of Nafion,[29-31] poly(ethylene oxide) sulfonic acid anion,[32] polyvinyl chloride (PVC)[33] and $C_3H_7SO_3H$,[34] while the potential forms are transformed to that of the OPLS-AA. The complete details of the force field parameters can be found in the supplementary information document. The spherically truncated charge-neutralized method developed by Wolf *et al.*[35] is used to evaluate the electrostatic energy. We simulated in the isobaric-isothermal (NpT) ensemble and implemented the Hamiltonian-based thermostat and barostat[36] with controller frequencies set to 10^{-4} fs^{-1}. The XI-RESPA NPT algorithm developed by Tuckerman *et al.*[37] was used to integrate the equations of motion. The large time step was 2 fs and the small time step was 0.2 fs. The parallel code was built in-house and was written in FORTRAN-90, using MPI for inter-processor communication. It has been tested rigorously across a variety of applications. The cut-off distance used was 15 Å for the atomistic simulation. For all the simulations in this work, we used 64 chains. The state point was set at 1 atm and 353 K, corresponding to future fuel cell application. Following the equilibration procedure described elsewhere,[12,22] we estimated the initial density and placed the particles in the simulation volume, avoiding significant overlap. We started with a higher temperature then

gradually decreased the temperature and equilibrated to the correct density. Data production followed and lasted for at least 10 ns.

6.2.2 CGMD simulations of sxPCHD with two chains and three chains cross-linked.

We propose that PCHD can be modeled at a coarse-grained level with assignments of CG beads shown in Figure 6.1, which corresponds to three monomer units of PCHD chains (bead A, B and C) and two cross-linkers (D) at the two ends. The stoichiometry of the A, B, C and D components corresponds to PCHD that has been experimentally synthesized in the laboratory.[9] The molecular fragments of each CG bead is shown in Figure 6.1. The mapping to CG bead is based on center of mass positions of the molecular fragments.

In order to construct PCFs for the coarse-grained beads from the short-chain atomistic simulations, the bead is placed at the center-of-mass of the atoms in the corresponding fragment, a convention that is adopted in most CG mapping schemes.[12,25] This model contains a great reduction in the number of degrees of freedom while at the same time it does not lose too many of the structural details of the atomistic chain conformations. The detailed structure is important for future study on the application of proton exchange membrane. In the CGMD simulations, two kinds of molecular architectures (two chains and three chains cross-linked) are investigated as shown in Figure 6.1.

In this model, the CG interaction modes include bond stretching, bond bending, bond torsion, and nonbonded interactions for both intra-molecular (for beads separated by at least four bonds) and inter-molecular pairs. The same CG nonbonded potential is used for both intra-molecular and inter-molecular interactions. Probability distribution functions (PDFs) for stretching, bending, torsion and nonbonded pair correlation functions (PCFs) between CG beads were generated from the atomistic simulations. In the development of coarse-grained (CG) bonded potentials, there are straightforward approximations that relate the interaction potential directly to the PDFs through eqn. 1. The effective bonded interaction potential between a particle of type α and a particle of type β, $\varphi_{\alpha\beta}$, as a function of the separation between particles, r, can be related to the PDF, $g_{\alpha\beta}(r)$, via[12,14,15]

$$\varphi_{\alpha\beta}(r) = -k_B T \ln\left(g_{\alpha\beta}(r)\right) + c_{\alpha\beta} \quad (1)$$

where k_B is Boltzmann's constant, T is temperature and $c_{\alpha\beta}$ is a constant to set the potential minimum to zero. Note here that the coordinates need to be changed for the bending (from *r* to θ (bending angle)) and torsion (from *r* to ϕ (torsion angle)) modes. In this work, we use the form of the bonded potentials from eqn. 1. Note here eqn. 1 is subject to the assumption that all the bonded interactions are independent of each other and of the nonbonded potential.[15] One straightforward way to show this independence is simply to show that the CG simulations using the CG potentials generate PDFs that agree with those obtained from the atomistic simulations.

The nonbonded potential for intra-molecular (for beads over four bonds) and inter-molecular interactions is generated by the IBI method.[21] In the IBI method, a tabulated potential is numerically determined by simulation iteration. The interaction potential is refined iteratively via

$$\varphi_{\alpha\beta,i+1}(r) = \varphi_{\alpha\beta,i}(r) + k_B T \ln\left(\frac{g_{\alpha\beta,i}(r)}{g_{\alpha\beta}(r)}\right) \tag{2}$$

with initial guess

$$\varphi_{\alpha\beta,0}(r) = -k_B T \ln\left(g_{\alpha\beta}(r)\right) \tag{3}$$

where $g_{\alpha\beta}(r)$ is the target PCF, which is from atomistic simulation. The challenging part of this method is obtaining PCFs from CG simulations iteratively. Convergence is slow especially in the CG models that include different CG beads. In this work, there are 10 nonbonded interactions modes (AA, AB, AC, AD, BB, BC, BD, CC, CD and DD). Generally, each mode takes 3 to 5 iterations to reproduce the structure of atomistic sampling, which is chosen to stop the iteration cycle. Each iteration takes 5 to 6 hours to obtain reliable PCFs. The whole procedure took about 3 weeks.

We also explored using the inverse Ornstein-Zernike equation with the Percus-Yevick approximation ($OZPY^{-1}$) procedure to obtain the CG potentials.[12,19] This method, which works well for $-(A\text{-}B)_n-$ architecture (like PET), had difficulty in finding a "mean" potential for a given bead type. For example in PCHD, beads of type C, are found in multiple local environments: (i) bound to two A beads, (ii) bound to one A and one B bead, or (iii) bound to one B and one D bead. (See Figure 6.1.) The $OZPY^{-1}$ procedure did not easily handle these multiple

environments for a given bead type. The IBI procedure was able to deliver a reasonable potential, despite this additional level of disorder within the chain.

After obtaining all the CG potentials, we performed CGMD simulations for PCHD systems with two chains and three chains cross-linked and compared the structures from these simulations with that of atomistic simulation. In the CGMD simulations of the shor chain cross-linked system, we used the same density and number of chains as that used in the atomistic simulation of the same polymer. For the longer chain cross-linked system, we estimated the initial density and placed the particles in the simulation volume carefully with proper bond length and angles, then gradually introduced the nonbonded interactions to avoid overlap, as has been done before.[12] We again simulated in the isobaric-isothermal (NpT) ensemble under the same pressure and temperature as the atomistic simulation. The cut-off distance used is 25 Å for this level simulation compared with 15 Å used in atomistic level simulation due to some features on the PCFs in the long range. The time steps of CGMD simulation are the same as those used in the atomistic MD simulation. Using bigger time steps impacts the conservation of Hamiltonian. In this case, the computational speed up is due strictly to the reduction in degrees of freedom. Based on wall-clock time, the CGMD simulations are approximately 300 times faster than the atomistic simulations. (We note that the atomistic simulations are not completely atomistic since we did employ a united atom description of CH_x groups. Had we done so, the speed-up would have been even greater.)

6.3 RESULTS AND DISCUSSION

In this section, we discuss (1) the results of the atomistic MD simulation of PCHD with two chains cross-linked system, (2) CG potentials from the IBI methods and (3) CGMD simulation results for PCHD with short chains and long chains. Finally, we compare the structural distribution functions from CGMD simulations with that of atomistic simulation.

In Figure 6.2, we show equilibrated snapshots from both the atomistic and the CGMD simulations. In Figure 6.2(b), (d) and (f), all molecules are shown to make it clear that we are simulating a dense melt. In Figures 6.2(a), (c) and (e), all but five chains are rendered invisible to better indicate the conformation of the individual chains. Because the atomistic simulation of the short chain cross-linked system and CG simulations of the long chain cross-linked systems

were run in the NpT ensemble, the density is an output. The output equilibrium densities of the two chains and three chains systems are respectively 1.195 and 1.192 g/cm^3. There is no experimental value reported for cross-linked or bulk PCHD polymers. The above densities generated are close to the findings of other polymeric systems with phenol ring embedded in the main chain.[12,22] Further comparison with the experimental density can be done when experimental density data is available.

6.3.1 Atomistic MD simulation of short chain cross-linked sxPCHD

In Figure 6.3, we show the bonded stretching distributions of the CG beads obtained from atomistic simulation. These distribution functions are based on the analysis of configurations from atomistic MD simulation. As shown in Figure 6.1, these distribution functions are calculated according to the center of mass position of CG beads. The stretching mode displays a bimodal distribution for modes AC and BC, with the major peak centered at 4.2 Å and 4.4 Å respectively, and the smaller peak centered at 5.4 Å and 5.3 Å respectively. The smaller peaks are probably caused by the asymmetric nature of the AC and BC stretching modes. Beads A and B are much heavier than C. For modes DD and CD, we observe a single peak behavior.

The bending angle distributions are shown in Figure 6.4. The bending angle distributions BCD, ACA and ACB shows a single asymmetric peak centered at 157˚, 155˚ and 150˚ respectively. The bending mode CAC shown a symmetric peak centered at 110˚. The mode CBC shows a bimodal distribution with two peaks centered at 100˚ and 130˚. The mode CDD shows an asymmetric distribution with center at 90˚.

In Figure 6.5, the torsion angle distributions ACAC, CBCD and CDDC show a single symmetric peak centered at 0˚ while the distributions of ACBC, BCDD and BCAC show multiple peaks. The features of these CG bonded distributions imply the complexity of structures of cross-linked PCHD systems, even at the CG level where some of the local atomistic structures have been neglected.

The nonbonded PCFs of the CG beads obtained from the atomistic simulations are shown in Figure 6.6. The PCFs shows multiple peaks with the first peaks centered between 6 Å and 8 Å. In the CG model proposed in this work, bead A has a sulfonic acid group while bead B has both sulfonic acid and hydroxyl groups on it. The existence of these side groups caused more correlations at short range for AA, AB, BB and BD pairs, which are reflected in the higher

intensities of these peaks. Note here the nonbonded PCF in this work include both intramolecular (for CG beads over four bonds) and intermolecular parts, where the CG nonbonded potentials based on these PCFs will be used. In this way, to a large extent we mimic the way nonbonded potentials are modeled at the atomistic level.

6.3.2 Generation of CG potentials and CGMD simulation of short chain cross-linked sxPCHD

Based on the bonded distribution functions obtained from the analysis of configurations from atomistic simulation, we obtained the bonded stretching, bending and torsion CG potentials through eqn. 1. These potentials are shown in the supplementary information document. As noted above, eqn. 1 is subject to the assumption that all the interactions are independent of each other. Validation of the assumption can be done through direct comparison of the PDFs from the atomistic and CG simulations, as shown below. Further understanding of the statistical interdependencies of the different bonded interaction modes can be found in the literature.[15] Note here that the IBI method can also be applied for the bonded modes. although that procedure was not used in this work.[21,25] The following results on the comparison of the PDFs from the atomistic and CG simulations were deemed sufficiently acceptable to proceed without further iteration.

In Figures 6.3 through 6.5, we compare the bonded PDFs from the CGMD simulations of short chains cross-linked PCHD with that of the atomistic simulation. The agreement in the stretching distribution from the atomistic and CG descriptions is relatively good, capturing the position and magnitude of all the major peaks. The comparison of the bending and torsion distribution is also very good capturing the correct position and magnitude of the peaks. This is indicates that there is no strong interdependencies between the bonded CG modes. In short, the bonded PDFs from the two level simulations match relatively well, providing evidence that the assumption of independence between the modes invoked for eqn. 1 is well-founded.

The nonbonded potentials are generated through the IBI method. Compared to the other methods of obtaining the nonbonded CG potentials, the IBI procedure has the advantage of reproducing the atomistic simulation structures. It impacts computational efficiency since each iteration requires a new CGMD simulation. However, if the iteration is done on relatively short chains, the exercise is still tractable. For example in this work, to obtain the PCF from CGMD

simulation of the PCHD (short chains cross-linked) system, each IBI iteration required 96 processor-hours on a cluster (6 hours using 16 processors) to finish a run of 5 ns. During the IBI procedure, the agreement between the PDFs of the bonded modes is not impacted by the procedures used here to generate the nonbonded potential. The bonded distributions for all iterations (not shown) are virtually the same as those presented above. This implies that there is no significant correlation between the bonded modes and nonbonded modes.

The nonbonded PCFs from CGMD simulation using CG potentials from last iteration of the IBI method along with that from atomistic simulation are shown in Figure 6.6. A good match is observed for all PCFs from the two level simulations. For some modes like AA, BC and CC, the agreements are nearly perfect. A small discrepancy exists on the comparison of PCFs for some modes (DD and CD). As has been noted previously, the PCF is not extraordinarily sensitive to changes in the potential.[17] Therefore, the inverse procedure suffers from some insensitivity to features with signal strengths commensurate with the statistical noise of the simulation. Another possible reason could be the existence of weak correlations between some of the nonbonded modes.[38] Further iterations will not significantly help improve the agreement between the PCFs obtained from the atomistic and CG simulations.

In Figure 6.7, we show the non-bonded interaction potentials from the last iteration of IBI method. The potentials are shifted to reach zero at cut-off distance. These potentials have multiple minima due to the features of corresponding PCFs. It is interesting to compare these potentials from the one used in atomistic simulation. In nonbonded potentials used in atomistic simulations one typically does not observe repulsion beyond that which is known at short-distances due to electron-electron repulsion. The PCFs can be qualitatively generated from physically meaningful potentials, such as a LJ 12-6 potential, where the repulsion term represents electron-electron repulsion and the attractive term represents induced-dipole-induced-dipole interactions. The pairwise potential gives rise directly to the first peak in the PCF. Subsequent peaks arise due to pairwise interactions involving two particles that are not the central particle. In this case, the potentials generated through IBI method are only effective potentials to reproduce the structure from atomistic sampling at the thermodynamic state specified. Their transferability to different thermodynamic states needs to be further tested. Recently, there are more interests on testing the transferability of CG potential to mixtures[24,25,39]

or different chain length.[25] In this work, the test of transferability of CG potential to different chain length (or density) is necessary since the objective of this project is to study the structure of long chain PCHD systems. We will address this issue in the following section.

6.3.3 Structural Properties of short and long chain cross-linked sxPCHD

One of the major tasks of this work is to generate a CG force field that can be used to study the structure of long chain systems. To test the transferability of CG models proposed for cross-linked PCHD system, we apply this model to a different network structure, namely three PCHD chains cross-linked. (See Figure 6.1.) We notice here this molecular architecture is relatively simple compared to the real polymer network structure. The simplicity nevertheless captures the effect of an increase in chain length. Since nothing but the total chain length is increased, significant changes in the structures from short chains and long chain cross-linked systems are not expected.

With the above CG potentials, we simulated short chain and long chain cross-linked PCHD. The snapshots are shown in Figure 6.1(c) to (f). The bonded PDFs and nonbonded PCFs along with those of atomistic MD simulation are shown in Figures 6.3 through 6.6. For the three bonded modes, the distribution function of CGMD simulation of two chains and three chains cross-linked systems match very well with that of atomistic simulation.

In Figure 6.6, the nonbonded PCFS from CGMD simulation match well with that of atomistic simulation and also shows no apparent chain length dependence. To this end, we have shown that newly proposed CG model of sxPCHD can be used to study the structures of sxPCHD with different network structures.

Having done the validation of the CG model on the reproduction of conformations from atomistic sampling, we can further investigate other physical properties from CG simulation of cross-linked PCHD system by using this model. In Figure 6.8, we show the distribution of chain end-to-end distance for two chains (black line) and three chains cross-linked (data points) systems from CGMD simulation. The chain end-to-end distance distribution from atomistic sampling (red line) is also presented in Figure 6.8. The end-to-end distance is defined as the distance between the two cross-linkers DD groups at the two ends of a single chain. The end-to-end curves in Figure 6.8 roughly show a Gaussian-like distribution. For the short chain cross-lined system, the comparison of end-to-end distance distributions from the two level (Atomistic

and CG) simulations is relatively good. This is further evidence that the CG model is able to capture the chain conformation of the atomistic description (at the end-to-end level). On the comparison end-to-end curves of two chains and three chains cross-linked systems, no significant change is observed, as expected. As shown in Figure 6.1, nothing changed between the two cross-linkers for two chain and three chains cross-linked systems.

6.4 CONCLUSIONS

Atomistic and coarse-grained (CG) models of Sulfonated Cross-linked Poly (1, 3-cyclohexadiene) (sxPCHD) were developed and implemented in Molecular Dynamics (MD) simulations of PCHD chains with different architectures. In the atomistic model, two PCHD chains are cross linked by sulfur-sulfur bonds. Sulfonic acid groups are evenly distributed along the chain. An atomistic force field for this architecture was tested and applied in the atomistic MD simulation of bulk PCHD for the first time. Meanwhile a CG model was proposed. The bonded structural probability distribution functions (PDFs) and nonbonded pair correlation function (PCF) of the CG beads were obtained by analyzing the atomistic simulation results. The bonded CG potentials are obtained by simple inversion of the corresponding PDFs. The CG nonbonded potential is parameterized to the PCF using the Iterative Boltzmann inversion (IBI) method. The CGMD simulations of the cross-linked PCHD system using potentials from the above method satisfactorily reproduce the structural properties from atomistic MD simulation of the same system. The new CG model was further tested through CGMD simulation of a long chain cross-linked PCHD system. No significant changes are observed on the comparison of PDFs and PCFs from CGMD simulations of two chains and three cross-linked systems, which means the potentials are transferable to other chain lengths. The new CG model can be further applied to study the structure and dynamics of PCHD longer chain network system through CG simulations. The study of structure of hydrated PCHD membrane is underway.

6.5 ACKNOWLEDGMENTS

This research was supported by a grant from the National Science Foundation (DGE-0801470). This research project used resources of the National Institute for Computational Sciences (NICS) supported by NSF under agreement number: OCI 07-11134.5.

References

[1]I. Natori, K. Imaizumi, H. Yamagishi, and M. Kazunori, J. Polym. Sci., Part B: Polym. Phys. **36**, 1657 (1998).

[2]S. I. Yun, K. Terao, K. L. Hong, Y. B. Melnichenko, G. D. Wignall, P. F. Britt, and J. W. Mays, Macromolecules **39**, 897 (2006).

[3]I. Natori and S. Natori, J. Polym. Sci., Part A: Polym. Chem. **47**, 2132 (2009).

[4]I. Natori, S. Natori, and K. Ogino, Macromolecules **42**, 1964 (2009).

[5]I. Natori, S. Natori, and H. Sato, Polymer **47**, 7123 (2006).

[6]J. L. David, S. P. Gido, K. L. Hong, J. Zhou, J. W. Mays, and N. B. Tan, Macromolecules **32**, 3216 (1999).

[7]K. Hong, P. F. Britt, and J. W. Mays, Polym. Prepr. (Am. Chem. Soc., Div. Polym. Chem.) **45**, 311 (2004).

[8]K. Hong, M. Liu, and J. W. Mays, Polym. Prepr. (Am. Chem. Soc., Div. Polym. Chem.) **44**, 657 (2003).

[9]J. W. Mays, S. Deng, K. A. Mauritz, M. K. Hassan, and S. P. Gido, Patent No. US20090306295A1 (2009).

[10]S. I. Yun, K. Hong, Y. B. Melnichenko, G. D. Wignall, and J. W. Mays, Polym. Prepr. (Am. Chem. Soc., Div. Polym. Chem.) **47**, 620 (2006).

[11]K. Kremer, Macromol. Chem. Phys. **204**, 257 (2003).

[12]Q. F. Wang, D. J. Keffer, D. M. Nicholson, and J. B. Thomas, Macromolecules **43**, 10722 (2010).

[13]Q. F. Wang, D. J. Keffer, S. Petrovan, and J. B. Thomas, J. Phys. Chem. B **114**, 786 (2010).

[14]V. A. Harmandaris, N. P. Adhikari, N. F. A. van der Vegt, and K. Kremer, Macromolecules **39**, 6708 (2006).

[15]V. A. Harmandaris, D. Reith, N. F. A. Van der Vegt, and K. Kremer, Macromol. Chem. Phys. **208**, 2109 (2007).

[16]C. X. Chen, P. Depa, V. G. Sakai, J. K. Maranas, J. W. Lynn, I. Peral, and J. R. D. Copley, J. Chem. Phys. **124**, 11 (2006).

[17]M. G. Guenza, J. Phys.: Condens. Matter **20**, 033101 (2008).

[18]J. McCarty and M. G. Guenza, J. Chem. Phys. **133** (2010).

[19]Q. F. Wang, D. J. Keffer, D. M. Nicholson, and J. B. Thomas, Phys. Rev. E **81**, 061204 (2010).

[20]G. S. Grest, Q. F. Wang, P. in't Veld, and D. J. Keffer, J. Chem. Phys. **134** (2011).

[21]D. Reith, M. Putz, and F. Muller-Plathe, J. Comput. Chem. **24**, 1624 (2003).

[22]K. Kamio, K. Moorthi, and D. N. Theodorou, Macromolecules **40**, 710 (2007).

[23]C. Peter, L. Delle Site, and K. Kremer, Soft Matter **4**, 859 (2008).

[24]D. Bedrov, C. Ayyagari, and G. D. Smith, J. Chem. Theory Comput. **2**, 598 (2006).

[25]J. Fischer, D. Paschek, A. Geiger, and G. Sadowski, J. Phys. Chem. B **112**, 13561 (2008).

[26]W. L. Jorgensen, D. S. Maxwell, and J. TiradoRives, J. Am. Chem. Soc. **118**, 11225 (1996).

[27]W. L. Jorgensen, J. P. Ulmschneider, and J. Tirado-Rives, J. Phys. Chem. B **108**, 16264 (2004).

[28]W. L. Jorgensen, J. D. Madura, and C. J. Swenson, J. Am. Chem. Soc. **106**, 6638 (1984).

[29]S. T. Cui, J. W. Liu, M. E. Selvan, D. J. Keffer, B. J. Edwards, and W. V. Steele, J. Phys. Chem. B **111**, 2208 (2007).

[30]S. S. Jang, V. Molinero, T. Cagin, and W. A. Goddard, J. Phys. Chem. B **108**, 3149 (2004).

[31]A. Vishnyakov and A. V. Neimark, J. Phys. Chem. B **105**, 7830 (2001).

[32]J. Ennari, M. Elomaa, and F. Sundholm, Polymer **40**, 5035 (1999).

[33]B. F. Abu-Sharkh, Computational and Theoretical Polymer Science **11**, 29 (2001).

[34]J. P. Dacquin, H. E. Cross, D. R. Brown, T. Duren, J. J. Williams, A. F. Lee, and K. Wilson, Green Chemistry **12**, 1383 (2010).

[35]D. Wolf, P. Keblinski, S. R. Phillpot, and J. Eggebrecht, J. Chem. Phys. **110**, 8254 (1999).

[36]D. J. Keffer, C. Baig, P. Adhangale, and B. J. Edwards, Mol. Simul. **32**, 345 (2006).

[37]M. Tuckerman, B. J. Berne, and G. J. Martyna, J. Chem. Phys. **99**, 2278 (1993).

[38]A. Villa, C. Peter, and N. F. A. van der Vegt, J. Chem. Theory Comput. **6**, 2434 (2010).

[39]J. R. Silbermann, S. H. L. Klapp, M. Schoen, N. Chennamsetty, H. Bock, and K. E. Gubbins, J. Chem. Phys. **124**, 074105 (2006).

Appendix E

Tables and Figures

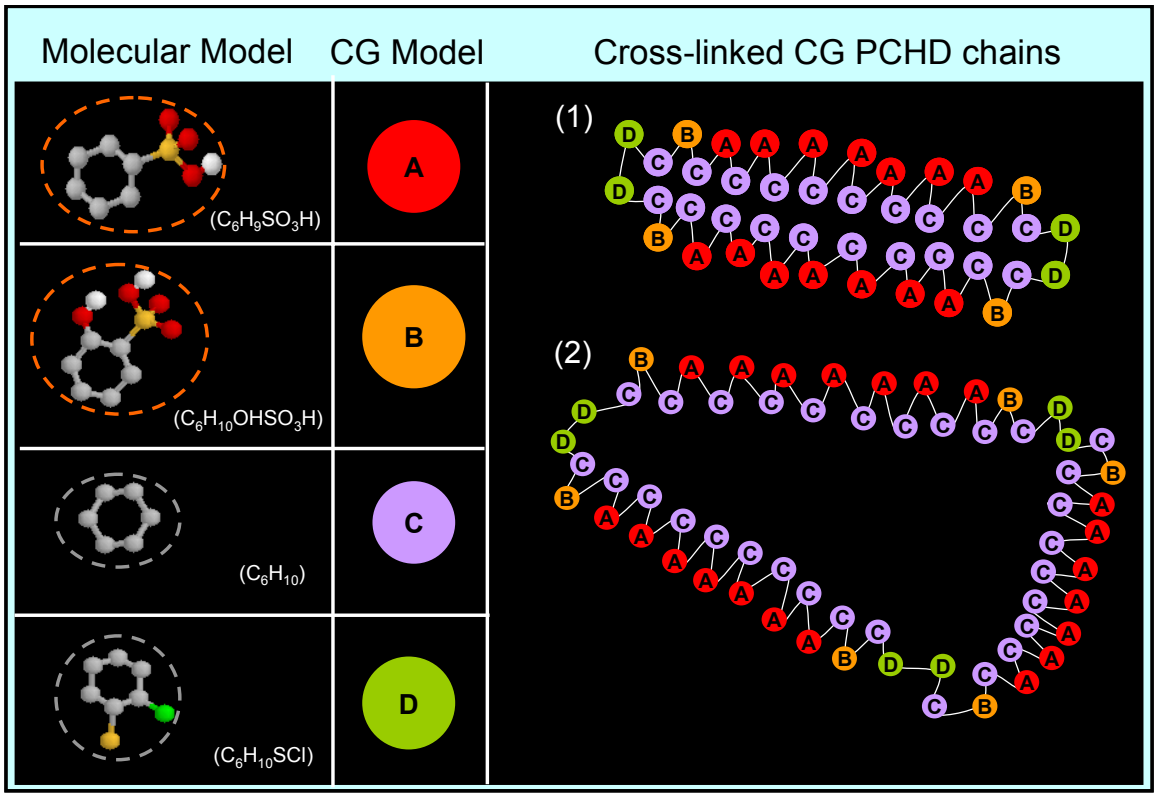

Figure 6.1. Molecular and CG model of sxPCHD polymer.

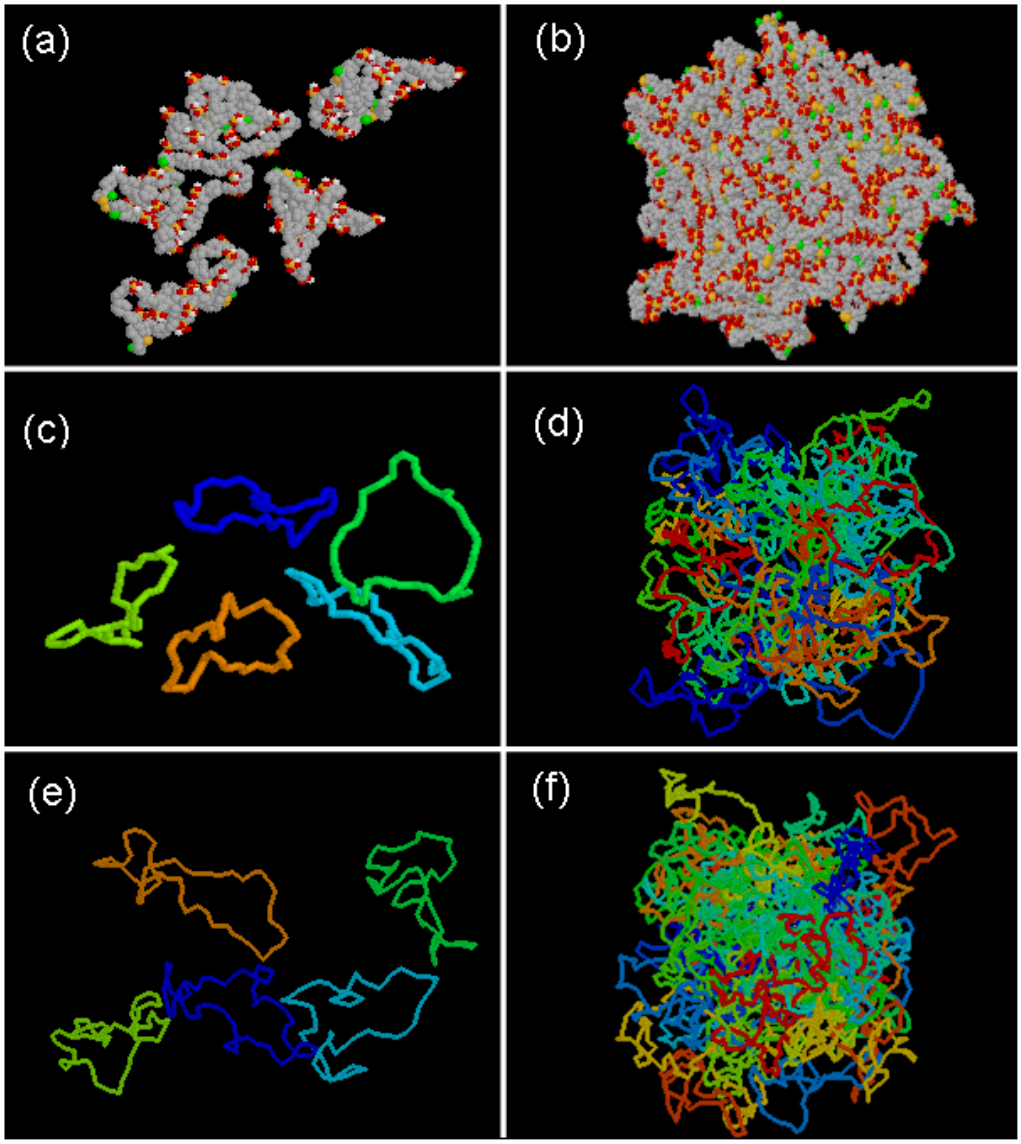

Figure 6.2. Snapshots of equilibrium configurations from atomistic ((a) and (b)) and CGMD ((c)-(f)) simulations at T = 353 K, p = 1 atm. (a) and (b): two chains cross-linked; (c) and (d) two chains cross-linked; (e) and (f): three chains cross-linked. The atomistic and CG representations of sxPCHD chains are shown in (a), (c) and (f), in which 5 molecules are taken from (b), (d) and (f) respectively.

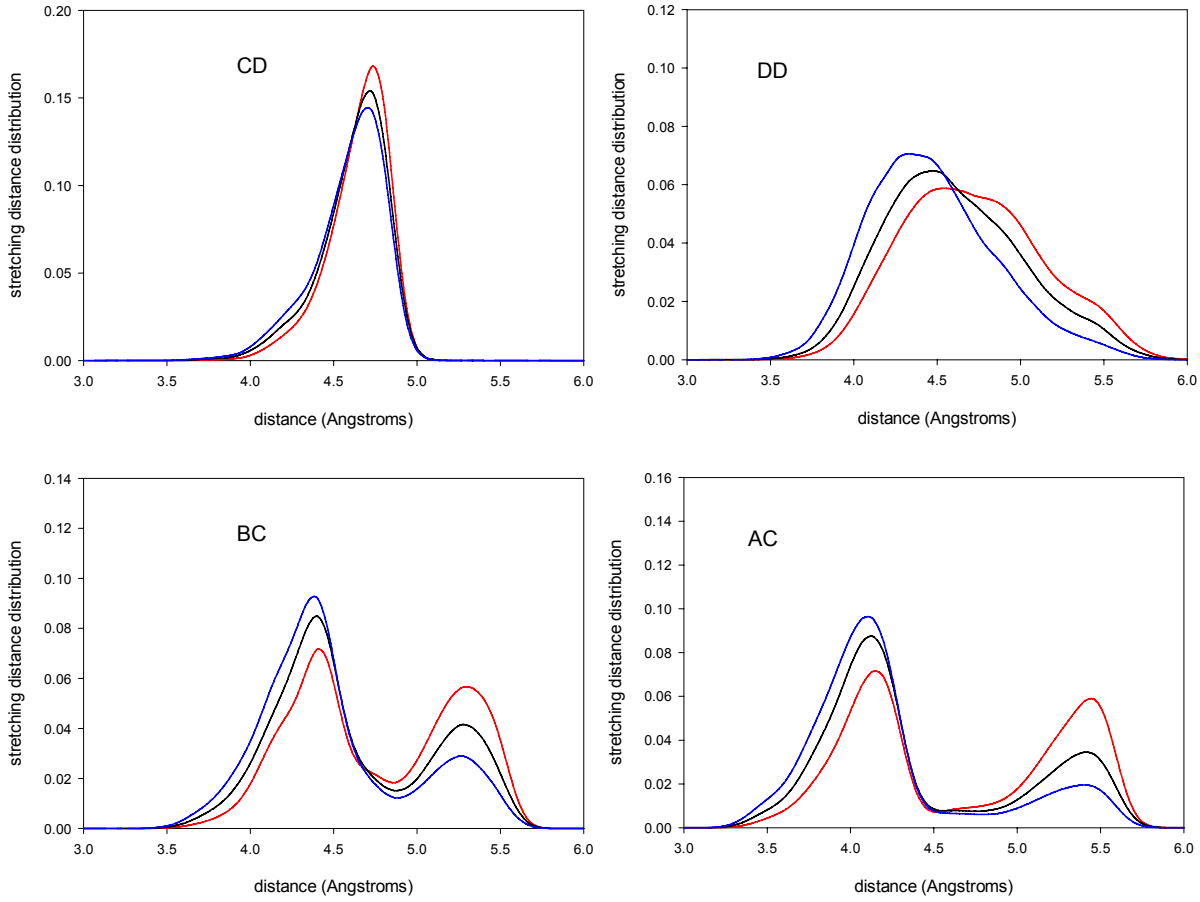

Figure 6.3. Bond stretching probability distribution functions for CG beads of sxPCHD from atomistic MD simulations (two chains cross-linked system: red line) and CGMD simulations (two chains cross-linked system: black line; three chains cross-linked: blue line). Same color representations are used in Figures 6.4. to 6.7. The GCMD simulations used the potentials from the IBI method.

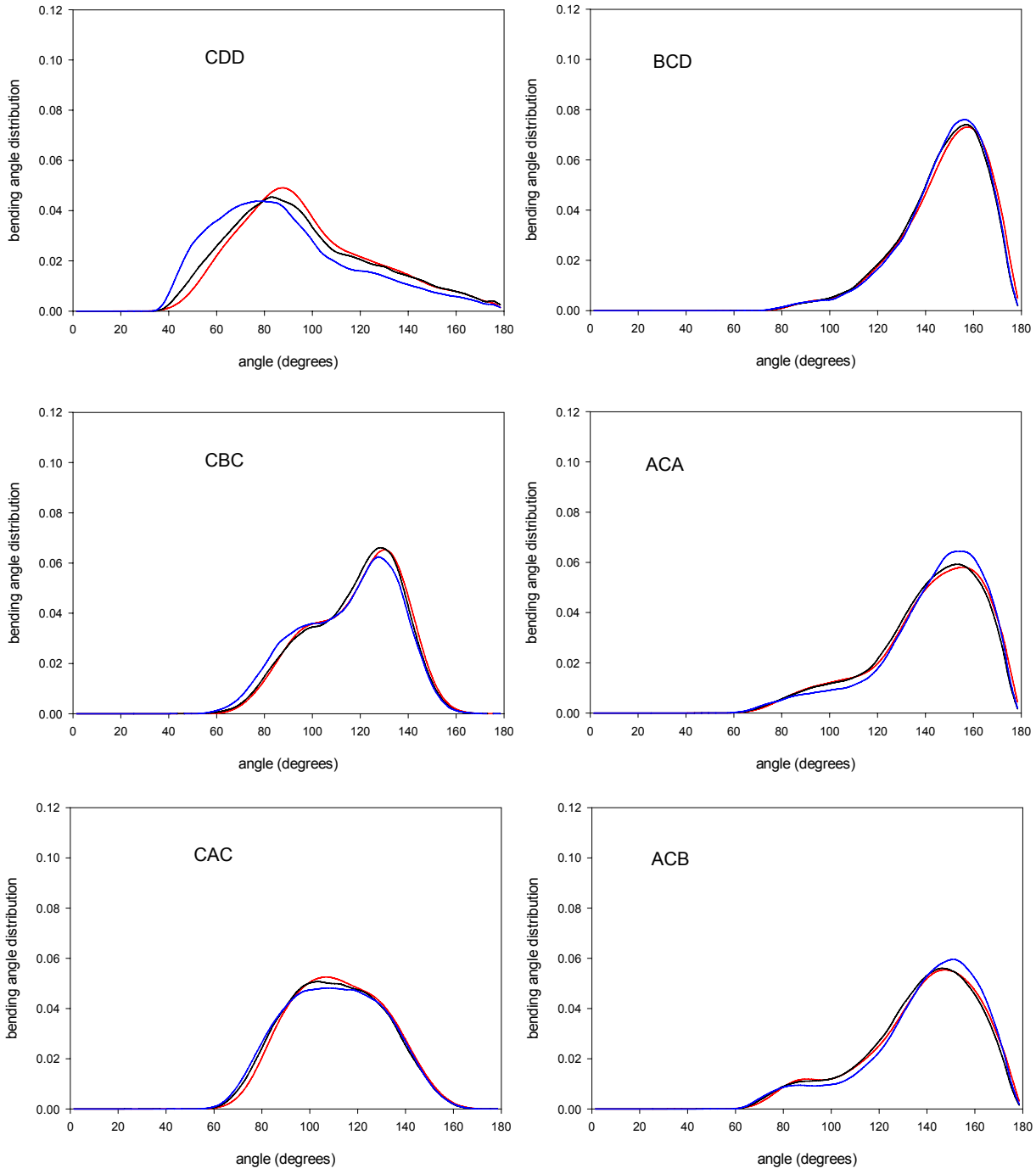

Figure 6.4. Bond bending probability distribution functions for CG beads of sxPCHD.

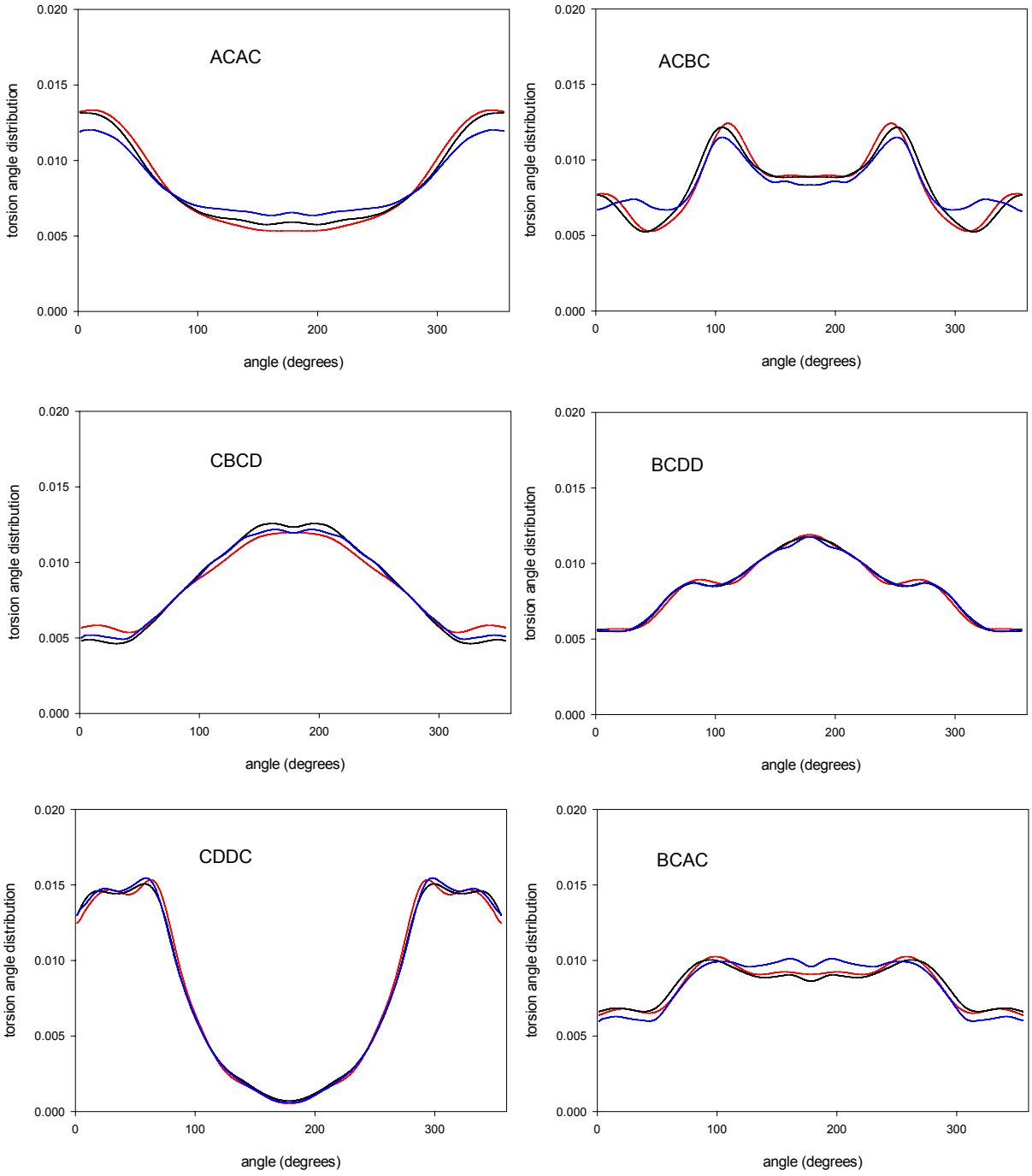

Figure 6.5. Bond torsion probability distribution functions for CG beads of sxPCHD.

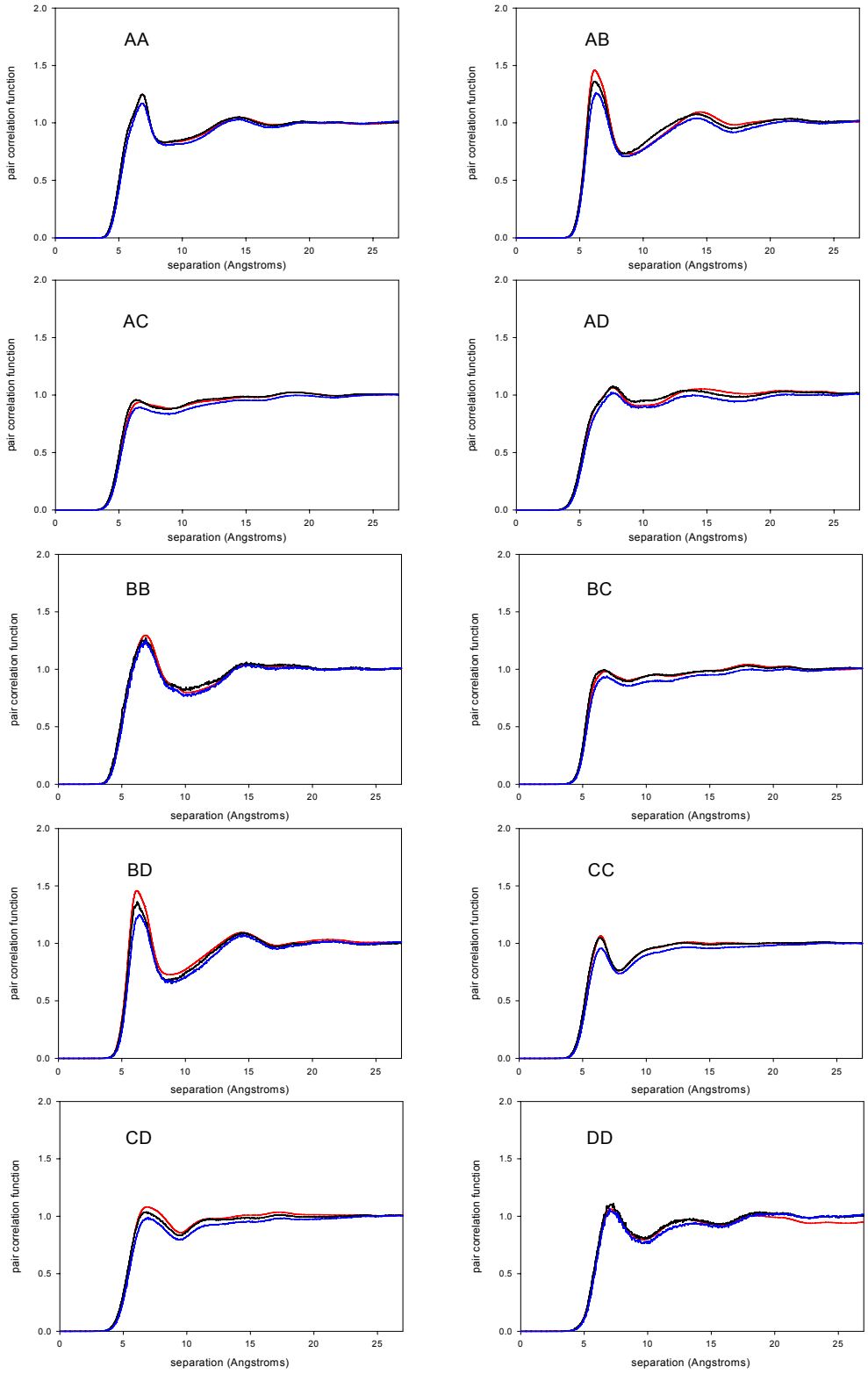

Figure 6.6. Comparison of CG nonbonded pair correlation functions for sxPCHD.

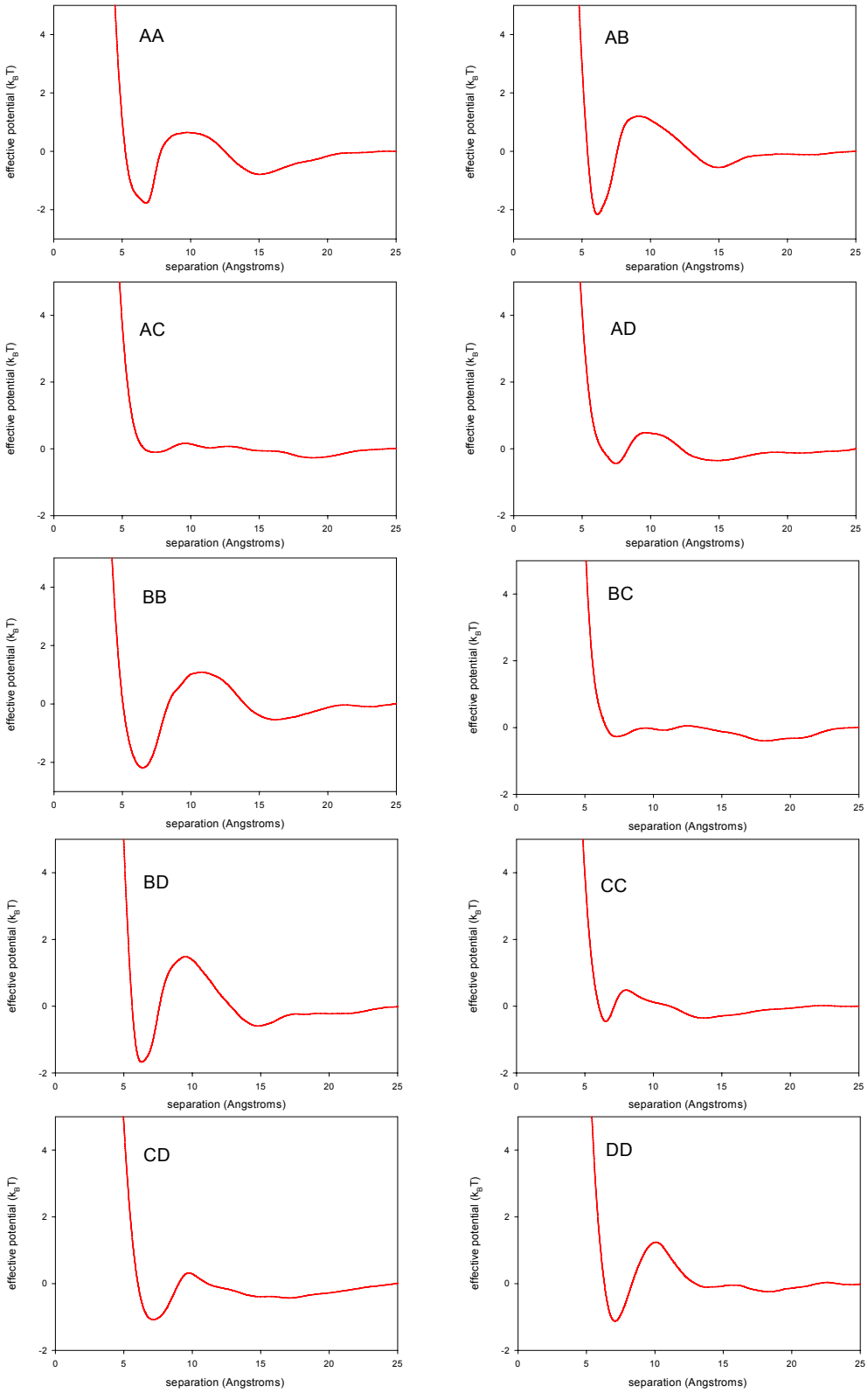

Figure 6.7. Coarse-grained nonbonded potentials for sxPCHD.

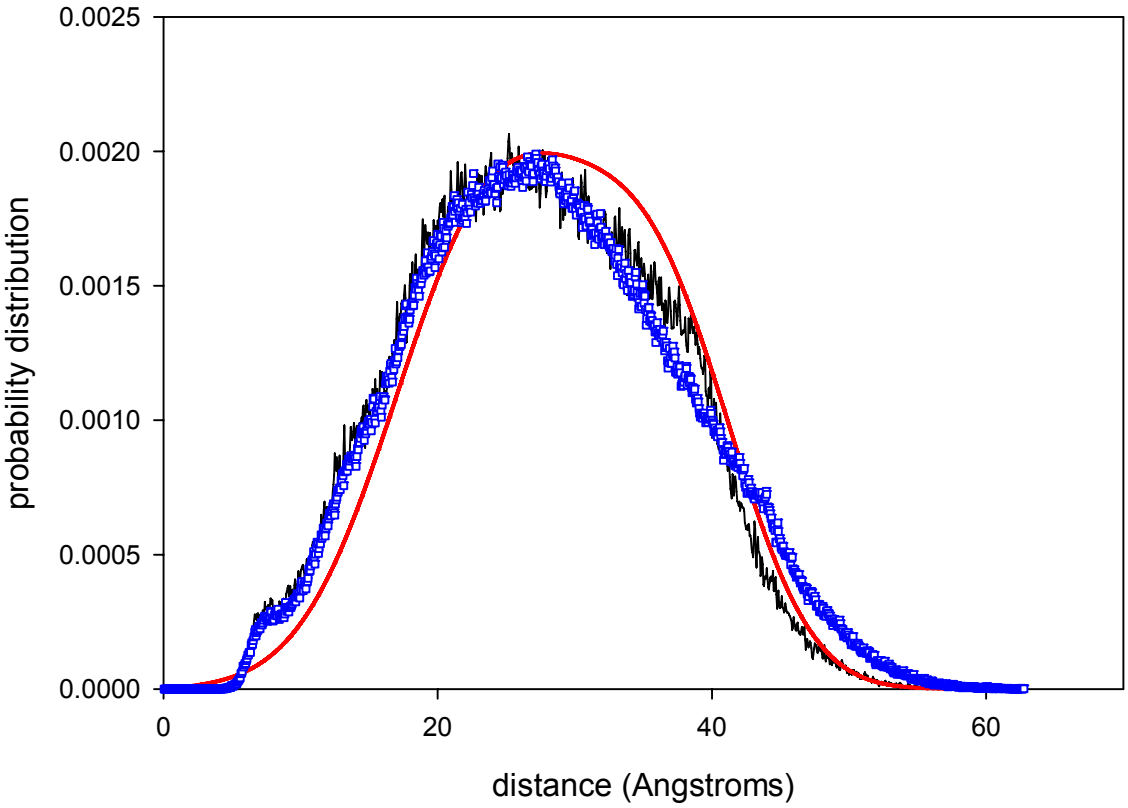

Figure 6.8. Comparisons of the chain end-to-end distance probability distributions for sxPCHD systems from atomistic MD (two chains cross-linked system: red line) and CGMD (two chains cross-linked system: black line, three chains cross-linked system: data points) simulations.

CHAPTER 7

Atomistic and Coarse-grained Molecular Dynamics Simulation of a Sulfonated Cross-linked Poly (1, 3-cyclohexadiene)-based Proton Exchange Membrane

This chapter is a revised version of a paper (minor revisions to reflect its inclusion as a chapter in the dissertation) by the same title in preparation for a journal by Qifei Wang, David J. Keffer, Suxiang Deng and Jimmy Mays:

The use of "we" in this part refers to the co-authors and the author of this dissertation. My primary contributions to this paper include (1) all of the simulation work (2) analysis of data, and (3) most of the writing.

Abstract

Atomistic and coarse-grained (CG) Molecular Dynamics (MD) simulations were conducted for a sulfonated and cross-linked Poly (1, 3-cyclohexadiene) (sxPCHD) hydrated membrane with $\lambda = 10$ H_2O/HSO_3. The bonded structural probability distribution functions (PDFs) and nonbonded pair correlation functions (PCFs) of the CG beads were obtained from the atomistic simulation of hydrated sxPCHD membrane. The PCFs include water-water, water-H_3O^+ ion, H_3O^+-H_3O^+, polymer-water, polymer-H_3O^+ ion and polymer-polymer pairs. The water self-diffusivity and H_3O^+ vehicular self-diffusivity are also obtained and compared with that in Nafion membrane under similar conditions. The study provides an understanding of water and H_3O^+ ion distribution and transport in the membrane. The bonded PDFs and polymer-polymer PCFs are compared with that of atomistic simulation of a dry sxPCHD melt. No significant changes are observed for the bonded PDFs. Since there are great changes in the nonbonded PCFs between the dry and hydrated state, the CG nonbonded potentials are then parameterized to the PCFs using the Iterative Boltzmann inversion (IBI) method. The CGMD simulations of sxPCHD chains using potentials from above method satisfactorily reproduce the polymer-polymer PCFs from atomistic MD simulation of hydrated membrane system. The potentials are used to study the membrane structure with different hydration levels.

7.1 INTRODUCTION

The unique phase separation behavior of sulfonated and cross-linked Poly (1,3-Cyclohexdiene) (sxPCHD) polymer in sxPCHD homopolymer, sxPCHD/PEG (polyethylene glycol) blend and sxPCHD-PEG block copolymer membranes generates higher proton conductivity than that of Nafion membrane at high temperatures.[1] Such phase behavior and many other properties strongly depend on the conformation of the polymer in solution or bulk.[2,3] Information on the molecular level (10 to 100 nm) membrane structures furthers the understanding of the mechanism of high proton conductivity in these systems. Classical molecular simulation has proved to be useful in the study of chain conformation when the length scale is less that 10 nm roughly.[4,5] To reach higher length scales, a multi-scaling modeling technique is needed.

The coarse-grained (CG) based multi-scaling modeling technique has been developed to study the structural and transport properties of long chain polymers at length scale that are larger than the classical molecular simulation can reach. In the CG procedure, normally a fully atomistic (or united atom (UA)) simulation of a short-chain (oligomer) system are conducted first. From the atomistic simulation, the CG structural distribution functions for different interactions modes assigned in the CG model are obtained. The CG potentials are then parameterized to these distribution functions. There are a variety of methods used to obtain the effective potentials. The iterative Boltzmann inversion (IBI) method[6] is widely used because of its advantage to reproduce the structure of atomistic sampling compared to the existing methods, especially when complicated nonbonded structures are obtained from the atomistic simulation.

The CG modeling work on polymer solutions, suspensions or hydrated proton exchange membranes (PEMs) shows that the solvent plays an important role in determining the polymer structure.[7-11] However, there is no well established method to obtain the CG effective potentials for solvent-polymer and solvent-solvent interactions to reproduce the structures from atomistic sampling when the solvent is treated explicitly in these systems. One may easily encounter convergence problems when apply the IBI to these inhomogeneous systems since interactions between beads of the same type may change with the local environment.

Alternatively, a successful way to deal with solvent in these works is by treating the solvent explicitly at the atomistic scale while treating it implicitly at the CG scale. Since the polymer structure at the atomistic level is reproduced using the IBI method at CG level, the effect of the solvent on the polymers structure is still accounted for in the CG simulation. Using this method, Fischer *et al.*[10] developed an implicit CG model for polyoxylethylene solution and studied the potential transferability to different chain length and mixture concentrations. The same method is adopted by Bedrov *et al.*[11] in their CG modeling work on poly(ethylene oxide)-poly(propylene oxide)-poly(ethylene oxide) triblock copolymer in solution.

In this work, we studied the structures of hydrated sxPCHD membrane at the atomistic and CG level. Previously, a multi-scale model for sulfonated cross-linked sxPCHD homopolymer was developed for the unhydrated (melt) state. The same model is used here but a CG force field for sxPCHD in hydrated membrane needed to be derived. To do so, we adopted the same multi-scale modeling procedure that was used for the sxPCHD polymer melt. First, an atomistic MD simulation of the hydrated short-chain sxPCHD system at low water content was conducted, from which bonded probability distribution functions (PDFs) and nonbonded pair correlation functions (PCFs) for all types of polymer beads were obtained. Water and H_3O^+ ion distribution and transport in the membrane are also studied at the atomistic level. Additionally, the bonded PDFs and nonbonded PCFs for sxPCHD polymer from the atomistic simulations hydrated membrane were compared with that of atomistic MD simulation of bulk sxPCHD at the same temperature to study the solvent effect on polymer's structure. Second, the nonbonded PCFs for sxPCHD polymer from the atomistic simulations were used to generate CG potentials, using the IBI method. Third, the CG potentials are implemented in CGMD simulations of the same system while water and H_3O^+ ion are treated implicitly. Finally, the nonbonded PCFs for sxPCHD polymer from CG level simulation are compared with those from the atomistic level simulation in order to validate the CG model.

7.2 SIMULATION METHOD

7.2.1 Atomistic simulation of hydrated sxPCHD membrane with $\lambda = 10$

The force field used for sxPCHD polymer,[12] which invoked potentials from the literature for each of the components in the polymer,[13-22] was used again here. The model is fully atomistic

with the exception of hydrogen atoms bonded to carbons, which are modeled as CH_x groups, as shown in Figure 7.1(a). The atomistic model includes bond-stretching, bond-bending, bond-torsion and intramolecular and intermolecular non-bonded interactions via both Lennard-Jones and Coulombic potentials. The only difference between the atomistic potential used in the simulation of the melt and that used in the simulation of the hydrated polymer is that the SO_3H group in the melt is dissociated into SO_3^- and H_3O^+ ions in the hydrated system. The SPC/Fw model by Wu *et al.*[23] was used for water and a fully flexible model of H_3O^+ used in hydrated Nafion simulations by Cui *et al.*[19] work was used. The simulation system includes 40 sxPCHD cross-linked chains, 720 H_3O^+ molecules and 6480 water molecules, corresponding to $\lambda = 10$ condition (1 H_3O^+ and 9 water molecules per sulfonic acid group). The spherically truncated charge-neutralized method developed by Wolf *et al.*[24] was used to evaluate the electrostatic energy. We simulated in the isobaric-isothermal (NpT) ensemble and implemented the Hamiltonian-based thermostat and barostat[25] with controller frequencies set to 10^{-4} fs^{-1}. The XI-RESPA NPT algorithm developed by Tuckerman *et al.*[26] was used to integrate the equations of motion. The large time step was 1 fs and the small time step was 0.1 fs. The cut-off distance used was 15 Å for this level simulation. The state point was set at 1 atm and 353 K, corresponding to future fuel cell applications. Following the equilibration procedure described elsewhere,[5,27] we gradually equilibrated to the correct density. Data production lasted for 10 ns. The equilibrium configuration is shown in Figure 7.2. To compare the water-water distribution, atomistic simulation of bulk water was also conducted. The same water model and simulation method was used. Data production lasted for 5 ns.

7.2.2 CGMD simulations of hydrated sxPCHD membrane with $\lambda = 10$.

As shown in Table 7.1 and Figure 7.1(b), the CG model for sxPCHD proposed in previous work is used here although the hydrogen on SO_3H is transferred to H_3O^+. There are three CG beads on sxPCHD chains (bead A, B and C) and two cross-linkers (D) at the two ends. The bead is placed at the center-of-mass of the atoms in the corresponding fragment. In this model, the CG interaction modes include bond stretching, bond bending, bond torsion, and nonbonded interactions for both intra-molecular (for beads separated by at least four bonds) and inter-molecular pairs. The same CG nonbonded potential is used for both intra-molecular and inter-molecular interactions. Probability distribution functions (PDFs) for stretching, bending, torsion

and nonbonded pair correlation functions (PCFs) between CG beads were generated from the atomistic simulations of hydrated sxPCHD membrane. As will be shown in detail below, a comparison of bonded PDFs from atomistic simulations of both melt and hydrated sxPCHD systems shows that there are no significant changes in the bonded PDFs. Consequently, the bonded CG potentials for the sxPCHD melt are directly used in the CG simulation of hydrated sxPCHD membrane.

The nonbonded potential for intra-molecular (for beads over four bonds) and inter-molecular interactions is generated by the IBI method.[6] In the IBI method, a tabulated potential is numerically determined by simulation iteration. The interaction potential is refined iteratively via

$$\varphi_{\alpha\beta,i+1}(r) = \varphi_{\alpha\beta,i}(r) + k_B T \ln\left(\frac{g_{\alpha\beta,i}(r)}{g_{\alpha\beta}(r)}\right) \tag{1}$$

with initial guess

$$\varphi_{\alpha\beta,0}(r) = -k_B T \ln\left(g_{\alpha\beta}(r)\right) \tag{2}$$

where $g_{\alpha\beta}(r)$ is the target PCF, which is from atomistic simulation. In CG level simulation, water and H_3O^+ ion are treated implicitly, as commonly adopted in the CG modeling work of polymer solutions.[10,11] Due to the complexity of CG model, there are still 10 nonbonded interactions modes (AA, AB, AC, AD, BB, BC, BD, CC, CD and DD) that need to be refined. First two iterations were done on all interactions modes simultaneously then additional 1 to 3 iterations were done on each mode individually. The number of iterations used for each mode depends on the complexity of the PCF. Generally, each mode took 3 to 5 iterations to reproduce the structure of atomistic sampling, which is chosen to stop the iteration cycle.

In the CGMD simulations, we use the same density as that used in the atomistic simulation. Sixty-four chains are used at this level of simulation. We again simulated in the NVT ensemble under the same temperature as the atomistic simulation. The cut-off distance used is 25 Å for the CG simulation. The time step of the CGMD simulation is twice that used in the atomistic MD simulation. Based on wall-clock time, the CGMD simulations are approximately 400 times faster than the atomistic simulations.

7.3 RESULTS AND DISCUSSION

In this section, we discuss (1) the results of the atomistic MD simulation of hydrated sxPCHD system, (2) comparison of structures from atomistic simulation of hydrated membrane with that of the sxPCHD melt, (3) generation of nonbonded CG potentials for hydrated sxPCHD from the IBI method, and comparison of the structural distribution functions from CGMD simulations of hydrated sxPCHD with that from atomistic simulation.

In Figure 7.2, we show equilibrated snapshots from both the atomistic and the CGMD simulations. In Figure 7.2(a), all molecules are shown to make it clear that we are simulating a multi-components system. In Figure 7.2(b), all polymer chains are rendered invisible to better indicate the shape of the aqueous domain. In Figure 7.2(c), all water molecules and $H3O^+$ ions are rendered invisible to better show the shape of the polymer domain. In Figure 7.2(d), the sxPCHD structure at the CG level is shown..More information is available on the website.[28]

One of the features that is clearly visible in these snapshots is the segregation at the nanoscale into hydrophobic (polymer) and hydrophilic (aqueous) domains. The sulfonate ions are located at the interface between the hydrophobic and hydrophilic domains. This sort of nanophase segregation has been observed for Nafion by many researchers using molecular simulation.[29] Characterization of the volume of the aqueous domain, the interfacial surface area and the connectivity of the aqueous domain depicted qualitatively in these snapshots has been shown to have direct impact on the mobility of water and protons in the membrane.[30]

Experimental studies of sxPCHD have shown that water channels are visibly connected at a 10 nm scale while the polymer domain is at 10 nm to 100 nm length scale.[1] Our simulations have a dimension of 10-15 nm. Therefore, they are capable of capturing the structure of the aqueous domain but not of the polymer domain. Work with Nafion has shown that, MD simulation of these smaller systems can still yield quantitive agreement with experimental measurements of water and charge self-diffusivities.[30] We would not expect simulations of this size to capture any crystallinity effects (as exist in Nafion) in the polymer phase, which are likely present at longer length scales.

7.3.1 Atomistic MD simulation of hydrated sxPCHD membrane with $\lambda = 10$.

In Figure 7.3, we show the water-water, H_3O^+-H_3O^+ and water-H_3O^+ PCFs of the CG beads obtained from atomistic simulation. These distribution functions are based on the analysis

of configurations from atomistic MD simulation. Although the aqueous phase will be treated implicitly at the CG level, these PCFs provide useful information on water and H_3O^+ distributions in the membrane. The following PCFs are based on positions of the center-of-mass of water molecules and hydronium ions.

In Figure 7.3(a), the water-water PCF for the hydrated membrane is compared to that of bulk water. There is significant difference in the water-water structure, including an enhanced first peak and the presence of a small second at about 4 Å. These same features are present in the water-water PCF in hydrated Nafion at $\lambda = 9$,[19] in which similar nanoscale segregation occurs. It is worth noting that, following standard convention, the PCFs are normalized by the bulk density. In a homogeneous system, like bulk water, there is no ambiguity associated with the bulk density. In an inhomogeneous system, such as the hydrated sxPCHD membrane, we have normalized by a density that includes the total system volume (since that is unambiguously available). Consequently, some of the discrepancy between these PCFs is due to the definition of the PCF. We notice here the CG level is low for water. We can observe this type of local structures. When CG level increases, the feature will disappear.[31]

In Figure 7.3(b), the H_3O^+-H_3O^+ PCF is shown. There is very little structure in the PCF, commensurate with the fact that two cations in solution will not aggregate, due to Columbic repulsion. What little structure there is can be attributed to the fact that the anions are fixed in close proximity to each other due to their covalent bonds to the polymer backbone. Since there may be association between the cation and anion, some weak cation-cation association may be evident.

In Figure 7.3(c), the water-H_3O^+ ion PCF is shown. We observe two peaks in this PCF. The first, larger peak occurs at about 2.60 Å, and the second peak occurs at a distance of 4.95 Å. The same feature has been found in the atomistic simulation work of Nafion at different water contents,[19] in which the PCF between oxygen of water and oxygen of H_3O^+ is used to represent water-H_3O^+ ion PCF. The first peak is much higher that the second one because of the tighter binding of water molecule with H_3O^+ ion at short distance. This feature is also in agreement with above atomistic modeling work of hydrated Nafion.

In Figure 7.4, we examine the PCFs obtained from atomistic simulations between the center-of-mass of various CG beads with water molecules and hydronium ions. Figure 7.4(a)

shows the PCFs between the beads on the polymer and a water molecule. We see the strong correlations with beads of type A and B, because these beads contain SO_3^- ions, which interact strongly with water molecules. Both A and B beads show a first peak around 5.0 Å, a second peaks around 7.0 Å and a third peak around 14.0 Å. Since beads A and B have very similar chemical structures, as shown in Table 7.1, we expect the correlation with water to be similar. The presence of the hydroxide group on the B bead lowers the correlation. We see the weakest correlation with particles of type D, which contain the cross-linking groups and are consequently surrounded by more polymer than water.

In Figure 7.4(b), we show the PCFs for polymer-H_3O^+ ion pairs. For all bead types, the peak heights are greater for the hydronium ion than they are for water molecules in Figure 7.4(a). This indicates that H_3O^+ ions are more strongly bound to polymer than are the water molecules, due to the stronger Columbic attraction between the hydronium ion and the sulfonate anion. In Figure 7.4(b), there is an apparent difference between the PCFs of A and B. The major peak around 5 Å is split into two peaks in the B PCF. We believe this is due to the existence of a hydroxyl group on bead B. The orientations of some H_3O^+ ions are likely altered due to hydrogen bonding with the hydroxyl group. Experimental results indicate that the presence of hydroxyl groups positively impacts the proton conductivity of the membrane.[1]

While the atomistic simulations are too short to capture relaxation times of the polymer, they may be capable of capturing relaxation of the solvent, which is much faster. The MSD is plotted in Figure 7.5 as a function of observation time for both water and the vehicular contribution of the hydronium ion. (Note that in these simulations we do not include a proton-hopping mechanism and thus are limited to measuring only one component of the overall charge self-diffusivity.) In the long-time limit of the Einstein relation, there should be a linear relationship between the MSD and the observation time. In the log-log plot, we show the slope is indeed unity at long time, indicating that we have simulated sufficiently long (10 ns) to obtain reliable self-diffusivities of the water molecules and hydronium ions. Invoking the Einstein relation then yields diffusivities of $1.18*10^{-9}$ m^2/s for water and $2.57*10^{-10}$ m^2/s for the vehicular component of the hydronium ion. Using the same method, a value of $9.24*10^{-9} m^2/s$ is obtained for bulk water at the same temperature and pressure. The self-diffusivity of water in sxPCHD membrane is 12.8% of that in bulk water. For comparison, the self-diffusivity of water in Nafion

membrane with similar hydration level is 9.7% of that in bulk water at 300 K.[19] In both cases, the water diffusion coefficient is significantly smaller than in bulk water, due to increased acidity, increased confinement and decreased connectivity in the membrane.[30]

7.3.2 Comparison of sxPCHD polymer structures from atomistic simulation of hydrated membrane with that of melt.

To understand the effect of hydration on polymer structure, we compare the structures of sxPCHD in the hydrated membrane with that in the melt. The CG bonded stretching, bending and torsion PDFs are shown in Figures 7.6 to 7.8, while the CG nonbonded PCFs are shown in Figure 7.9. In all cases, these distribution functions were generated from atomistic simulations of short chains. It is important to remember that while the C and D beads are identical in the hydrated and melt systems, the A and B beads are not identical. In the melt, the A and B beads contain the complete sulfonic acid group, HSO_3, while in the hydrated state, the A and B beads contain the dissociated sulfonate ion, SO_3^-.

In Figure 7.6, we compare the PDFs for each of the four stretching modes. These modes are generally the same for both the melt and the hydrated membrane. The peak positions and peak heights are largely reproduced. We do observe a slight change in the peak position of the second peak in the AC bond stretching PDF to shorter distances in the hydrated system.

In Figure 7.7, we compare the PDFs for each of the six bending modes. Again, these modes are generally the same for both the melt and the hydrated membrane. The peak positions and peak heights are largely reproduced. We observe small population shifts from the large peak at 150-160° in the ACA and ACB bending PDFs to the small peak at 80-90°, due to the presence of the water and hydronium around the A and B beads.

In Figure 7.8, we compare the PDFs for each of the six torsion modes. Again, these modes are largely the same for both the melt and the hydrated membrane. The peak positions and peak heights are largely reproduced. To the level of approximation in the CG simulations, these potentials can be considered to be the same.

In Figure 7.9, we compare the PCFs for each of the ten polymer-polymer nonbonded modes. For those modes that involve ions in the hydrated state (AA, AB and BB) there are significant differences in the PCFs. The first peak in the melt is reduced significantly in magnitude and pushed to slightly larger distances in the hydrated system, due to electrostatic

repulsion. Some modes are relatively unchanged by the introduction of water, including the AC, AD, BC, and CC modes. However, the structure around the D bead has changed significantly, resulting in very different PCFs for BD, CD and DD. The nonbonded interaction modes are correlated with each other. A change in the distribution of one mode may cause the changes in the distributions of the other modes.

Interactions between water and polymer, or H_3O^+ and polymer could possibly make a great contribution on the packing of polymer chains. The findings from the literature give some hints on this issue. In the study of homogeneous polymer melts, previous work shows that these distributions functions have no apparent chain length dependence. [5,27] In the CG modeling work of aqueous poly(oxyethylene) solutions, Fischer *et al.*[10] show that the nonbonded PCFs have similar trends but apparent differences at different concentrations. It depends very much on the mixture and CG model used. A better understanding of sxPCHD structure changes with water content can be obtained through the study of these distribution functions as a function of hydration level (λ).

7.3.3 Generation of CG potentials for hydrated sxPCHD membrane with $\lambda = 10$.

One aim of this research is to derive a CG force field for sxPCHD in a hydrated membrane. Previously, we derived a CG model for sxPCHD in the melt using the IBI method. First and foremost, we cannot use the CG potential form the melt for the hydrated state due to the fact that A and B are now charged beads in the hydrated state. These beads are fundamentally difference. Second, the effective potentials obtained from the IBI method are dependent on thermodynamic state (density and temperature).[6] Its transferability to temperatures or chain length needs to be tested, even for homogeneous polymer melts.[27] In this work, we simulated the sxPCHD hydrated membrane at the same temperature as that of bulk sxPCHD simulation. However, the density changed for sxPCHD in hydrated membrane because we maintained a constant pressure of one atm. In the previous section, we compared the bonded and nonbonded structures for sxPCHD in the melt and in the hydrated membrane. Since there were no significant changes, we chose to use the bonded CG potentials from the sxPCHD melt. However, there were great changes on nonbonded PCFs. Therefore, we have to generate the nonbonded CG potentials for hydrated sxPCHD. To do so, we made the aqueous phase implicit at the CG level as mentioned above. Thus, ten polymer-polymer non-bonded modes were iteratively refined to

reproduce the PCFs from atomistic simulation. Effective potentials from the last iterations are shown in Figure 7.10. For comparison, also shown are the CG potentials from the sxPCHD melt. The first obvious observation is that there is significant change in the CG potentials between the hydrated and melt states. The most distinctive difference occur for AA, AB and BB, modes in which the beads have become charged in the hydrated state. In these cases the depth of the attractive well has been greatly reduced and the position of the minima has been pushed to larger distances. For interactions between non-ionic beads, such as CC, the well depth has increased in the hydrated state. This can be explained by remembering that the water is treated implicitly. In an atomistic simulation, we observe phase segregation into hydrophobic and hydrophilic regions because the water-water interaction is much stronger than any other interaction. However, in the CG simulation where water is not present, we observe phase segregation due to the attraction of hydrophobic beads, like C. This observation is also observed for the strictly uncharged CD and DD modes. For modes involving one charged bead and one uncharged bead, no uniform difference between the potentials of the hydrated and melt states is observed.

To further understand the features of these potentials, we can revisit the PCFs from which the potentials were extracted. In Figure 7.9, the first peaks of the CC, CD and DD (uncharged-uncharged) modes are sharper than that of the other modes for the hydrated system. Correspondingly, the potentials of CC, CD, and DD show deep first minima in Figure 7.10. As noted above, the PCFs of the charged-charged modes (AA, AB and BB) shows much smaller and more distant first peaks, which corresponds to the observed changes in the CG potential. The PCFs of the charged-uncharged modes (AC, AD, BC, and BD) modes are relatively unchanged by the introduction of water, with the exception of BD. However, the CG potentials may be significantly changed even in the absence of strong changes in the PCF, e.g. AD.

In order to validate the CG potential, one should compare structures obtained from the atomistic and CG simulations of the same system. That validation has been performed here. The comparisons of the distributions of the stretching, bending and torsion modes are provided in the supplementary information. In general, the agreement is very good.

We also can validate the CG model through comparison of the non-bonded PCFs. In Figure 7.11, a comparison of PCFs from the atomistic and CG simulations of the hydrated membrane is provided. In general, good agreement is obtained for all modes. All peaks present in

the atomistic simulation are also present in the CG simulation. For the PCFs in which multiple peaks are present, the relative magnitude of the peaks observed in the atomistic simulations is reproduced by the CG simulations in all cases except for the CC mode. There is admittedly some quantitative discrepancy for a few of the modes (AC, CC and CD). However, we believe that this level of agreement is sufficient to allow the CG simulations of hydrated sxPCHD to capture the essential structures of the atomistic simulations.

7.4 CONCLUSIONS

Atomistic and coarse-grained (CG) Molecular Dynamics (MD) simulations were conducted for sulfonated and cross-linked Poly (1, 3-cyclohexadiene) (sxPCHD) in a hydrated state with $\lambda = 10$. From the atomistic simulation of hydrated sxPCHD membrane, the bonded structural probability distribution functions (PDFs) and nonbonded pair correlation functions (PCFs) of the CG beads were obtained and compared favorably with that of the sxPCHD melt. The CG PCFs for water-water, water-H_3O^+ ion, H_3O^+-H_3O^+, polymer-water, polymer-H_3O^+ ion and polymer-polymer pairs provide an understanding of water and H_3O^+ the nature of the interface in the hydrated membrane. The water and H_3O^+ ion diffusivities are also obtained and compared with that in Nafion membrane under similar condition. No significant changes in the stretching, bending and torsion distributions of the sxPCHD were observed between the melt and hydrated state. Some of the non-bonded PCFs changed dramatically due to dissociation of the sulfonic acid group leading to a charged bead in the hydrated system. The CG nonbonded potentials were generated using the Iterative Boltzmann inversion (IBI) method, with the aqueous phase being treated implicitly. The CGMD simulations of hydrated sxPCHD using potentials from the above method satisfactorily reproduce the polymer-polymer PCFs from atomistic MD simulation of the same system. The study of transferability of derived CG potentials to different hydration level and a predictive understanding of water and proton transport in the sxPCHD based membrane are underway.

7.5 ACKNOWLEDGMENT

This research was supported by a grant from the National Science Foundation (DGE-0801470). This research project used resources of the National Institute for Computational Sciences (NICS) supported by NSF under agreement number: OCI 07-11134.5.

References

[1]J. W. Mays, S. Deng, K. A. Mauritz, M. K. Hassan, and S. P. Gido, Patent No. US20090306295A1 (2009).

[2]S. I. Yun, K. Terao, K. L. Hong, Y. B. Melnichenko, G. D. Wignall, P. F. Britt, and J. W. Mays, Macromolecules **39**, 897 (2006).

[3]S. I. Yun, K. Hong, Y. B. Melnichenko, G. D. Wignall, and J. W. Mays, Polym. Prepr. (Am. Chem. Soc., Div. Polym. Chem.) **47**, 620 (2006).

[4]K. Kremer, Macromol. Chem. Phys. **204**, 257 (2003).

[5]Q. F. Wang, D. J. Keffer, D. M. Nicholson, and J. B. Thomas, Macromolecules **43**, 10722 (2010).

[6]D. Reith, M. Putz, and F. Muller-Plathe, J. Comput. Chem. **24**, 1624 (2003).

[7]G. S. Grest, Q. F. Wang, P. in't Veld, and D. J. Keffer, J. Chem. Phys. **134** (2011).

[8]K. Malek, M. Eikerling, Q. P. Wang, T. C. Navessin, and Z. S. Liu, J. Phys. Chem. C **111**, 13627 (2007).

[9]K. Malek, M. Eikerling, Q. P. Wang, Z. S. Liu, S. Otsuka, K. Akizuki, and M. Abe, J. Chem. Phys. **129** (2008).

[10]J. Fischer, D. Paschek, A. Geiger, and G. Sadowski, J. Phys. Chem. B **112**, 13561 (2008).

[11]D. Bedrov, C. Ayyagari, and G. D. Smith, J. Chem. Theory Comput. **2**, 598 (2006).

[12]Q. F. Wang, D. J. Keffer, S. Deng, and J. W. Mays, J. Chem. Phys., In preparation (2011).

[13]W. L. Jorgensen, J. D. Madura, and C. J. Swenson, J. Am. Chem. Soc. **106**, 6638 (1984).

[14]W. L. Jorgensen, D. S. Maxwell, and J. TiradoRives, J. Am. Chem. Soc. **118**, 11225 (1996).

[15]W. L. Jorgensen, J. P. Ulmschneider, and J. Tirado-Rives, J. Phys. Chem. B **108**, 16264 (2004).

[16]S. S. Jang, V. Molinero, T. Cagin, and W. A. Goddard, J. Phys. Chem. B **108**, 3149 (2004).

[17]J. P. Dacquin, H. E. Cross, D. R. Brown, T. Duren, J. J. Williams, A. F. Lee, and K. Wilson, Green Chemistry **12**, 1383 (2010).

[18]B. F. Abu-Sharkh, Computational and Theoretical Polymer Science **11**, 29 (2001).

[19]S. T. Cui, J. W. Liu, M. E. Selvan, D. J. Keffer, B. J. Edwards, and W. V. Steele, J. Phys. Chem. B **111**, 2208 (2007).

[20]S. J. Weiner, P. A. Kollman, D. T. Nguyen, and D. A. Case, J. Comput. Chem. **7**, 230 (1986).

[21]J. C. Smith and M. Karplus, J. Am. Chem. Soc. **114**, 801 (1992).

[22]A. Vishnyakov and A. V. Neimark, J. Phys. Chem. B **105**, 7830 (2001).

[23]Y. J. Wu, H. L. Tepper, and G. A. Voth, J. Chem. Phys. **124** (2006).

[24]D. Wolf, P. Keblinski, S. R. Phillpot, and J. Eggebrecht, J. Chem. Phys. **110**, 8254 (1999).

[25]D. J. Keffer, C. Baig, P. Adhangale, and B. J. Edwards, Mol. Simul. **32**, 345 (2006).

[26]M. Tuckerman, B. J. Berne, and G. J. Martyna, J. Chem. Phys. **99**, 2278 (1993).

[27]K. Kamio, K. Moorthi, and D. N. Theodorou, Macromolecules **40**, 710 (2007).

[28]D. J. Keffer, *Molecular Simulation Structures from the Computational Materials Research Group at the University of Tennessee Knoxville, TN* (2010).

[29]J. W. Liu, N. Suraweera, D. J. Keffer, S. T. Cui, and S. J. Paddison, J. Phys. Chem. C **114**, 11279 (2010).

[30]M. E. Selvan, E. Calva-Munoz, and D. J. Keffer, J. Phys. Chem. B **115**, 3052 (2011).

[31]K. R. Hadley and C. McCabe, J. Phys. Chem. B **114**, 4590 (2010).

Appendix F

Tables and Figures

Table 7.1. CG beads representations in the hydrated sxPCHD membrane. The same symbols A and B in bulk CG sxPCHD model are still used while H atom in SO_3H is dissociated in these beads.

CG bead	Molecular fragments
A	$(C_6H_9SO_3^-)$
B	$(C_6H_{10}OHSO_3^-)$
C	(C_6H_{10})
D	$(C_6H_{10}SCl)$

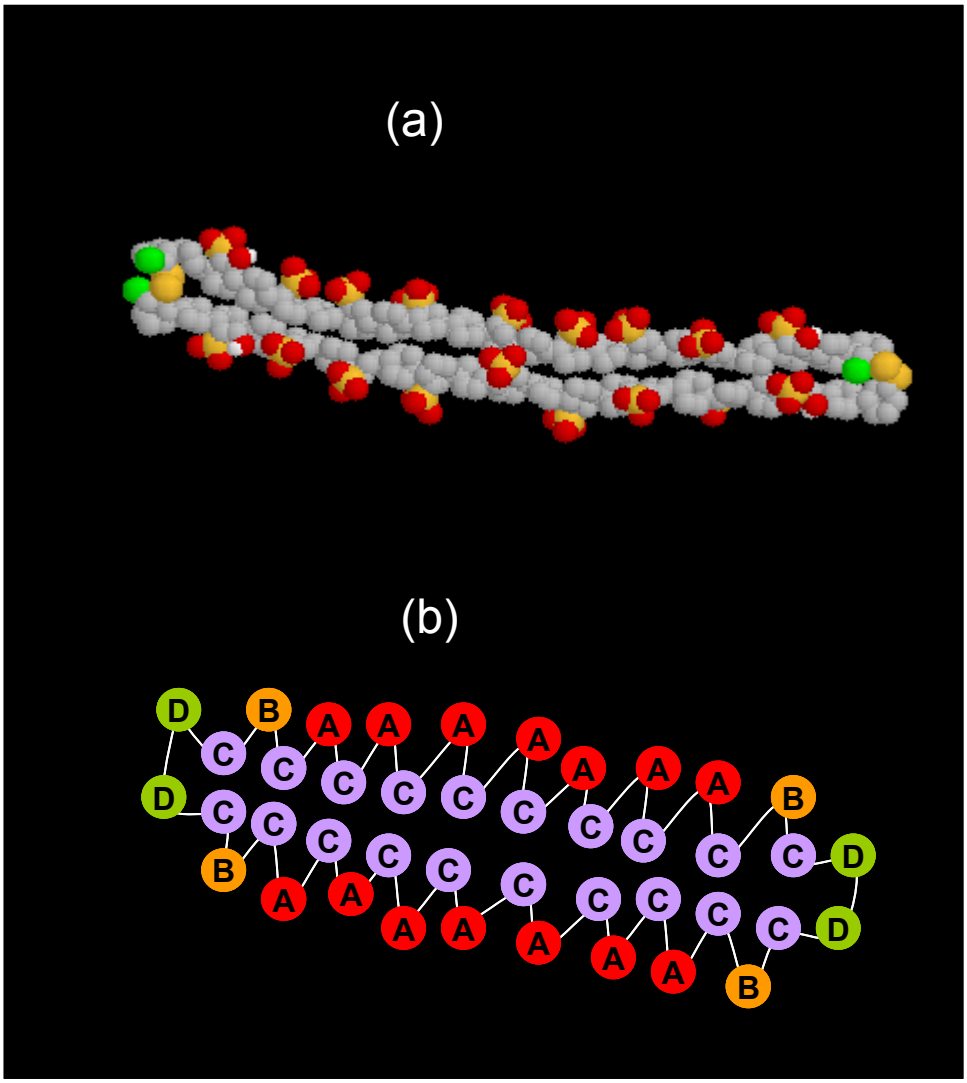

Figure 7.1. Atomistic (a) and CG (b) representations of sxPCHD polymer.

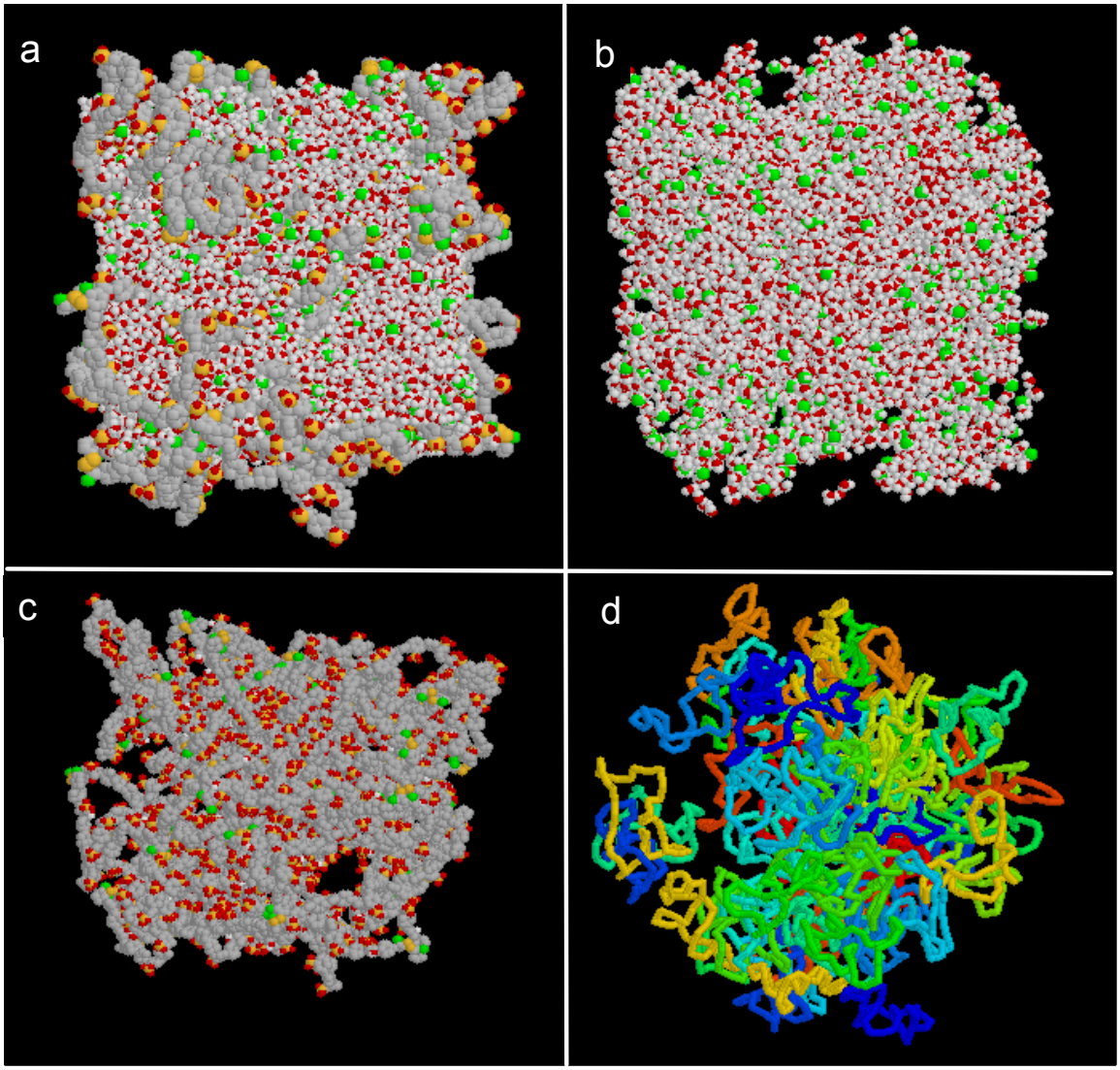

Figure 7.2. Snapshots of equilibrium configurations from atomistic ((a), (b) and (c)) and CGMD ((d)) simulations of sxPCHD membrane at T = 353 K, p = 1 atm. In atomistic simulation, water and hydronium ion are treated explicitly (a). From (a), water and hydronium ion (b), and sxPCHD polymer (c) are taken respectively. In CG simulation, water and hydronium ion are treated implicitly.

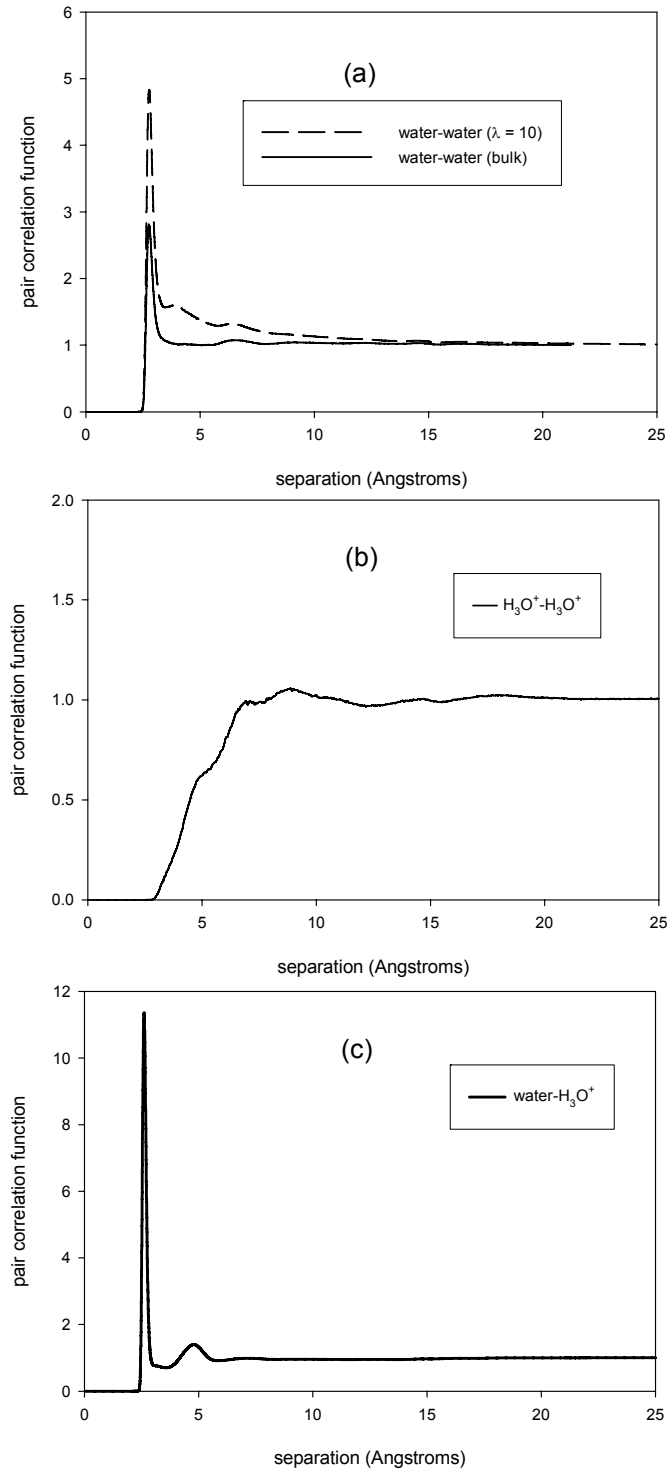

Figure 7.3. Pair correlation functions (PCFs) for CG beads involved in (a): water-water, (b): H_3O^+-H_3O^+ and (c): water-H_3O^+ interactions.

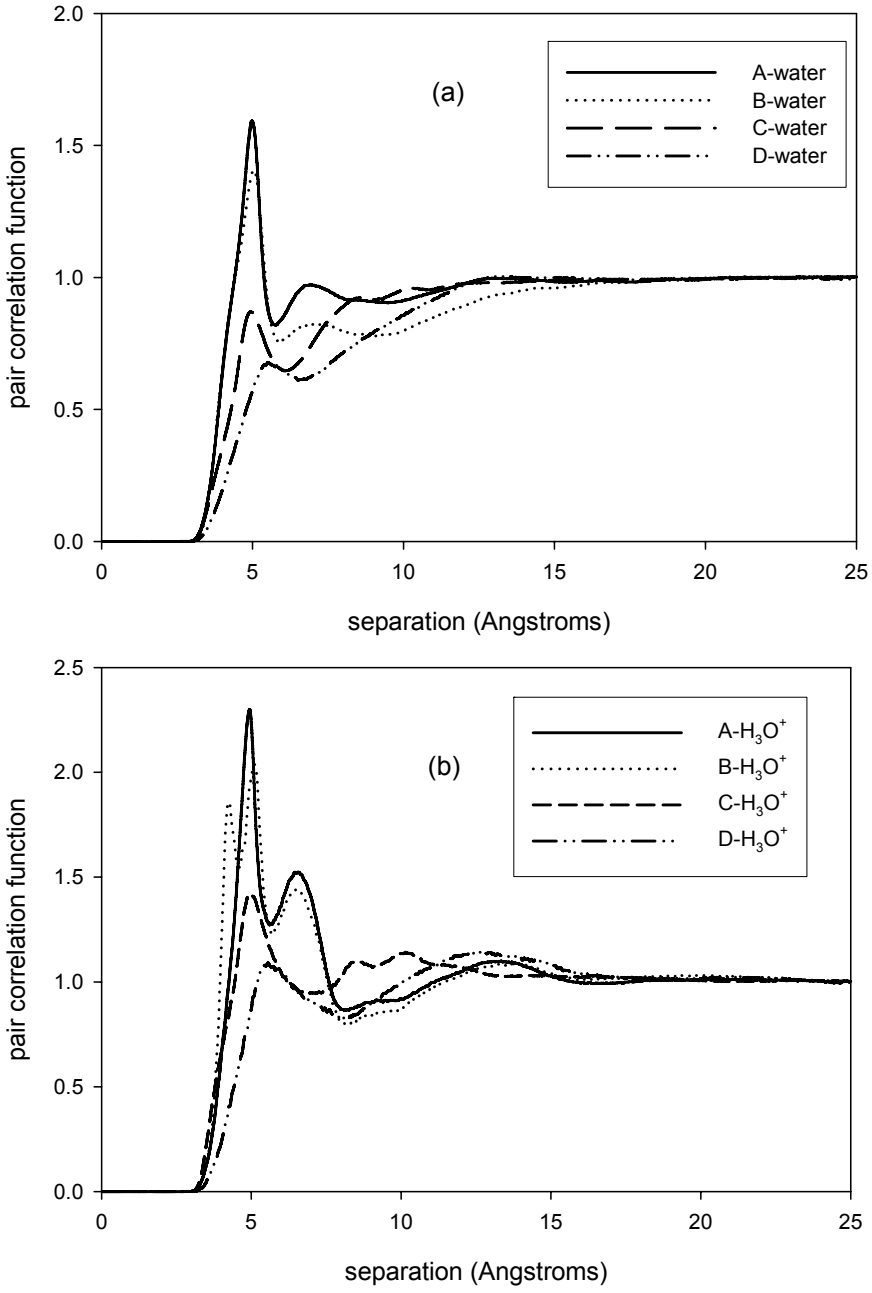

Figure 7.4. PCFs for CG beads involved in (a): polymer-water interactions and (b): polymer-H_3O^+ interactions.

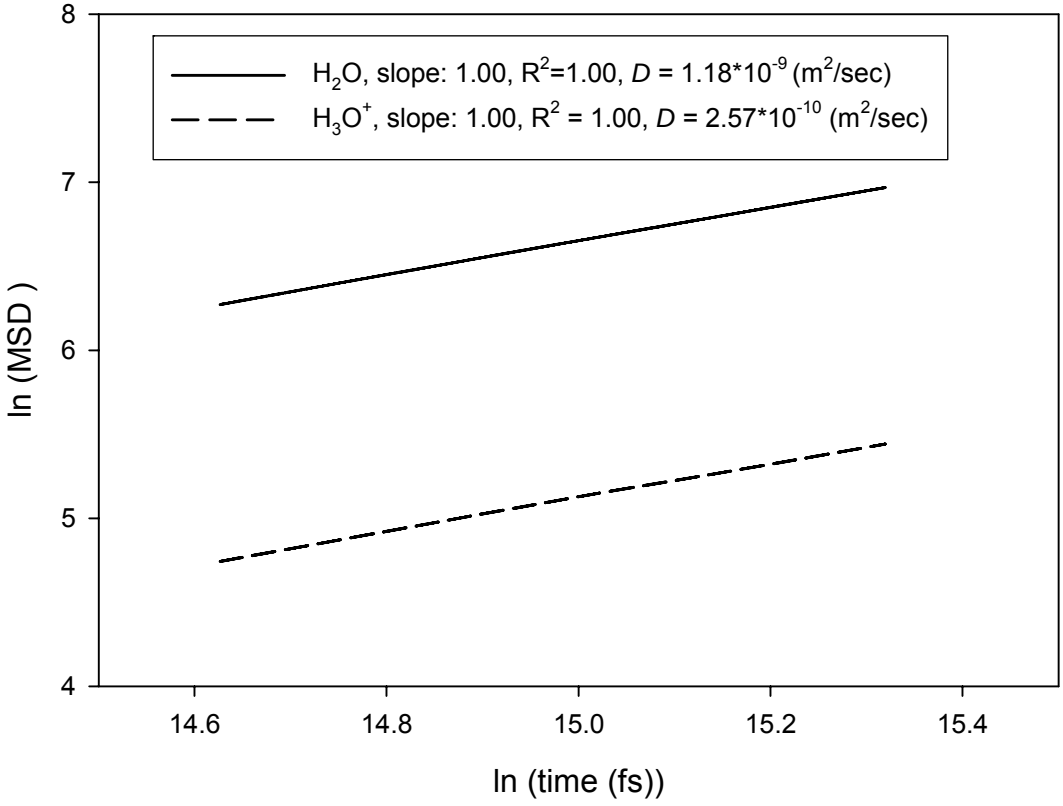

Figure 7.5. Mean square displacement (MSD) for water and hydronium ion as a function of observation time. The diffusion coefficient (*D*) for each component is also shown.

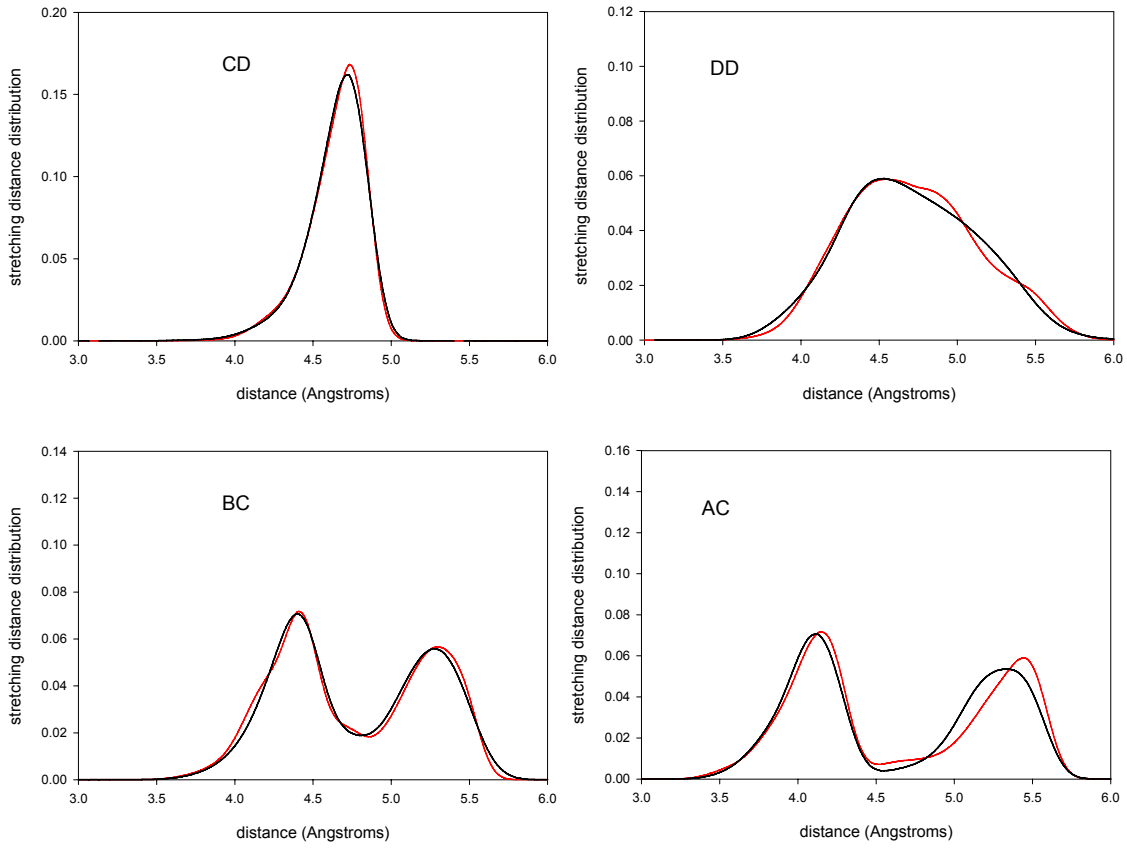

Figure 7.6. Comparison of stretching probability distribution functions (PDFs) from atomistic simulation of sxPCHD under melt (red line) and hydrated (black line) conditions. No significant change is observed.

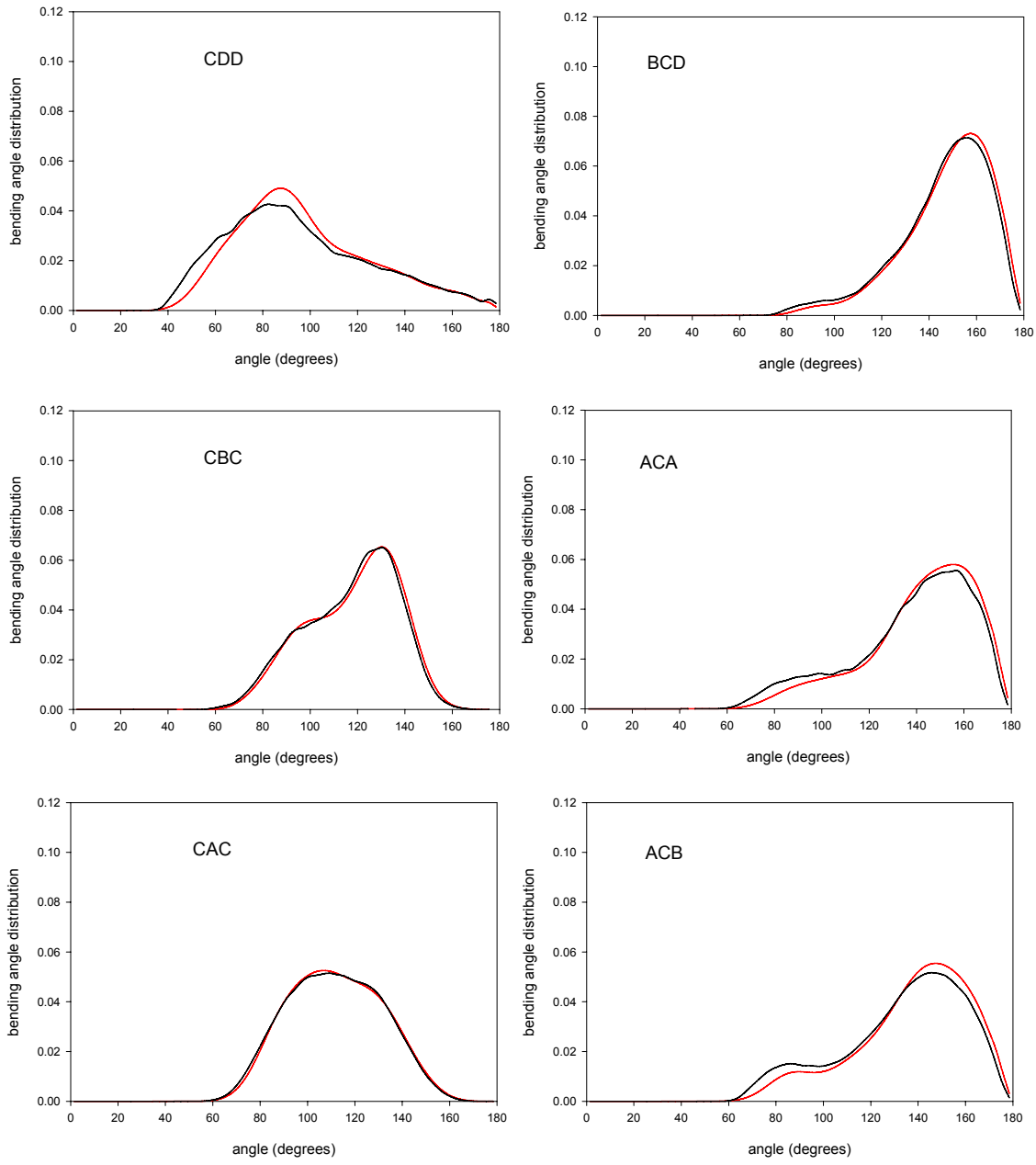

Figure 7.7. Comparison of bending probability distribution functions (PDFs) from atomistic simulation of sxPCHD under melt (red line) and hydrated (black line) conditions. No significant change is observed.

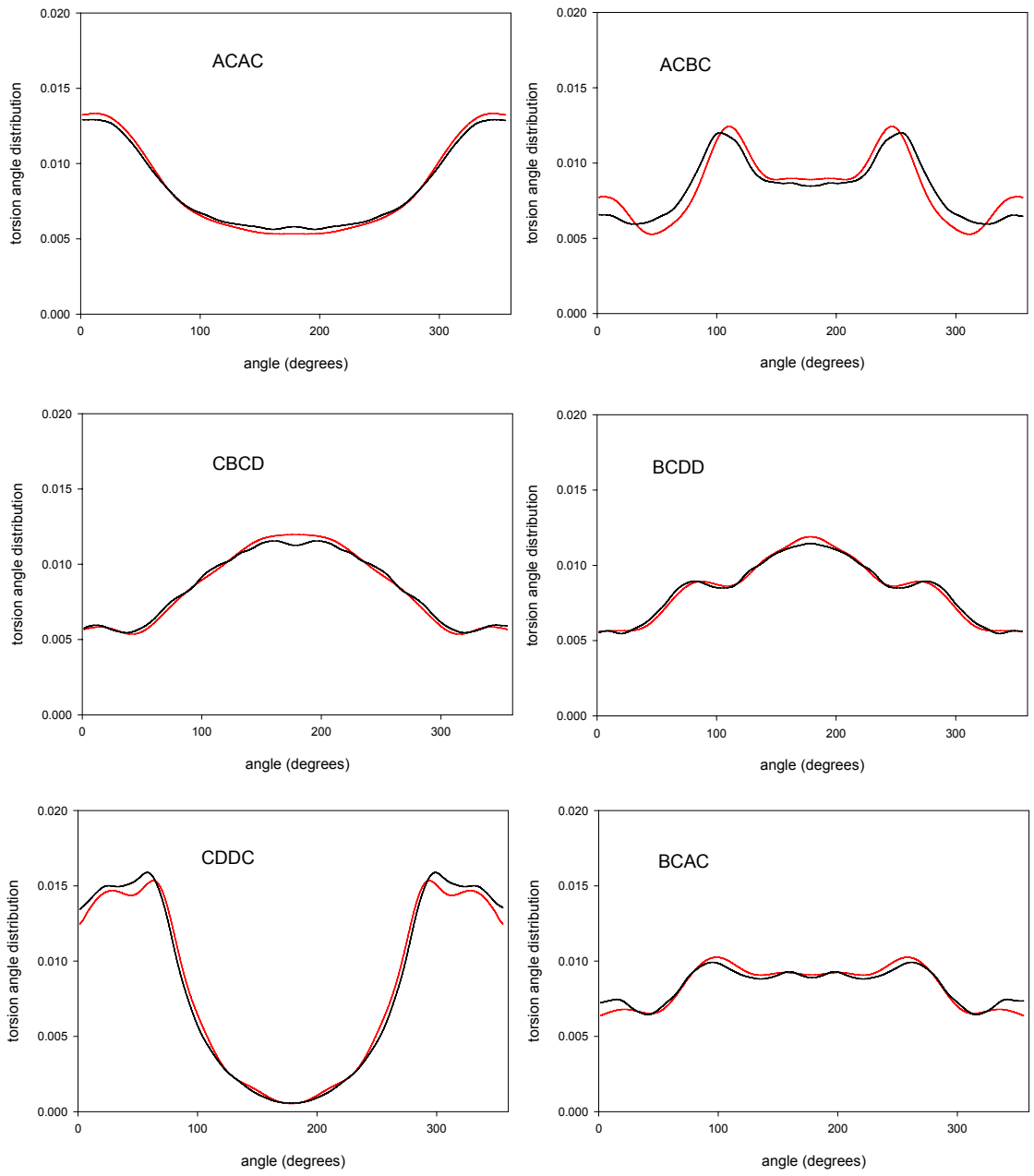

Figure 7.8. Comparison of torsion probability distribution functions (PDFs) from atomistic simulation of sxPCHD under melt (red line) and hydrated (black line) conditions. No significant change is observed.

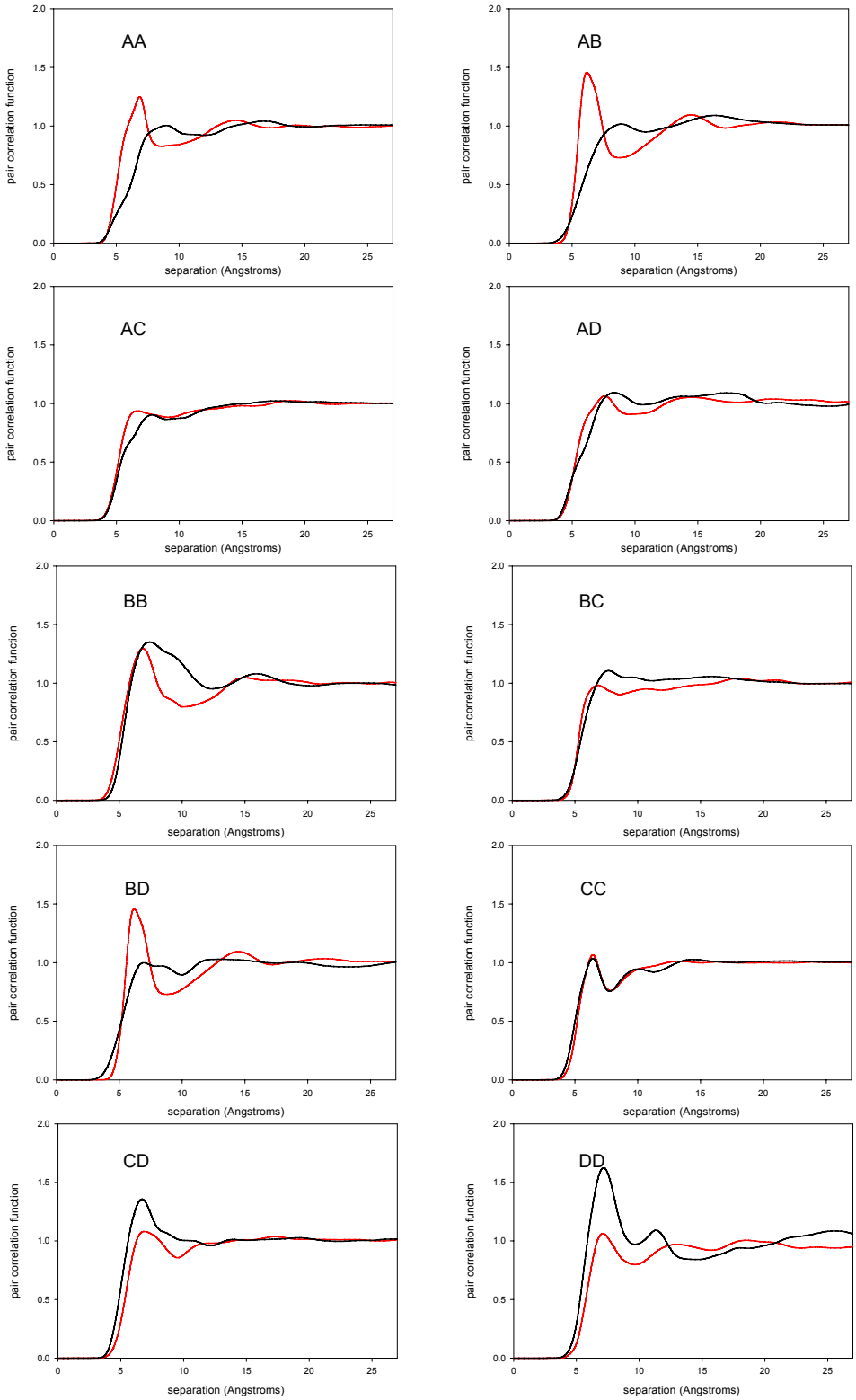

Figure 7.9. Comparison of PCFs from atomistic simulation of sxPCHD under bulk (red line) and hydrated (black line) conditions. Great changes are observed.

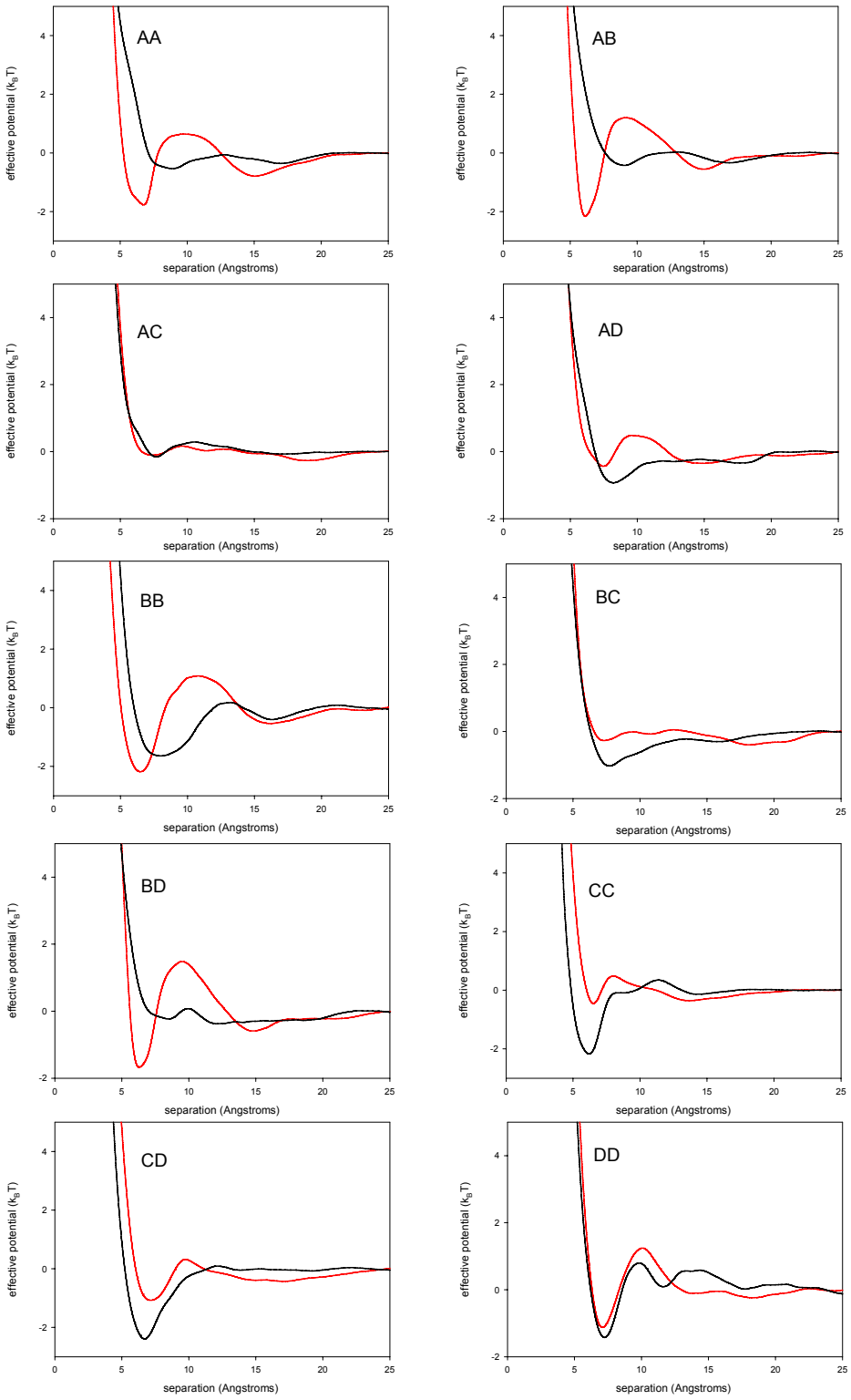

Figure 7.10. Comparison of CG potentials from IBI method for sxPCHD under melt (red line) and hydrated (black line) conditions. Great changes are observed.

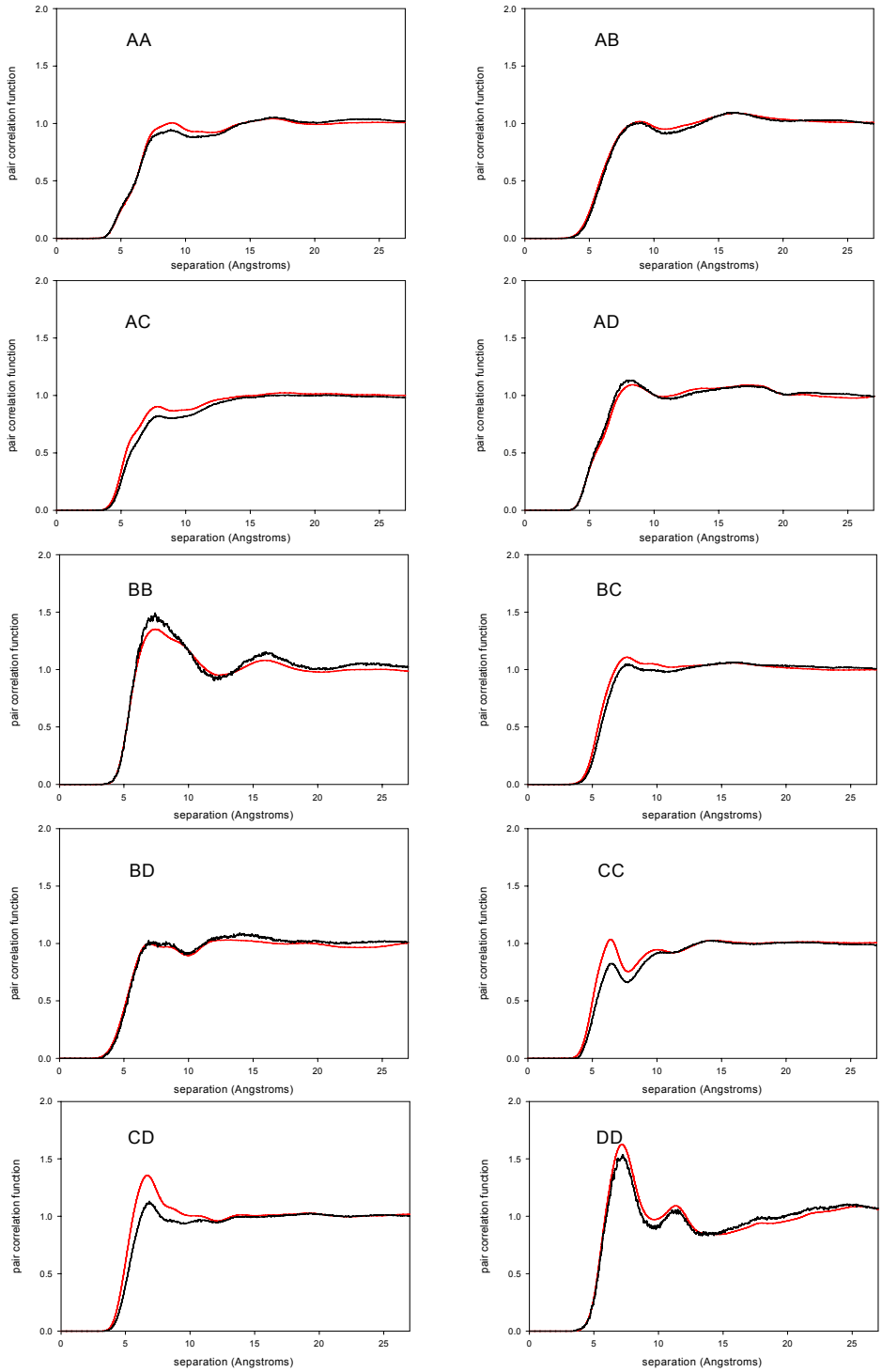

Figure 7.11. Comparison of PCFs from atomistic (red line) and CG simulation (black line) using effective potential from the IBI method.

CHAPTER 8

Conclusions

In this final part, the conclusions from each chapter are summarized, followed by the overall impact on current work and some future proposed work.

8.1. CHAPTER SUMMARIES

In this work, a CG based multi-scale modeling technique was applied to different polymeric systems. These systems include: bulk PET, bulk PEG, bulk sxPCHD and hydrated sxPCHD. Both $OZPY^{-1}$ and IBI method have been explored to parameterize the CG force fields. The structural, thermodynamic and transport properties of the polymers at different time and length scales were studied though CG level simulation. The main conclusions from each chapter are summarized in the following paragraphs.

In Chapter 2, the OZPY theory was used to generate interaction potentials from PCFs for monatomic and diatomic Lennard-Jones fluids. The $OZPY^{-1}$ procedure is completely self-consistent for the monatomic fluid in the whole range of densities studied (reduced density up to 0.55, under reduced temperature 2.0). In the diatomic case, we find that the procedure is generally self-consistent under both low and high densities, although there is a systematic deviation at high densities. The method is able to reproduce the two parameters (ε and σ) of the input Lennard-Jones potential model to within about 1%.

In Chapter 3, MD simulations of PET oligomers were performed in the isobaric-isothermal (NpT) ensemble at a state point typical of a finishing reactor. The oligomer size ranged from one to ten repeat units. Structural, thermodynamic and transport properties were calculated for systems with different oligomer size. The distribution of the end-to-end distance is bimodal for the dimer and gradually shifts to a single peak as the degree of polymerization (DP) increases. The scaling exponents for the average chain radius of gyration and end to end distance are 0.594 and 0.571, respectively. The values of the heat capacity, isothermal compressibility, and thermal expansivity agree well with the available experimental data, which are of much longer PET chains. The scaling exponents for the self-diffusivity and zero-shear-rate viscosity are respectively -2.01 and 0.96; the latter one is close to the theoretical predictions 1.0 for short chain polymers.

In Chapter 4, a CG model of PET was developed and implemented in CGMD simulations of PET chains with degree of polymerization up to 50. The CG potential was parameterized to

structural distribution functions obtained from atomistic simulations using $OZPY^{-1}$. The CGMD simulation of PET chains satisfactorily reproduced the structural and dynamic properties from atomistic MD simulation of the same systems. For the longest chains, we found the scaling exponents of 0.51, 0.50 and -2.00 for average chain end-to-end distance, radius of gyration and self-diffusivity respectively. The exponents are very close to the theoretical values of entangled polymer melt systems (0.50, 0.50 and -2.0). The study of entanglement in the longer chains shows that the tube diameter, number of monomers between entanglement points and interentanglement strand length are in close agreement with the reported values for entangled PET melt.[1]

In Chapter 5, a CG model of PEG was developed and implemented in CGMD simulations of PEG chains with degree of polymerization (DP) 20 and 40. The CG nonbonded potential was parameterized to the PCF using both $OZPY^{-1}$ and a combination of $OZPY^{-1}$ with the IBI method ($OZPY^{-1}$+IBI). As a simple one step method, the $OZPY^{-1}$ method possesses an advantage in computational efficiency. Using the potential from $OZPY^{-1}$ as an initial guess, the IBI method showed fast convergence. The CGMD simulations of PEG chains with DP = 20 using potentials from both methods satisfactorily reproduced the structural properties from atomistic MD simulation of the same systems. The $OZPY^{-1}$+IBI method yielded better agreement than the $OZPY^{-1}$ method alone. The new CG model and CG potentials from $OZPY^{-1}$+IBI method were further tested through CGMD simulation of PEG with DP = 40 system. No significant changes were observed in the comparison of PCFs from CGMD simulations of PEG with DP = 20 and 40 systems, indicating that the potential was independent of chain length.

In Chapter 6, atomistic and CG models of sxPCHD were developed and implemented in MD simulations of sxPCHD chains with architectures that are specifically aimed for application as a proton exchange membrane used in fuel cells. An atomistic force field for the architectures was tested and applied in the atomistic MD simulation of sxPCHD for the first time. The CG nonbonded potential was parameterized to the PCF using the IBI method. The CGMD simulations of cross-linked sxPCHD system using potentials from above method satisfactorily reproduced the structural properties from atomistic MD simulation of the same system. The new CG model and CG potentials was further tested through CGMD simulation of sxPCHD with three chains cross-linked system. No significant changes were observed on the comparison of

PDFs and PCFs from CGMD simulations of two chains and three cross-linked systems.

In Chapter 7, atomistic and CG models of sxPCHD were further applied in hydrated sxPCHD membrane system. The atomistic level simulation generated sxPCHD structures in an aqueous environment. The effective potentials obtained from IBI method for sxPCHD polymer in hydrated membrane, where water and hydronium ion were made implicit, satisfactorily reproduce the structural properties from atomistic MD simulation of the same system, where water and hydronium ion was explicit. Both the structures and potentials are greatly different from that of bulk sxPCHD.

8.2. SIGNIFICANCE

In this work, both atomistic MD and CGMD simulation approaches have been used to study the structural, thermodynamic and transport properties of polymeric systems at equilibrium. The atomistic MD was used to parameterize the CG effective potentials. The dissertation focused on both the development of techniques for generating CG potentials as well as the application of CG potentials in CGMD simulations. It is approached through three categories of efforts. The first effort was to develop an improved procedure for generated CG potentials from structural data obtained from atomistic simulation of short chains. An inverse procedure based on the Ornstein-Zernike integral equation with the Percus Yevick approximation ($OZPY^{-1}$) was developed to meet this purpose. The applications on monatomic and diatomic Lennard-Jones fluid, showed that the $OZPY^{-1}$ method is simple, fast and straightforward, compared with existing methods on obtaining the effective potentials. Since it is based sound statistical mechanics, the method also has an advantage on computational accuracy. Moreover, it can be generalized to different systems of interests since the only input needed is structural distributions (PCFs).

The second effort was to apply the $OZPY^{-1}$ to CG modeling of PET and PEG. In the case of PET, we performed a thorough analysis of structural, thermodynamic and transport properties from the monomer to a DP of 50. The information can help modeling of finishing reactor of PET production. We were able to study these properties' chain length dependence and extract the scaling exponents. The information can be used to study polymer physics. For example, by studying the scaling exponents from polymer physics, we were able to show for each property

where they obeyed Rouse-like behavior at short chain lengths, where they obeyed reptation theory at long chain lengths, and where deviations from these theoretical expectations occurred. In the case of PEG, we developed an understanding of the strengths and limitations of various procedures for generating CG potentials. In a CG model that have only one or two types of CG beads, both $OZPY^{-1}$ and IBI methods can satisfactorily reproduce the structural properties from atomistic MD simulation while the $OZPY^{-1}$ method has advantage on computation efficiency. As the complexity of the CG model increases, the traditional IBI method begins to show its advantage on generating effective CG potentials. As the local environment becomes heterogeneous around each bead, the traditional IBI method may also fail. This understanding will eventually help the future application of CG procedure to different polymeric systems.

The third effort was to apply the CG procedure to a model sulfonated and cross-linked Poly (1, 3-cyclohexadiene) (sxPCHD) polymer that is designed for future application as a proton exchange membrane material used in fuel cell. The traditional IBI method proved successful for the homogeneous sxPCHD melt, which had four types of beads. Using the effective potentials from the IBI method, the CGMD simulations generate structures of sxPCHD melt with different architecture, which will help understanding the properties of this membrane material. Even the traditional IBI method failed for the heterogeneous hydrated sxPCHD membrane, which had six types of beads. There the solution involved the implicit incorporation of some bead types into the CG potentials of the remaining beads. Using the derived potentials, the CGMD simulation provides the first glimpses of the nanoscale morphology of the hydrated membrane. An understanding of this structure is important in the prediction of proton conductivity in the membrane. Subsequent design of membranes can be guided by the understanding of this structure/property relationship.

All these efforts will eventually provide understanding on (i) polymer physics at different time and length scales, (ii) strengths and limitations of various CG effective potential generation methods, and (iii) polymer structures in melt and solution under effective CG level interactions. These understandings will help on new polymer product development, polymer processing technology improvement and new application design.

8.3. FUTURE WORK

The findings based on current work enable us to foresee some future work. First, the $OZPY^{-1}$ method can be applied to various CG modeling systems, including polymer melt, polymer solutions, simple fluid either pure or mixture. It has been successfully applied to obtain the effective potentials for the nanoparticles in suspension.[2] Since density is a key issue in the OZPY theory, an iterative method can be developed in the future to improve the performance of the $OZPY^{-1}$ method on high density liquid.

Second, the dynamic properties for long chain polymeric systems can be further studied with a better understanding of the artificially accelerated dynamics in CG level simulation. Some efforts have been made towards this direction by the other groups.[3,4] For both the Rouse and reptation model, the local motion is governed by a scalar friction coefficient. For modeling of a polymer melt, the bead friction depends on the specific model used to represent the polymer. Compared with atomistic model, softer potentials result in a reduced friction coefficient and faster dynamics in the CG model. The problem can be solved by introducing a time scaling factor based on mapping of mean squared displacement (MSD) from CGMD simulation to that of atomistic MD simulation. All dynamic properties (D, η) can be scaled using this single time scaling factor.

Third, Since the CG force fields for sxPCHD and PEG have been parameterized, Molecular level structures at large length scales can be studied using the proposed CG models. Then water and proton transport can be further studied using a procedure developed by the group.[5-7] An analytical model for water and charge transport in highly acidic and highly confined systems such as proton exchange membranes of fuel cells was developed in that work. The model accounts for three factors in the system including acidity, confinement, and connectivity. The model uses the concentration of H_3O^+ ion to characterize acidity, interfacial surface area per water molecule to characterize confinement, and percolation theory to describe connectivity. Once the system is defined, the acidity is known. The CGMD simulation can provide information on confinement and connectivity. This procedure and the transferability of the obtained CG potentials can be further tested through the applications on CG simulation sxPCHD/PEG blends and sxPCHD-PEG copolymers, using procedures described in the literature.[8]

References

[1]K. Kamio, K. Moorthi, and D. N. Theodorou, Macromolecules **40**, 710 (2007).

[2]G. S. Grest, Q. F. Wang, P. in't Veld, and D. J. Keffer, J. Chem. Phys. **134** (2011).

[3]J. McCarty and M. G. Guenza, J. Chem. Phys. **133** (2010).

[4]I. Y. Lyubimov, J. McCarty, A. Clark, and M. G. Guenza, J. Chem. Phys. **132** (2010).

[5]E. M. Calvo-Munoz, M. E. Selvan, R. C. Xiong, M. Ojha, D. J. Keffer, D. M. Nicholson, and T. Egami, Phys. Rev. E **83** (2011).

[6]M. E. Selvan, E. Calva-Munoz, and D. J. Keffer, J. Phys. Chem. B **115**, 3052 (2011).

[7]V. A. Harmandaris, D. Reith, N. F. A. Van der Vegt, and K. Kremer, Macromol. Chem. Phys. **208**, 2109 (2007).

[8]D. Bedrov, C. Ayyagari, and G. D. Smith, J. Chem. Theory Comput. **2**, 598 (2006).

Vita

Qifei, Wang was born in Dehui, Jilin (China) on May 13, 1980. He grew up in the same town and did his schooling in Dehui Shiyan high School. After graduating high school in 1999, He went to Dalian Polytechnic University, Liaoning (China), where he received a Bachelor of Science Degree in Polymer Materials Science and Engineering in 2003. After then he continued his study on polymer science in Shanghai JiaoTong University (China). He received a Master of Science Degree in Polymer Chemistry and Physics in 2006. He then worked as a Technical Service Engineer at LG Chem company and Research and Development Lab Engineer at BASF Polyurethane Specialties (China) company. In August 2007, he started his Ph.D. study in the Department of Chemical and Biomolecular Engineering at the University of Tennessee, Knoxville, TN (USA). His PhD research focused on the computational study of polymeric materials' structures and properties using multi-scale modeling and molecular simulation techniques.

Qifei, Wang completed his doctorate in Chemical Engineering at the University of Tennessee, Knoxville, TN, in August, 2011.